Etude numérique des paramètres de contrôle du couplage entre l'hémodynamique artérielle et le stent à élution médicamenteuse

Jianfei Song

▶ **To cite this version:**

HAL Id: tel-03407901

https://pastel.hal.science/tel-03407901

Submitted on 28 Oct 2021

THÈSE

Présentée par : **Jianfei SONG**

Soutenue le : **15 Février 2021**

Pour obtenir le grade de : **l'École Nationale Supérieure d'Arts et Métiers**

Spécialité : **Biomécanique et ingénierie pour la santé**

Numerical study of control parameters on hemodynamic and drug eluting stent coupling

DIRECTEUR DE LA THÈSE :

Professeur Smaïne KOUIDRI

ET CO-DIRECTEUR DE LA THÈSE :

Professeur Farid BAKIR

Jury

R. BENNACER	Prof. ENS Paris-Saclay, LMT	Président	**T**
A. TREMANTE	Prof. Florida International University	Rapporteur	**H**
I. VALLET	Dr. HDR MC Sorbonne Université	Rapporteur	**È**
F. KOSKAS	Prof. chirurgien vasculaire, Hôpital Pitié-Salpêtrière	Examinateur	
B. MAUREL	Prof. chirurgienne, Département de chirurgie vasculaire, CHU de Nantes	Examinatrice	**S**
F. BAKIR	Prof. Arts et Métiers, LIFSE	Examinateur	
S. KOUIDRI	Prof. Arts et Métiers, LIFSE	Examinateur	**E**

Acknowledgements

Contents

List of Tables

List of Figures

Nomenclature

Fluid-related parameters

μ Dynamic viscosity

ν Kinetic viscosity

ρ Density

Geometrical and structural parameters

$2D$ Two dimensional

$3D$ Three dimensional

a Stent length

AS Aspect ratio of stent

e Tissue thickness

L Artery length between stenosis and tortuosity

L_1, L_2, L_3 Horizontal length of recirculation formed in bifurcated artery

l_2 Stenosis length at main branch

L_{pH}, L_{dH} Horizontal length of recirculation

L_{pV}, L_{dV} Vertical length of recirculation

R Radius

s Stenosis length at side branch

Dynamic and temporal parameters

$\dot{\gamma}$ Shear rate

ω Angular frequence

$\overline{u}, V_0$ Time-averaged cross sectional mean velocity

τ Shear stress

f Frequency

p Pressure

$P(t)$ Instantaneous pressure

$Q(t)$ Instantaneous flow rate

U, u Flow velocity

V Sectional mean velocity

$V(t)$ Instantaneous sectional mean velocity

$V_{0,os}$ Oscillating component of cross sectional mean velocity

Dimensionless parameters

Pe Peclet number

Re Reynolds number

Re_{ta} Time-averaged Reynolds number

Wo Womersley number

Parameters related to mass transfer

β Dissolution rate

ϕ Porosity

B Initial drug concentration

b Drug concentration in solid state

B_{max} Density of binding site

c Drug concentration in dissolved state

c_f Drug concentration in flow domain

c_p Drug concentration in polymer domain

c_t Drug concentration in tissue domain

D Diffusion coefficient

D_f Diffusion coefficient in flow domain

D_p Diffusion coefficient in polymer domain

D_t Diffusion coefficient in tissue domain

k Total binding coefficient

k_b Association rate

k_u Dissociation rate

M_0 Initial drug mass in polymer

M_t Instantaneous mass release from polymer

R_i Reaction term

S Solubility of drug in fluid

Other Parameters

S_p Surface percentage for WSS below 0.5 Pa

S_{TA} Artery surface for TAWSS below 0.4 Pa

Abbreviations

AoB Angle of bend

BMS Bare metal stent

bpm beats par minute

CDP Pressure drop coefficient

CFD Computational fluid dynamic

CFL Courant–Friedrichs–Lewy

CR Curvature radius

CT Coronary tortuosity

DES Drug-eluting stent

LAD Left anterior descending coronary artery

LFC Lesion flow coefficient

LM Left main artery

OSI Oscillatory shear index

PU Polyurethane

RPD Relative pressure drop

RRT Relative residence time

$SMCs$ Smooth muscle cells

$TAWSS$ Time-averaged wall shear stress

$TAWSSGs$ Time-averaged WSS gradient in space

WSS Wall shear stress

Introduction

Cardiovascular disease has occupied 1/3 deaths in developing and developed countries. Atherosclerosis is one of the most serious and common forms of cardiovascular disease caused by the accumulation of fatty deposits, cholesterol, and calcified materials in arterial wall, especially in coronary artery. Based on the clinical statistics, coronary artery is more prone to form stenosis compared to most of the other arteries. Any disorder or disease of coronary artery can cause one in dangerous condition with a heart attack or stroke. As a consequence of atherosclerosis, the narrowed artery is developed leading to reduction of blood supply to heart (myocardial ischemia), lack of oxygen (hypoxia) or cell damage (necrosis). Thus confronting this huge threat to our lives, several effective treatments have been developed and utilised in practice through tremendous efforts of researchers such as balloon angioplasty, bare metal stent (BMS) and drug-eluting stent (DES). However, the follow-up complications still require the optimizations of the current treatments. Balloon angioplasty was developed as the first non-surgical procedure to enlarge the obstructed arteries commonly followed by the restenosis in response to the vessel wall injury caused by balloon expansion. BMS improved the clinical outcomes by reducing the restenosis rate but still of more than 20% through positioning a inflated metal mesh at the blockage site. In an attempt to reduce this rate further, DES was put forward with the BMS coated by anti-proliferative drugs. The incidence of in-stent restenosis was reduced to less than 5% through the inhibition of intima proliferation. However, the late thrombosis followed can cause a sudden occlusion of an artery. Thus confronting the two major causes (restenosis and thrombosis) of stent failure, having a thorough understanding of pathology and mechanisms of disease occurrence is highly necessary currently.

Blood as a type of biofluid owns quite complicated physical and hemodynamic properties especially in the artery with irregular diameters, curvatures and even bifurcations. Stenosis and stent are both considered to be the geometrical singularities of artery resulting in the flow disturbance. Low shear rate is found to benefit the proliferation of muscle cells in artery wall especially at the recirculation regions upstream and downstream the strut. The variations of hemodynamic parameters have been commonly focused and used to predict the potential disease sites in the existing studies. Moreover, the alterations of hemodynamics are greatly related to the arterial geometrical singularities such as the presence of stent. In addition to the human factors, the stent performance is strongly related to the implanting ways taken by cardiologist, the geometrical designs of stent and even the pharmaceutical principle in the case of DES.

Based on the current state of knowledge related to this subject, great efforts are still needed to master the internal mechanisms and improve the stent performance as a number of questions keeps open and need to be resolved. Thus the present study is put forward aiming to acknowledge the hemodynamics in the human body and avoid the alterations caused by the sent. The active stent has been concerned as well. Specific interest has been given to the mass transfer from polymer into lumen and tissue. The research works achieved during this thesis have been displayed as follows:

- Numerical and mathematical modeling establishment followed by the preliminary study: effects on flow topology and hemodynamic variations caused by arterial geometrical singularities: arterial bifurcation and tortuosity. The potential sites and orientation of stenosis development affected

by the specific arterial geometrical singularity have been evaluated. In order to have a direct guidance to clinical treatment from numerical works, the diagnostic analysis has been adopted to give evaluations which has not been paid enough attention yet.

- With the necessary requirement of stent performance optimization, the interaction between stent design factors and hemodynamic variations has been analyzed in the cases of 2D and 3D models respectively. Interspace between struts and aspect ratio (AR) of strut section have been focused as the important design factors of stent. Evaluations have been made based on the wall shear stress (WSS)-based descriptors and flow topology.

- Coupling between flow mechanics and mass transfer from DES has been carried out. 2D model of DES in coronary artery has been built based on the validation that the drug distribution in tissue tends to be symmetrical radially in 3D model and a good fitting of drug release from polymer between 2D and 3D cases. Mass transfer process from DES into lumen and tissue has been investigated with considerations of several controlling parameters. The effects of disturbed flow on drug concentration have been discussed as well. In addition to the numerical works, experimental works have been carried out as well focusing on the drug release process from polymer. Different initial drug dosages (10%, 20% and 30%) in polymer has been investigated with the drug release profiles in each case. The corresponding diffusion coefficients are calculated based on the experimental data along with a good fitting with numerical results respectively. Based on the determination of diffusion coefficients in these three conditions, a linear relationship has been predicted between initial drug dosage and diffusion coefficient in polymer. A good comparison has been achieved between numerical and experimental results with the case of 15% drugs in polymer through the linear prediction of diffusion coefficients.

State of the art

Contents

In this chapter, an introduction of investigation background is well displayed firstly aiming to lay a strong foundation about cardiovascular disease. The physiological and hemodynamic characteristics are presented focusing on coronary artery. The development of diseases and treatments is stated in order to indicate the direction of the present study. Literature reviews regarding bare metal stent (BMS) and drug-eluting stent (DES) are then discussed. The motivations are finally introduced contributing to the framework of the current research works.

1.1 Physics in coronary arterial system

Cardiovascular disease is responsible for 1/3 deaths in developing and developed countries for people over 35 years old especially in western countries [1, 2]. Coronary circulation as a part of highly sophisticated cardiovascular system acts a key role to supply blood flow to the heart for meeting matabolic needs [3]. A disruption in blood flow due to obstructive disease in coronary vessels is a common form of heart disease affected by aging, smoking and drinking, etc. Fatty deposition on vessel wall can happen as a result of slowed metabolism. Over time the deposition will be developed into plaques blocking blood flow termed as atherosclerosis. As shown in Figure 1.1, more complicated conditions are developed over time along with calcification cores and even plaque ruptures. Meanwhile, the formation of clot (thrombosis) leads to the more risky conditions. Due to the extensive and continued efforts from clinicians and researchers worldwide, significant advancements in clinical treatments have been made especially in the last decade. Nowadays the use of stent is widely accepted by patients to recover the narrowed arteries [4]. Immediate relieve of patients can be achieved for urgent cases by means of stent strategy. However, the follow-up complications can not be neglected due to the hemodynamic variations. Therefore, a better understanding of the physical and mechanical characteristics of blood flow is required necessarily for the optimisation of stent performance. The relationship between variations of hemodynamic parameters and stent design factors has caused many researchers' attention [5]. Moreover, based on the clinical statistics, coronary artery is more prone to form stenosis compared to most of other arteries. Therefore, the mechanisms inside coronary artery will be the main focus for the current study.
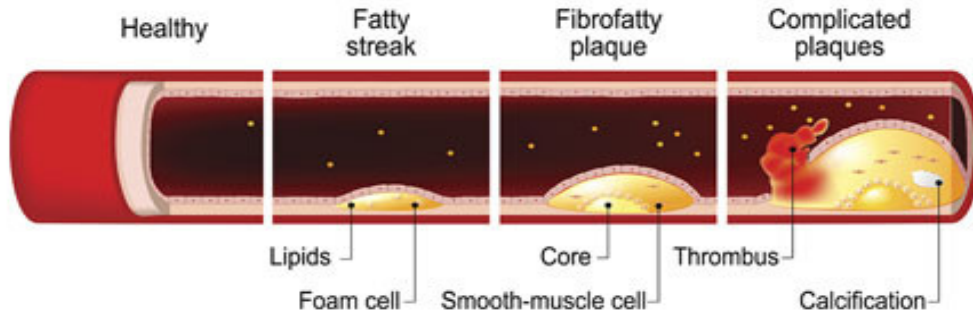
Figure 1.1: The formation of plaques

Coronary arteries in the circulation system are shown in Figure 1.2 mainly including left coronary arteries and right coronary arteries. Arterial bifurcation and tortuosity as two conspicuous geometrical characteristics have been observed. Normally, coronary circulation as the first branch of aorta can ensure sufficient blood supply to the heart. Blood flow in coronary circulation of one person is about 250 ml/min at rest [6], which can be increased to $1-1.5\ l/min$ during exercise condition in order to meet the oxygen demand of myocardial fibers. Due to the important role of carrying blood flow to heart, any disorder or disease of coronary artery can cause one in dangerous condition with a heart attack or stroke.
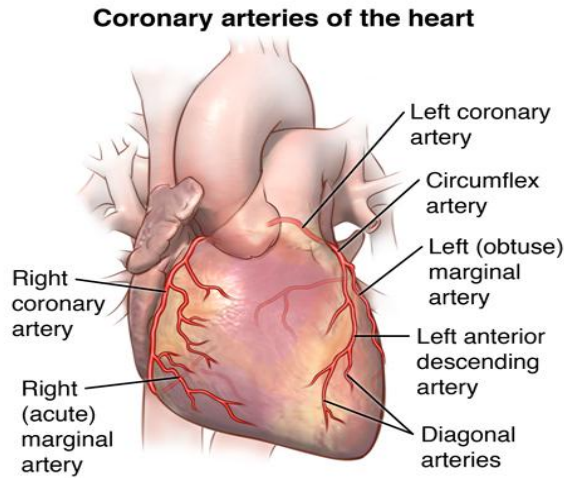
Figure 1.2: Coronary arteries in the circulation system

Atherosclerosis occurs along with the buildup of plaques on vessel wall which is the direct disease location. Therefore, the vessel wall structure of coronary artery is studied through Figure 1.3 in order to acknowledge the physics in tissue. A healthy coronary artery wall mainly consists of three distinctive parts [7]: intima, media and adventitia. The intima facing lumen is formed of lined endothelial cells, and also is the explicit location of lipid accumulation. Media is made of extracellular matrix, smooth muscle cells (SMCs) and external elastic lamina. Adventitia is composed of connective tissue and fibroblasts. There are several main causes for contributing to a narrowed lumen: 1) thickening of intima through proliferation of smooth muscle cells; 2) formation of scar tissue by a healing response in the adventitia; 3) hypercontraction of smooth muscle cells in the media. Among these causes, the proliferation of SMCs has been proved to play a central role in the onset of plaque. SMCs as the basic structural and functional

components in vessel wall are responsible for its homeostasis. An imbalance in their functions inevitably results in wall dysfunction and vascular disease. As a response to various environmental stimuli such as changes in blood flow patterns, growth factors, and cell to matrix interactions, SMCs are capable to switch from the contractile phenotype to a proliferative phenotype. Especially in reaction of artery injury, the activated proliferation of SMCs can finally lead to the vascular disease.
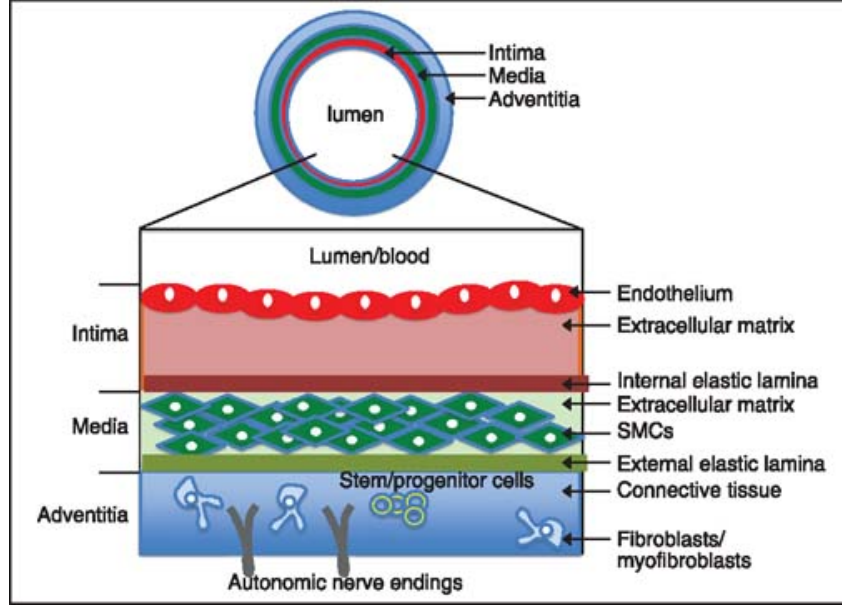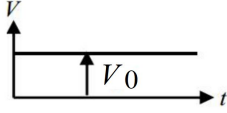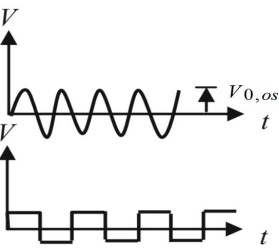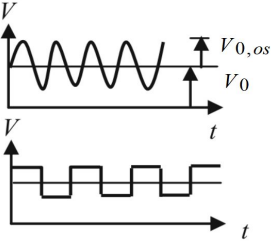
Figure 1.3: Blood vessel wall composition [7]

Blood flow as the main body in artery needs to be paid more attention regarding its physical and dynamical properties. Even though many of the existing investigations assume the blood flow as steady [8–11], it's known actually that blood flow is a typical pulsating flow [12]. Pulsating flow as a type of periodic flow oscillates around a non-zero mean value. Similarly, oscillatory flow as another periodic flow oscillates around a mean value of zero [13,14]. In Table 1.1, comparisons are made among different types of flow in view of mechanical definitions [15]. The velocity for pulsating and oscillating flow varies periodically contrary to the time independence of velocity with steady flow. The oscillatory flow is seen as a type of special pulsatile flow with a zero steady flow component. Moreover, pulsating flow is also called Womersley flow named after John R. Womersley (1907–1958) who firstly derived the flow profiles with blood flow. The velocity profile of pulsatile flow greatly depends on the Womersley number (Wo) defined in equation 1.1. Wo represents the ratio between inertial force and viscous force, which is similar with the definition of Reynolds number Re. Figure 1.4 [16] clearly shows how flow profiles are affected by different Wo value. As can be seen that when $Wo < 2$, a parabolic profile can be maintained and the flow is dominated by the viscous force. When $Wo \geq 2$, the flow profile gets more flattened because of the dominant inertial forces in central core and dominant viscous forces near boundary layers.

$$Wo = R\sqrt{\frac{\omega\rho}{\mu}} \tag{1.1}$$

Where R is artery radius, ω is angular frequency, ρ is density and μ is dynamic viscosity.

3

Table 1.1: Definitions and related terminology in steady and periodic flows [15]

Type of flow	Steady	Oscillating	Pulsatile
A typical velocity-time record			
Velocity	$V_{0,os}=0$	$V_{0,os} \neq 0$; $V_0 = 0$	$V_{0,os} \neq 0$; $V_0 \neq 0$
Frequency Womersley number	$f = 0$	$f \neq 0$ $\sqrt{Wo}' = R\sqrt{\omega/\nu} \neq 0$ $\omega = 2\pi f$	$f \neq 0$ $\sqrt{Wo}' = R\sqrt{\omega/\nu} \neq 0$ $\omega = 2\pi f$
Reynolds number	$Re_{ta} = \dfrac{2V_0 R}{\nu}$	$Re_{ta} = 0$	$Re_{ta} = \dfrac{2V_0 R}{\nu}$

The characteristic parameters involved in the table above are explained as follows:

- Time-averaged velocity, V_0

- Oscillating component of velocity, $V_{0,os}$

- Frequency for the periodic flow, f

- Kinetic viscosity, ν.

- Time-averaged Reynolds number, Re_{ta}.
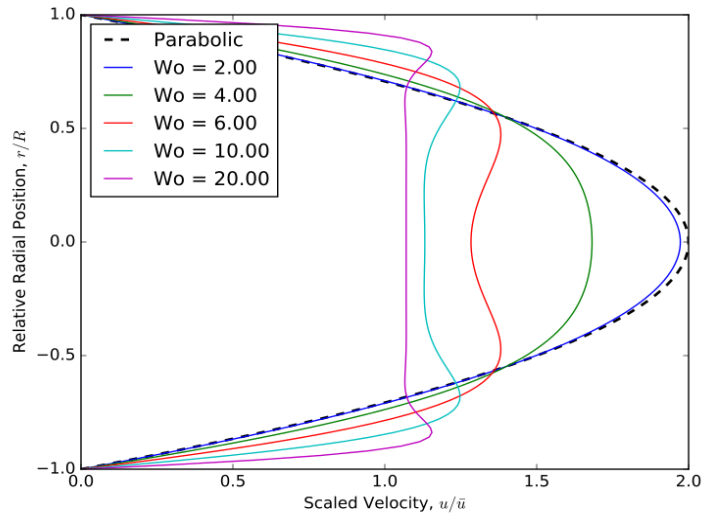
Figure 1.4: Velocity profile of pulsed flow at different Wo [16]

As we focus on blood flow in the left coronary artery for the current study, the practical flow profile has been obtained through works of N. Bénard [17] in 2005 as shown in Figure 1.5. Two phases of systole and diastole exist during one cycle of $T = 0.8s$ corresponding to heart contraction and relaxation. Systole phase happens corresponding to the heart contraction pumping blood out, afterwards diastole phase will be followed by relaxation. According to American Heart Association, the heart normally beats about $60-100$ times per minute at rest condition depending on physical condition and age. Checkout of pressure is a normal way to reflect the health condition of people in reality. The high pressure is measured during diastole process corresponding to the force of blood against artery wall. By contrast, the low pressure is measured during systole period. In table 1.2 [3], the mean blood flow parameters of several different types of vessels commonly subjected to the atherosclerosis are listed. It can be noticed that mean shear rate normally ranges from 200 to 500 s^{-1} and mean flow Reynolds number ranges from 100 to 400 among these arteries.
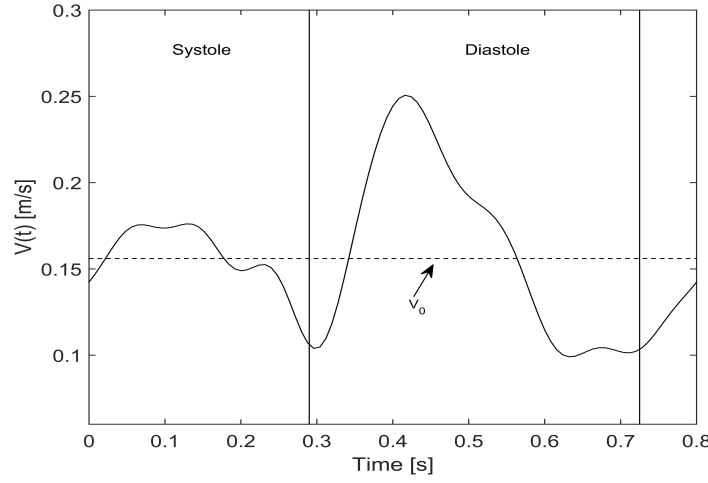
Figure 1.5: Coronary flow in one cycle at 75 bpm [17]

Table 1.2: Mean blood flow parameters for human arteries commonly subject to occlusive thrombosis in atherosclerosis [3]

Vessel	Diameter (mm)	Average flow rate (ml/s)	Mean Reynolds number	Mean wall shear rate (s^{-1})	Mean wall shear stress $(dyne/cm^2)$
Femoral artery	5.0	3.7	280	300	11
Common carotid	5.9	5.1	330	250	8.9
Internal carotid	6.1	5.0	220	220	8
Left main coronary	4.0	2.9	240	460	16
Right coronary	3.4	1.7	150	440	15

As shown in Figure 1.2 above, the morphological characteristics of coronary artery have been observed: bifurcation and tortuosity. High relevance has been found between these morphological characteristics and artery stenosis in the past two decades. Artery tortuosity exists commonly through human body. Moderate tortuosity can be asymptomatic, however, severe tortuosity can cause attacks in distal organs. Clinical studies have associated tortuous arteries with atherosclerosis, aging, genetic syndrome,

hypertension. In general, arteries with atherosclerosis show more tendency to be tortuous, however, the formation and development of tortuosity are not clear yet. A. Buradi et al. [18] simulated the blood flow in 3D tortuous artery. The time-averaged wall shear stress (TAWSS) distribution is displayed with different values of curvature radius (CR) when the angle of bend (AoB) is 150°. As known that low TAWSS means more possibilities to form plaques, the vulnerable locations for atherosclerosis have been observed as shown in Figure 1.6. H.C. Han [19] summarized various types of tortuous form through reported clinical investigations shown in Figure 1.7. They are separately named by curving, angulation, looping and spiral twisting from left to right.
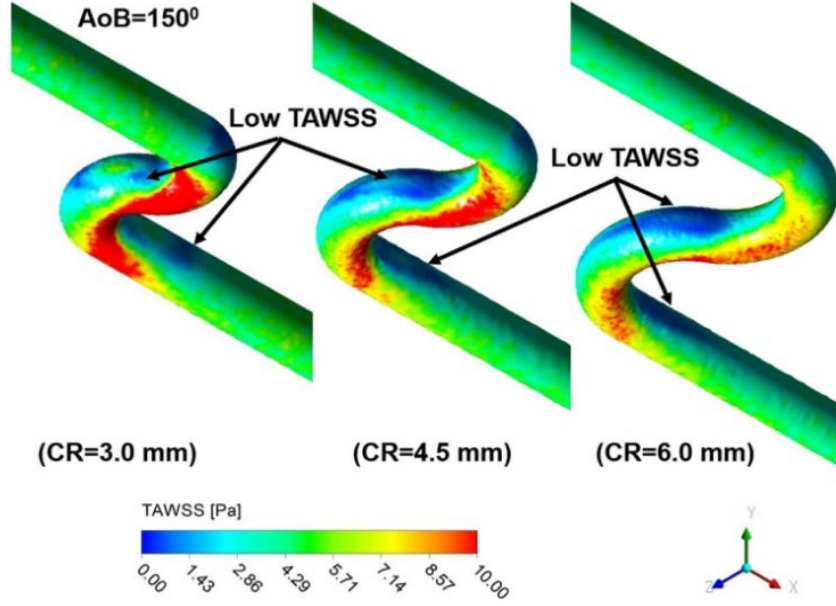
Figure 1.6: TAWSS distribution in tortuous artery of different CRs [18]
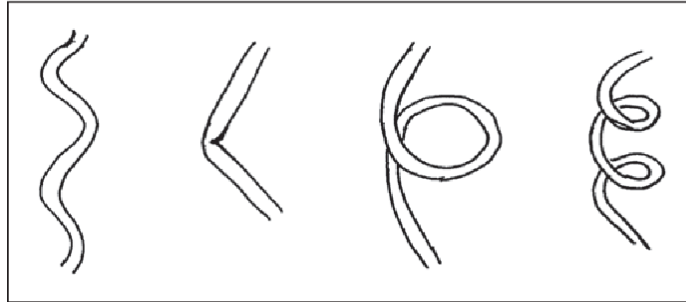
Figure 1.7: Different forms of tortuous artery [19]

Coronary bifurcation lesions can occupy 20% of percutaneous coronary intervention (PCI). According to the clinical statistics, locations near bifurcation has been the major lesion sites. As shown in Figure 1.8 [20], the bifurcated artery characterizes three anatomic segments: (1) proximal main vessel, (2) distal main vessel and (3) side branch. Many investigations have been carried out focusing on hemodynamic variations caused by the bifurcation. In the works of [21–26], the effect of different bifurcation angles, physical properties of flow and deformability of coronary bifurcation on the hemodynamic variations have been investigated. Pinto et al. [27] simulated the 3D bifurcated artery without stenosis and the low TAWSS is observed near bifurcation structure shown in Figure 1.9.
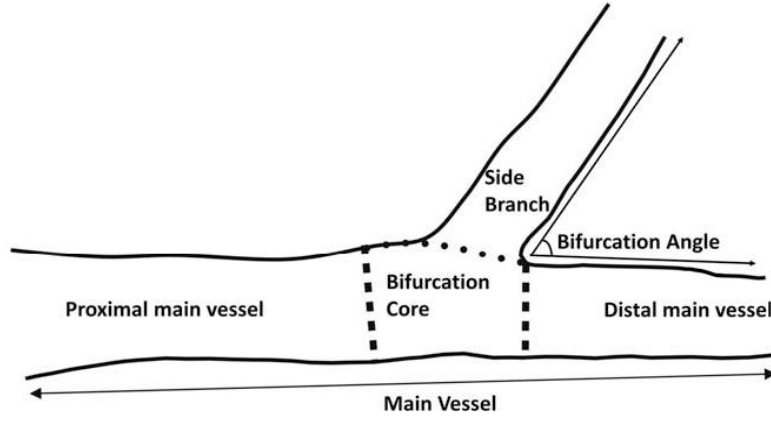
Figure 1.8: Scheme of bifurcated coronary artery [20]
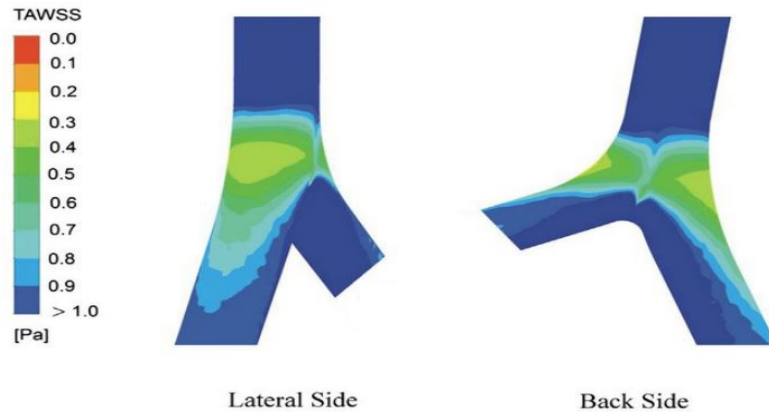
Figure 1.9: Distribution of TAWSS in bifurcated artery [27]

Based on the discussions above and literature [5], there are some essential facts regarding coronary artery: i) The blood flow features small Womersley number below 3. ii) Higher blood flow can be obtained during diastole process, which is reverse with the other most arteries. iii) The irregularity of vessel geometry (curvatures and bifurcations) can cause secondary flow during the cardiac cycle.

1.2 Diseases and treatments concerning coronary artery

Atherosclerosis is a type of vascular disease. The lipid-based plaques cause hardening and stenosis of vessels [28]. Atherosclerotic plaques occur most often at the arterial intima, especially when it gets traumatized [29]. Normally human body can give timely response to the dynamic changes or risky signals inside the system. This protection regime helps us to deal with various attacks or injuries. However, sometimes some pathological diseases will be caused by the arterial reaction [30]. In the case of intima injury, the response of platelet adherence and activation will be triggered. A risky deposition will be formed leading to the stenosis with more platelet accumulated at the trauma site for repairing. Shear stress plays a key role related to the platelet accumulation. Higher shear stress contributes to shorter retention time of platelets over injury site, and the adherence can only happen in milliseconds. Natural plaque progression includes lipid expansion and micro-calcifications within lipid pools as shown in Figure

1.10 [28]. If the spotted calcifications are developed into speckles and fragments, vessel wall stresses can be greatly decreased contributing to plaque stability.
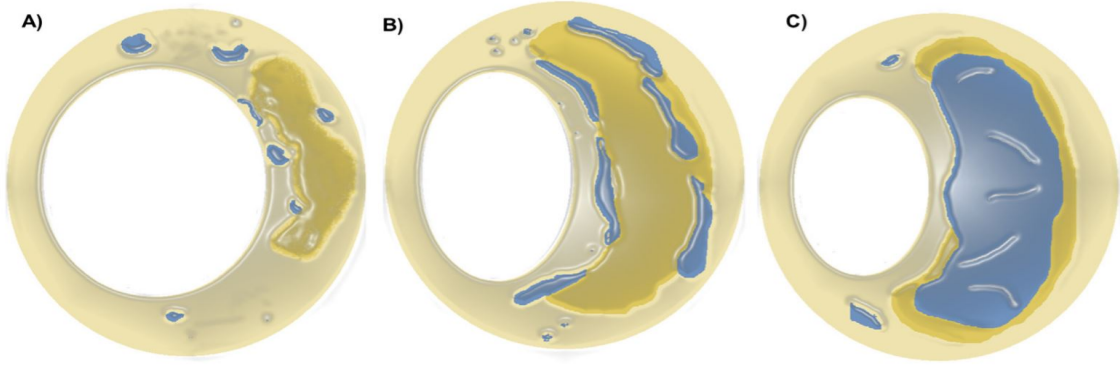
Figure 1.10: Scheme of plaque calcification (in blue): A) spotty calcification, B) sheet-like fragment, C) segments of continuous calcification [28]

Plaque development depends on multiple factors. Considering the geometrical complexity introduced above, irregularity of artery geometry is undoubted to be a part of decisive role on lesion locations due to flow disturbance. Bifurcation lesions have always been a major challenge to percutaneous treatment [31]. The reason is partly related to the wide range of anatomical morphologies of coronary lesions located at arterial bifurcation. Through clinical statistics, the prone lesion conditions at bifurcated artery have been classified as shown in Figure 1.11 [32].
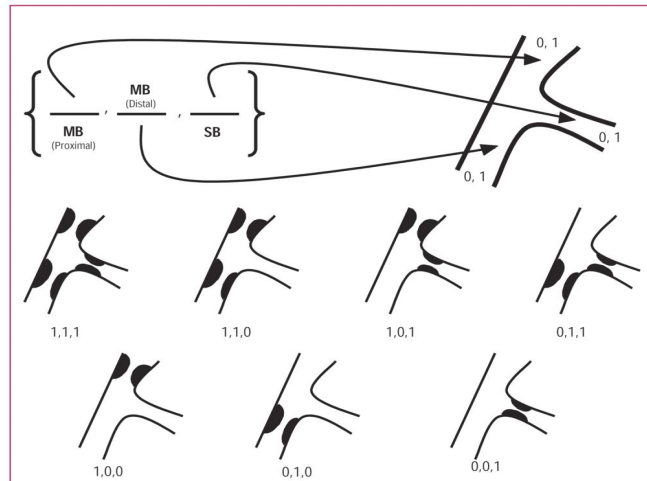
Figure 1.11: Summary of lesion conditions at bifurcation [32]

Among the existing treatments developed to stenosis, stent implantation is trending recently for its significant developing progress. However, as a normal body regime, the implanted stent will be considered as a foreign body leading to body reaction. Consequently the accumulated platelets around stent lead to the thickening of intima again which is then called restenosis [33] as shown in Figure 1.12. Thus, it is still a big challenge to optimize the stent performance. Hemodynamic variations play a key role in the initiation and progression of atherosclerosis. Numerous Studies have shown that arterial zones exposed

to low shear stress are more prone to develop atherosclerotic lesions [34–36]. Thus the relationship between local hemodynamics and design factors of stent has been paid great attention. According to the literature [37], the intimal thickening tends to be generated more easily when the WSS is below 0.5 Pa. Thrombosis size depends greatly on the accumulated platelet amount which is directly related to the shear rate as defined in equation (1.2) as the blood flow has been commonly considered to be Newtonian fluid within the existing literature. WSS represents the ability to take away depositions from vessel wall. When WSS is below the critical value of 0.5 Pa, the shear force generated is too weak to prevent the depositions on vessel wall.

$$\dot{\gamma}_{i,j} = \frac{\partial u_i}{\partial x_j} + \frac{\partial u_j}{\partial x_i} \tag{1.2}$$

Where $\dot{\gamma}$ is the shear rate, s^{-1}. u is the velocity, m/s. i,j ϵ (x, y, z) and i$\neq$ j.
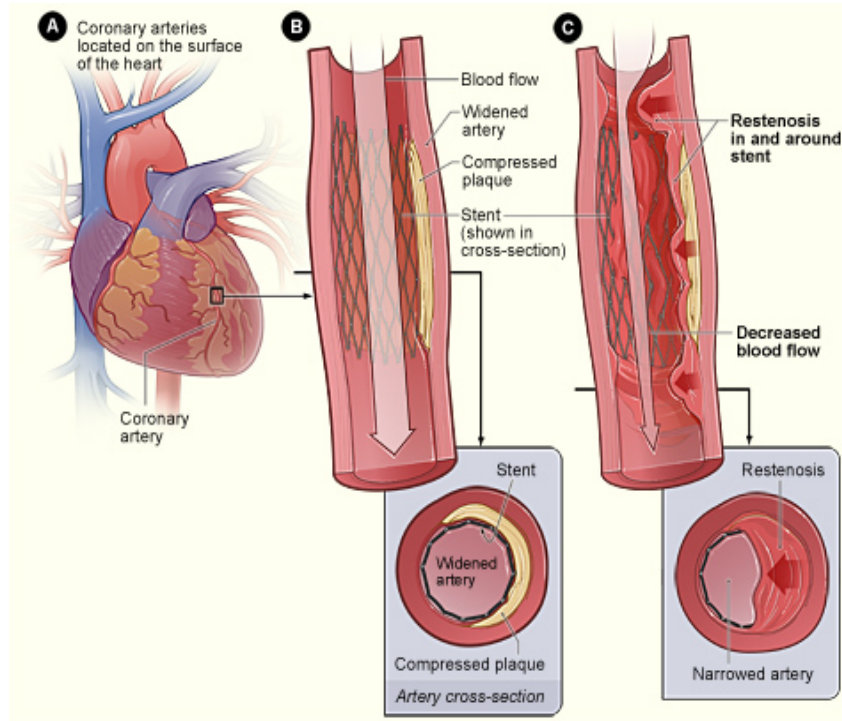
Figure 1.12: Restenosis following the stent implantation

Following the discussions above, the coronary atherosclerosis concerns stenosis and restenosis. It's known through clinical statistics in France cardiovascular disease is the cause of 180000 deaths, 130000 strokes and 120000 hear attacks each year. Confronting this threat, many treatments has been developed and implemented with efforts progressively including bypass grafting, balloon angioplasty and stent deployment separately:

- Bypass grafting [38]: It needs to take the patient's own blood vessels connecting the distal end of the stenotic coronary artery with the aorta. Then the blood is allowed to flow without passing the narrowed part. Thereby, the purpose of relieving the symptoms of angina pectoris can be achieved (Figure 1.13).
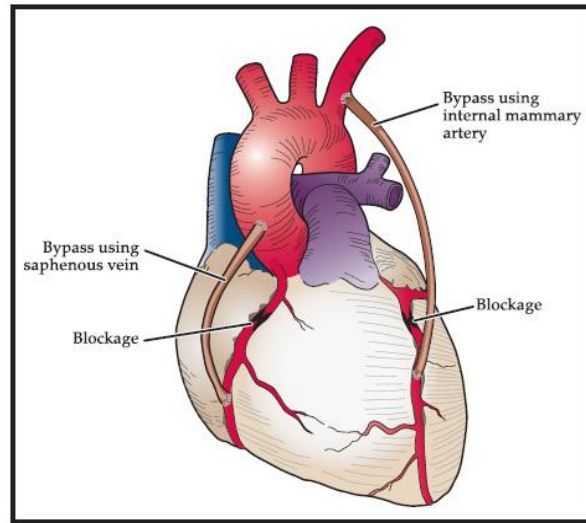
Figure 1.13: The process of bypass grafting

- Balloon angioplasty [38]: A deflated balloon will be placed at the stenotic part. With the inflating of the balloon, the larger pressure leads to reduced tension in the vessel wall and enlargement of the luminal diameter (Figure 1.14).
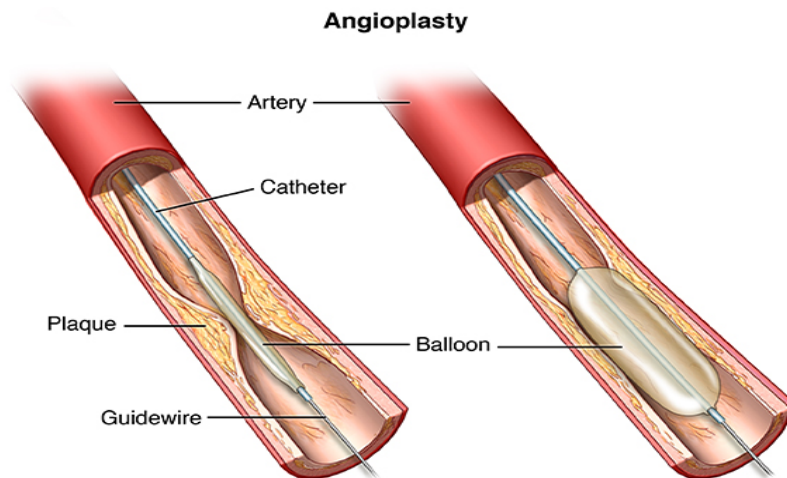
Figure 1.14: The process of balloon angioplasty

- Bare metal stent [39]: In the early 1980s, an Argentinian doctor imagined to enlarge the hardened, narrowed heart coronary artery by stent, subsequently the metal stent was born. The metal stent successfully worked out in the clinical treatment resolving the urgent occlusion as shown in Figure 1.15. However, as our body deems the stent as a foreign body, contacting sites between the stent and the arterial membrane will be treated as a wounded area. As a consequence, an inflammatory reaction occurs. Many patients, especially diabetics, get severe scar tissue around the metal stent. This type of scar tissue hyperplasia can cause severe arterial re-stenosis [40] (Figure 1.15). In france around 120000 stents are implanted for patients every year.

Figure 1.15: Restenosis after a procedure [40]

- Drug-eluting stent [17]: As depicted in the metal stent part, the restenosis is an urgent challenge. For a further improvement of the treatment, the researchers started to combine the medicine with the stent together. Namely a layer of drug film will be plated on the surface of the metal stent, termed drug-eluting stent (DES). The common sectional structure of DES is showed in Figure 1.16 [41]. When the DES is implanted into the body, the drug will be released inhibiting the growth of scar tissue around the stent. The development of DES is a significant progress in the clinical treatment which has occupied 78% of cardiac stent implantation. However, the risks still exist that drugs on the stent surface will be used up finally and a thrombosis can be developed.
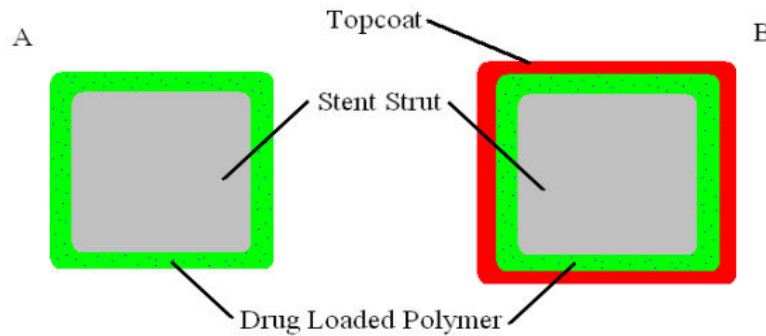
Figure 1.16: Cross section of drug eluting stent [41]

- Soluble stent [42]: At the beginning of the 21st century, the Belgian scientists reported on a novel arterial stent. This stent will be dissolved and absorbed by the body. When the stent is implanted, blood vessel will be reshaped, over time the stent can dissolve and disappear. Thereby, the local inflammatory reactions can be avoided. However, it is still in development and not used widely.

Among these treatments, stent implantation accounts for 60%-80% accepted by the patients [17]. The stent is widely used today dealing with the decreased artery diameter termed stenosis. However, the complications still remain challenging [43]. The endothelial layer can be damaged and lose its ability to regulate the proliferation of SMCs after stent implantation. As a result, the wall may thicken over the stent and block the lumen again.

1.3 Investigation development of bare metal stent

BMS is the first generation of stent and also the onset of effective treatment for atherosclerosis. However, approximately 20% to 30% of patients require additional intervention after stent implantation [44].

The performance of stent depends on multiple factors: stent designs, hemodynamics of blood, implantation procedures, vessel injury and chronic inflammation [45]. Among the literature, the optimization of stent designs have been paid a lot of attention by the researchers in order to improve the implantation performance [46].

Computational fluid dynamic (CFD) as a research tool can help to better understand the blood flow and improve stent optimization. The stent design was firstly found to be linked with adverse clinical outcome inside stented rabbit iliac arteries in 2000, and variation of WSS is greatly associated with neointimal hyperplasia. The main considerations of stent geometrical characteristics are summarized through Figure B.1 [47]. These two types of designed stents are compared through different geometrical features: stent cell, mean cell spacing, strut valley and peak, strut angle and if it is cell off-set or cell alignment. It is demonstrated that adverse hemodynamic variations of specific design features (such as narrow strut space and large strut size) can be mitigated while combining the other beneficial design features. Moreover, more luminal protrusion of stent can worsen the hemodynamic conditions significantly.
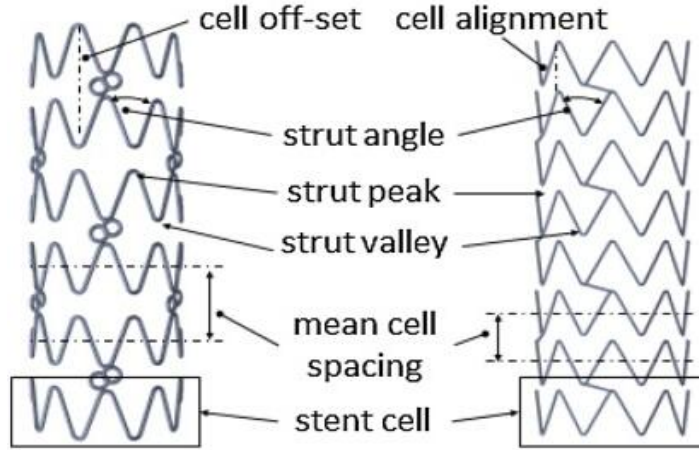
Figure 1.17: Geometries with stent design labels [47]

Rheological properties and hemodynamic distributions are the main focuses of outputs among the investigations. The works of N. Benard [17], H.M. Hsiao [48, 49], F. Chabi [50] and A. Rouhi [51] have proved the disturbed flow caused by the presence of stents. Larger inter-strut spacing was found beneficial to restore disturbed flow. Through works of V. Dehlaghi et al. [45], instead of strut spacing, he focused on the effect of ratio between strut spacing to strut height on hemodynamics. The ratios of 2, 3, 4, 6 have been studied and found out that When the ratio is below 3, the secondary flow is full of the whole strut space. When the ratio is above 6, the reattached point can be obtained with two separate vortices. According to the works of [52], When struts follow more the direction of blood flow, the area of flow recirculation tends to be reduced. Smaller strut angle means the strut orientation is more consistent with the flow direction. Decreased deflection between the strut orientation and flow direction can induce less flow turbulence inhibiting the development of recirculation. Moreover, strut thickness has been the focus of many numerical and clinical studies. The common conclusion demonstrated that thicker strut is more prone to generate adverse outcomes [53–55]. Thinner strut will cause less obstacle effect and confine the recirculation size. I.C. Hudrea et al. [56] studied the formation of recirculations with struts of malapposition as shown in Figure B.2. The streamlines are more disturbed with a limited increasing

of stent protrusion into lumen. Afterwards when the stent is closer to the center flow, the disturbance of flow is more relieved.
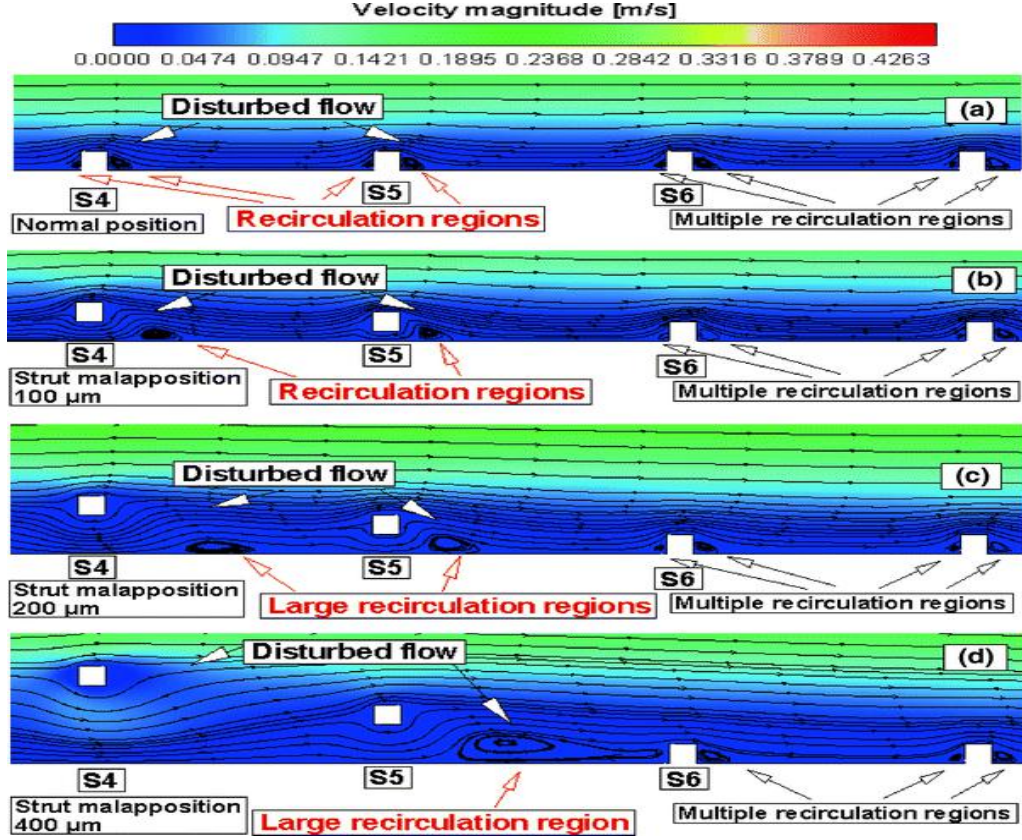
Figure 1.18: Streamlines with stents of malapposition [56]

Low shear stress, high particle residence time, and non-laminar flow are common hemodynamic attributes at locations where the neointimal hyperplasia is prone to happen [57, 58]. Therefore, many researches have been carried out aiming to optimize the stent design based on the evaluation of hemodynamic parameters variations. Even though part of the researches have verified the symmetrical hemodynamic distribution in 3D model with simplified circular stent, a more complete 3D modeling is still necessary to have a global view of hemodynamic distribution, especially taking into account of the practical geometrical complexity of artery and stent. R. Balossino et al. [59] used 3D models to analyse the spatial and temporal distribution of arterial WSS under differently designed stent shapes and different strut thicknesses. The low value region of WSS below 0.5 Pa was observed to be increased with thicker strut. Similar conclusion has been obtained in works of N. Duraiswamy et al. [60]. Four stents of different designs were studied and the near-wall WSS distribution was investigated as shown in Figure B.3. The low value of WSS is always found to follow the near region of stent.
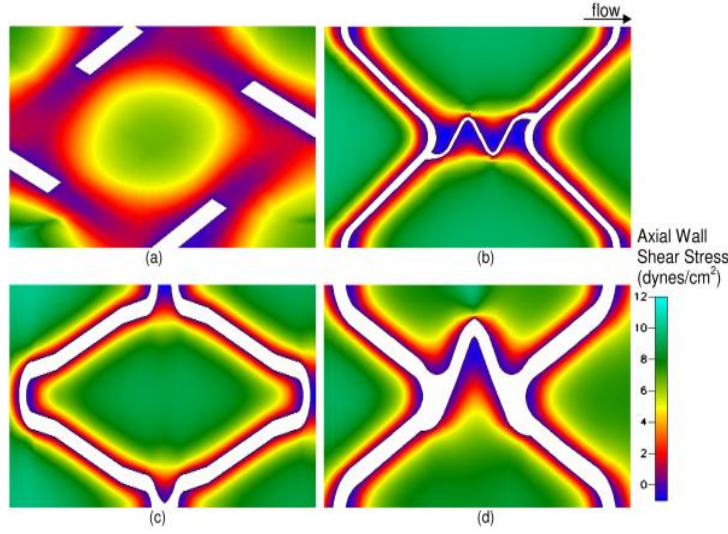
Figure 1.19: WSS distribution for (a) Wallstent, (b) Bx Velocity stent, (c) Aurora stent, and (d) NIR stent [60]

1.4   Investigation development of drug-eluting stent

DES has brought significant benefits in hindering the development of arterial restenosis after stent implantation compared to BMS [61–63]. The first BMS termed as Palmaz-Schatz was authoritatively approved in 1994 confronting the threat of cardiovascular disease [64]. However, the restenosis as the subsequent complication strongly limits the wide use of BMS which is required to make further evolvement and improvement [65–67]. Until 2003, the first DES was approved by the Food and Drug Administration in US. As a newly developed stent, the therapeutic effect has been greatly improved with the designed anti-proliferative drug coatings. However, due to the durable existence of stent after drug release, new risks emerge with the very late thrombosis after one year's DES implantation [68–70]. Thus, the development of DES is still required despite the significant progress has been made. As the trending of stent development, the soluble and polymer free stents have been put forward in recent years [71–73], but they are still limited in researches to date. The soluble stent is designed to be dissolved or absorbed in the body gradually after stent implantation which can reduce the risks of later thrombosis compared to BMS [74]. For the polymer free stent, the drugs will be directly filmed on the stent surfaces instead of using the polymer carrier which acts as a potential chronic inflammatory stimulus [75].

Extensive researches have been carried out in order to better understand the drug release mechanism and improve the stent. Numerical method has been widely adopted modeling DES physically and mathematically which is more cost-effective compared to the experiments/clinical trials [76]. In the view of physical modeling, three domains are related to the drug release: polymer domain, blood flow domain and tissue domain. A number of studies have been carried out to study the drug release from DES in the ways of one-dimensional [77], two-dimensional [78, 79] and three-dimensional models [80, 81] separately. The first paper considering the simultaneous drug transport both in tissue and blood domain was released in 2007 [82]. The earlier publications focus on the drug transport either in tissue domain or in blood domain [83, 84]. In addition, in many studies the polymer domain is simplified as a boundary where an initial drug concentration will be imposed and keep unchanged which obviously doesn't fit with the practical case [85–88]. Simplifications and assumptions are commonly found through the numerical

works. Drug flux is commonly supposed to be continuous across the interface boundaries which is reasonable when the drug solubility is similar between the two neighboring domains. In the case of hydrophobic drugs, they are more prone to partition into the tissue which will lead to the discontinuities. In addition, because of the distinguished difference of time scale between the pulsed blood flow and the drug transport in tissue, the steady flow is considered while coupling with drug transport. Recently the works of R.S. Pujith [89] have verified that the flow-mediated drug transport from DES is negligible even though more works need to be further completed. Moreover, it is interesting to found out that opposite results exist among the existing studies which indicate the importance of the established models more complying the reality. With the purpose of stent optimization, several controlling parameters have been considered to investigate the influence in the drug concentration especially the role of detailed geometrical features [54, 90, 91] and the polymer properties [92]. Y. Chen et al. has studied the effect of drug coating positions, artery bending angles and Reynolds number on the drug concentration [85, 86, 93] in 3D modeling. A.I. Barakat et al. have modeled the drug transport process of two different types of drugs [94] and studied the effect of release kinetics on drug concentration in tissue [95]. J.A. Ferreira et al. investigated the influence of different plaque eccentricity on drug transport in the stenotic vessel [96]. More controlling parameters such as diffusion coefficient, strut spacing, struts apposition, and strut shape have received extensive attention by the researchers as well [97–99]. Larger strut spacing is demonstrated to decrease the peak value of drug concentration but increase the average drug concentration in tissue [90]. It is interesting for the numerical works carried out by T. Seo et al. [100] in 2016 who introduced a new dimensionless index: Stent penalty Index (SPI) to quantify the flow disturbance and drug concentration at the endothelial surface. A number of researches carried out in the cases of steady flow and steady drug release concluded that the recirculations formed around stent had a significant effect on the drug transport and the asymmetrical drug distribution in tissue was observed [87]. However, many recent works of unsteady drug release have denied the results previously in steady case. Instead of asymmetry of drug distribution affected by the flow in steady case, symmetrical drug distribution around strut in tissue will be found in unsteady case and the influence of flow rheology in drug transport can be neglected. As shown in Figure B.4 done by P.R.S. Vijayaratnam et al. [89, 101], the drug concentration was compared between steady and unsteady cases. Figure B.4-(a) shows the drug concentration around stent in 2D steady case of flow and drug release. The polymer is considered as a boundary with a constant initial drug concentration. It can be found that drug depositions beside the stent occupied the same order of the drug concentration compared to that in tissue which indicates that drug concentration is greatly affected by the flow. However, with the further investigation in 2018, the polymer domain was established more completely as shown in Figure B.4-(b) and (c). The drug concentration in blood and tissue domains has no big difference between the steady flow and pulsatile flow cases. The magnitude of drug concentration around stent is low enough compared to that in tissue indicating that the influence of flow pulsatility in drug transport can be neglected. With these results, it confirmed that it is reasonable to consider the drug transport in steady blood flow case.
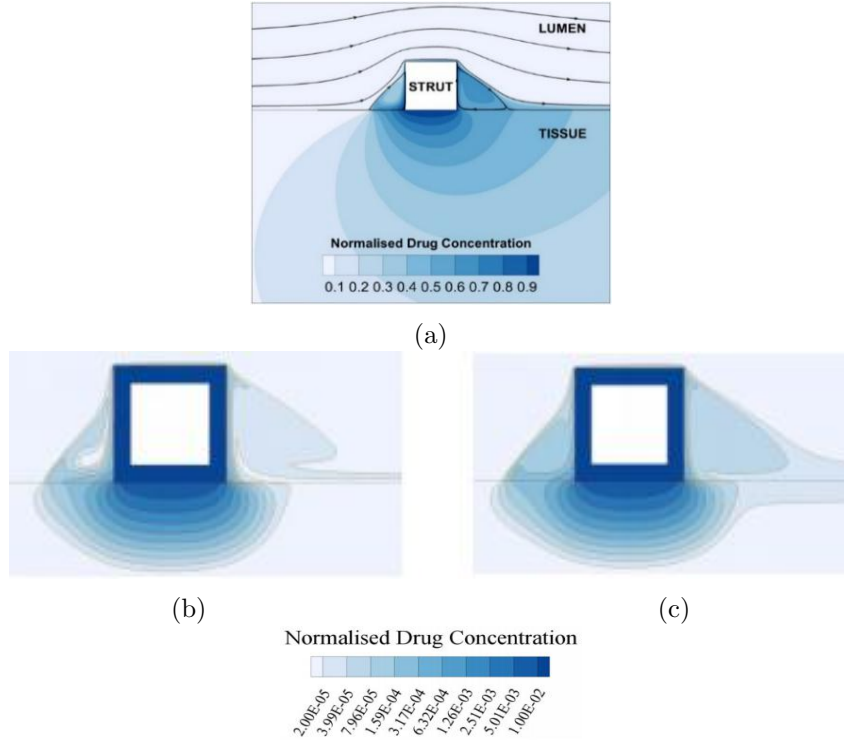
Figure 1.20: The normalized drug concentration in steady case (flow and drug transport) in (a), and unsteady drug accumulation at 60 s with (b) steady flow and (c) pulsatile flow [89].

1.5   Motivations

This study is carried out based on the background of atherosclerosis in coronary artery. In the light of literature, the influences of stenosis and stent implantation in hemodynamic variations as well as mass transfer from DES have caused great interest among researchers. However, the mechanisms related have not been fully explored yet due to the complex physics in artery especially confronting the threat of arterial restenosis following the stent implantation. Therefore, in the present study motivations on numerical analysis to study the effects of arterial geometrical singularity in flow topology and hemodynamics are put forward aiming to optimize the stent performance as well as the mass transfer from DES validated by experimental data.

Based on the complicated artery structure and physics related, the modeling characteristics regarding blood flow in coronary artery and even the mass transfer from DES are required to be discussed and determined separately in order to establish the related numerical and mathematical models. Stenosis as the emerged symptom contributes to the narrowed artery with disturbed flow which has been revealed to be greatly related to the geometrical charateristics. Thus, following the modeling establishment, the preliminary study has been carried out regarding blood flow in stenotic coronary artery coupling the main artery geometrical characteristics: bifurcation and tortuosity separately as the modeling validations. Despite the hemodynamic analysis employed commonly in literature, the practical diagnostic parameters have been introduced and analyzed as well to evaluate the further development of stenosis, predict the potential lesion sites and even provide the guidance to practical treatments.

Following the modeling characteristics and validations, the stent implantation as one type of the

arterial geometrical singularity has been focused as passions from researchers on optimization of stent are greatly motivated by the complications following the stent implantation. BMS and DES are considered as the representatives of recent development in our study focusing on the hemodynamics and mass transfer respectively. With BMS, the interactions between stent performance with different geometrical design factors and hemodynamic variations have been focused in view of stent geometrical optimization. Furthermore, with DES, the physical coupling between blood flow and mass transfer has been established aiming to better acknowledge the physics of interaction between flow and drug transport process. The experimental validations have been achieved during this PhD regarding drug release from polymer.

Modeling characteristics and validations regarding blood flow in coronary artery

Contents

2.1 Introduction

As discussed in chapter 1, motivations of this research have been put forward based on the background of atherosclerosis and the corresponding treatments. Therefore, in this chapter, the establishment of numerical and mathematical models regarding blood flow in coronary artery has been thoroughly discussed based on the practical physics in the first place. Despite the considerations of modeling characteristics such as the fluid properties, governing equations and boundary conditions, the related analysis method has been presented as well. With the determination of flow modeling through coronary artery, the preliminary study has been carried out with the stenotic artery coupling the geometrical singularities: bifurcation and tortuosity, which are the main artery geometrical characteristics as discussed in Chapter 1. As reviewed from literature, the hemodynamic variations in artery play a key role as the disease indicators and have been widely investigated. In this study, the potential sites and orientation of stenosis development affected by the arterial bifurcation structure with different stenosis severities and locations have been evaluated based on the flow topology and hemodynamic analysis. Moreover, in order to have a direct guidance to clinical treatment from CFD works, the diagnostic analysis has been adopted to give evaluations which has not been paid enough attention yet. As the consideration of artery tortuosity has been trending recently, the blood flow in tortuous artery and the relationship between artery tortuosity and stenosis occurrence have caused great interest among researchers. In the current research, flow topology and hemodynamic variations through 3D tortuous artery model with symmetrical and asymmetrical stenosis located upstream the tortuous segment have been considered. As the previous studies focused mainly on the curved artery, in this study, both curved and spiral tortuosity have been considered here

based on the clinical review by H.C. Han [19]. Different stenosis severities, different pulse rates and different distances between stenosis and tortuosity as controlling parameters have been investigated.

2.2 Numerical and mathematical models of blood flow in coronary artery

Blood flow as the main body in the coronary artery is required to be well defined corresponding to the physical characteristics in numerical model. Based on the clinical statistics [102, 103], the coronary artery as the carrier of blood has been observed to have the changeable diameter highly depending on anatomic dominance, sex and branch length. For the left coronary arteries, the left main artery (LM) was measured around 4.5 +/- 0.5 mm, the proximal left anterior descending coronary artery (LAD) is 3.7 +/- 0.4 mm, and the distal LAD is 1.9 +/- 0.4 mm. Among the investigations, the average value of artery diameter has been commonly adopted considering the artery as a cylinder [89, 101]. Since Kelle et al. [104] demonstrated that diseased coronary vessels experience peak circumferential strain below 5%, it is reasonable to consider the diseased vessel wall as rigid. Ozolanta et al. [105] has presented that the elastic modulus of coronary arteries can be increased from 1.2 MPa (0–1 year) to 4.1 MPa (60–80 years). Moreover, P. Siogkas et al. [106] compared the WSS distribution between rigid and deformable vessels and a good agreement has been obtained in these two conditions. Comparatively, blood flow as a more physically sophisticated biological fluid, higher attention is required. Therefore, in the present section, the numerical and mathematical characteristics of blood flow in coronary artery have been thoroughly discussed.

2.2.1 Blood flow characteristics in numerical model

The flow nature in a pipe involves three regimes [107, 108]: laminar, transient and turbulent, highly depending on flow velocity demonstrated by Reynolds in 19th century. Dimensionless Reynolds Number (Re) was put forward to predict flow patterns as shown in equation (2.1). When Re < 2300, laminar flow occurs along with small pipe and small velocity. The transient flow is observed with turbulence in the center and laminar flow near the edges of pipe when 2300 < Re < 4000. The flow is totally turned into turbulent when Re > 4000, where the generated vortices, eddies and wakes make the flow more unpredictable.

$$Re = \frac{\rho u D}{\mu} \tag{2.1}$$

Where ρ is flow density, kg/m^3, u is flow velocity, m/s, D is the characteristic length, m, and μ is dynamic viscosity, $Pa \cdot s$.

Generally blood flow is laminar in the body especially in small arteries. For the left coronary artery, the averaged and peak values of $Re_{average}$ and Re_{peak} are evaluated to be 166 and 431 respectively [83] when one is in rest condition. Therefore, the governing equation involved with flow is the unsteady Navier-stokes equations and the general form of Navier-Stokes equations is described below:

$$\frac{\partial \rho}{\partial t} + \triangledown \cdot (\rho V) = 0 \tag{2.2}$$

$$\rho \frac{\partial V}{\partial t} + \rho V \cdot \triangledown V = - \triangledown p + \triangledown \cdot \tau + f \tag{2.3}$$

Where f represents the body force, $-\bigtriangledown p$ is the volumetric stress tensor and $\bigtriangledown \cdot \tau$ is the stress deviator tensor as shown below:

$$p = \begin{pmatrix} p & 0 & 0 \\ 0 & p & 0 \\ 0 & 0 & p \end{pmatrix} \tag{2.4}$$

$$\tau = \begin{pmatrix} \sigma_{xx} + p & \tau_{xy} & \tau_{xz} \\ \tau_{yx} & \sigma_{yy} + p & \tau_{yz} \\ \tau_{zx} & \tau_{zy} & \sigma_{zz} + p \end{pmatrix} \tag{2.5}$$

$$\tau_{i,j} = \mu(\frac{\partial u_i}{\partial x_j} + \frac{\partial u_j}{\partial x_i}) \quad i, j \epsilon (x, y, z) \quad and \quad i \neq j \tag{2.6}$$

The dynamic viscosity of blood has been commonly accepted as a constant of $0.0035\ Pa \cdot s$ by the researchers [49, 82]. However, it is known that blood flow is a type of Non-Newtonian fluid with the variable of viscosity instead of constant value for Newtonian fluid. Several Newtonian and Non-Newtonian models of blood flow have been presented in the literature as discussed below:

- Newtonian model

$$\mu = 0.0035\ Pa \cdot s \tag{2.7}$$

- Power law model [109]

$$\mu = \mu_0(\dot{\gamma})^{n-1} \tag{2.8}$$

Where $\mu_0 = 0.0035\ Pa \cdot s^n$ and $n = 0.6$. $\dot{\gamma}$ is shear rate, $1/s$.

- Carreau model [110]

$$\mu = \mu_\infty + (\mu_0 - \mu_\infty)[1 + (\lambda\dot{\gamma})^2]^{(n-1)/2} \tag{2.9}$$

Where μ_0, μ_∞, λ and n are material coefficients. $\mu_0 = 0.056\ Pa \cdot s$ representing the dynamic viscosity at shear rate of 0. $\mu_\infty = 0.0035\ Pa \cdot s$ describing the dynamic viscosity at shear rate of infinity. $\lambda = 3.313$ s corresponding to the relaxation time. $n = 0.3568$ as the power index.

- Casson model [111]

$$\mu = [(\eta^2 J_2)^{1/4} + 2^{-1/2}\tau_y^{1/2}]^2 J_2^{-1/2}$$
$$|\dot{\gamma}| = 2\sqrt{J_2}, \tau_y = 0.1(0.625H)^3. \tag{2.10}$$
$$\eta = \eta_0(1 - H)^{-2.5}.$$

For the blood, $\eta_0 = 0.012\ Pa \cdot s$, $H = 0.37$. Based on the definitions of Newtonian and Non-Newtonian models, S.S. Shibeshi et al. [112] compared the viscous properties of blood flow as shown in Figure 2.1. It's seen that the Newtonian model gives a linear relationship between viscosity and shear rate. However, for the other three non-Newtonian models, a shear-thinning property has been displayed. With the increasing of shear rate, the viscosity will be decreased. Specific to the effects of these models on hemodynamic variations, R. Vinoth et al. [113] investigated the Non-Newtonian and Newtonian blood flow in human

aorta, and found out that the overall velocity and pressure distributions with Non-Newtonian model are similar to that in Newtonian model. Through the works of P.S.R. Vijayaratnam et al. [89], it is concluded that the flow-mediated drug transport from DES can be negligible. Moreover, referring to the works of E.W. Merrill et al. [114] and D.A. Mcdonald [115], non-Newtonian characteristics generally occur in small vessels for low values of shear rate $\dot{\gamma} < 100 \; s^{-1}$ and Womersley number $Wo < 1$. In our case, the Womersley number is 2.7, and the shear rate is estimated as $114 \; s^{-1}$. Therefore, for our investigations it is reasonable to define the blood flow with Newtonian model.
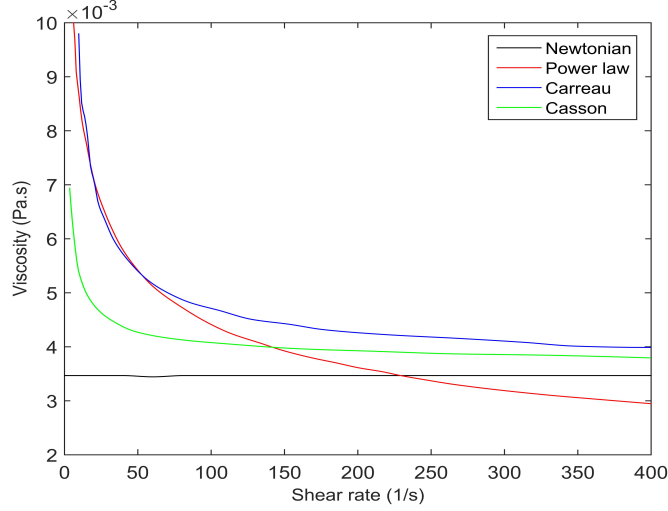
Figure 2.1: Comparison of viscosity versus shear rate as predicted by different blood constitutive equations [112]

Following the blood flow characteristics of laminar and Newtonian fluid, the further discussion will focus on the velocity profiles. Among the literature, several velocity profile models have been developed which can be divided into steady and unsteady cases as presented below.

- Poiseuille parabolic profile model

Poiseuille flow describes incompressible and Newtonian fluid for laminar flow through a cylindrical pipe experimentally derived by Jean Léonard Marie Poiseuille in 1838 [116] and Gotthilf Heinrich Ludwig Hagen [117] as defined below:

$$u(r) = 2V(1 - \frac{r^2}{R^2})$$
(2.11)

Where V is the cross sectional average velocity, m/s. R is artery radius, m. As can be seen that the model won't capture the unsteady characteristics for unsteady flow.

- Plug velocity profile model

Plug velocity profile model gives uniform sectional velocity distribution at initial boundary condition [118]. In laminar pipe flow case, the plug velocity profile will develop into the parabolic form consistent with the Poiseulle model. However, when it is in turbulent pipe flow case, the following governing

equations will be followed.

$$\delta_s = \frac{5\nu}{u^*}, u^* = (\frac{\tau_\omega}{\rho})^{1/2}$$
$$\tau_\omega = \frac{D\Delta p}{4L}, \frac{\Delta p}{L} = \frac{f\rho V^2}{2D} \tag{2.12}$$
$$\frac{1}{\sqrt{f}} = -2log_{10}(\frac{\epsilon/D}{3.7} + \frac{2.51}{Re\sqrt{f}})$$

Where f is the friction factor and D is the diameter, m. V is the sectional average velocity, m/s. Δp represents the pressure loss, Pa. ϵ is the relative roughness of the pipe and τ_ω is the shear stress on the wall (Pa), defined as $\mu\frac{\partial u_x}{\partial y}|_{y=0}$, x is the flow direction and y is the normal direction to the wall. u^* is the friction velocity, m/s, δ_s is the sub-laminar layer, m.

- Simplified pulsatile model

Derived from the steady Poiseuille model of blood flow profile, the simplified pulsatile model is developed in order to capture the unsteady characteristics of blood flow [119]:

$$u(r,t) = 2V(t)(1 - \frac{r^2}{R^2}) \tag{2.13}$$

As can be seen, the simplified pulsatile model is similar with the steady parabolic model. The disparity is that $V(t)$ is the instantaneous sectional average velocity versus time instead of constant, but still the parabolic velocity profile at each time instant will be remained.

- Womersley velocity profile model

Womersley solved the unsteady Stokes equation for the flow in a rigid circular vessel [120]:

$$u(r,t) = Real\left\{\frac{\tilde{a}}{i\rho\omega}(1 - \frac{J_0Wo(i^{3/2}r/R)}{J_0Wo(i^{3/2})})e^{i\omega t}\right\} \tag{2.14}$$

The equation (2.14) depicts the exact solution for the unsteady flow. Because of linearity of the Stokes equation, the combination of the steady solution (equation (2.11)) and unsteady solution will make it complete as shown below.

$$u(r,t) = \frac{\Delta p R^2}{4\mu L}(1 - \frac{r^2}{R^2}) + Real\left\{\frac{\tilde{a}}{i\rho\omega}(1 - \frac{J_0Wo(i^{3/2}r/R)}{J_0Wo(i^{3/2})})e^{i\omega t}\right\} \tag{2.15}$$

In this velocity profile model, an important dimensionless parameter is Womersley number defined as $Wo = R\sqrt{\frac{\omega}{\nu}}$. Similar with the Renolds number it represents the ratio between the inertial force and viscous force. As discussed in chapter 1, when $Wo < 2$, viscous force dominates the flow, and the flow is considered as quasi-steady with a parabolic profile. However, with the increasing of Womersley number, the inertial force are becoming more dominant. As a consequence, the velocity profile will tend to be flat, especially after $Wo = 10$. As mentioned that Wo equals to 2.7 in our case, thus the slight influence of flow pulse is ignored here following the parabolic velocity profile.

2.2.2 Reconstruction of coronary pulsed flow

As discussed in Chapter 1, the pulsed blood flow in coronary artery at frequency of 1.25 Hz can be obtained through works of N. Bénard as shown in Figure 2.2. In order to reconstruct the flow profile numerically, an eight-coefficient Fourier equation is established with Matlab as shown in equation (2.16). The calculated coefficients are shown in Table 2.1 referring to the works of F. Chabi [83].
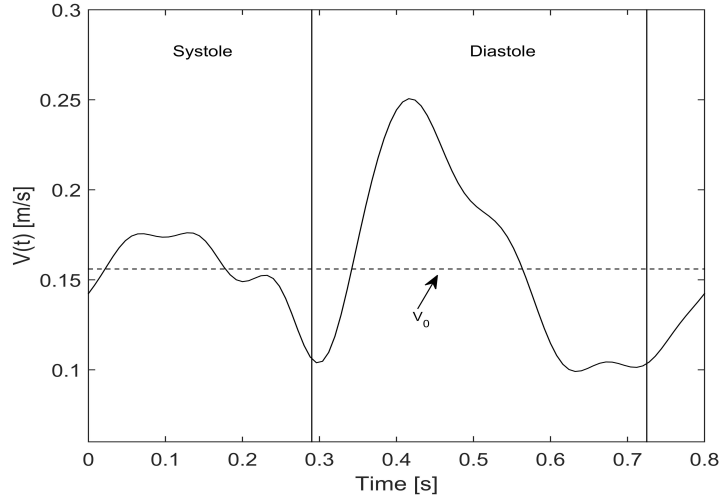
Figure 2.2: Inlet blood flow profile at $f = 1.25$ [83]

$$V(t) = V_o + \sum_{n=1}^{8}(V_n cos(nwt) + W_n sin(nwt)) \tag{2.16}$$

Where $V_0 = \frac{1}{T}\int_0^T V(t)dt$ for $n = 0$, $V_n = \frac{2}{T}\int_0^T V(t)cos(nwt)dt$ for $n \geq 1$, $W_n = \frac{2}{T}\int_0^T V(t)sin(nwt)dt$ for $n \geq 1$.

Table 2.1: Numerical values of coefficient W_n and V_n [83]

harmonic order	V_n (m/s)	W_n (m/s)
0	0.15634	0
1	-0.02995	0.00808
2	0.02458	0.03887
3	-0.01182	-0.00838
4	0.00985	0.0028
5	-0.01009	0.00313
6	0.00618	-0.00113
7	0.00133	$8.74149 * 10^{-4}$
8	-0.0036	$-2.35276 * 10^{-4}$

Physical activities lead to flow variations which have a crucial influence in the disease progress. Thus following the reconstruction of flow profile at $f = 1.25$ Hz corresponding to heart beats of 75 in one minute (75 bpm), flow profiles at 100 bpm and 120 bpm are developed as well covering one in the

exercise condition [121, 122] as shown in Figure 2.3.
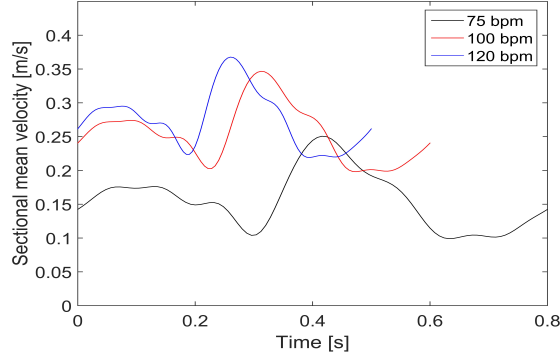
Figure 2.3: Inlet blood flow profile at different pulse rates

2.2.3 Hemodynamic and diagnostic analysis

As mentioned previously, the hemodynamic variations in artery play an important role in onset of disease and have been commonly focused among the investigations. WSS evaluation has been the mostly used way to describe the artery conditions with its critical limit value and several WSS-based descriptors as indicators of endothelial wall dysfunction have been introduced as well by researchers. Moreover, in view of having a direct guidance to clinical treatment from numerical works, diagnostic analysis can give evaluations on treatments which has not been paid enough attention yet. Thus in the present section the related methods of hemodynamic and diagnostic analysis will be both presented.

- Hemodynamic parameters

- WSS

$$WSS = n \cdot \mu(\frac{\partial u_i}{\partial x_j} + \frac{\partial u_j}{\partial x_i})|_{wall} \quad i, j\epsilon(x, y, z) \ \ and \ \ i \neq j \tag{2.17}$$

μ is the dynamic viscosity, n is tangential vector along the vessel wall. The critical value of WSS is 0.5 Pa.

- Time-averaged WSS (TAWSS)

$$TAWSS = \frac{1}{T} \int_0^T |WSS| dt \tag{2.18}$$

Where T is the total time of one cycle for blood flow. TAWSS represents the shear load over time the arterial wall is subjected to and the threshold value is 0.4 Pa [33].

- Relative pressure drop (RPD)

$$RPD = \frac{(p_{proximal} - p_{distal})}{p_{distal}} \cdot 100 \tag{2.19}$$

Where $p_{proximal}$ is the proximal pressure before the stenosis, p_{distal} is the distal pressure after the stenosis.

- Artery surface of TAWSS below 0.4 Pa (S_{TA})

$$S_{TA} = \int_{S_T} if(TAWSS < 0.4, 1, 0)ds \qquad (2.20)$$

Where S_T is the total surface of artery wall. The "if" function has been used in order to integrate the surface where TAWSS<0.4 Pa (=1 if so, =0 if not). Thus S_{TA} represents the surface area of potential disease sites.

- Surface percentage of WSS below 0.5 Pa (S_p)

$$S_p = \frac{S_b}{S_T} \cdot 100 \qquad (2.21)$$

Where S_b is the arterial surface for WSS below 0.5 Pa.

- Diagnostic parameters

- Pressure drop coefficient (CDP)

$$CDP = \frac{\Delta \bar{p}}{0.5 \rho V_0^2} \qquad (2.22)$$

Where $\Delta \bar{p} = \bar{p}_{proximal} - \bar{p}_{distal}$, $\Delta \bar{p}$ indicates the difference between the time averaged proximal pressure and the time averaged distal pressure.

- Lesion flow coefficient (LFC)

$$LFC = \frac{AS}{\sqrt{\frac{\Delta \bar{p}}{0.5 \rho V_0^2}}} \qquad (2.23)$$

Where $AS = \frac{S_{original} - S_{remained}}{S_{original}}$, $S_{original}$ represents the original surface of vessel cross section, $S_{remained}$ is the remained surface of vessel cross section because of stenosis formation.

2.3 Validations with geometrical singularities

With the determination of coronary artery modeling establishment, preliminary study is carried out with stenotic artery coupling the arterial geometrical singularities. Two cases are conducted: bifurcation and tortuosity.

2.3.1 Case 1 : Stenosis development in coronary artery coupling bifurcation

Stenosis in the bifurcated coronary artery has attracted wide attention among the researchers. Many investigations have been carried out focusing on the hemodynamic variations affected by stenosis and bifurcation structure [123–125]. Jahromi et al. [126] demonstrated that low WSS will be located proximal to the stenosis when the initial stenosis is located in both of the two branches after the bifurcation. The recent works have found out the existence of bifurcation broke the linearly decreased tendency of pressure from mother tube [127]. Frattolin et al. [128] studied the effect of different stenosis severities (22.5%, 30% and 50%) on WSS and flow distribution by considering that any two of the three branches were

stenotic. The final results concluded that when the stenosis is located both in the main branch proximal and side branch, the patient will be at the most risky condition which is also consistent with clinical findings. Thus, the cases of stenosis located at the main proximal and side branch separately have caused our interest to investigate the independent effects on potential stenosis development which are within the cases listed in Figure 1.11 above. Moreover, in view of the state of the art in this subject, the analysis of practical diagnostic parameters is really limited among the published numerical works. In addition, there is few investigations for the prediction of further stenosis orientation in the bifurcated coronary artery. Most of the studies mainly focused on the influence of stenosis severity related to the stenosis height [129–131], however, the stenosis length as another main geometrical parameter has been paid few attention. Moreover, the physical activities of a person have been well known to directly affect the pulse rate and result in the altered flow patterns [132]. Thus, in the present study, the hemodynamic and diagnostic parameters have been both investigated. The evaluations have been made for further stenosis orientation based on initial stenosis of different severities, stenosis lengths, pulse rates and different locations.

2.3.1.1 Geometrical model and computational mesh distribution

As the stenosis inside artery is assumed to be axisymmetrical, thus the 2D geometrical model of the stenotic bifurcated artery is established referring to the literature [133]. The geometrical model is composed of the left main coronary artery and two daughter vessels with a 45° bifurcation termed as main branch proximal, main branch distal and side branch as shown in Figure 2.4. Two cases with different stenosis locations have been displayed. The diameters are 3 mm, 2.5 mm and 1.7 mm separately [134]. In the case of a (1) in Figure 2.4, the stenosis is located in the main branch proximal. The stenosis height h was studied for these different values: 0.45 mm, 0.75 mm and 1.05 mm corresponding to the diameter stenosis 30%, 50% and 70% respectively based on the diameter stenosis definition: $\frac{h}{r} * 100\%$ where r is the vessel radius. The stenosis length l_2 as another controlling parameter will change from 3 mm to 6 mm and 9 mm keeping the same distance to the bifurcation. In order to keep the results independent from the geometrical parameters, the artery lengths for main branch proximal, main branch distal and side branch are 50 mm, 90 mm and 80 mm separately. In the case of a (2) in Figure 2.4, the stenosis is located in the side branch instead of the main branch proximal keeping all the other geometrical parameters the same.
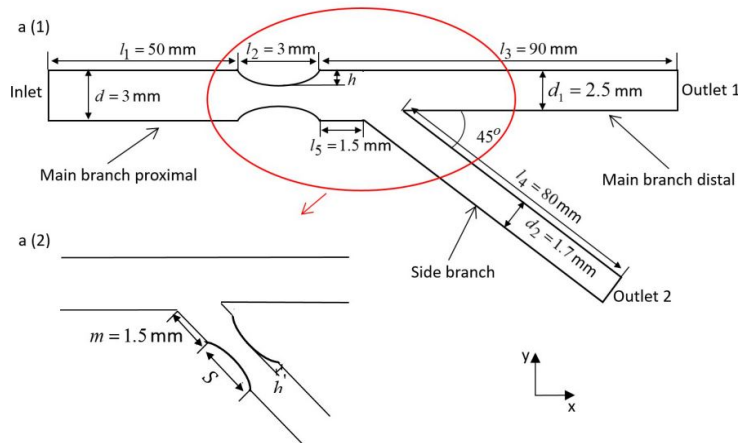
Figure 2.4: 2D geometrical model of bifurcated artery with stenosis

In order to study the mesh independence, the mesh sizes of 322645, 683246, 1159651 and 1535788 are established to check WSS value downstream the stenosis located in the main branch proximal. The accuracy can be controlled under 2% after mesh size of 1159651. Therefore, the determined mesh distributions around stenosis and bifurcation when the stenosis is located either in the main branch proximal or side branch are both obtained respectively as shown in Figure 2.5.
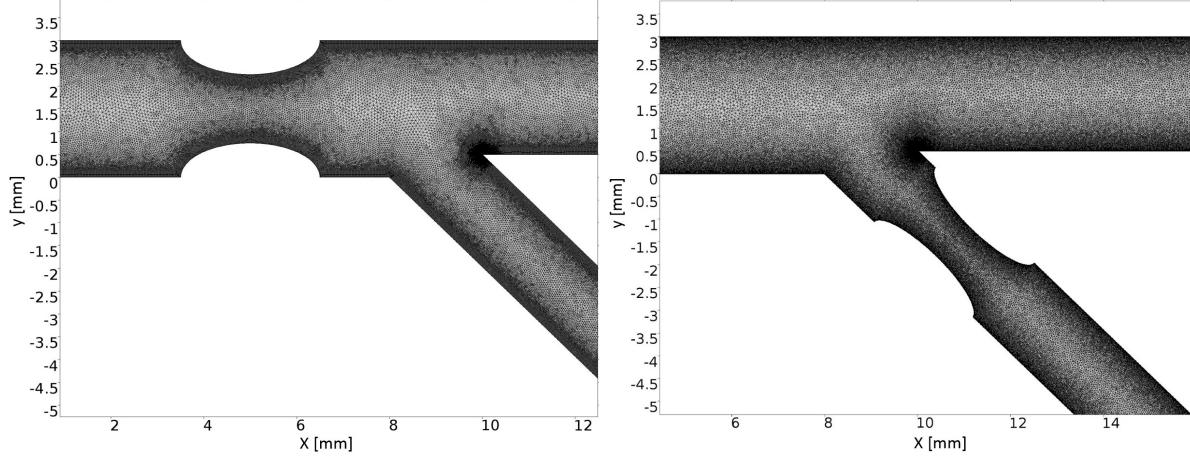
Figure 2.5: Mesh distribution around the stenosis and bifurcation

2.3.1.2 Mathematical model and boundary conditions

The blood flow is considered as incompressible and Newtonian fluid which has been commonly accepted through the literature [135, 136]. Accordingly, the density of blood is 1060 kg/m^3, the dynamic viscosity is 0.0035 $Pa \cdot s$. Therefore, the governing equations of Navier-stokes equations in general form can be simplified as shown in equation (2.24) and equation (2.25) in unsteady case. The body force has been neglected.

$$\bigtriangledown \cdot V = 0 \tag{2.24}$$

$$\rho \frac{\partial V}{\partial t} + \rho V \cdot \bigtriangledown V = - \bigtriangledown p + \mu \bigtriangledown^2 V \tag{2.25}$$

For boundary conditions, the vessel wall is considered as rigid referring to the literature [50, 137, 138] which is consistent with the discussions above. At inlet and outlets, the pulsed flow and pressure at different pulse rates will be imposed separately as shown in Figure 2.6. The inlet flows at pulse rates of 75 bpm, 100 bpm and 120 bpm have been employed as discussed above. For the outlet boundary condition, a pressure waveform with different frequencies is prescribed corresponding to different flow pulse rates. A two-element model is used as shown in equation (2.26) [139]:

$$Q(t) = \frac{P(t)}{R} + C \frac{dP(t)}{dt} \tag{2.26}$$

Where $Q(t)$ is the input pulsatile volumetric flow rate of blood, m^3/s. $P(t)$ is the output pulsatile pressure waveform, Pa. R is peripheral resistance, $1e10$ $Pa \cdot s/m^3$. C is arterial compliance, $1e-11$ m^3/Pa. It has been proved that two-element model well reconstructs the pressure fluctuation at outlets of arterial domain with lower frequency (< 5 Hz) [34]. Considering the Reynolds number range of $90 - 570$, the laminar blood flow is considered to be fully developed with parabolic velocity profile.
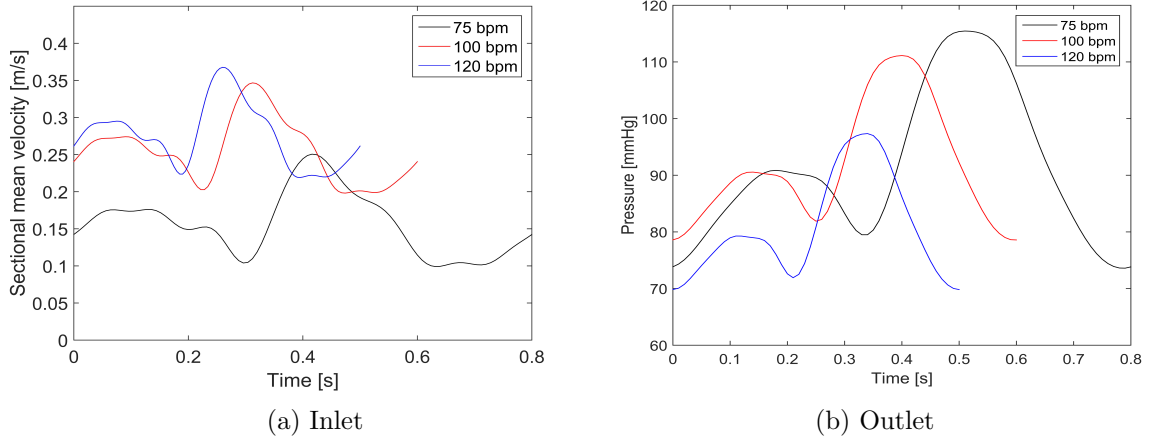
(a) Inlet

(b) Outlet

Figure 2.6: Inlet pulsed flow and outlet pressure versus time in one cycle at different pulse rate

The works concerning modeling, meshing and computing all have been done with Comsol 5.1. The unstructured tetrahedral mesh elements have been generated and multigrid method has been employed to accelerate the convergence speed of a basic iterative method. The iterative methods have chosen GMRES with the maximum iteration number of 500. The initial time step is set to be 0.001 s in order to ensure $CFL < 1$ which will be adaptively determined by Comsol based on the physics related. To make sure the periodic stability of the results, the simulations were carried out for four pulsatile cycles.

2.3.1.3 Development of recirculation with different locations of initial stenosis

Figure 2.7 shows the streamlines and shear stress distribution at different time instants in the case without stenosis. The recirculation can be observed at the side branch affected by the bifurcation structure and no recirculation is formed at the main branch. The low value of shear stress is found to be located at the recirculation region. The recirculation size is varied because of the velocity oscillation.
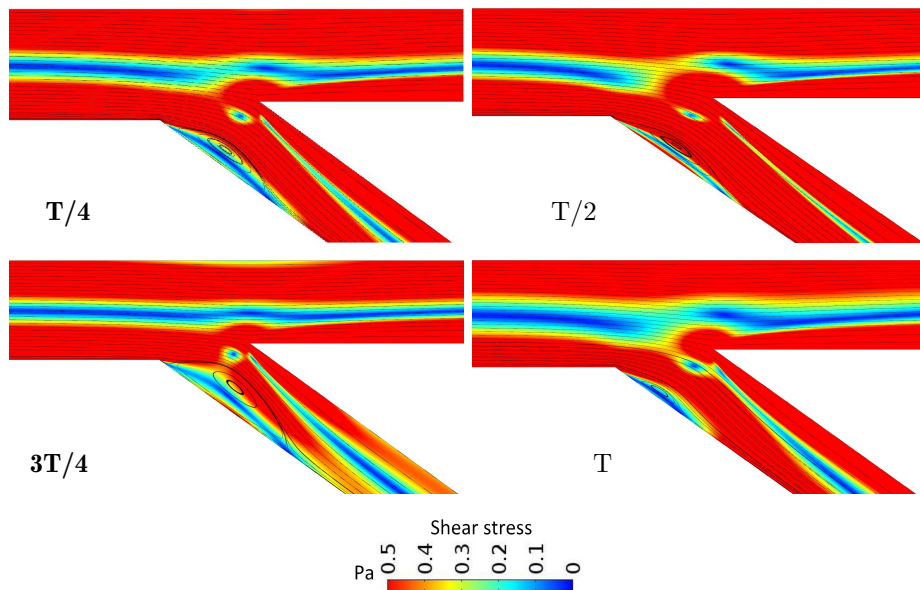
Figure 2.7: The streamlines and shear stress distribution (Pa) at different time instants without stenosis

29

Figure 2.8 illustrates the streamlines and shear stress distribution at different time instants when the stenosis of 50% is located in the main branch proximal and the stenosis length is 3 mm. Due to the existence of stenosis, the recirculation is formed and developed both into the main branch distal and the side branch. The shape and the size of recirculation varies at different time instants due to the velocity oscillation. Regarding the shear stress distribution, the low values of shear stress below 0.5 Pa are mainly located in the recirculation regions. At t=3/4T, the low value of shear stress below 0.5 Pa tends to extend over the entire lumen of the side branch which is consistent with the clinical finding: the side branch tends to be easier to form the deposition [128]. Similar phenomena are found when the stenosis is 30% and 70% not shown here. Moreover, the streamlines and shear stress distribution are checked also with other stenosis lengths of 6 mm (Figure 2.9) and 9 mm. With the increasing of stenosis length, the occurance of attachment in location 2 will be more frequent in one cycle.
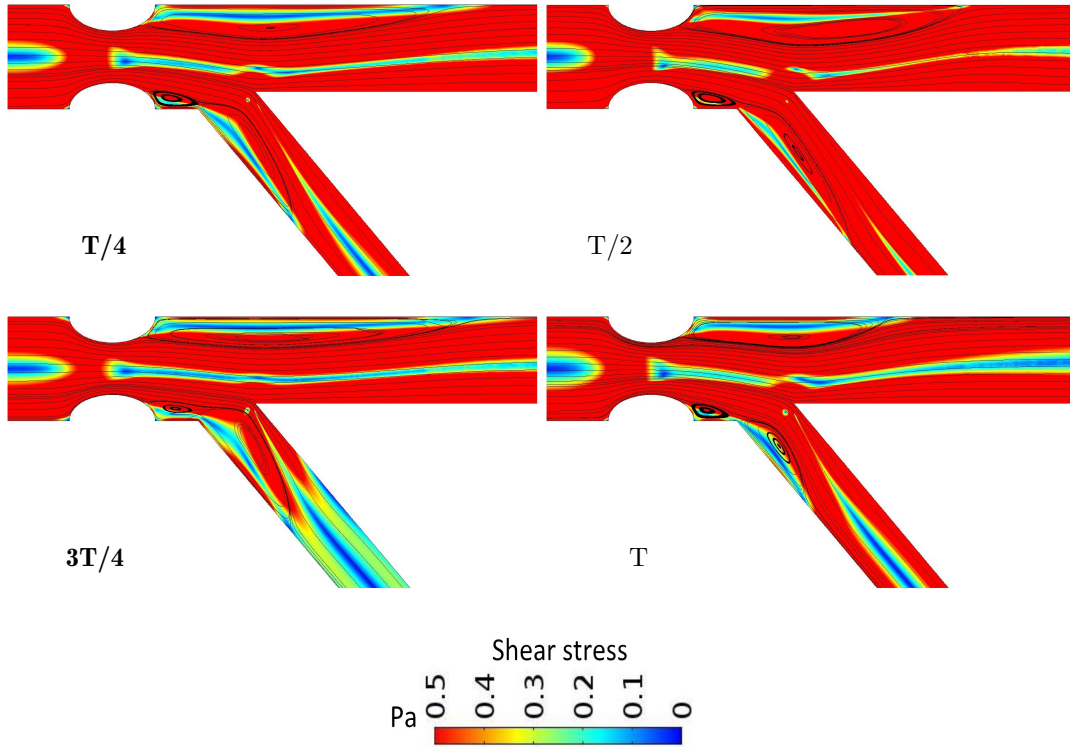
Figure 2.8: The streamlines and shear stress distribution (Pa) at different time instants with stenosis of 50% located in the main branch proximal and $l_2 = 3$ mm

Figure 2.10 shows the streamlines and shear stress distribution at different time instants when the stenosis of 50% is located in the side branch and the stenosis length is 3 mm. When the stenosis is located in the side branch, the recirculation regions with low value of shear stress below 0.5 Pa are formed both upstream and downstream the stenosis due to stronger effect of the bifurcation angle. However, the main branch is less affected by the initial stenosis source. Similar with results above, the recirculation size is greatly changed over time caused by the varied inertial force. At $t = 3T/4$, the low value of shear stress tends to extend the entire lumen of the side branch.
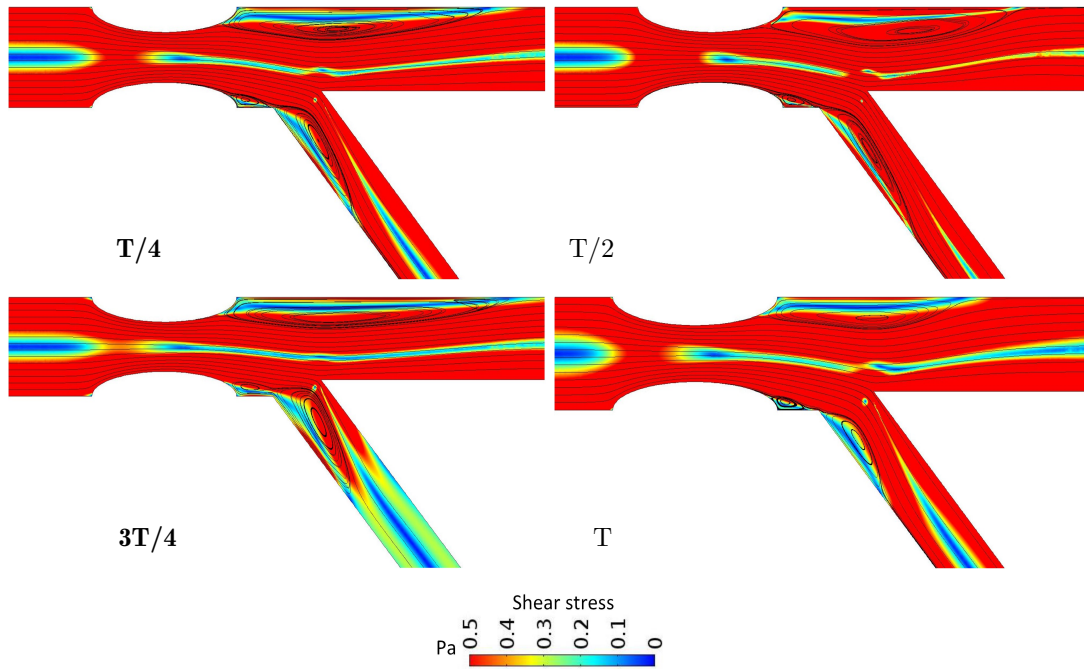
Figure 2.9: The streamlines and shear stress distribution (Pa) at different time instants with stenosis of 50% located in the main branch proximal and $l_2 = 6$ mm
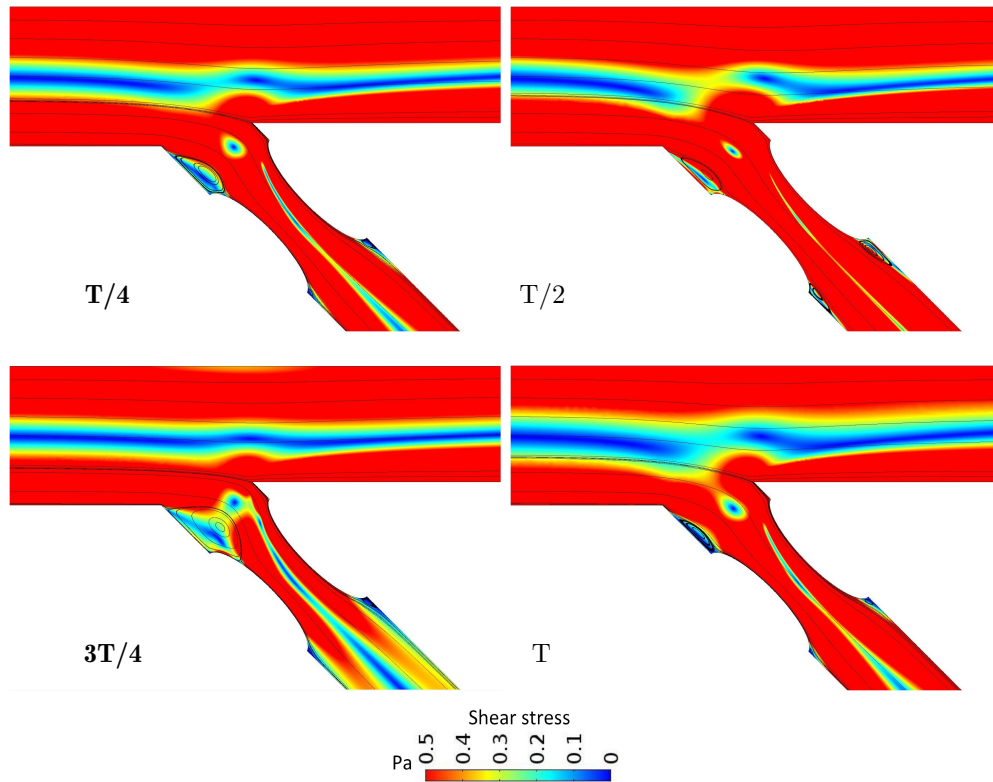
Figure 2.10: The streamlines and shear stress distribution (Pa) at different time instants with stenosis of 50% located in the side branch and $s = 3$ mm

Based on the results above, the main locations of recirculations have been found at different locations

of the initial stenosis as shown in Figure 2.11. When the initial stenosis is located in the main branch proximal (Figure 2.11-a), the formation of recirculations mainly follows the orientation of blood flow. Thus, three locations of recirculations are defined downstream the stenosis. However, when the initial stenosis is located in the side branch (Figure 2.11-b), three main locations of recirculation are generated both upstream and downstream. In order to make a better analysis, the definitions of recirculation length of L_1, L_2 and L_3 have been made corresponding to each location when the stenosis is located in the main branch proximal (Figure 2.11-a).
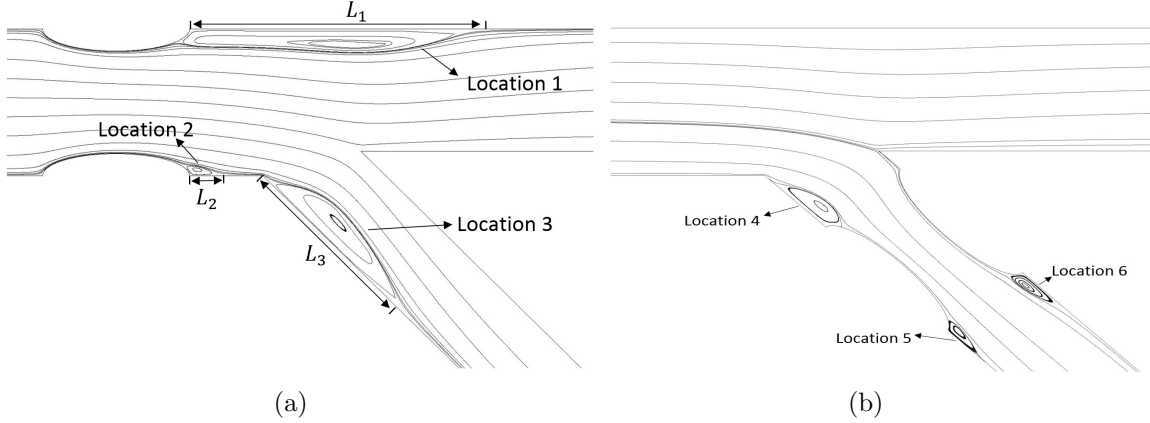
Figure 2.11: The main locations of recirculation with stenosis located in the main branch proximal (a) and side branch (b)

Figure 2.12 displays the variation of recirculation lengths (L_1, L_2, L_3) in one cycle at different stenosis severity levels (a, c, e) with stenosis length $l_2 = 3$mm and different stenosis lengths (b, d, f) with stenosis severity of 50%. As expected, with the increasing of stenosis severity, the recirculation length L_1 is increased (Figure 2.12-a) due to the rising of inertial force downstream the stenosis. When focusing on the peak values between 0.4 s and 0.5 s, it is consistent with the peak value of velocity (shown in Figure 2.6) even though the time lag exists under different stenosis conditions. As shown in Figure 2.12-(c), when the stenosis severity is under the condition of 50% and 70%, the value of L_2 almost keeps constant. This is due to the connection of the recirculations at location 2 and location 3 and the attachment point won't be formed along location 2. Therefore, the value of L_2 is considered to be the total length of the artery wall between the stenosis and the bifurcation. Slight variation of L_2 is observed from the constant value with stenosis of 50% between 0.3s and 0.4s, corresponding to the minimum value of velocity. Smaller inertial force will be obtained limiting the development of recirculation. Thus, the attachment point is located at location 2 again. When the stenosis severity is 30%, the attachment point remains at location 2 in the whole cycle, and is affected by the velocity oscillation. In Figure 2.12-(e), L_3 is increased when the stenosis severity changes from 30% to 50%. However, when it changes from 50% to 70%, L_3 is decreased. The flow will be more strongly disturbed especially in the side branch with larger stenosis of 70%. Meanwhile, other vortices will appear and disappear during the whole cycle inhibiting the development of recirculation. Regarding the effect of different stenosis lengths, it is obvious that the recirculation length is less affected by the stenosis length compared to the stenosis severity. Figure 2.12-(b) shows that increased stenosis length tends to increase the amplitude variation of L_1 especially when we focus on the maximum and minimum peak values. The maximum peak value is increased with the increasing of stenosis length. However, the minimum peak value is decreased with the increased stenosis length. In Figure 2.12-(d) and 2.12-(f), L_2 and L_3 are both decreased with the increasing of

stenosis length. The reason is the increased stenosis length will slow down the velocity change resulting in reduction of inertial force. Therefore, L_2 and L_3 are both decreased which is also restricted by the bifurcation structure. Similar with Figure 2.12-(c), the constant value of L_3 when $l_2 = 3$mm and 6mm is observed equaling to the total length of location 2 between stenosis and bifurcation which remains unchanged all the time. The recirculation length L_1 is developed into the main branch distal with a decreased diameter, thus the inertial force of blood flow will be promoted again even though the increased stenosis length contributes to the decreased recirculation length.
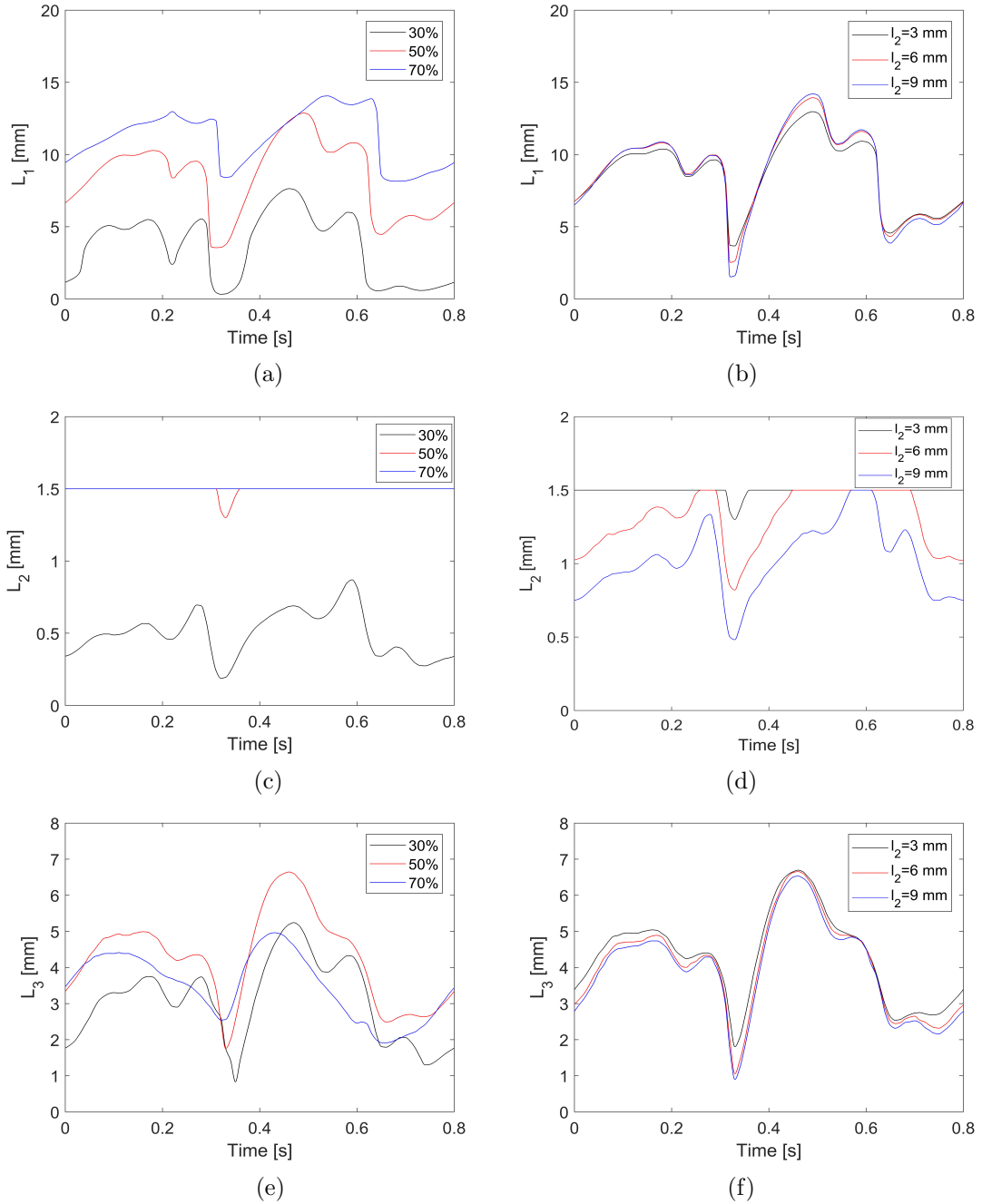
Figure 2.12: The variation of recirculation lengths versus time at different stenosis severities (30%, 50% and 70%) and stenosis lengths (3 mm, 6 mm and 9 mm) located in the main branch proximal

2.3.1.4 Analysis based on the hemodynamic and diagnostic parameters

The relative pressure drop (RPD) defined in equation (B.9) versus time in one cycle at different stenosis severity levels (a) and stenosis lengths (b) are plotted in Figure 2.13. The RPD is increased with the increasing of stenosis severity level, especially when the stenosis changes from 50% to 70% as shown in Figure 2.13-(a). Thus, the stronger disturbance brought by the severe stenosis is consistent with the larger RPD. Here too, the RPD is slightly increased with the larger stenosis length shown in Figure 2.13-(b).
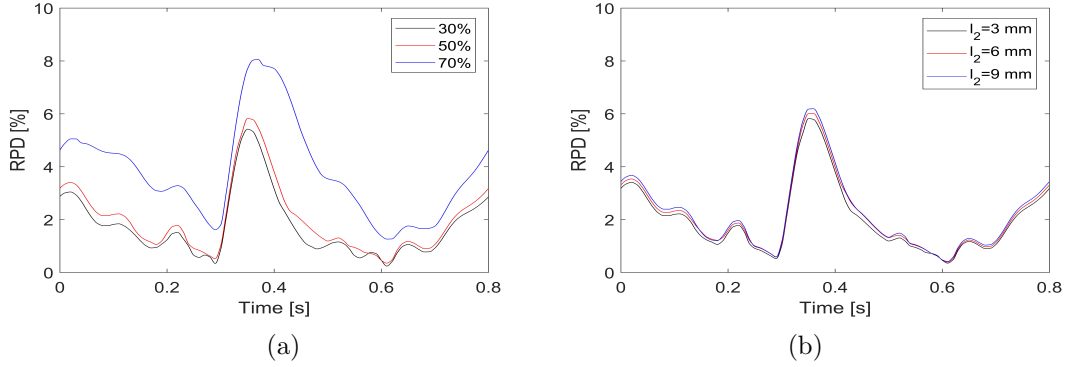
Figure 2.13: The variation of RPD versus time at different stenosis severities (a) and stenosis lengths (b) located in the main branch proximal

The RPD is studied versus time in one cycle at different stenosis severity levels (a) and different stenosis lengths (b) when the stenosis is located in the side branch as shown in Figure 2.14. With the increasing of stenosis severity and stenosis length, the RPD tends to be increased even though the absolute difference is not significant. Through the inset figures to check the variation of peak value, it can be found that relative difference of RDP is 1% and 4% with stenosis changing from 30% to 50% and 70%. The relative difference of RPD caused by the stenosis length is below 2% in our case. Thus, it can be concluded that when the stenosis is located in the side branch, the evaluation of stenosis severity through RPD is quite difficult.
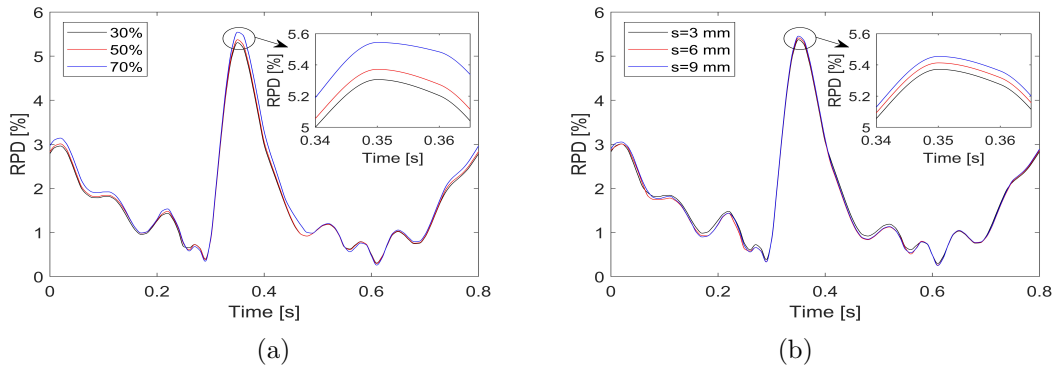
Figure 2.14: The variation of RPD versus time at different stenosis severities (a) and stenosis lengths (b) in the case of side branch stenosis

As mentioned above, WSS is an important parameter which represents the ability of the blood flow to take away the depositions. Figure 2.15 plots the wall shear stress along the stenosis at up location

and down location separately under different stenosis severity levels when the stenosis is at main branch proximal. The stenosis length is 3 mm. From this figure, the distribution of WSS along stenosis at up and down location is not symmetrical. With the increasing of stenosis severity, WSS is increased and the occurrence of WSS peak value is delayed leading to a smaller difference between WSS value at up and down locations. Before the peak value, there is no significant difference between up and down locations. However, after the peak value, the WSS at up location is smaller compared to that at down location influenced more by the bifurcation structure.
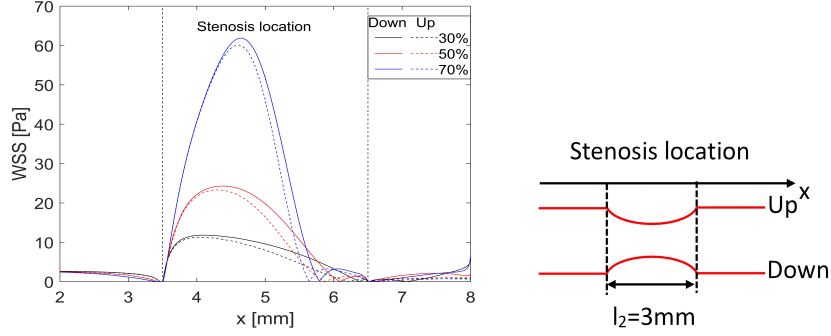
Figure 2.15: WSS distribution around stenosis at up and down locations under different stenosis severities at T/2

Similarly, Figure 2.16 represents the variation of WSS along stenosis of 50% at up and down location under different stenosis lengths when $t = T/2$. The length before and after stenosis are both 1.5mm. Different from the effect of stenosis severity above, with the increasing of stenosis length, WSS is reduced at both up and down locations. Meanwhile, the WSS difference between up and down location is more significant with smaller stenosis length. The larger stenosis length will more slow down the change of the flow velocity. Consequently, the lower WSS is generated by the decreased velocity gradient.
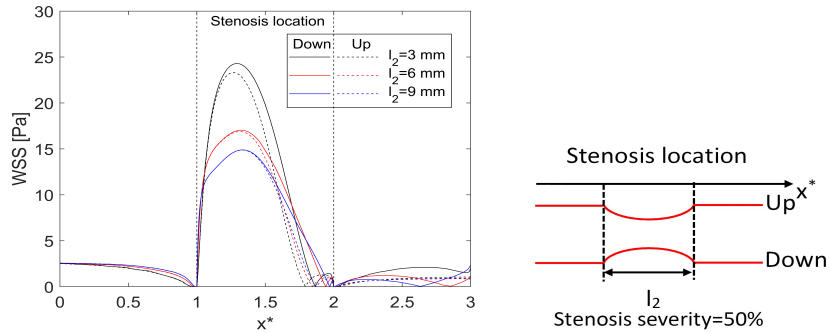
Figure 2.16: WSS distribution around stenosis at up and down locations under different stenosis lengths at T/2

When the initial stenosis is located in the side branch, the WSS is studied along the stenosis at different stenosis severities as shown in Figure 2.17. The stenosis length remains 3mm. Figure 2.17-(a) displays the WSS along stenosis of different severities at up location. The increased stenosis severity contributes to the increased WSS. The peak value occurred at the stenosis location is developed from one peak for 30% and 50% to two peaks for 70% with the increasing of stenosis severity affected by strongly disturbed flow with severe stenosis. Figure 2.17-(b) shows the WSS distribution along stenosis

of different severities at down location. Larger WSS is obtained with the increasing of stenosis severity caused by the drastic velocity variation. Different behavior is observed between the up side and the down side. This is due to the overpressure occurred at upside caused by the flow coming from the bifurcation.

(a)   (b)
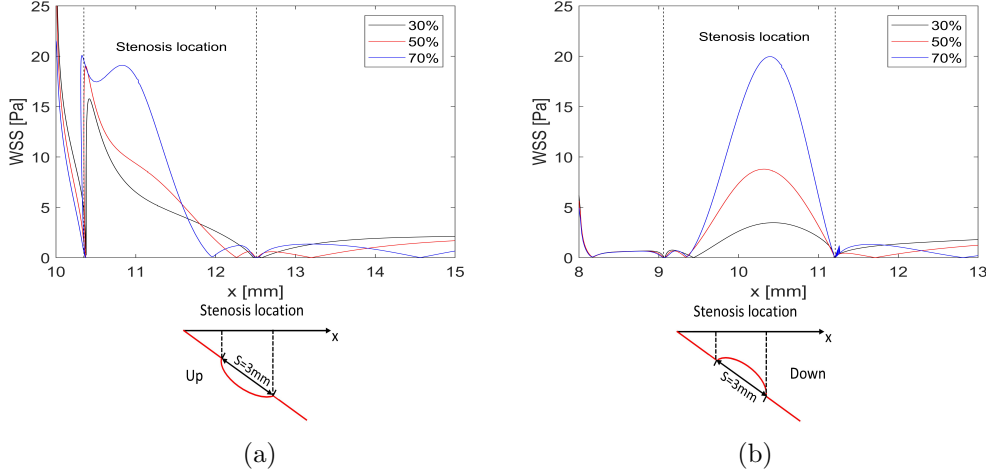
Figure 2.17: WSS distribution around stenosis at up (a) and down (b) locations under different stenosis severities at T/2

Figure 2.18 shows the WSS along stenosis at up (a) and down (b) locations under different stenosis lengths when it is located in the side branch at T/2. The stenosis severity keeps constant of 50%. When focusing on the WSS along the stenosis location, it is found that the increased stenosis length contributes to larger WSS, especially at the up location. For this location, it is easier to get the peak value at the beginning of the stenosis caused by the drastically changed flow direction due to the closer distance to the bifurcation edge. Consistent with above analysis, WSS at upside tends to be larger compared to that at down side.

(a)   (b)
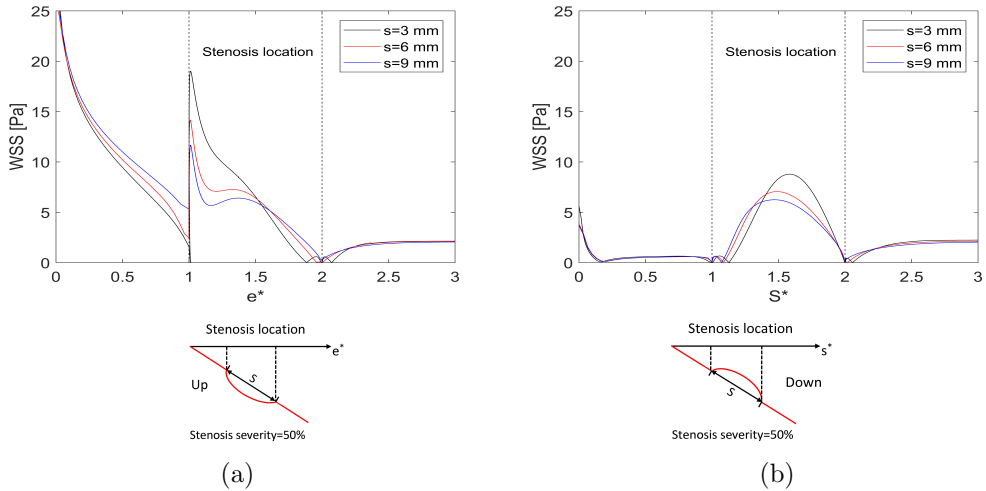
Figure 2.18: WSS distribution around stenosis at up (a) and down (b) locations under different stenosis lengths at T/2

Figure 2.19 shows the influence of stenosis length (a) and flow pulse rate (b) in the pressure drop coefficient (CDP) defined in equation (B.12) at different stenosis severities when the stenosis is located

in the main branch proximal. As can be seen in Figure 2.19-(a), with the increasing of stenosis length, the CDP tends to be increased. The difference caused by the stenosis length is more obvious with the increasing of stenosis severity. Focusing on the effect of stenosis severity on CDP, the increased stenosis severity contributes to the higher CDP and the relationship between them tends to be nonlinear. With larger stenosis severity, the variation of CDP becomes more drastic. According to the literature [140], the cut-off value used by doctors for CDP is 27.9. In our case, when the stenosis severity is 70%, the value of CDP exceeds the critical value under all these different stenosis lengths. Meanwhile, Figure 2.19-(b) shows that CDP is decreased with the increasing of flow pulse rate. Thus, when the patient is in exercising condition to make the clinical test, it is possible to misinterpret the clinical outcome especially in the case of stenosis of 70%.
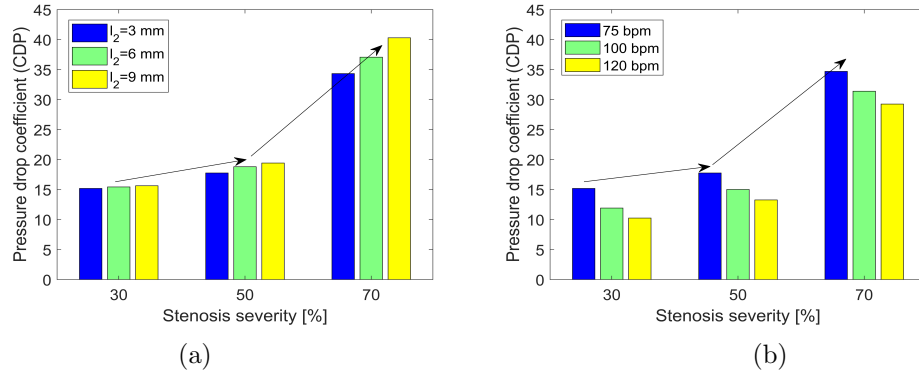
Figure 2.19: Effects of stenosis length (a) and flow pulse rate (b) on CDP at different stenosis severities

Figure 2.20 illustrates the influence of stenosis length (a) and flow pulse rate (b) in the lesion flow coefficient (LFC) defined in equation (B.13) at different stenosis severities when the stenosis is located in the main branch proximal. As can be seen in Figure 2.20-(a), the increased stenosis length brings decreased LFC which is more obvious with larger stenosis severity. However, the larger stenosis severity increases the value of LFC, and the relationship between them tend to be linear. In Figure 2.20-(b), it is found that increased flow pulse rate contributes to larger value of LFC. According to the literature [141], the critical value of LFC is 0.36. The value of LFC larger than 0.36 indicates the higher possibility of induced ischemia and revascularization. In our case, the LFC value over 0.36 can be got when the stenosis is up to 50%. The variation of the stenosis length and the pulse rate don't affect the final functional evaluation in our case referring to the critical value.
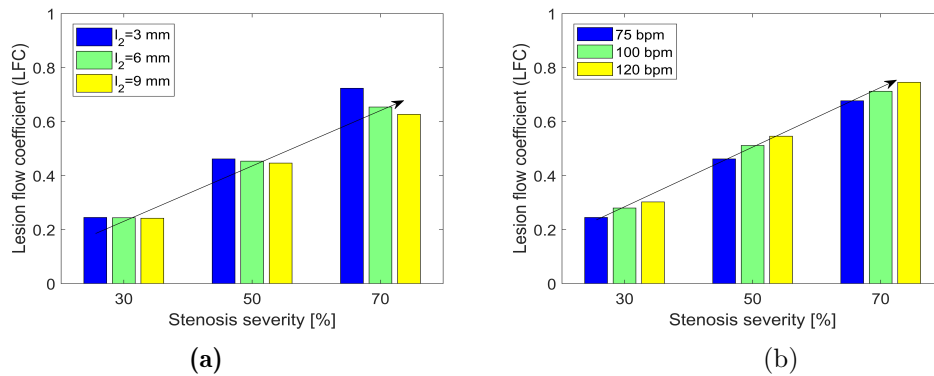
Figure 2.20: Effects of stenosis length (a) and flow pulse rate (b) on LFC at different stenosis severities

2.3.2 Case 2 : Hemodynamics in stenotic coronary artery coupling tortuosity

Artery tortuosity as another main geometrical characteristic is commonly observed in human body especially in the left anterior descending coronary artery [142]. Thus, the blood flow in tortuous artery and the relationship between artery tortuosity and stenosis occurrence have caused great interest among researchers.

Figure 2.21: Significant coronary artery [142]

Many studies have been carried out focusing on the curved artery [143–145]. M. Jarrahi et al. [146], M.R. Najjari et al. [147] and J.H. Siggers et al. [148] have experimentally studied the flow pattern in curved pipe to better understand the development of vortices structure through curvature. Recently numerical simulation as a research tool has been employed widely to investigate the physics of blood flow in the tortuous vessel [149]. The effects of morphological parameters of curvature on flow pattern and hemodynamics have been commonly discussed among the existing literature [150–152]. WSS as a key hemodynamic indicator to potential atherosclerosis sites has been found to be strongly affected by tortuosity. X. Xie et al. [153] have shown that the increased curvature angle larger than 120° contributes to a lower WSS zone, and the diastole pressure obtains a maximum increase of 96% compared to the non-tortuous artery model during exercise. Through works in 2019 by A. Buradi et al. [18], it has revealed that severe coronary tortuosity with small curvature radius, small distance between two curvatures and high angle of curvature contributes to low WSS zones at inner wall downstream of tortuosity section. Pressure drop caused by the tortuosity was demonstrated to negatively relate to coronary tortuosity angles and positively relate to coronary tortuosity numbers by Li et al. [154]. Among these existing investigations, many of them focus on the effects of vessel tortuosity or focus on the effects of stenosis. The studies considering both stenosis and tortuosity are really limited. G.Y. Liu et al. [155], B.Y. Liu [156] and M. Biglarian et al. [157] have considered the stenosis located at curvature site and studied the flow topology and WSS distribution at inner wall and outer wall. However, it should be notable that through clinical investigations in 2018 [158], the stenosis located at the non-tortuous segment before the tortuosities has been confirmed and the hemodynamic variations affected by the interactions between stenosis and tortuosity still remain interesting in this case.

The present section aims to investigate the flow topology and hemodynamic variations through 3D tortuous artery model with symmetrical and asymmetrical stenosis located upstream the tortuous seg-

ment. As the previous studies focused mainly on the curved artery, in this study, both curved and spiral tortuosity have been considered here based on the clinical review by H.C. Han [19]. Different stenosis severities of 20%, 35%, and 50%, different pulse rates of 75 bpm, 100 bpm and 120 bpm, and different distances of 0 mm, 3 mm and 6 mm between stenosis and tortuosity as controlling parameters have been investigated.

2.3.2.1 Geometrical and mathematical models

As the present study focuses on the blood flow in tortuous artery with stenosis. 3D geometrical models of coronary artery have been established both for curved and spiral tortuosity as shown in Figure 2.22-(a) and (b). In order to make the geometrical independence, the artery lengths before and after tortuosity are 40mm and 50mm. The stenosis is located upstream tortuosity with stenosis length of 6 mm. The horizontal length of one single curvature is 20 mm. The heights of curved and spiral tortuosity are 8 mm and 6 mm separately. The distance between stenosis and curvature as controlling parameter is named L taking the following values: 0mm, 3mm and 6mm. Comparison has been made between symmetrical and asymmetrical stenosis as shown in Figure 2.22-(c). Stenosis severity as another controlling parameter is defined as $(D - d)/D * 100$. D is the artery diameter of 3 mm. Different stenosis severities of 20%, 35% and 50% have been studied.
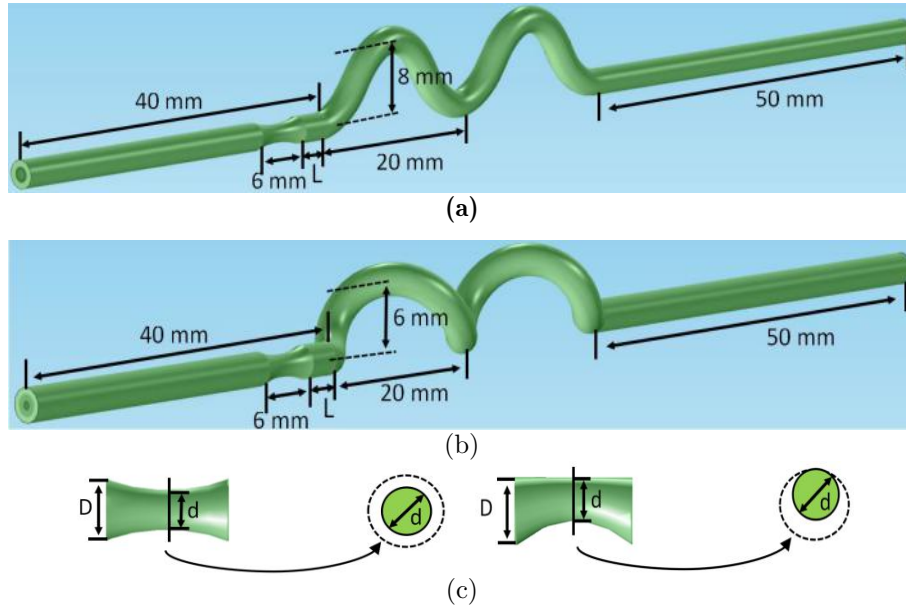
Figure 2.22: 3D geometrical model of curved artery (a) and spiral artery (b) with stenosis of symmetrical and asymmetrical structure (c)

In order to check the mesh independence, four mesh sizes of 210078, 570010, 1524838 and 2352717 have been studied. The WSS is investigated at these four different mesh sizes. After the third mesh size, WSS accuracy can be achieved around 2%. Taking the same way, the final determined mesh distributions can be obtained both for curved and spiral artery as shown in Figure 2.23 as an example. The multigrilles method is used to generate the unstructured tetrahedral mesh elements.

The mathematical models keep the same with the above case of arterial bifurcation except that a constant pressure of 0 pa is imposed at the outlet instead of the pulsed wave.

(a) Curved artery
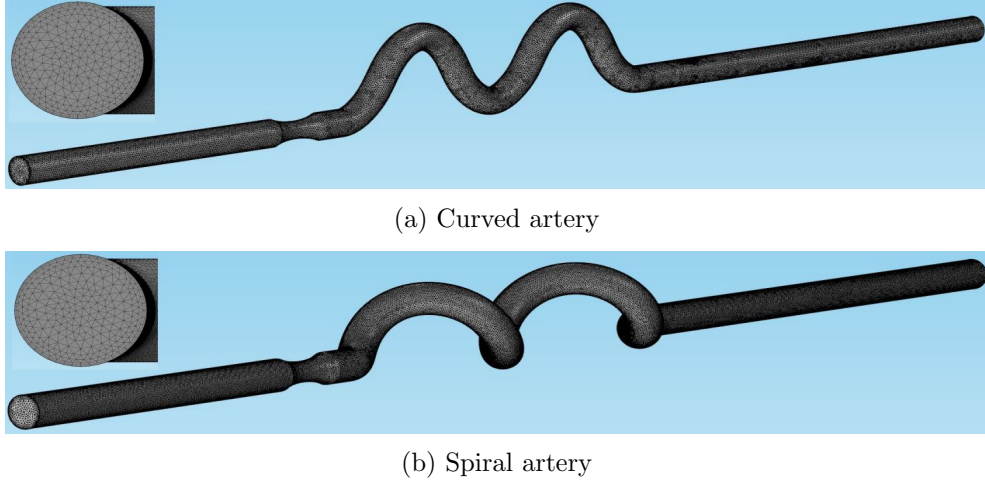
(b) Spiral artery

Figure 2.23: Mesh distribution for curved artery (a) and spiral artery (b) spiral artery

2.3.2.2 Blood flow in curved artery with symmetrical and asymmetrical stenosis

Table 2.2 displays the TAWSS distribution for curved artery at different stenosis severities of 0%, 20%, 35% and 50% under symmetrical and asymmetrical cases at 75 bpm. In order to better understand the results analysis, some locations used in the analysis have been displayed in Figure 2.24 with curved artery. It's commonly known that TAWSS is an important indicator to potential sites of stenosis with critical value of 0.4 Pa [159]. Lower value than 0.4 Pa indicates larger possibility of plaques. When we focus on the case of 0%, it is noticed that low value regions of TAWSS are located at outer wall upstream and inner wall downstream for each curvature. As the influence of stenosis located upstream the tortuosity is limited to the near region of curvatures, the zone in the black box is mainly focused in the subsequent analysis. TAWSS is greatly increased with larger stenosis severity both for symmetrical and asymmetrical stenosis focusing on the stenosis region and inner wall of tortuosity. The reason is the narrowed artery lumen brings more drastically varied velocity and stronger inertial force. Larger TAWSS at up wall downstream asymmetrical stenosis can be found compared to the symmetrical case. Because the geometrical change of stenosis is mainly at down wall for asymmetrical stenosis, stronger inertial force is remained near the up wall. Quantified results regarding the artery surface with TAWSS below 0.4 Pa (S_{TA}) defined in equation (B.10) have been plotted in Figure 2.25 which has well confirmed the observations through Table 2.2. Larger value of S_{TA} has been observed with asymmetrical case compared to symmetrical case. Because asymmetrical stenosis brings more disturbed flow downstream the stenosis due to the uneven effects on the arterial wall radially compared to the symmetrical stenosis.
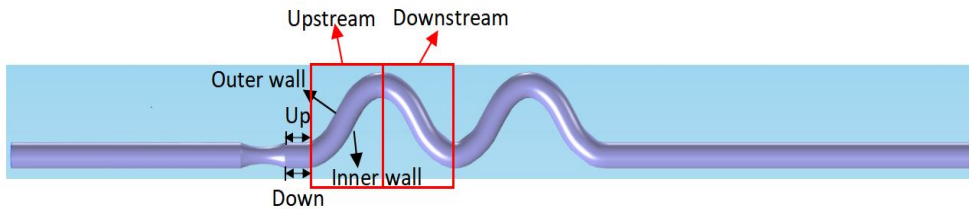
Figure 2.24: Location definitions with curved artery coupling stenosis
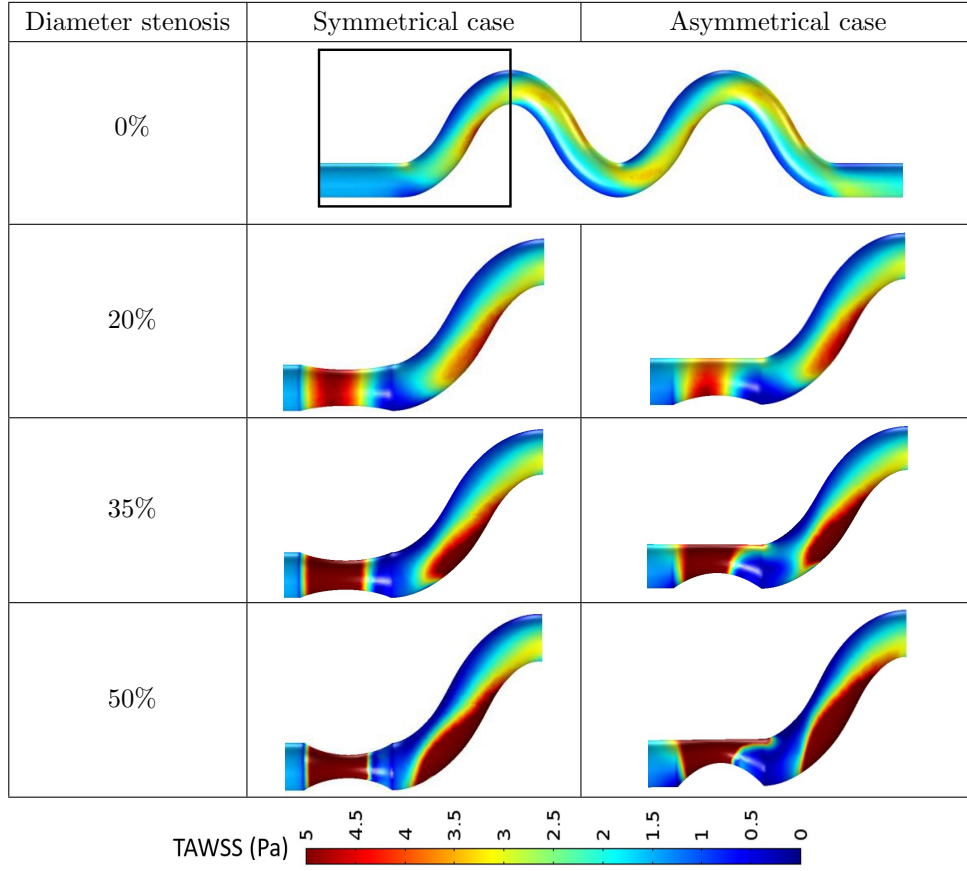
Table 2.2: TAWSS distribution at different stenosis severities for curved artery with symmetrical and asymmetrical stenosis at 75 bpm
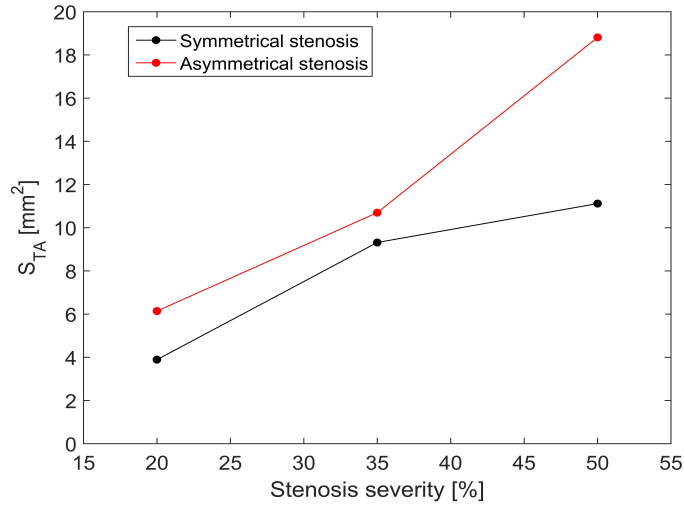
Figure 2.25: Artery surface of TAWSS below 0.4 Pa at different stenosis severities for curved artery

In order to better analyze the influence of symmetrical and asymmetrical stenosis in WSS variation at different stenosis severities, the area percentage of WSS below 0.5 Pa (S_p) defined in equation (B.11) over the total artery surface is plotted in one cycle shown in Figure 2.26. As can be seen that two

maximum peaks are obtained corresponding to the minimum velocities in one cycle, and the minimum value of S_p around 0.4 s corresponds to the maximum velocity in each case. Sharper velocity variation is obtained near vessel wall with the increased sectional mean velocity of blood flow. Asymmetrical stenosis tends to almost get higher value compared to the symmetrical case especially in the case of 50% stenosis where the difference between symmetrical and asymmetrical stenosis is more obvious. Increased stenosis severity results in stronger flow disturbance especially for the asymmetrical stenosis due to the more drastic radius variation downstream stenosis. Increased stenosis severity results in stronger flow disturbance especially for the asymmetrical stenosis due to the uneven effects on the arterial wall radially compared to the symmetrical case.

(a) 20%

(b) 35%

(c) 50%
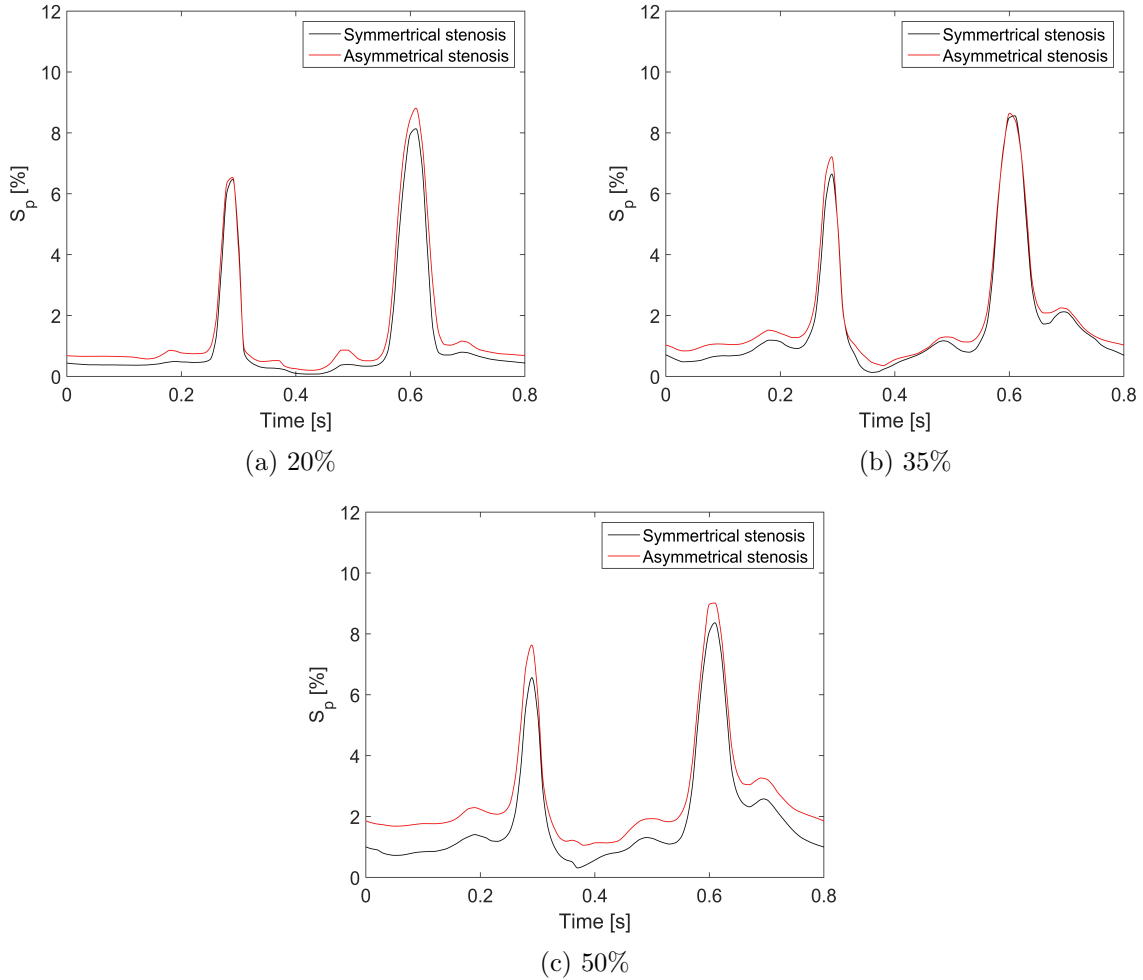
Figure 2.26: Area percentage of WSS below 0.5 Pa at different stenosis severities at 75 bpm

Physical activities of patients are closely related to the hemodynamic variation through changed flow pattern [142]. Thus, the TAWSS distribution is also studied at different pulse rates of 75 bpm, 100 bpm and 120 bpm with symmetrical and asymmetrical stenosis of 35% as shown in Table 2.3. Even though the changed pulse rate will bring hemodynamic variation overall the artery, in order to be consistent to the analysis above we still mainly focus on the stenosis part and the near part of tortuosity. As can be seen that larger pulse rate greatly increases the TAWSS value and low TAWSS regions located right downstream the stenosis and at the outer wall of tortuosity are both decreased because of the more

sharply varied velocity pattern. The quantified comparisons between symmetrical and asymmetrical stenosis regarding arterial surface area of TAWSS below 0.4 Pa affected by different pulse rates are shown in Figure 2.27. The obviously negative relationship between S_{TA} and pulse rate has been proved and a larger value of S_{TA} at asymmetrical case can be always observed.

Pulse rate	Symmetrical case	Asymmetrical case
75bpm		
100bpm		
120bpm		
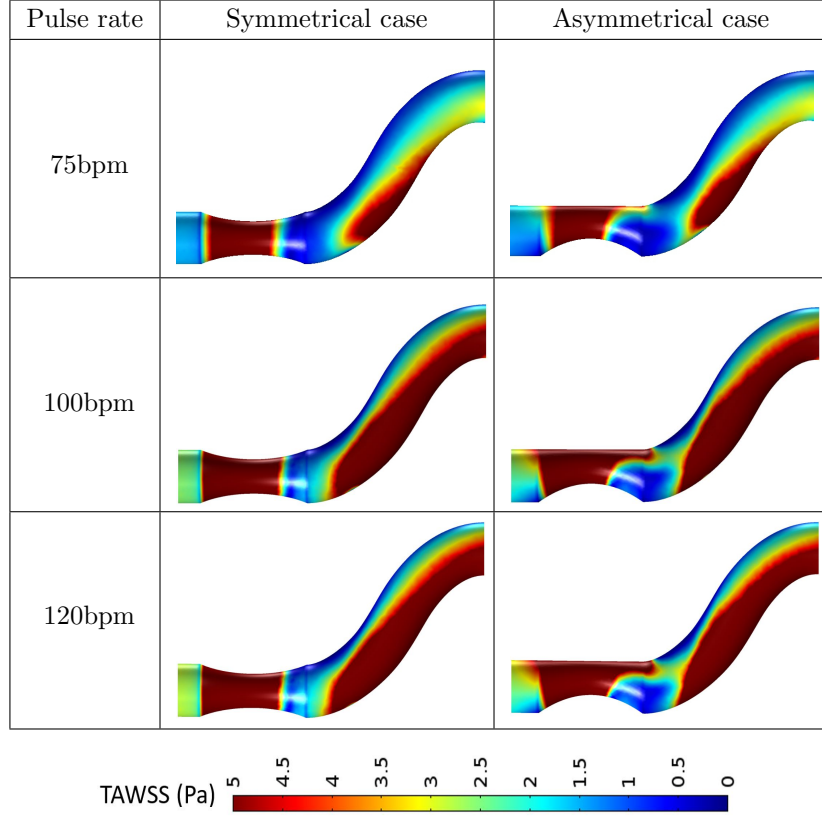
Table 2.3: TAWSS distribution at different pulse rates for curved artery with symmetrical and asymmetrical stenosis of 35%
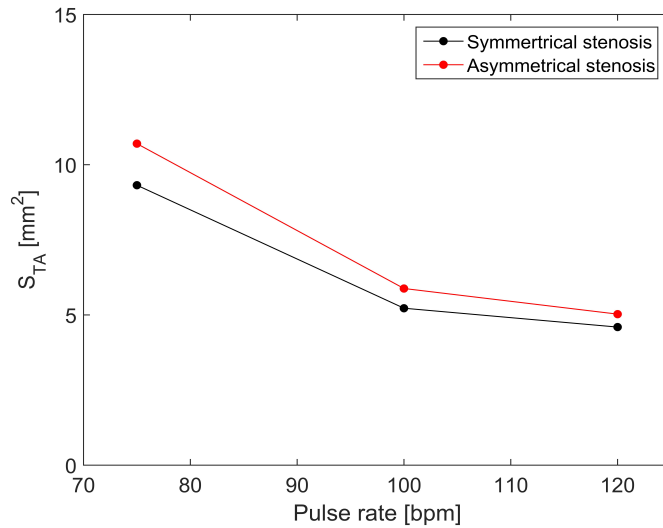
Figure 2.27: Artery surface of TAWSS below 0.4 Pa at different pulse rates for curved artery

Figure 2.28 shows the area percentage (S_p) of WSS below 0.5 Pa in one cycle at different pulse rates of 75 bpm, 100 bpm and 120 bpm with symmetrical and asymmetrical stenosis of 35%. In each case of pulse rate, the value of S_p with asymmetrical stenosis almost tends to be higher compared to the symmetrical stenosis. The variation tendency of S_p is negatively proportional to the velocity oscillation in one cycle. With the increasing of pulse rate, the area percentage of WSS below 0.5 Pa is greatly decreased both for symmetrical and asymmetrical cases because of the increased velocity variation rate near wall. Despite slight fluctuation at peak values, the value of S_p keeps higher at asymmetrical stenosis during one cycle.

(a) 75 bpm

(b) 100 bpm

(c) 120 bpm
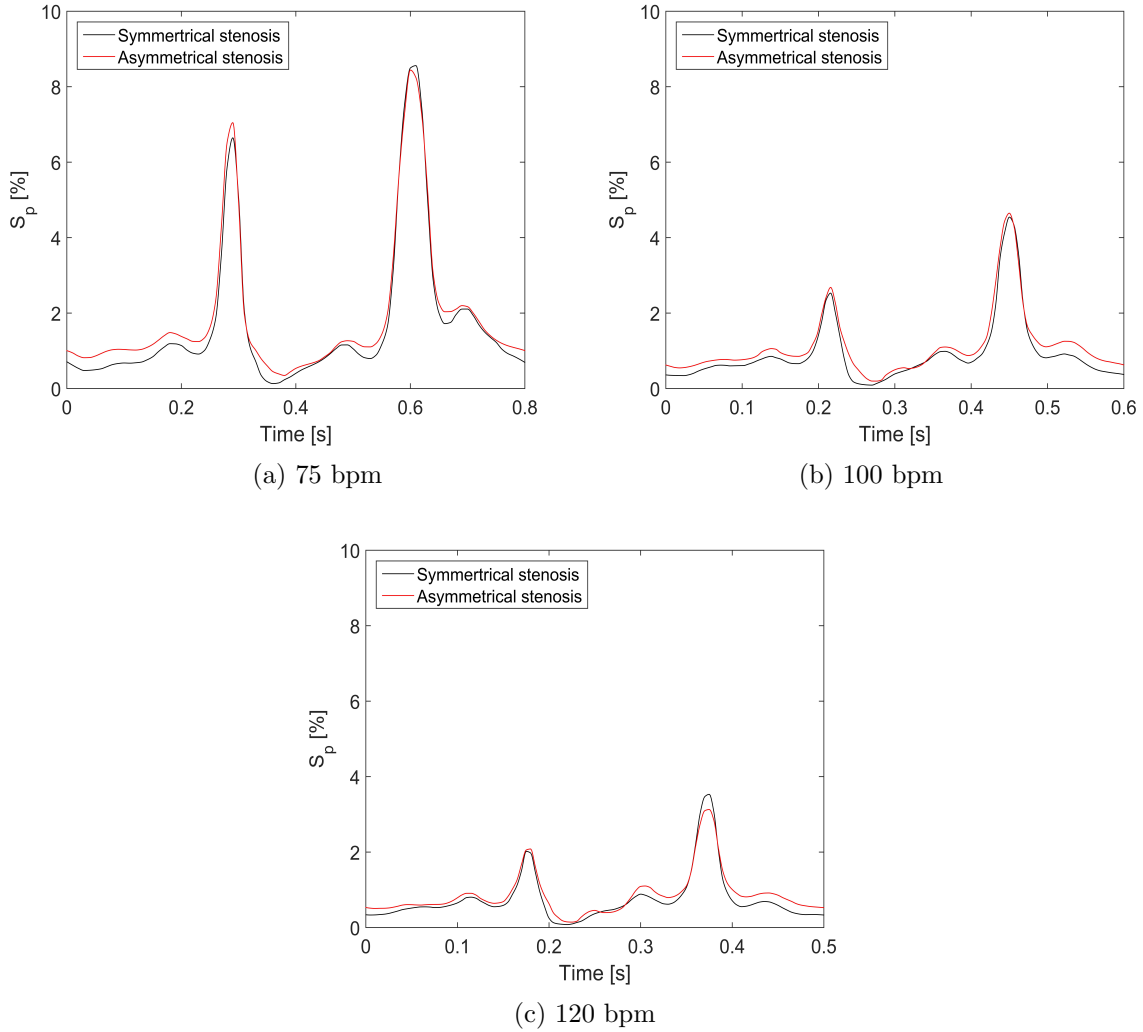
Figure 2.28: Area percentage of WSS below 0.5 Pa at different pulse rates with symmetrical and asymmetrical stenosis of 35%

Following the effect of stenosis severities and pulse rates on hemodynamic variation, the influence of distance between stenosis and tortuosity is discussed as well. Similarly, Table 2.4 shows the TAWSS distribution at different distances of 0 mm, 3 mm and 6 mm between stenosis and tortuosity with symmetrical and asymmetrical stenosis of 35% at 75 bpm. As can be seen, the increased distance between stenosis and tortuosity contributes to lower value of TAWSS especially when we focus on the upstream inner wall of tortuosity. The reduction of TAWSS is more obvious for symmetrical case. The increased

distance in our case also brings increased regions of low TAWSS. The reason is that increased distance after stenosis contributes to a more fully developed and stable flow which can weaken the inertial force into tortuosity. Compared to the symmetrical stenosis, larger value of TAWSS can be got at up wall after asymmetrical stenosis because there is no geometrical change along up wall. Similarly, the corresponding quantified analysis has been made with Figure 2.29 investigating the effects of distances between stenosis and tortuosity on the surface area of TAWSS below 0.4 Pa for symmetrical and asymmetrical cases. It is displayed that the value of S_{TA} is increased in asymmetrical case with the increasing of distance between stenosis and tortuosity. However, for symmetrical case, the value of S_{TA} is decreased with distance increased from 3 mm to 6 mm. The reason is because the flow after stenosis is still not be able to fully developed with effects of the formed recirculation downstream the asymmetrical stenosis and tortuosity. However, for symmetrical stenosis, the flow has been recovered to be fully developed when the distance is 6 mm. The larger value of S_{TA} at symmetrical case has been observed compared to the asymmetrical case which is in contrast to the results with effects of stenosis severity and pulse rate.
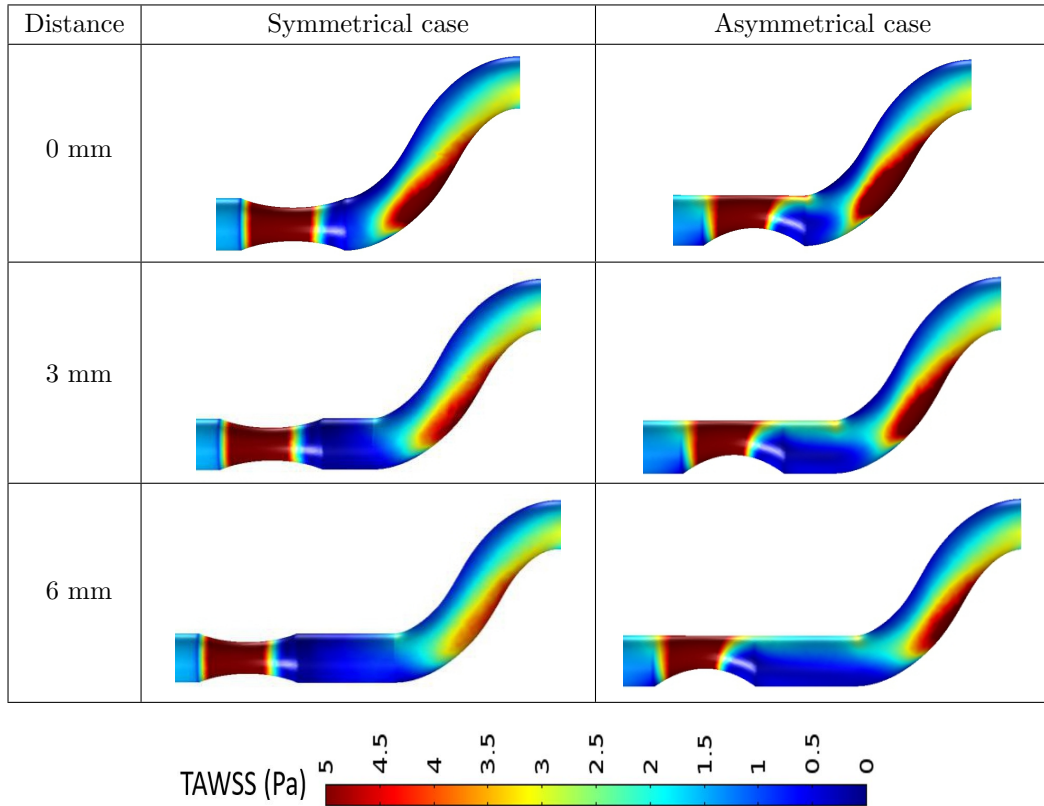
Table 2.4: TAWSS distribution at different distances between stenosis and toruosity for curved artery with symmetrical and asymmetrical stenosis of 35% at 75 bpm

Figure 2.29: Artery surface of TAWSS below 0.4 Pa at different distances between stenosis and tortuosity for curved artery

Qualified analysis is made through Figure 2.30 which plots the area percentage of WSS below 0.5 Pa in one cycle at different distances of 0 mm, 3 mm and 6 mm between stenosis and tortuosity with symmetrical and asymmetrical stenosis at 75 bpm. Similar phenomena can be found that the variation of S_p is negatively consistent to the velocity oscillation in one cycle. With the increasing of distance between stenosis and tortuosity, the area percentage of WSS below 0.5 Pa is increased because of more fully developed flow. When it is in the case of 0 mm, the value of S_p with asymmetrical stenosis is slightly higher compared to the symmetrical stenosis. However, when it is under the cases of 3 mm and 6 mm, the value of S_p at symmetrical case tends to be larger even though some sight fluctuations exist. For the reason, it is because the increased distance between stenosis and tortuosity leads to more low value region for the symmetrical case compared to the asymmetrical case which can balance and even over the effect of stenosis geometrical characteristics.

In Table 2.5, the effects of different curvature height on TAWSS distribution have been studied. The original height of curvature is defined as h_c, and then both $h_c/2$ and $h_c/4$ are considered here. As can be observed that the low value region of TAWSS always locates at stenosis downstream, the outer wall upstream and inner wall downstream along the tortuous segment. With the decreasing of curvature height, the distribution of TAWSS tends to be decreased because the decreased curvature height leads to the less disturbed flow. Similarly, in order to have a quantitative analysis of the low value distribution of TAWSS, the area percentage of TAWSS below 0.5 Pa (S_p) versus time has been plotted in Figure 2.31 at different curvature heights. Two peak values can be observed corresponding to the low value of velocity, however, the minimum value of S_p corresponds to the maximum velocity. Larger velocity bring sharper variation of velocity near vessel wall. With the decreasing of curvature height, the value of S_p tends to be increased except the peak values.

(a) 0 mm

(b) 3 mm

(c) 6 mm
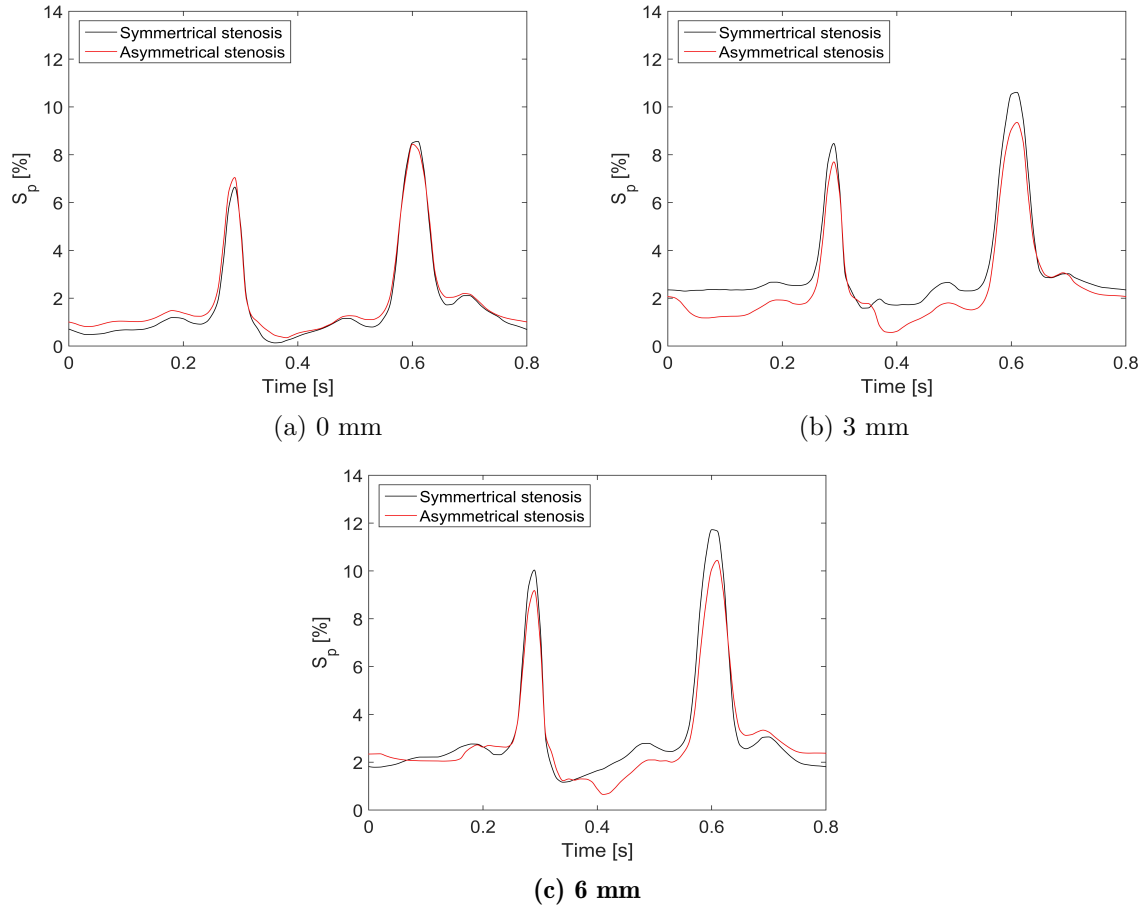
Figure 2.30: Area percentage of WSS below 0.5 Pa at different distances between stenosis and tortuosity with symmetrical and asymmetrical stenosis of 35% at 75 bpm

Curvature height	Front view
h_c	
$h_c/2$	
$h_c/4$	

TAWSS (Pa)

Table 2.5: TAWSS distribution at different curvature height for curved artery with symmetrical stenosis of 35% at 75 bpm

Figure 2.31: Area percentage of WSS below 0.5 Pa at different curvature height for curved artery with symmetrical stenosis of 35% at 75 bpm

Along the analysis of homogeneous curvature along curved artery, the non-homogeneous curvatures are considered and compared with different conditions. As shown in table 2.6, the TAWSS distribution at different curvature height ratios has been displayed.It's observed that in the case of curvature ratio of 1:2, the height of the first curvature is decreased compared to the case of curvature ratio of 1:1. The TAWSS distribution along the first curvature tends to be decreased, and there is no big change with that along the second curvature. In the case of curvature ratio of 2:1, it is observed that the second curvature height is decreased keeping the first curvature the same with that in the case of 1:1. It's seen that the distribution of TAWSS along the first curvature keeps the same with that in case 1:1. The results shows us the obvious influences of geometrical variation of curvature in TAWSS distribution. The smaller height of curvature tends to obtain larger region of low value region of TAWSS especially at the first location facing the coming flow.
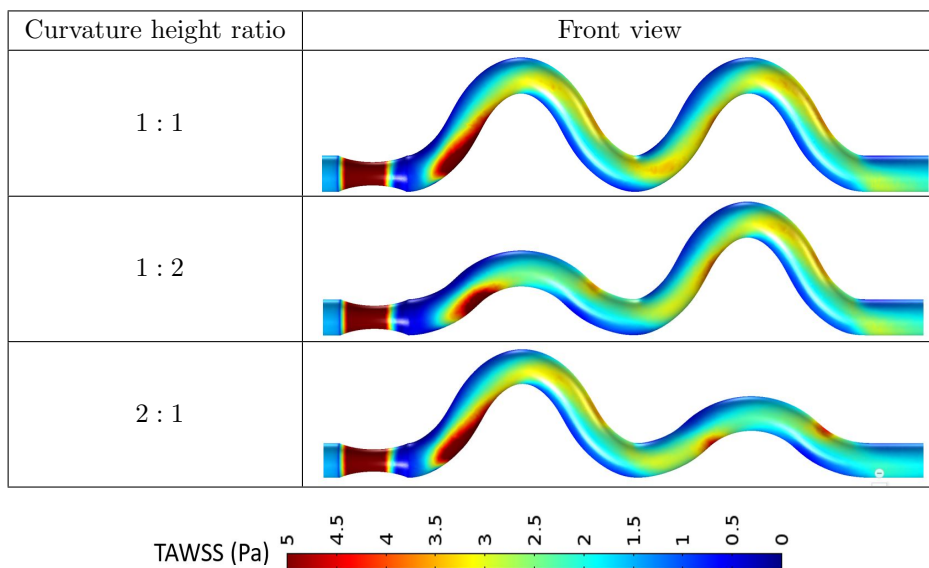
Table 2.6: TAWSS distribution at different height ratio for the two curvatures in curved artery with symmetrical stenosis of 35% at 75 bpm

Following the TAWSS distribution, the area percentage of WSS below 0.5 Pa versus time at different curvature height ratio with symmetrical stenosis of 35% at 75 bpm is plotted in Figure 2.32. It is seen that the value of S_p is negatively proportional to the inlet velocity variation. Larger velocity contributes to stronger inertial force and more sharply varied velocity near vessel wall. In the case of 1:2, the value of S_p keeps the highest during one cycle.However, in the cases of 1:1 and 2:1, the value of S_p tends to be superimposed most of the time in one cycle. Thus the results proves the important role of the curvature at first location facing the incoming flow.
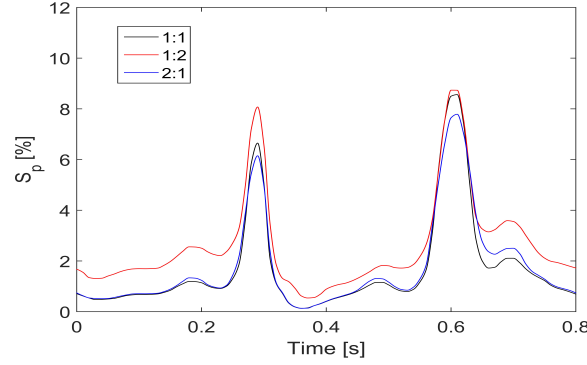
Figure 2.32: Area percentage of WSS below 0.5 Pa at different height ratio for the two curvatures in curved artery with symmetrical stenosis of 35% at 75 bpm

In order to check out the flow variation affected by stenosis severity, pulse rate and distance between stenosis and tortuosity, two cross sections S1 and S2 are selected as shown in Figure 2.33. The streamlines on these two cross sections are studied in Figure 2.34, Figure 2.35 and Figure 2.36 separately. When focusing on S1 in Figure 2.34, it is found that the high value region of velocity corresponds to the stenosis throat region and higher velocity value is consistent to larger stenosis severity both for symmetrical and asymmetrical cases. The streamlines is more disturbed with increased stenosis severity especially for symmetrical case even though there is no vortice formed. However, when focusing on S2 both in symmetrical and asymmetrical cases, the velocity distrubution is prone to be more affected by the tortuosity and no big changes occur to the peak value of velocity with the increased stenosis severity. The streamlines on S2 is more significantly disturbed compared to S1 especially for asymmetrical case. The vorties can be observed and the vortice number is developed from 2 into 4 with increased stenosis severity. Compared to symmetrical case, asymmetrical stenosis contributes to stronger flow disturbance at the same stenosis severity. Similar phenomena can be found out with the effects of different pulse rates shown in Figure 2.35 and distances between stenosis and tortuosity in Figure 2.36. Increased flow pulse rate brings larger velocity especially at S1 which is more affected by the stenosis. Stronger disturbance at S2 especially in asymmetrical case has been observed with increased pulse rate compared to symmetrical case. Moreover, the increased distance between stenosis and tortuosity greatly decreases the velocity value at S1 because of the more fully developed flow after stenosis.
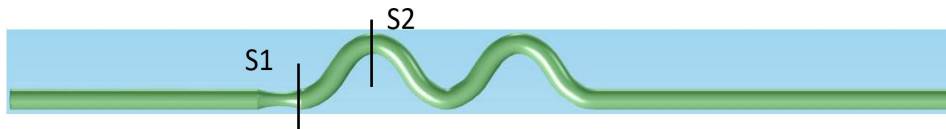
Figure 2.33: Positions of cross section selection
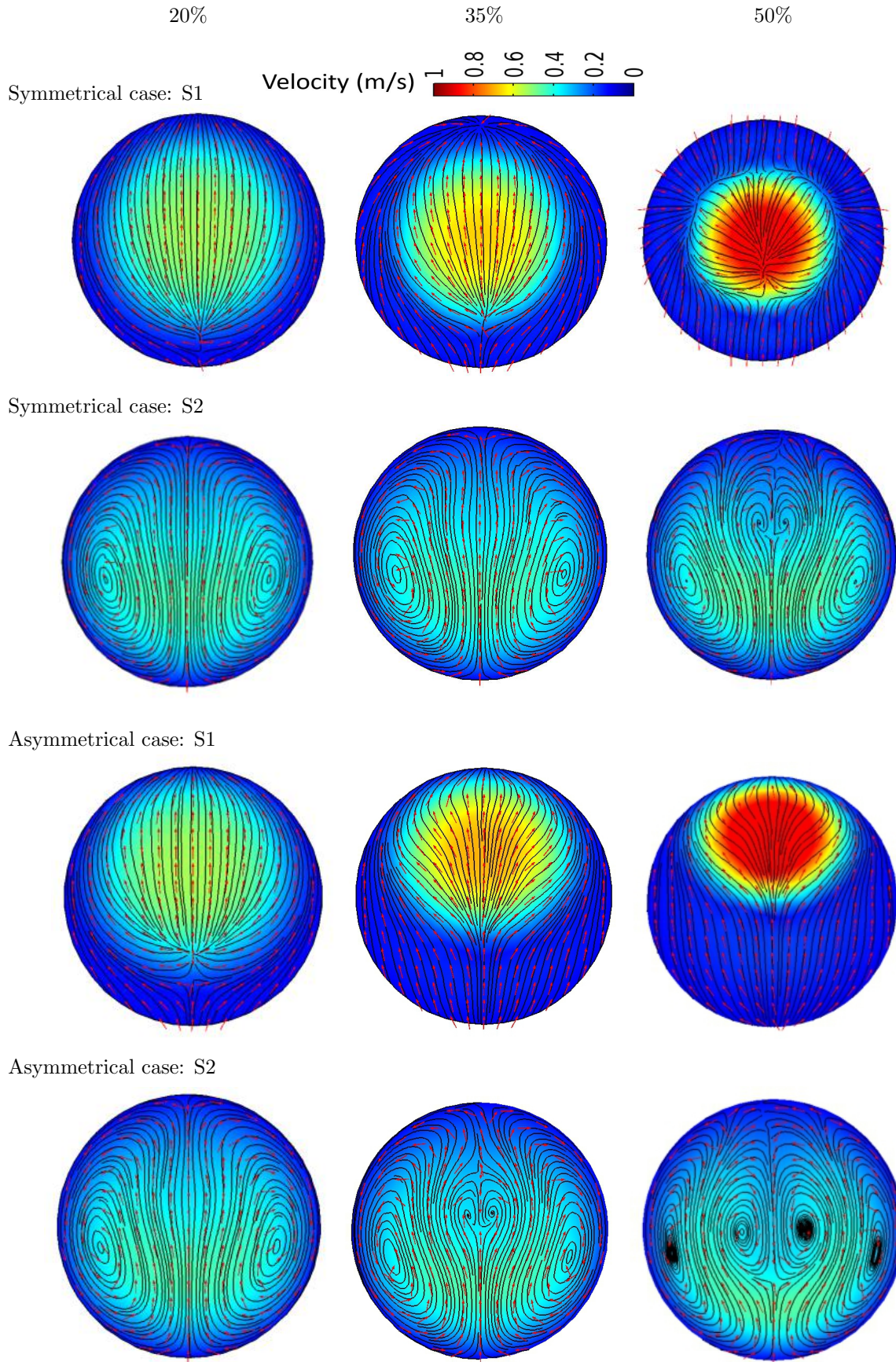
Figure 2.34: Streamlines with colored velocity distribution and vectors at S1 and S2 for different symmetrical and asymmetrical stenosis severities at 75 bpm at T/2
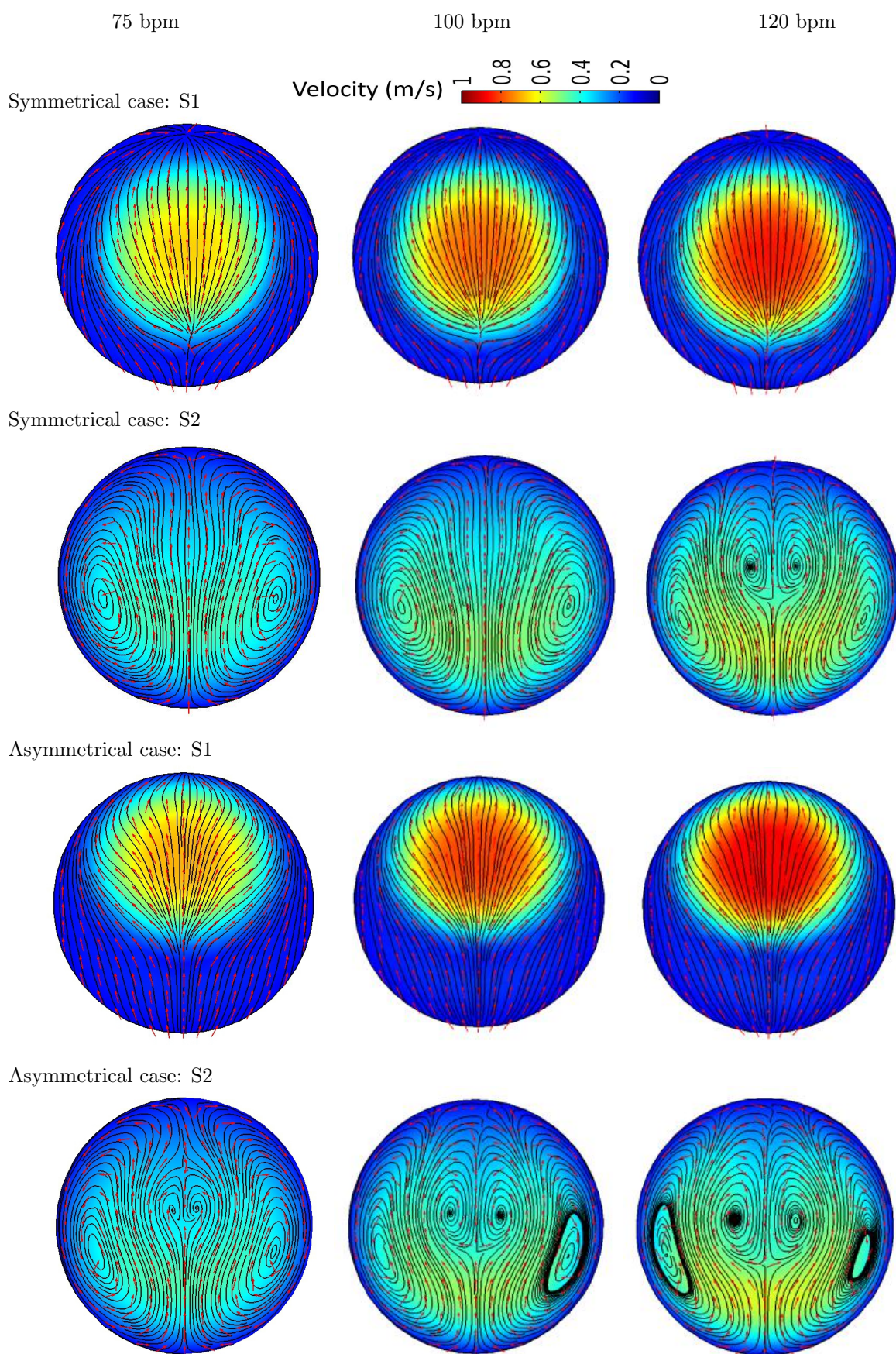
Figure 2.35: Streamlines with colored velocity distribution and vectors at S1 and S2 for symmetrical and asymmetrical stenosis of 35% for different pulse rates at T/2
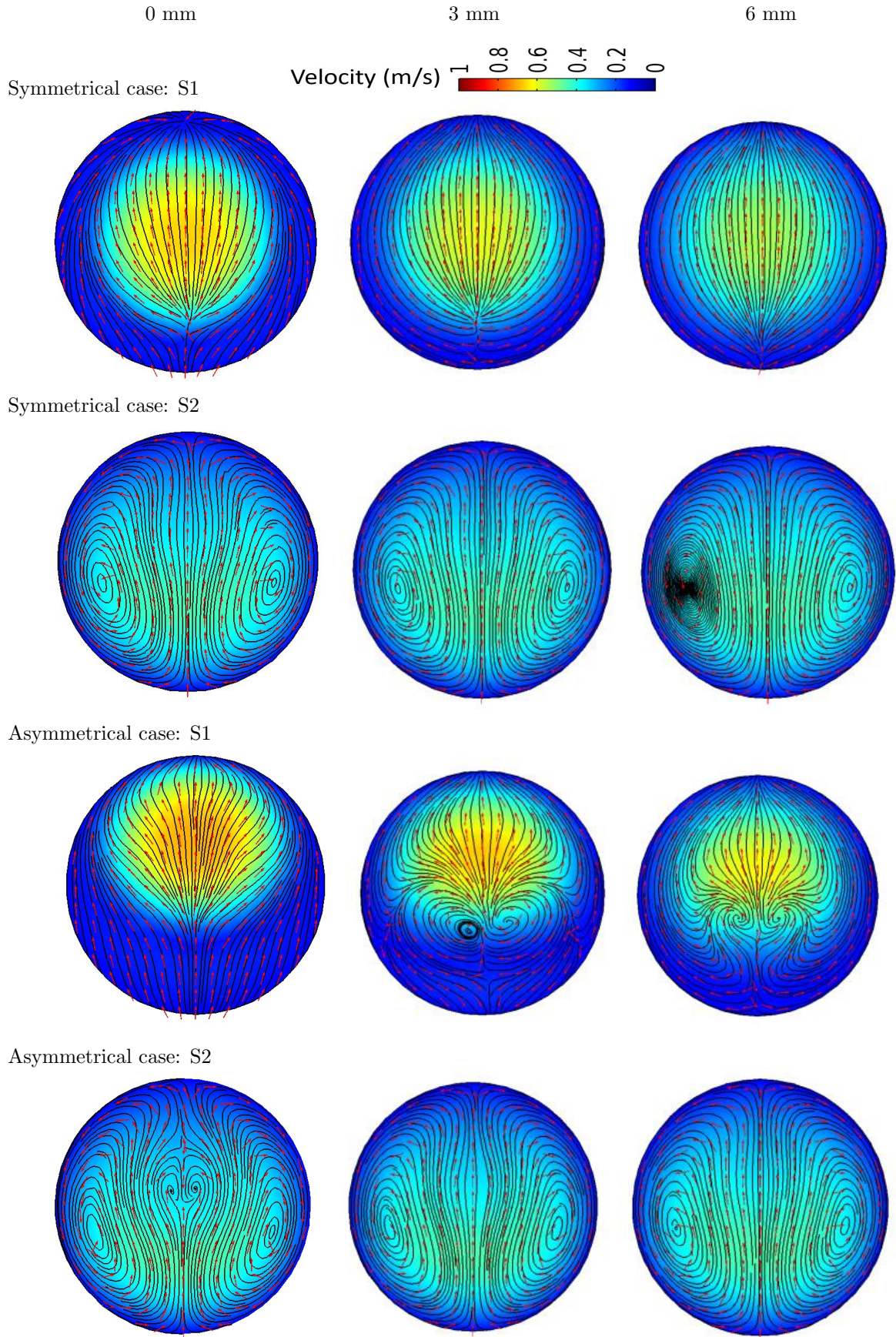
Figure 2.36: Streamlines with colored velocity distribution and vectors at S1 and S2 for symmetrical and asymmetrical stenosis of 35% at 75 bpm with different distances between stenosis and tortuosity at T/2

2.3.2.3 Blood flow in spiral artery with symmetrical and asymmetrical stenosis

As spiral tortuosity is one of the existing arterial morphological states found in human body, it is necessary to study how the hemodynamics are affected by spiral non-planar structure of artery instead of curved planar structure. Similarly, some location definitions used in analysis have been shown in Figure 2.37. Table 2.7 shows the TAWSS distribution with symmetrical and asymmetrical stenosis of 0%, 20%, 35% and 50% at 75 bpm for the spiral artery. The results are displayed from front and back views. When focusing on the case of 0%, it is found that low value of TAWSS is mainly located at entry and exit parts of the tortuosity. Along the tortuosity, larger value of TAWSS is always found at outer wall compared to the inner wall. Since the effect of stenosis is limited to the near region, in the following analysis the region in black box is mainly focused. With the increasing of stenosis severity, the high value region of TAWSS is greatly increased. The low value region of TAWSS is mainly located at stenosis downstream which tends to be decreased from front and back view with larger stenosis severity. Quantified analysis has been followed with Figure 2.38 which evaluates the surface area of TAWSS below 0.4 Pa under different stenosis severities for symmetrical and asymmetrical stenosis. It is found that the positive relationship between S_{TA} and stenosis severity in curved artery has been disturbed with symmetrical stenosis in spiral artery.
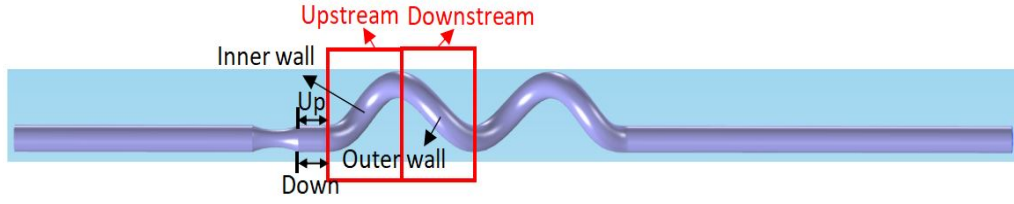
Figure 2.37: Location definitions with spiral artery coupling stenosis
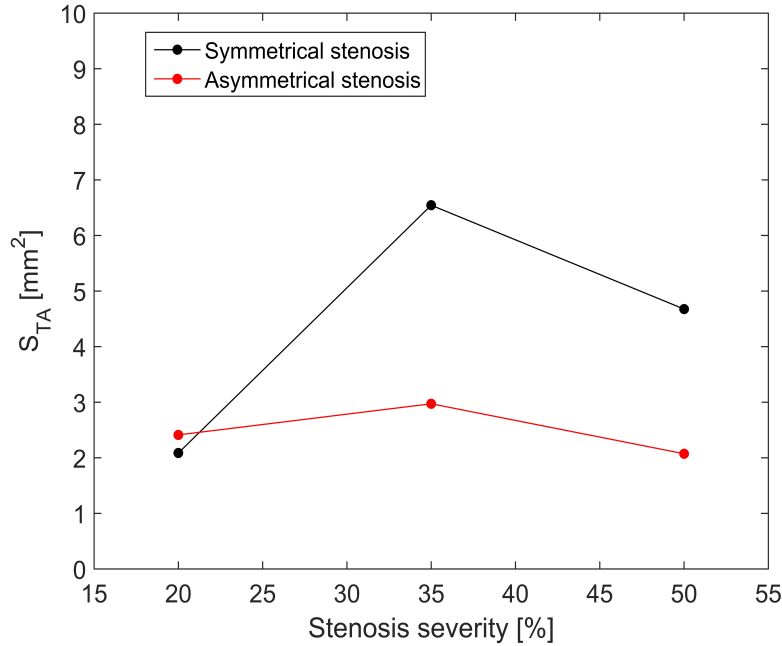
Figure 2.38: Artery surface of TAWSS below 0.4 Pa at different stenosis severities for spiral artery
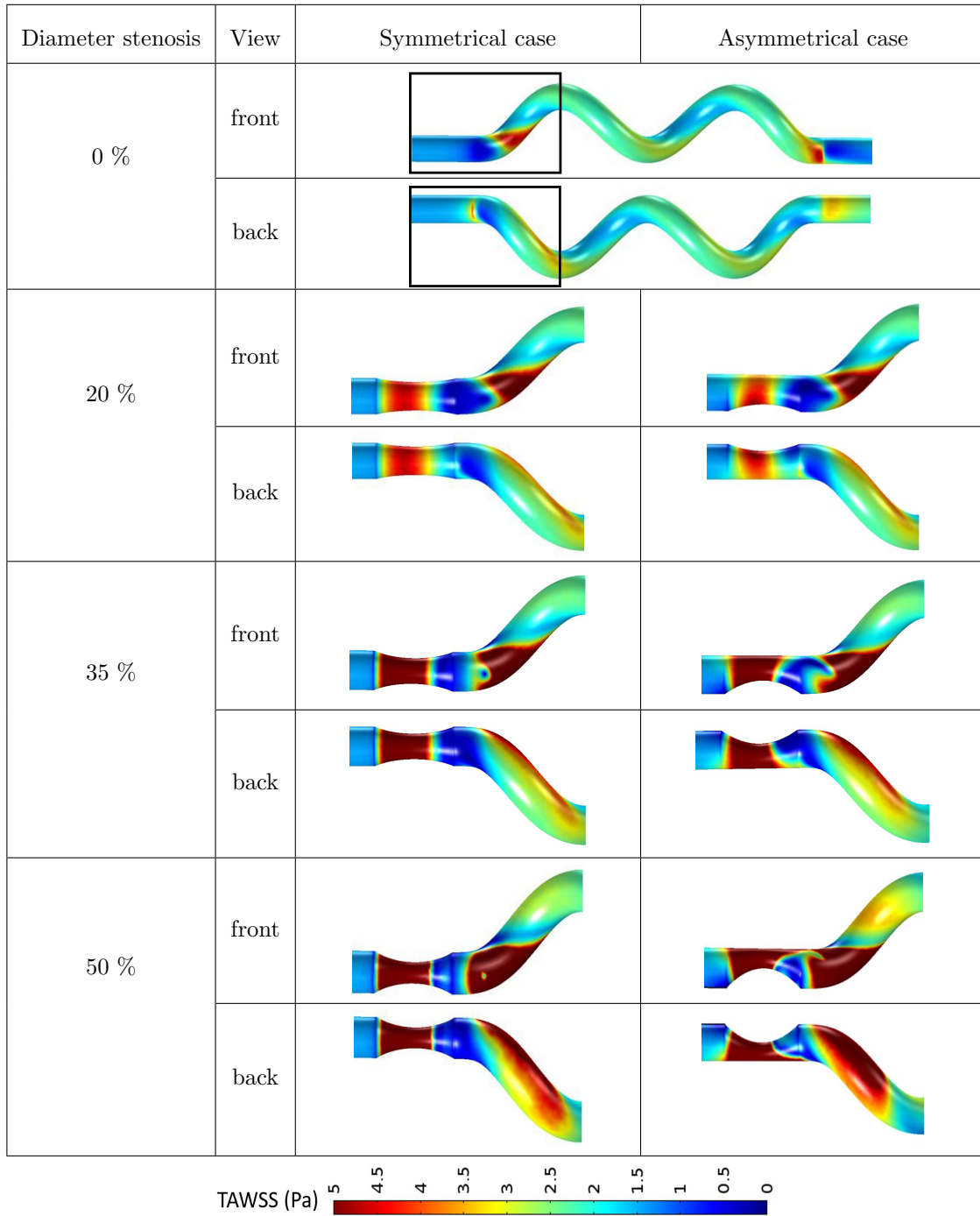
Table 2.7: TAWSS distribution at different stenosis severities for spiral artery with symmetrical and asymmetrical stenosis at 75 bpm

The qualified comparison between symmetrical and asymmetrical cases is studied in Figure 2.39 where the area percentage S_p of WSS below 0.5 Pa in one cycle is plotted at different stenosis severities. Larger value of S_p is always found at symmetrical case compared to asymmetrical case. The difference between symmetrical and asymmetrical stenosis is more obvious with increased stenosis severity. Because of more complicated geometrical characteristics of spiral artery compared to curved artery, the hemodynamic variations are prone to be more sensitive to the stenosis geometrical change.

(a) 20%

(b) 35%

(c) 50%
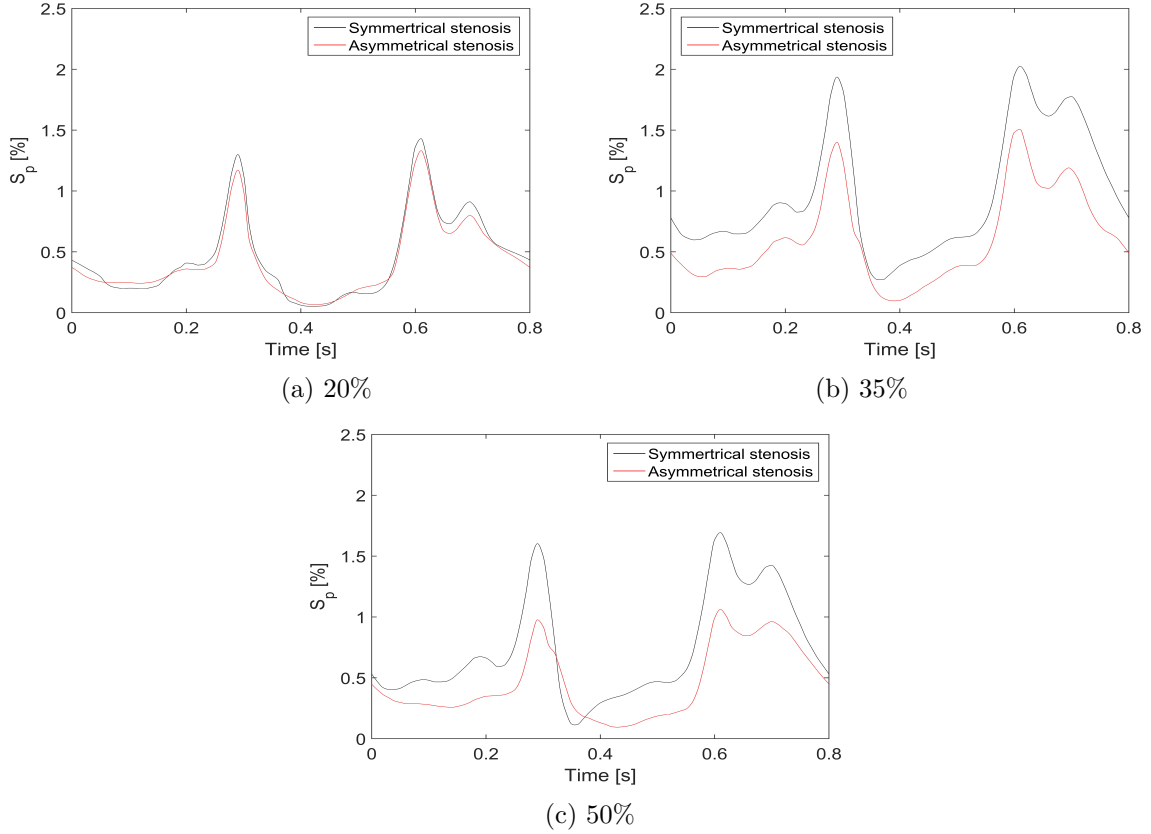
Figure 2.39: Area percentage of WSS below 0.5 Pa at different stenosis severities at 75 bpm

Table 2.8 shows TAWSS distribution at different pulse rates for symmetrical and asymmetrical stenosis of 35% for spiral artery. Larger pulse rate leads to overall increased TAWSS because of the increased velocity variation near wall. The low value region downstream stenosis is decreased at both front and back views with increased pulse rate. The corresponding quantified analysis has been made in Figure 2.40 where the surface area of TAWSS below 0.4 Pa at different pulse rates has been plotted for the cases of symmetrical and asymmetrical stenosis. The negative relationship between S_{TA} and pulse rate can be observed and the larger value of S_{TA} is obtained with symmetrical stenosis compared to the asymmetrical stenosis.
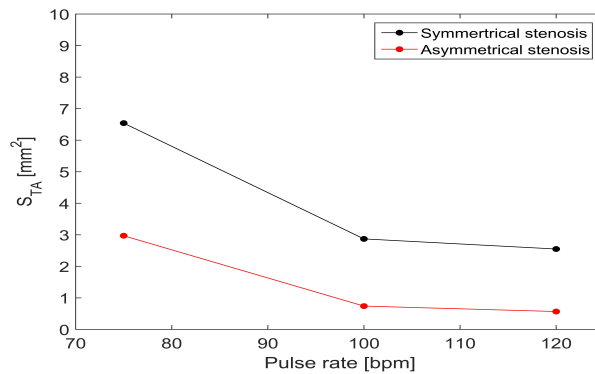
Figure 2.40: Artery surface of TAWSS below 0.4 Pa at different pulse rates for spiral artery
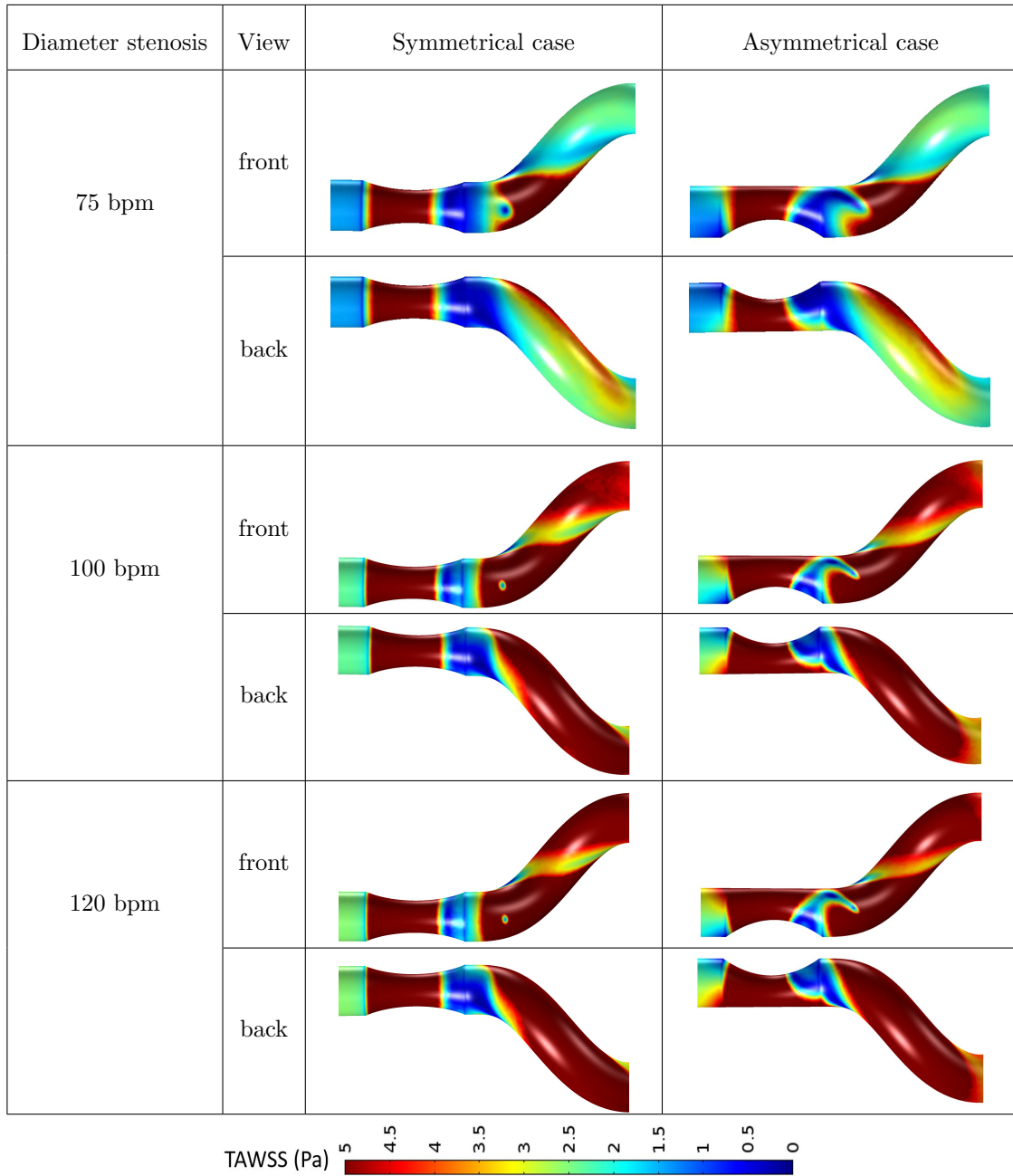
Table 2.8: TAWSS distribution at different pulse rates for spiral artery with symmetrical and asymmetrical stenosis of 35%

Consistently, the qualified study of area percentage of WSS below 0.5 Pa in one cycle at different pulse rates with symmetrical and asymmetrical stenosis of 35% is studied in Figure 2.41. As observed that the reduction of S_p is significant with larger pulse rate and the value of S_p is always higher at symmetrical case compared to asymmetrical case.

(a) 75 bpm

(b) 100 bpm

(c) 120 bpm
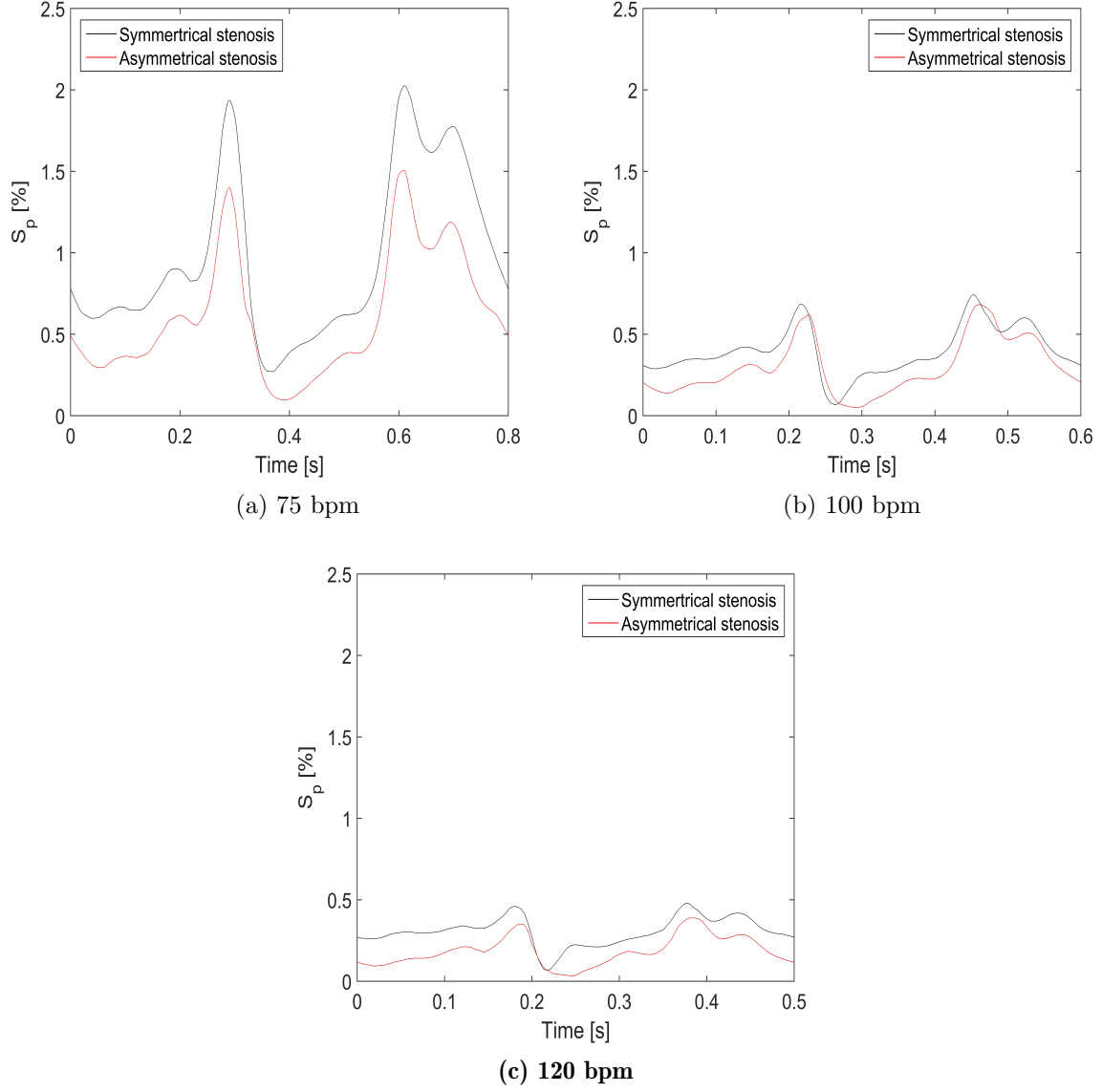
Figure 2.41: Area percentage of WSS below 0.5 Pa at different pulse rates with symmetrical and asymmetrical stenosis of 35%

As the stenosis is located at the non-tortuous segment before the spiral tortuosity, the distance between stenosis and spiral tortuosity need to be considered. Table 2.9 shows the TAWSS distribution at different distances of 0 mm, 3 mm and 6 mm between stenosis and tortuosity for symmetrical and asymmetrical stenosis of 35% at 75 bpm. Similar with curved artery, larger distance between stenosis and tortuosity greatly increases the low value region of TAWSS either at front view or back view. Compared to the asymmetrical stenosis case, larger low value region of TAWSS is observed at symmetrical case. Figure 2.42 shows the surface area of TAWSS below 0.4 Pa at different distances and confirmed the observations from Table 2.9. The value of S_{TA} is greatly increased with larger distance between stenosis and tortuosity as the flow is not able to be fully developed affected by the spiral tortuosity.
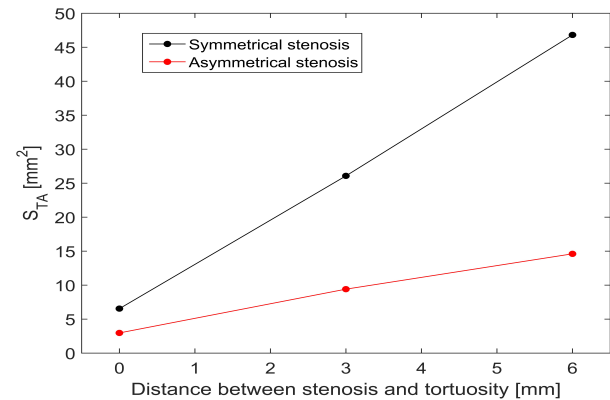
Figure 2.42: Artery surface of TAWSS below 0.4 Pa at different distances between stenosis and tortuosity for spiral artery

| Diameter stenosis	View	Symmetrical case	Asymmetrical case
0 mm	front		
	back		
3 mm	front		
	back		
6 mm	front		
	back		

Table 2.9: TAWSS distribution at different distances between stenosis and tortuosity for spiral artery with symmetrical and asymmetrical stenosis of 35% at 75 bpm
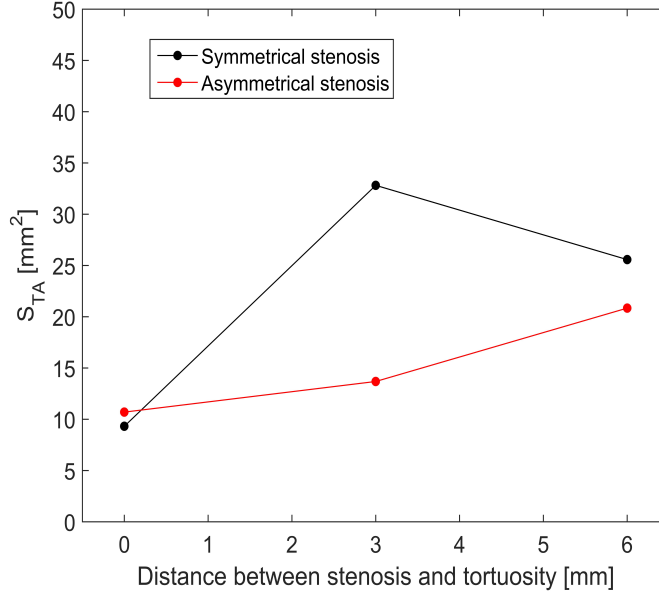
Qualified analysis is made in Figure 2.43 where area percentage of WSS below 0.5 Pa in one cycle at different distances for symmetrical and asymmetrical stenosis is plotted. The results show that larger value of S_p is obtained at symmetrical stenosis. The difference between symmetrical and asymmetrical cases is increased with increased distance. The distance between stenosis and tortuosity makes the blood flow more fully developed and the asymmetrical stenosis geometry can more maintain the inertial force within regions where the original artery geometry is remained.

(a) 0 mm   (b) 3 mm

(c) 6 mm
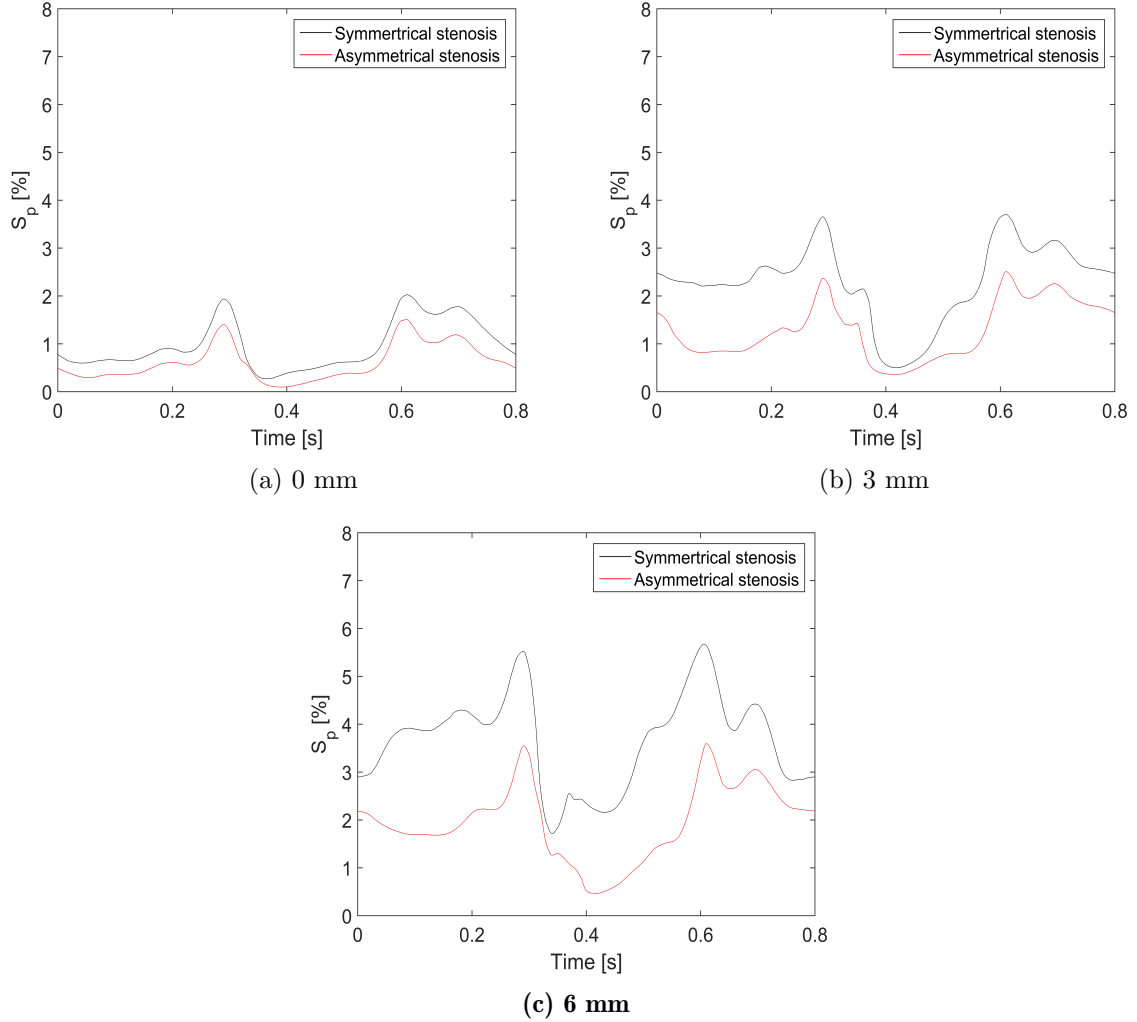
Figure 2.43: Area percentage of WSS below 0.5 Pa at different distances between stenosis and tortuosity with symmetrical and asymmetrical stenosis of 35% at 75 bpm

In addition to the effects of pulse rate, stenosis severity and distance bewteen stenosis and tortuosity, the effects of different curvature height on TAWSS distribution have been investigated as well as shown in Table 2.10. It is obviously observed that with the decreasing of the curvature height the distribution of TAWSS has been greatly decreased, the low value region tends to be enlarged along the curvature. The detailed analysis is studied through Figure 2.44 where plots the area percentage of low WSS below 0.5 Pa (S_p) versus time in one cycle at different spiral curvature height. The significant difference can be observed affected by the curvature height. With the decreasing of curvature height, the low value region of WSS below 0.5 Pa is increased in the whole cycle. Compared to the results of curved artery in Figure

2.31, WSS distribution is more sensitive to the variation of curvature height in spiral artery.
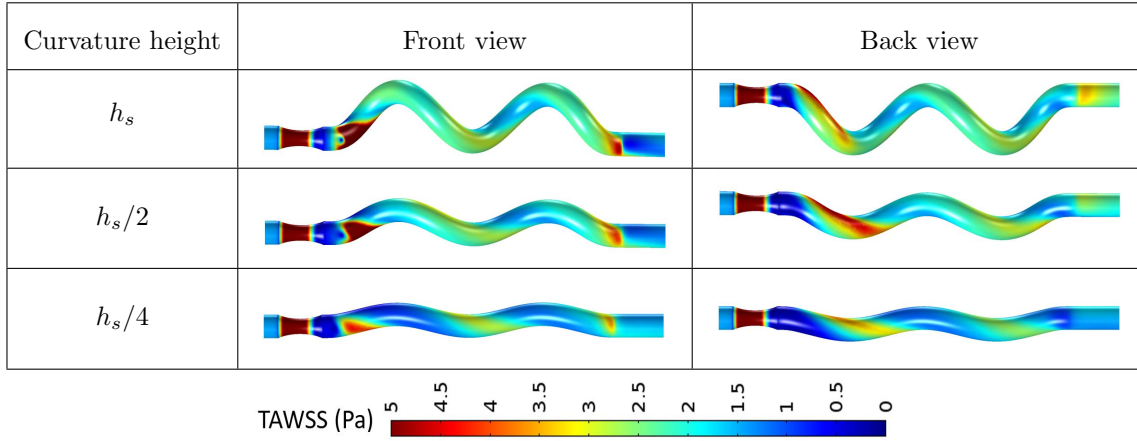
Table 2.10: TAWSS distribution at different curvature height of spiral artery with stenosis of 35% at 75 bpm.
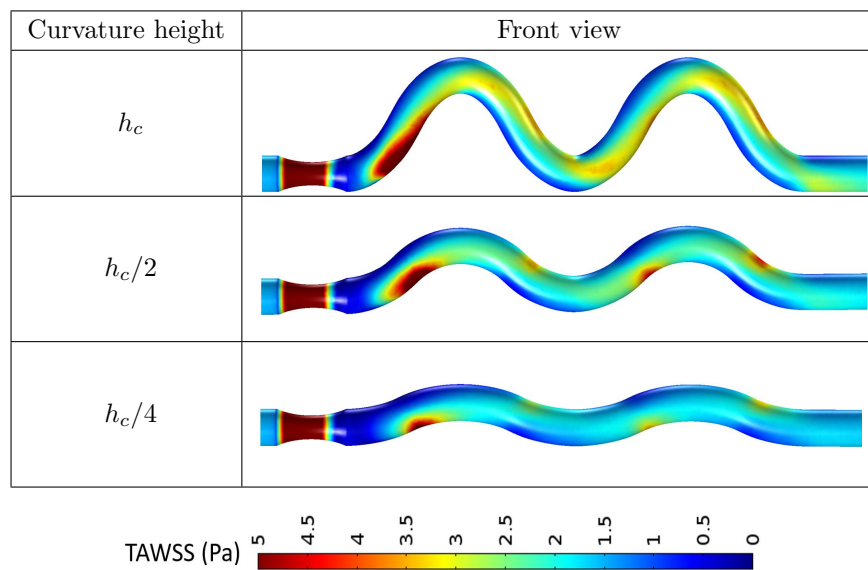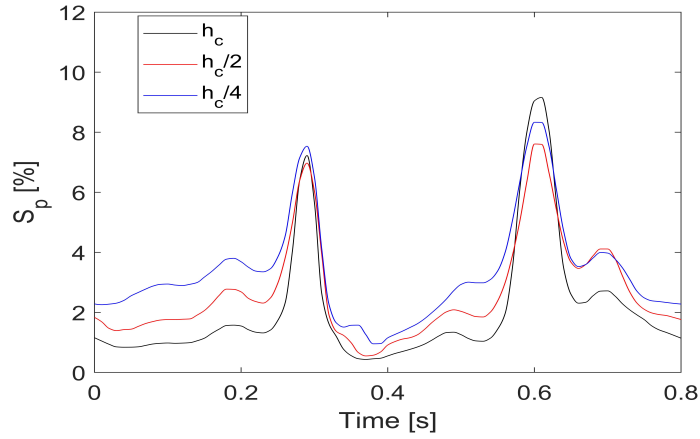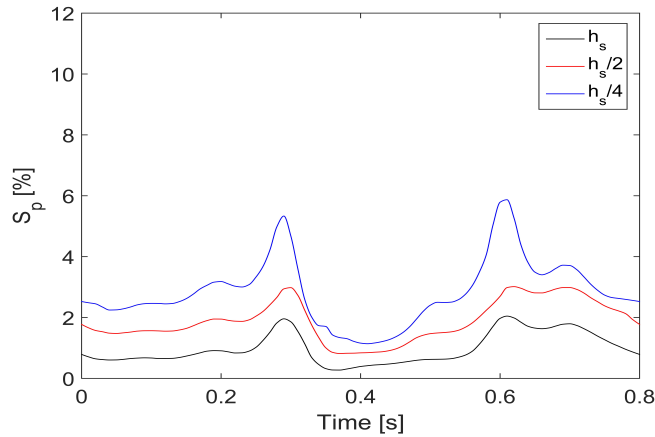

Figure 2.44: Area percentage of WSS below 0.5 Pa at different curvature height of spiral artery with symmetrical stenosis of 35% at 75 bpm

Spiral tortuosity as non-planar geometry makes the flow disturbance is more complicated. Compared to the curved tortuosity, both vertical and lateral curvature variations affect the blood flow for spiral artery instead of only vertical curvature variation. Thus the flow streamlines are studied in view of 3D instead of the 2D cross section compared to the planar curved artery. Table 2.11, 2.12, and 2.13 have given the views of streamlines colored with velocity around stenosis and tortuosity at different stenosis severities, different pulse rates and different distances between stenosis and tortuosity separately. Flow disturbance downstream stenosis and streamlines moving forward spirally along the tortuosity can be easily observed. As shown in Table 2.11, the peak value of velocity can be obtained at the stenosis site both in symmetrical and asymmetrical cases affected by the reduced artery diameter and the peak value is increased with larger stenosis severity. Moreover, with the increasing of stenosis severity, the flow disturbance is more complicated especially at stenosis of 50% and the recirculation downstream stenosis is more clearly observed. Compared to symmetrical case, the formation of recirculation downstream stenosis in asymmetrical case is more obvious which is affected by the stenosis height.

Stenosis severity	Symmetrical case	Asymmetrical case
20%		
35%		
50%		

Velocity (m/s) 1 0.8 0.6 0.4 0.2 0
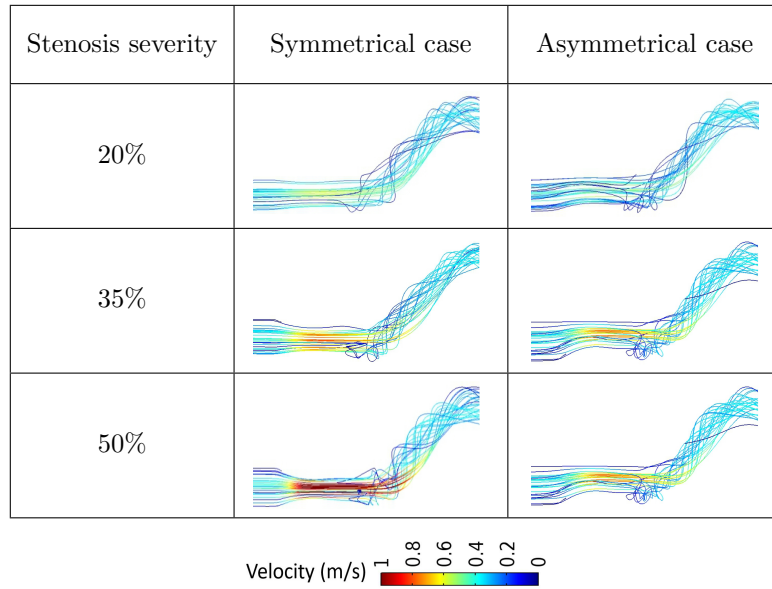
Table 2.11: Streamlines at different stenosis severities for spiral artery with symmetrical and asymmetrical stenosis at 75 bpm at T/2

When focusing on Table 2.12, similarly it is found that the increased pulse rate contributes to larger velocity especially at stenosis site and the inertial force can be enforced. Regarding the streamlines, the larger pulse rate tends to benefit the formation of recirculation downstream stenosis. Because of the larger stenosis height to vessel wall in asymmetrical case, a larger region of recirculation downstream stenosis is obtained compared to symmetrical case. In Table 2.13, the effects of different distance between stenosis and tortuosity on flow streamlines is studied. It is found out that larger distance between stenosis and spiral tortuosity is beneficial to the development of recirculations downstream stenosis which is more obvious for asymmetrical stenosis. The peak velocity is slightly decreased with increased distances because of fewer influences of the following tortuosity.

Pulse rate	Symmetrical case	Asymmetrical case
75 bpm		
100 bpm		
120 bpm		

Velocity (m/s) 1 0.8 0.6 0.4 0.2 0
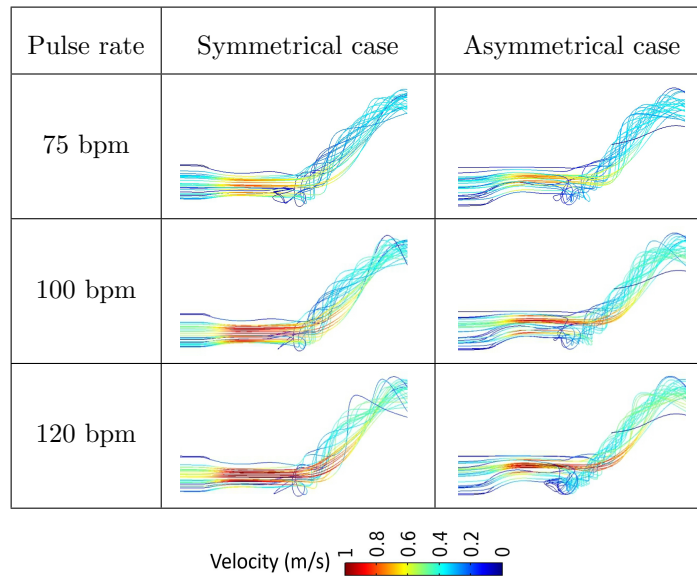
Table 2.12: Streamlines at different pulse rates for spiral artery with symmetrical and asymmetrical stenosis of 35% at T/2

Distance	Symmetrical case	Asymmetrical case
0 mm		
3 mm		
6 mm		

Velocity (m/s)
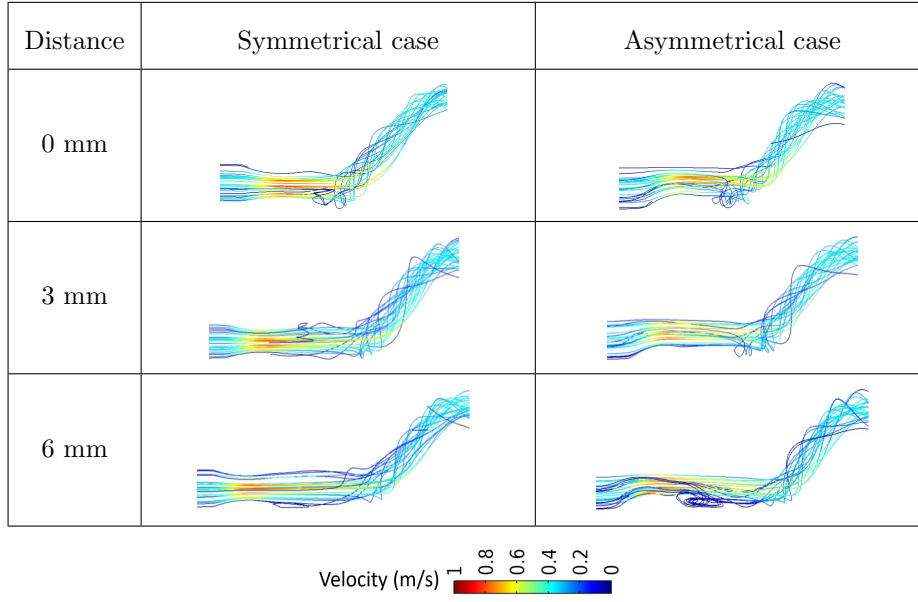
Table 2.13: Streamlines at different distances for spiral artery with symmetrical and asymmetrical stenosis of 35% at 75 bpm at T/2

Based on the results above, it revealed that larger risks of atherosclerosis generally go with larger stenosis severity, smaller pulse rate and larger distance between stenosis and tortuosity. However, some exceptions have been observed with the cases of symmetrical stenosis in curved artery with distance of 6 mm and stenosis severity of 50% in spiral artery. This is due to the fully developed blood flow after the stenosis site in the case of symmetrical case in curved artery with distance of 6 mm. For spiral artery, when the stenosis severity is increased to 50%, the low value region of TAWSS will be greatly reduced and restricted by the spiral tortuosity structure. Regarding the comparisons between symmetrical and asymmetrical stenosis, it is found that the values of S_p and S_{TA} tend to be higher for asymmetrical stenosis compared to symmetrical stenosis for curved artery which is in contrast to spiral artery under the effects of stenosis severity and pulse rate. Asymmetrical stenosis brings more disturbed flow downstream the stenosis due to the uneven effects on the arterial wall radially compared to the symmetrical stenosis. However, the effects of asymmetrical stenosis have been totally disturbed and weakened by the spiral tortuosity with more complicated geometrical variations. Moreover, in the case of different distances between stenosis and tortuosity, larger values of S_p and S_{TA} are obtained with symmetrical stenosis compared to asymmetrical stenosis both for curved and spiral artery. Because the asymmetrical stenosis means uneven effects on vessel wall which makes the peak inertial force tend to the less narrawed side of vessel wall from the center. Thus larger WSS has been obtained at up wall compared to the down wall in asymmetrical case instead of comparatively even distribution of smaller WSS in symmetrical case.

The vortices indicating the flow disturbance level have been found affected by the curvature, and the streamlines moving forward spirally along the spiral tortuosity can be easily observed affected by the spiral structure. An amplified effect on flow and hemodynamic variations from spiral tortuosity structure has been clearly demonstrated compared to curved artery under the effects of stenosis mophology, pulse rate and distances between stenosis and tortuosity. It is notable that when we compare the values of S_p between curved and spiral tortuosities through Fig. 24, 26 28 and Fig. 34, 36, 38 respectively, the obviously smaller values have been always obtained under each condition for spiral artery. This finding

is consistent with the investigations by the group of X. Deng et al. [160,161]: swirling/spiral flows could suppress platelet adhesion.

2.4 Conclusions

In this chapter, numerical and mathematical models regarding blood flow in the coronary artery have been discussed. As presented above, the blood flow is established as Newtonian fluid limited by the small vessel with low values of Womersley number and shear rate. Based on the low Re number within laminar regime, parabolic velocity profile is set in our study and the blood flow is governed by the Navier-Stokes equations. Since the circumferencial strain of artery wall can be neglected when the disease happens confirmed in the literature, the vessel wall is considered as rigid. The numerical reconstruction of blood flow profile has been accomplished through eight-coefficient Fourier equations by Matlab. Taking into account the physical activities, velocity profiles with different pulse rates have been constructed. Moreover, the hemodynamic and diagnostic parameters as the evaluation methods have been introduced as well.

Following the determinations of modeling characteristics about the blood flow in coronary artery, the preliminary study is carried out with stenotic artery coupling the arterial geometrical singularities, even though the coupling between blood flow and arterial geometrical singularities is unidirectional. Two cases are conducted with arterial bifurcation and tortuosity separately focusing on effects on the flow disturbance. The results reveal that in the case of bifurcated artery, when the stenosis is located in the main branch proximal, the recirculation follows the flow orientation. However, when the stenosis is located in the side branch, the recirculation will be formed both upstream and downstream the stenosis. The stenosis severity plays a key role for the recirculation size and the relative pressure drop compared to the stenosis length in the case of stenosis at main branch proximal. However, in the case of stenosis at side branch, the influences of stenosis severity and stenosis length in relative pressure drop can be neglected. For WSS along the stenosis either at main branch proximal or at side branch, the distribution at up and down location is asymmetrical affected by the bifurcation structure. The increased stenosis severity contributes to the larger WSS which is in contrast with the stenosis length. For the diagnostic evaluation, when the stenosis is at main branch proximal, the variation of stenosis length and pulse rate in our case doesn't affect the final evaluation results.

The second case is related to curved and spiral tortuosity with the existence of symmetrical and asymmetrical stenosis upstream. The results concluded that the low value of TAWSS located downstream the stenosis can be observed. Along curved tortuosity, the low value region of TAWSS is located outer wall upstream and inner wall downstream for each curvature. However, the low value of TAWSS tends to be always located at inner wall along the spiral tortuosity. Larger area percentage of WSS below 0.5 Pa and area of TAWSS below 0.4 Pa go with larger stenosis severity, smaller pulse rate and larger distance between stenosis and tortuosity both for curved and spiral artery except in the cases of symmetrical stenosis in curved artery with distance of 6 mm and stenosis severity of 50% in spiral artery. Spiral artery is more sensitively affected by stenosis morphology from symmetrical to asymmetrical state compared to curved artery. The value of S_p tend to be higher for asymmetrical stenosis compared to symmetrical stenosis within the effect of stenosis sevetrity and pulse rate which can be reversed by increasing the distance between stenosis and tortuosity for curved artery. However, for spiral artery the higher value of S_p always goes with symmetrical stenosis compared to asymmetrical stenosis. Meanwhile the flow disturbance tends to be stronger with larger stenosis severity and pulse rate, and smaller distance

between stenosis and tortuosity especially for asymmetrical stenosis in curved artery. Flow disturbance downstream stenosis and streamlines moving forward spirally along the tortuosity can be easily observed in spiral artery.

Blood flow through coronary artery treated by stent

Contents

3.1 Introduction

Through chapter 2, the modeling characteristics of blood flow in coronary artery have been presented and an initial view of the effects of artery geometrical singularities on hemodynamics has been provided. Therefore, based on the background of atherosclerosis and the treatments of stent implantation, in this chapter the coupling between blood flow and stent has been carried out. Even though the stent has achieved effective progress among the treatments, the risks of follow-up complications can not be ignored and still remain challenging. As known commonly through literature, artery restenosis can happen with the cell proliferation after stent implantation and relates strongly to the low value of WSS affected by the disturbed flow. The presence of stent in artery as a type of geometrical singularity has a direct influence in flow disturbance which in turn acts on the hemodynamic variations and potential stenosis generation along the stent. Therefore, the stent performance optimization is necessarily required in order to minimize the negative influences with effective clinical outcome.

The stent design was firstly found to be linked with adverse clinical outcome inside stented rabbit iliac arteries in 2000, and the variation of WSS is found to be greatly associated with neointimal hyperplasia. The disturbed flow has been commonly found with the vortices formation upstream and downstream the stent and the low value of WSS in recirculation region has been demonstrated as well [48–50]. Many considerations of stent design characteristic have been taken into account among the existing literature with the purpose of minimizing the flow alteration such as the stent location, stent type and specific design parameter of strut. 2D model has been more commonly established with the consideration of cross section shape of strut, inter-strut space and stent thickness in literature. The thinner strut and larger

inter-strut space has been commonly demonstrated to be beneficial to improve the stent performance. However, in practice of stent fabrication some conflicts need to be balanced between the required stent strength and optimal design factors of stent as well.

In view of exploring more possible methods of stent optimization and contributing to the current research data, the interaction between stent design factors and hemodynamic variations has been analyzed in this chapter and the effects of physical activities on hemodynamics have been covered in this research as well. Both 2D and 3D artery models with stent have been established focusing on the evaluations of flow topology and the WSS-based descriptors with different influential factors.

3.2 Modeling establishment and methodology

In view of geometrical design factors of stent, the studies have been carried out both in 2D and 3D models separately. Thus the corresponding modeling establishment has been discussed as follows:

- 2D case

As the artery is considered as axisymmetrical cylinder with one simplified circular stent, the corresponding 2D geometrical model is established as shown in Figure 3.1. The cross section of strut is of squared shape, and the height of strut is 0.1 mm. The radius of artery is 1.75 mm according to the coronary artery. In order to make sure that the results are independent on the geometry, the vessel lengths before and after the stent are 4 mm and 6 mm separately.
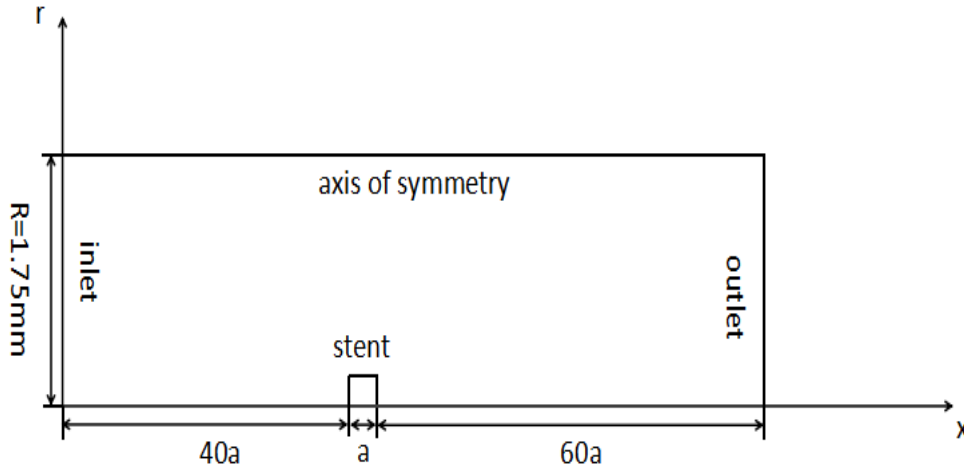
Figure 3.1: 2D computing domain of artery with stent

Following the establishment of 2D geometrical model above, the mathematical model keeps the same with works in chapter 2 as the blood flow is considered to be incompressible and Newtonian fluid. The density and dynamic viscosity are 1060 kg/m^3 and 0.0035 $Pa \cdot s$. The inlet pulsed flow and outlet pressure waveform at different pulse rates have been displayed in Figure 3.2-(a) and (b). As observed, velocity profiles at pulse rates of 60 bpm, 75 bpm, 100 bpm and 120 bpm have been considered referring to the literature [121, 122, 162]. A parabolic velocity profile has been imposed since the Re number is below 600. The corresponding pressure waveform at different pulse rate is constructed based on the two-element model as discussed in chapter 2.
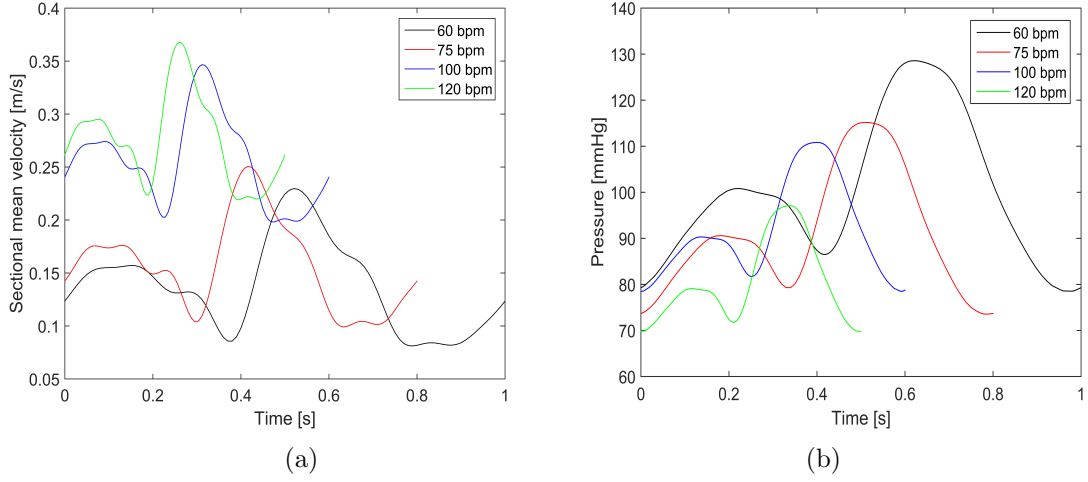
Figure 3.2: Inlet pulsed flow and outlet pressure waveform at different pulse rates

Regarding the mesh distribution, due to the more complex flow disturbance around the strut, a finer mesh element is required in the vicinity of strut as shown in Figure 3.3. The final mesh distribution is determined based on the mesh independence study shown in Figure 3.4-(a). Two points are selected upstream and downstream the stent within the recirculation region. The distances to the wall and to the strut both equal to 0.05 mm. Six different mesh sizes are studied, Figure 3.4-(b) and Figure 3.4-(c) show the shear rate at the two points respectively versus the mesh size. With the increase of mesh size, the shear rate tends to be more independent of the mesh size. Even though a slight oscillation of the shear rate value exists, the accuracy can be controlled under 1% for point 1 and under 3% for point 2 after the third mesh size.
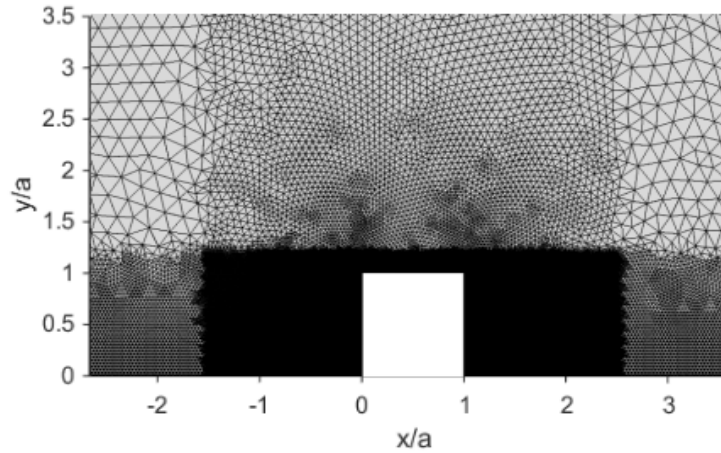
Figure 3.3: Mesh distribution around the stent

(a)

(b)

(c)
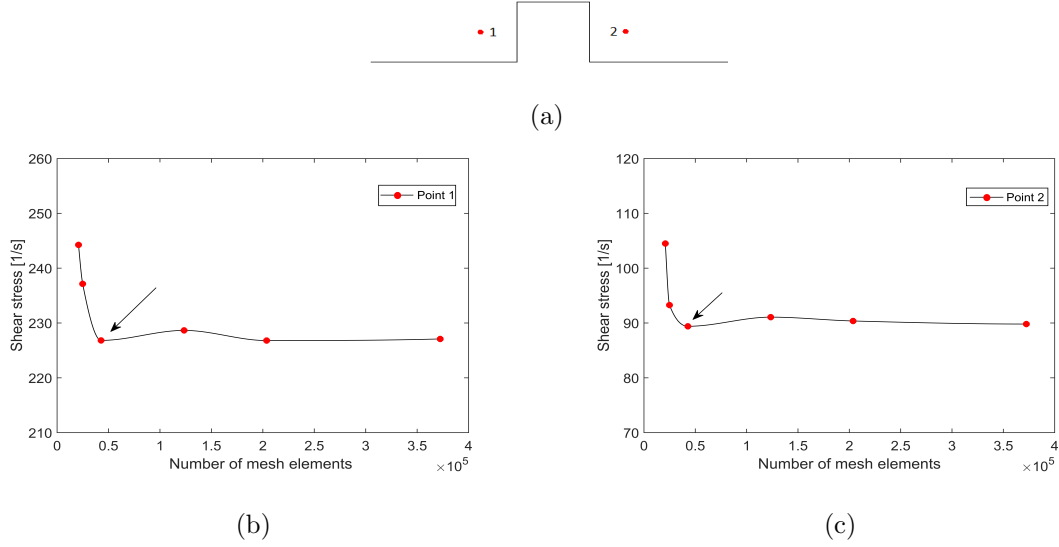
Figure 3.4: Independence of the shear rate with the quality of the mesh

In order to validate the simplified pulsatile flow model at inlet used in our case, a comparison has been made between our results with this model and works of Chabi et al. [50] where a Womersley velocity profile was adopted. As shown in Figure 3.5, the comparison of wall shear stress at one point downstream in one cycle has been made at 75 bpm for these two conditions. As observed, a satisfactory agreement has been obtained with a peak difference of 6%.
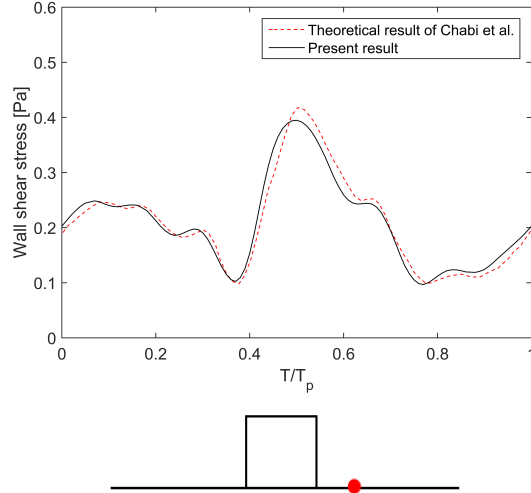
Figure 3.5: Comparison of wall shear stress at one position downstream at 75 bpm

- 3D case

Referring to the commercial stent geometry of Palmaz-Schatz [163, 164], the 3D stent geometry is established as shown in Figure 3.6. Along the direction of z axis (flow direction), the cross section of single strut is displayed with different aspect ratio (AR): 1, 2 and 4 separately where a=0.1 mm. The total length of stent is 4.475 mm. The external radius equals to 1.75 mm consistent with the internal radius of coronary artery. Following that, the complete 3D stented artery model has been obtained shown

in Figure 3.7. Similarly, the artery length before and after the stent is 4 mm and 6 mm separately. The boundaries can be divided into inlet boundary, outlet boundary and vessel wall.
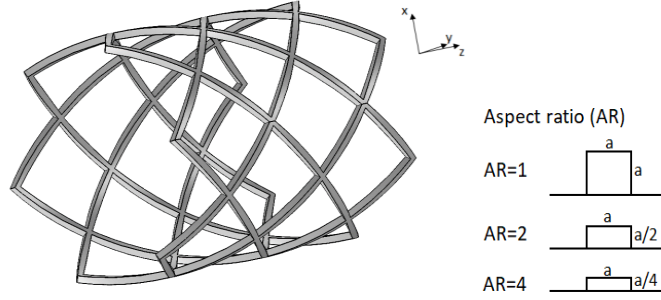
Figure 3.6: Schematic of the 3D stent model
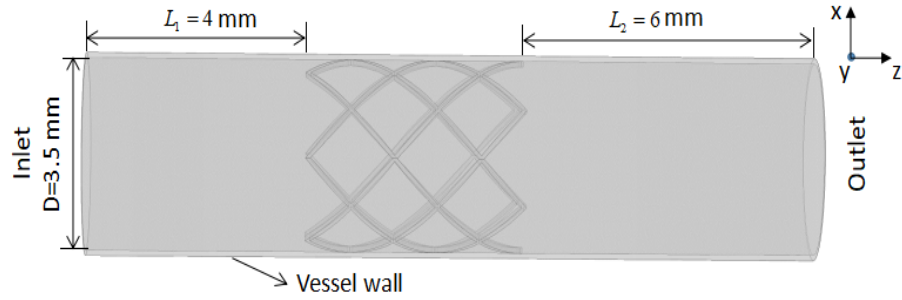
Figure 3.7: Schematic of the 3D artery model with stent

In 3D study, both steady and unsteady cases have been considered. The mathematical models and boundary conditions keep the same with 2D case except the inlet boundary condition. A constant sectional mean velocity of V_0=0.1 m/s, 0.158 m/s and 0.2 m/s respectively has been imposed at inlet for steady case. However, for unsteady case a simplified pulsatile waveform of velocity is imposed in order to reduce cost as shown in Figure 3.8. The simplified velocity profile has referred the velocity range covered in the case of 75 bpm presented in Figure 3.2 with mean velocity of $V_0 = 0.175 \ m/s$. Thus the Reynolds number related is 90-265 belonging to laminar regime.
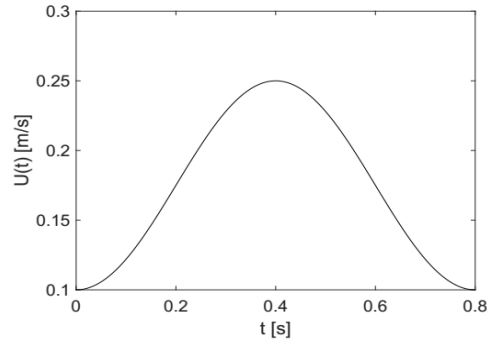
Figure 3.8: Instantaneous sectional mean velocity during one cycle

In order to check the mesh independence, the velocity at four points around the strut is studied versus mesh size. The final mesh distribution and the selected point locations are shown in Figure 3.9.

69

Along Z axis four points are selected beside the strut joint and the space location of these four points can be observed through the section extracted along the red line and oriented by the radial direction. The distance of each point to the vessel wall and the strut is 0.05 mm. The determination of final mesh size is based on the sensitivity of velocity value at these four points to the mesh size as shown in Figure 3.10. The four different mesh sizes are respectively 1553196, 2060240, 3166236 and 7215890. As can be seen with the increase of mesh size the velocity at these four points tends to be flat. Especially after the third mesh size point, the accuracy can be controlled under 3%.

(a)   (b)
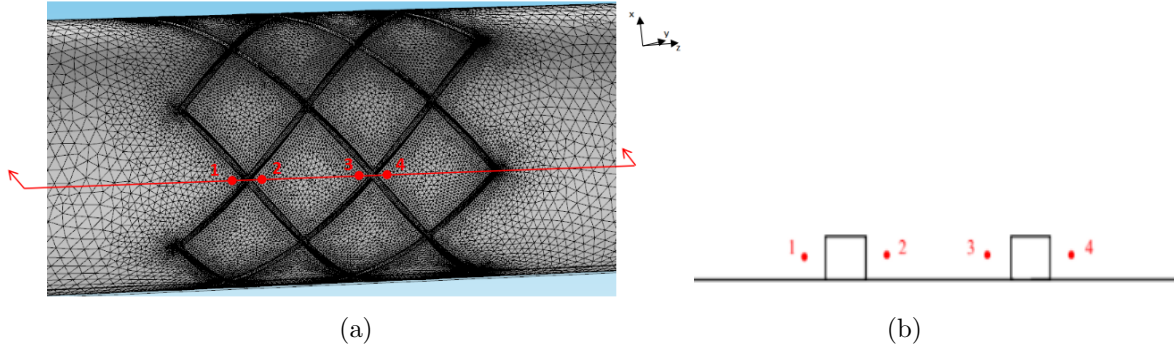
Figure 3.9: Mesh distribution around stent (a) and spacial location of selected points (b)

(a)   (b)

(c)   (d)
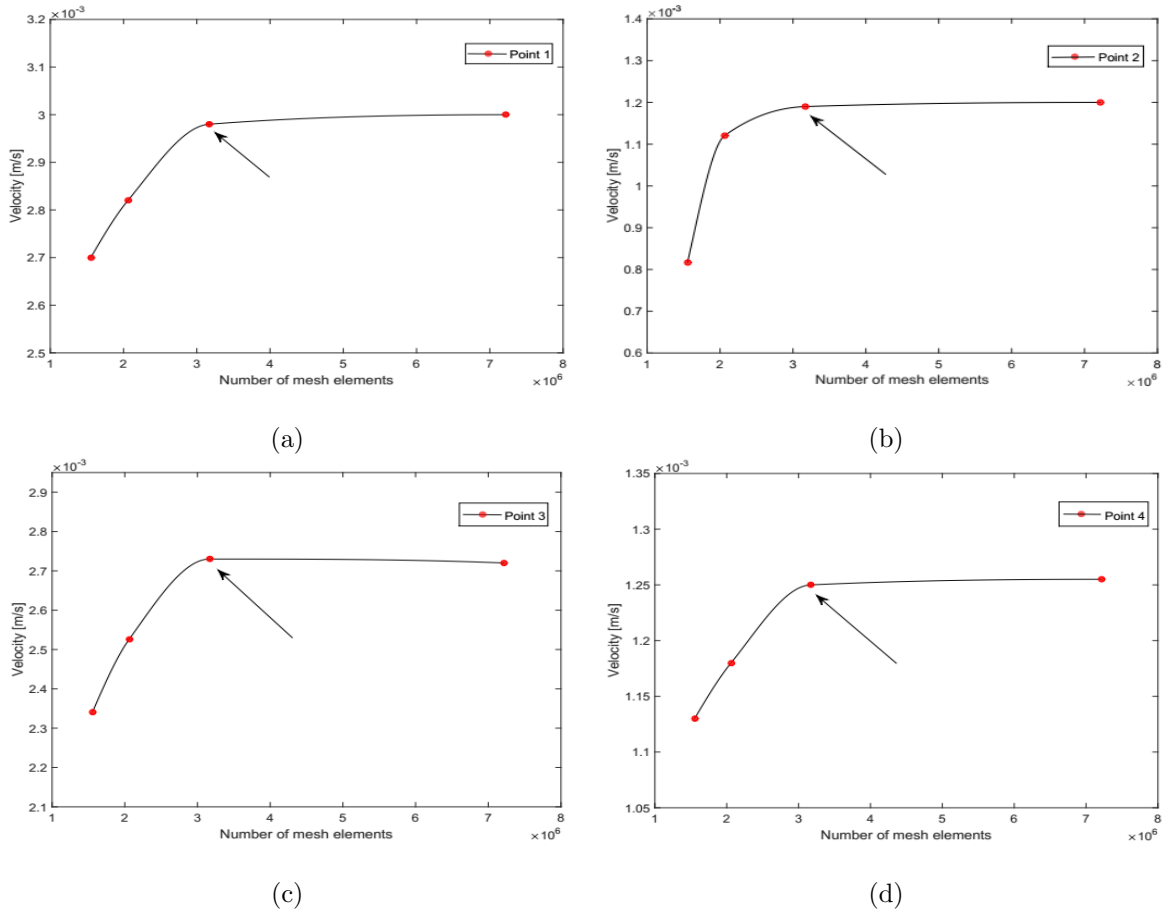
Figure 3.10: Mesh independence versus the velocity at different points

3.3 Hemodynamic parameters related

For the evaluation methods, the related hemodynamic parameters have been presented below as well as the WSS and TAWSS introduced in Chapter 2.

Time-averaged WSS gradient in space (TAWSSGs)

$$TAWSSGs = \frac{1}{T} \int_0^T \sqrt{(\frac{\partial WSS_x}{\partial x})^2 + (\frac{\partial WSS_y}{\partial y})^2 + (\frac{\partial WSS_z}{\partial z})^2} dt \tag{3.1}$$

According to the literature, high value of TAWSSGs indicates high possibility of deposition and the critical value of TAWSSGs is 200 Pa/m [47, 165].

Oscillatory shear index (OSI)

OSI as another WSS-based parameter is defined in the form of equation (3.2). It represents the deflection between the WSS vector and the blood flow direction. When the direction of WSS is consistent with blood flow, it is beneficial to take the depositions away from the vessel wall. However, if the WSS direction oscillates frequently, it is easier to form depositions over one location of vessel wall. According to the literature [47], the critical value of OSI is 0.1. When it is higher than 0.1, the possibility of deposition will be highly increased.

$$OSI = 0.5 \times (1.0 - \frac{|\int_0^T WSSdt|}{\int_0^T |WSS|dt}) \tag{3.2}$$

Relative residence time (RRT)

The definition of RRT is introduced in equation (3.3). The RRT value relies on the effects of OSI and TAWSS. High RRT value indicates more opportunity to deposit on the vessel wall.

$$RRT = [(1 - 2.0 \times OSI) \times TAWSS]^{-1} \tag{3.3}$$

3.4 Results analysis in 2D case

2D model is established focusing on the effect of cross section geometry of strut on flow disturbance. As shown in Figure 3.11, recirculations are formed both upstream and downstream the strut due to the existence of stent geometry. Definitions of recirculation size are made horizontally and vertically termed as L_{pV}, L_{dV}, L_{pH} and L_{dH} representing proximal vertical length, distal vertical length, proximal horizontal length and distal horizontal length. All the definitions of recirculation length are determined by the point where the wall shear stress is close to 0.
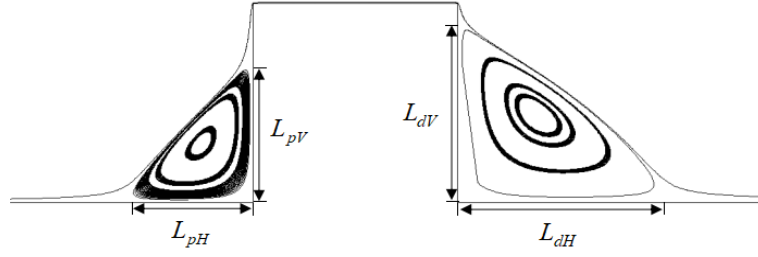
Figure 3.11: The definition of recirculation size upstream and downstream

In Figure 3.12, the recirculation lengths upstream and downstream are plotted at different pulse rates in one cycle. The horizontal lengths of recirculation upstream and downstream are plotted in Figure 3.12-(a). The variations of horizontal length upstream and downstream are nearly reversible to each other in one cycle. When $T/T_p = 0.5$ corresponding to the peak flow rate, the maximum horizontal length downstream is obtained, by contrast the minimum horizontal length upstream is observed. Larger flow rate contributes to stronger inertial force which inhibits the formation of recirculation upstream and promotes the formation of recirculation downstream. Therefore, with the increase of pulse rate, the horizontal length upstream is decreased and the horizontal length downstream is increased. Apparently, the horizontal length downstream is more affected by the pulse rate comparing to horizontal length upstream. Figure 3.12-(b) describes the vertical length upstream and downstream. It is found out that the vertical length upstream varies more rapidly comparing to vertical length downstream which is greatly confined by the height of stent.

(a) Horizontal

(b) Vertical
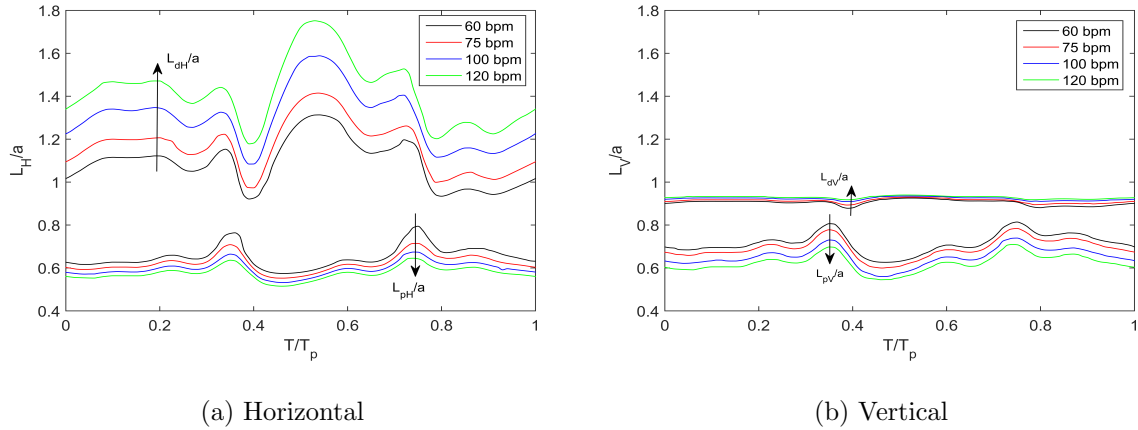
Figure 3.12: Recirculation length at different pulse rates

As observed above, the recirculation formation is strongly related to the presence of stent geometry intruded into the blood domain, the concerned design factors of stent geometry are necessary to be considered thoroughly. Thus, instead of one singular strut, two struts with different strut spacings are considered as shown in Figure 3.13. The strut spacing is defined as D. In the present study, D equals to a, $3a$ and $5a$ ($a = 0.1$ mm) respectively. The other geometrical parameters and mathematical conditions keep unchanged. The streamlines and shear stress distributions have been investigated around the struts affected by the strut spacing and pulse rate.
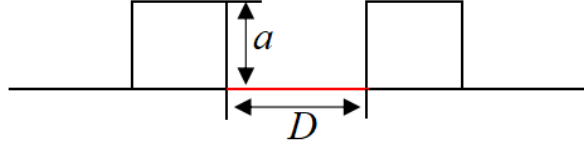
Figure 3.13: The stent geometry with two struts

In Figure 3.14, the distributions of shear stress and velocity vectors around the struts are both displayed at different strut spacing when the pulse rate is 75 bpm and $t = T/2$. The formation of recirculation is observed and varied at different strut spacing. Focusing on the region between the two struts, When $D = a$, one recirculation is formed without attachment points. When $D = 3a$, two recirculations are formed but still there are no attachments between struts. With a further increasing of strut spacing to $D = 5a$, attachment points start to be located between struts with two independent recirculations. The low value of shear stress below 0.5 Pa always resides in the recirculation region contributing to the potential sites of deposition.
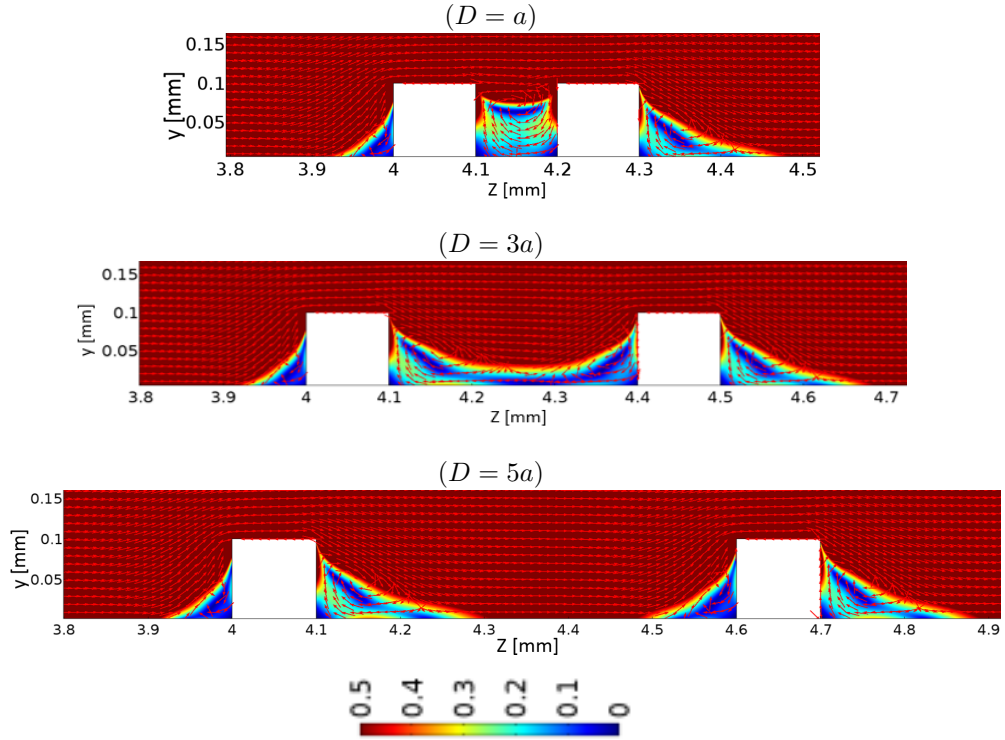
Figure 3.14: Velocity vector and shear stress distribution (Pa) around the stent at different strut spacing when pulse rate is 75 bpm and $t = T/2$

In Figure 3.15, the wall shear stress between struts is studied quantitatively at different strut spacings and different pulse rates. With the increase of pulse rate, higher wall shear stress is obtained under different strut spacing. When $D = a$, there is no point where wall shear stress equals to 0. With the increasing of strut spacing to $D = 5a$, the points where wall shear stress close to 0 are observed. The first attachment point downstream the first strut tends to be more affected by the pulse rate compared to the second attachment point. Taking the case of $D = 3a$ as an example, the influences of pulse rate on distribution of shear stress and velocity vectors around two struts have been studied in Figure 3.16

when $t = T/2$. It is notable that larger value of wall shear stress will be found along with larger pulse rate, especially in the downstream region which is influenced more by the inertial force.
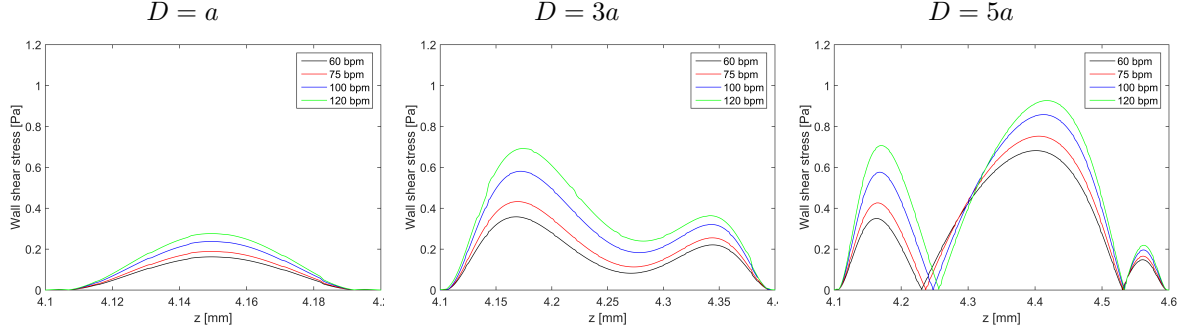
Figure 3.15: Wall shear stress distribution along the wall between struts at different strut spacings and different pulse rates at $t = T/2$
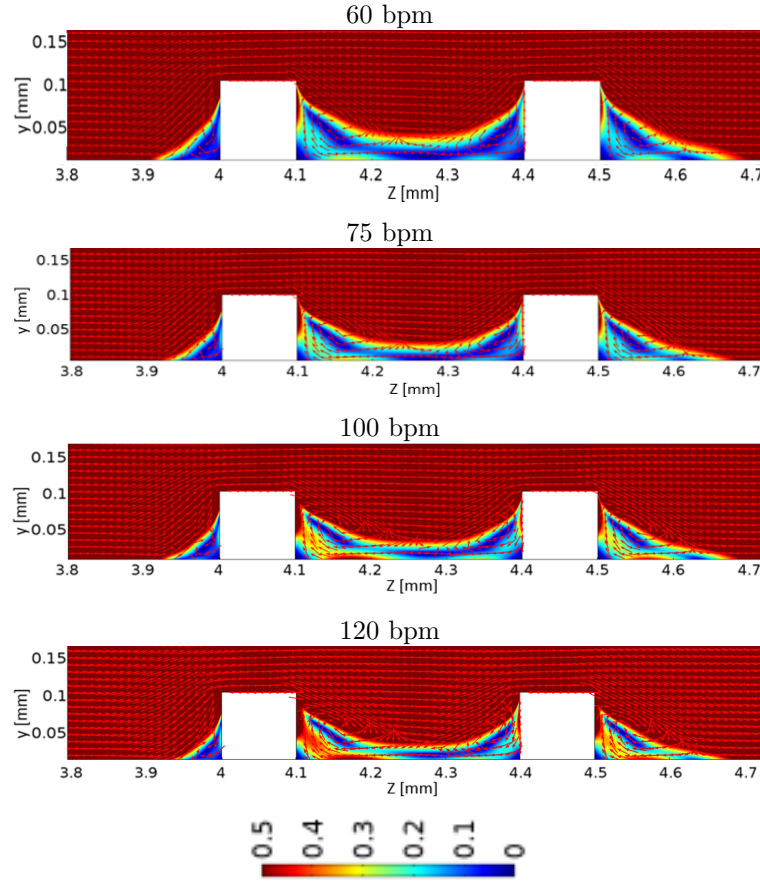
Figure 3.16: Velocity vectors and wall shear stress distribution (Pa) around the stent at different pulse rates when $t = T/2$ and $D = 3a$

Space-averaged WSS along the wall between struts is studied here as another view to analyse the effect of strut spacing at different pulse rate as shown in Figure 3.17 when $t = T/2$. It is observed the space-averaged WSS is positively affected by the pulse rate, even though the variation rate alters at different strut spacing. Larger strut spacing can bring higher space-averaged WSS. When $D = a$,

the space-averaged WSS varies slowly with the increasing of pulse rate compared with the other two conditions. Moreover, the largest variation rate of space-averaged WSS versus pulse rate is found when $D = 3a$. This phenomenon greatly depends on the vortice state between struts. As observed in Figure 3.14, When strut spacing is increased into 3a, the vortice number is developed into two from one without attachment points. Correspondingly, the sensitivity of space-averaged WSS to pulse rate is significantly increased from case of D=a to D=3a. However, along with the appearance of attachment points ($D = 5a$) the sensitivity is decreased which is affected by the non-recirculation section.
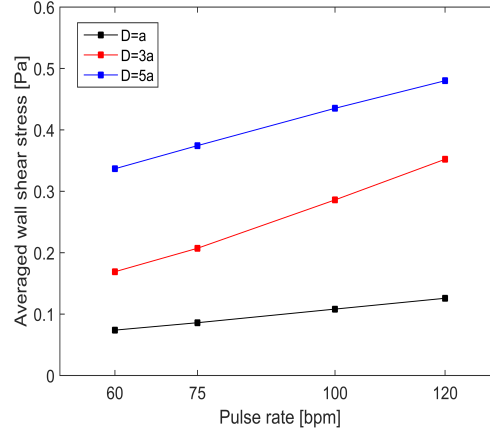
Figure 3.17: Averaged wall shear stress between the struts versus the pulse rate at different strut spacing when $t = T/2$

In Figure 3.18 the space-averaged WSS versus strut spacing is investigated under different pulse rates when $t = T/2$. Instead of linear relationship between space-averaged WSS and pulse rate shown in figure above, non-linear relationship of space-averaged WSS versus strut spacing is observed. Focusing on the variation from $D = a$ to $D = 3a$, increased pulse rate brings larger variation rate, however, when the strut spacing is increased from $D = 3a$ to $D = 5a$, the variation rate is decreased with larger pulse rate. Thus, in our cases, it can be concluded that higher space-averaged WSS will be obtained with higher pulse rate and larger strut spacing.
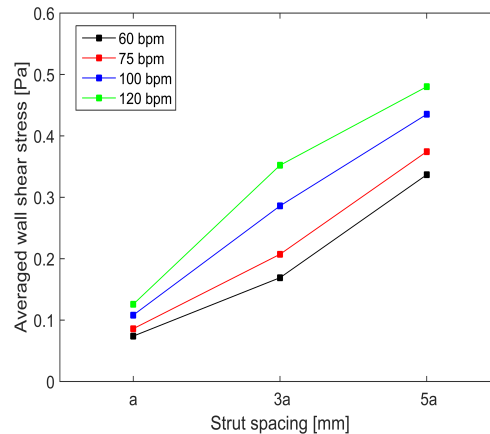
Figure 3.18: Averaged wall shear stress between the struts versus the strut spacing at different pulse rate when $t = T/2$

3.5 Results analysis in 3D case

In addition to focusing on the effect of strut cross section on flow topology in 2D case above, the global hemodynamic distribution on vessel wall has been investigated by means of 3D model taking into account the geometrical complexity of stent both in steady and unsteady cases.

3.5.1 Steady flow

In steady case, the effect of inlet mean velocity on the wall shear rate distribution around stent is studied in Figure 3.19. Three different inlet velocities are investigated: 0.1 m/s, 0.158 m/s and 0.2 m/s. With the increasing of inlet mean velocity, the global distribution of wall shear rate gets increased, even though the existence of stent causes low value region near the strut. At the vicinity of strut the wall shear rate is obviously under 140 1/s corresponding to WSS of 0.5 Pa, which brings more possibilities to deposit on vessel wall. In addition, with the increase of inlet mean velocity the low value region will decrease which can be further verified in the following studies. Larger velocity means the inertial force will be more dominating which can offset the effect of stent intrusion into lumen to some extend.

$V_0 = 0.1$ m/s

$V_0 = 0.158$ m/s

$V_0 = 0.2$ m/s
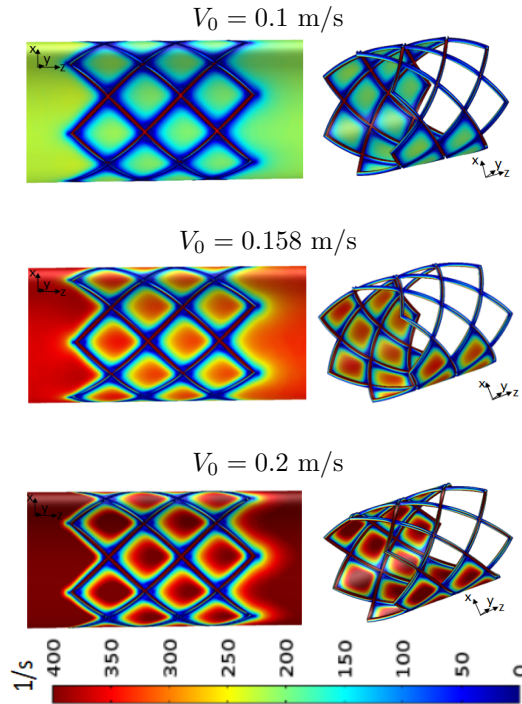
Figure 3.19: Wall shear rate distribution under different inlet mean velocities

Subsequently, WSS-based descriptors as another view have provided evaluations of stent performance. Figure 3.20 shows the wall shear stress gradient (WSSGs) in space around stent at different mean velocities. It can be seen the existence of stent causes large value of WSSGs at the vicinity of struts, especially at the corners formed by the struts. With the increase of mean velocity, WSSGs near the stent will be significantly increased. Referring to the literature [47], when WSSGs is larger than 200 Pa/m, the deposition is more prone to be formed which is obviously observed at the vicinity region of strut in our case.
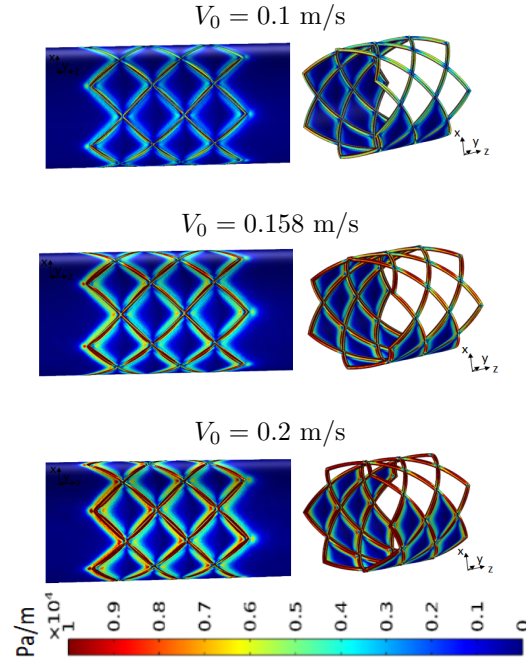
Figure 3.20: Wall shear stress gradient in space distribution under different inlet mean velocities

Specific to the pressure distribution around stent at different mean velocities which is shown in Figure 3.21. Along the flow direction (z axis), the pressure is decreased globally from upstream to downstream of stent. With the increase of mean velocity, the overall pressure distribution gets increased. As for the details of hemodynamic variation affected by stent, the following quantitative analysis has been presented.
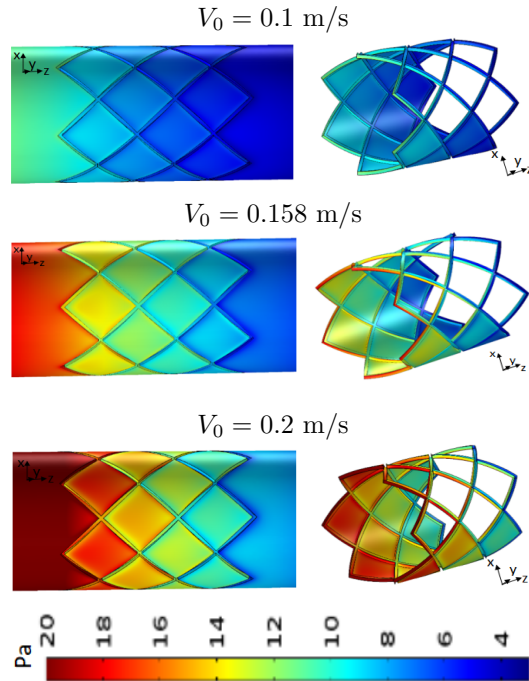
Figure 3.21: Pressure distribution under different inlet mean velocities

Along z axis, an extraction of lines is made as shown in Figure 3.22. The lines can be divided into two parts because of the existence of struts. In order to see the spacial location of lines, the projection of lines on the lateral surface is shown with the red point. The distance between the red point and the radial vessel wall is defined as S, and the following research will be carried out with different values of S: 0.025 mm, 0.05 mm, and 0.075 mm.
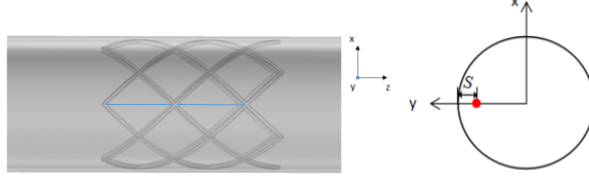
Figure 3.22: Schematic of spacial line extraction in artery

In Figure 3.23, the velocity along lines at different locations and different inlet mean velocities is studied. It is observed that the increased values of S and inlet mean velocity both contribute to larger velocity along the line. Increased value of S means to be closer to the flow center with larger velocity. Two peak values can be observed located beside the strut joint separately with similar profile, even though a slight decrease can be noticed of the second peak compared to the first one.

$V_0 = 0.1$ m/s

$V_0 = 0.158$ m/s

$V_0 = 0.2$ m/s
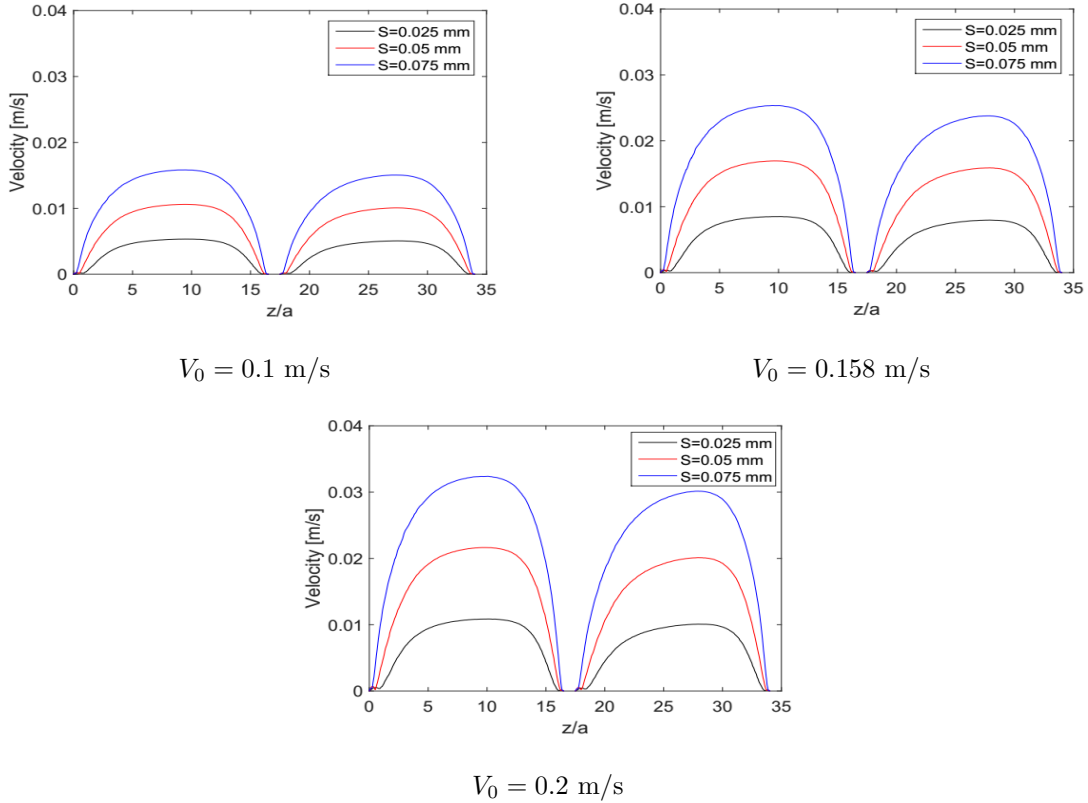
Figure 3.23: Velocity along line at different locations when $V_0 = 0.1$ m/s, 0.158 m/s, 0.2 m/s.

Following the analysis of velocity along the extracted line, the wall shear rate is studied as well when $S = 0$ at different Re number as shown in Figure 3.24. With the increasing of Re number, the wall shear rate gets increased. The low value regions where the recirculation resides can be observed located near

the strut region. In addition, comparing these low value regions the wall shear rate distal to one strut is larger than the wall shear rate proximal to the strut. The reason is that the existence of strut can increase the inertial force of flow downstream.
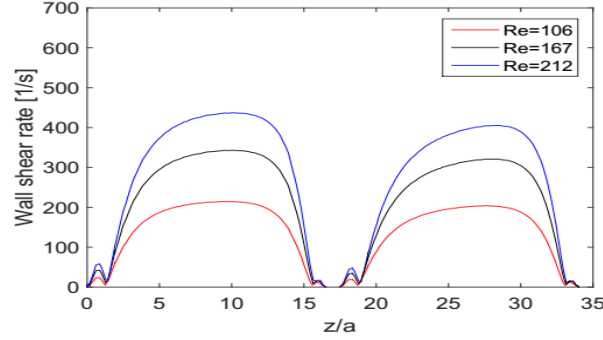
Figure 3.24: Wall shear rate along the line at different Re number

The pressure distribution along the lines at different Re number is plotted in Figure 3.25. With the increasing of Re number the pressure along the lines will be increased globally. The existence of strut has divided the line into two parts: upstream part and down stream part and the difference between these two parts is getting larger with increased Re number. When the flow passes over one strut, a significant pressure decrease is observed between upstream and downstream. Except for the pressure leap in the near regions of strut affected by the disturbed flow, the pressure tends to be decreased gradually.
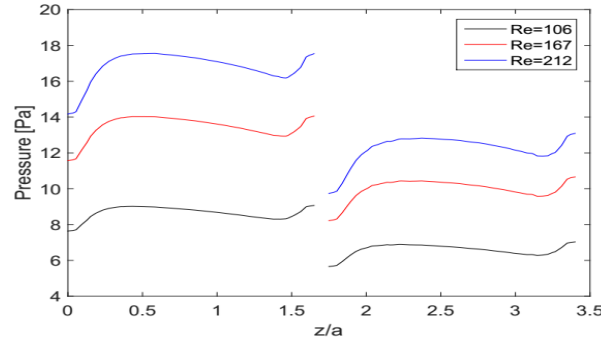
Figure 3.25: Pressure along the line at different Re number

Figure 3.26 displays the wall shear rate distribution on the cross section extracted along the red line at different inlet mean velocities. Focusing on the strut regions, the peak value of wall shear rate is obtained on the top surface of strut and is increased with larger inlet velocity. The low value of shear rate affected by the strut spacing resides beside the struts.

Considering the geometrical factor of stent, the effect of strut thickness on hemodynamics is studied. The wall shear rate distribution is shown in Figure 3.27 at different AR value of 1, 2 and 4 corresponding to the strut thickness of 0.1 mm, 0.05 mm and 0.025 mm. With the increase of AR, the overall distribution of wall shear rate gets increased and the low value region near the strut gets decreased. The coming flow gets less influenced passing through thinner strut and easier to recover afterwards. Thus it is consistent with the literature that thinner strut can be more beneficial to optimize the stent performance.
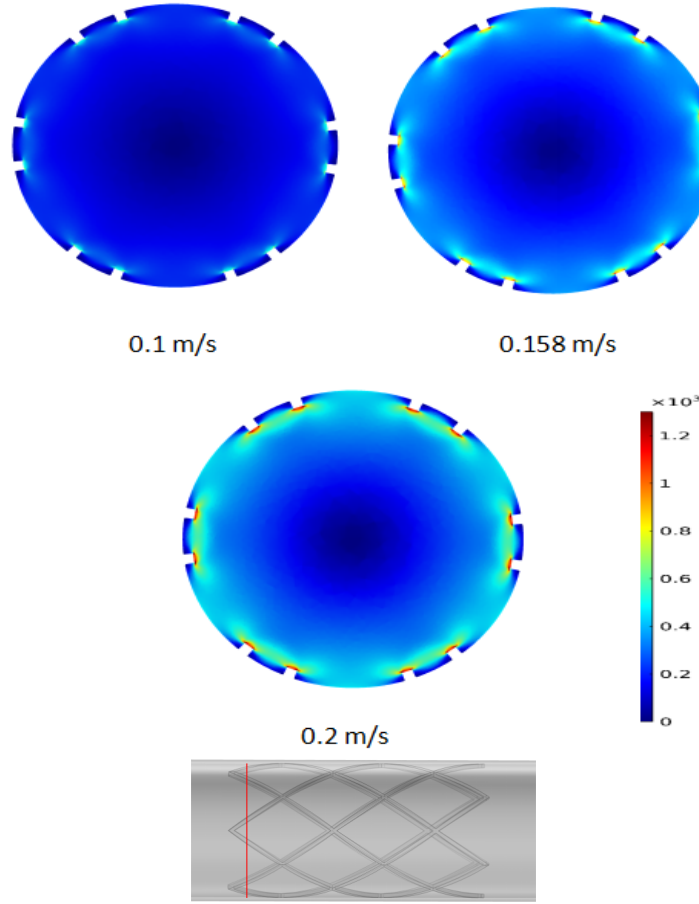
Figure 3.26: Shear rate distribution on cross section along the red line at different Re number (unit: 1/s)
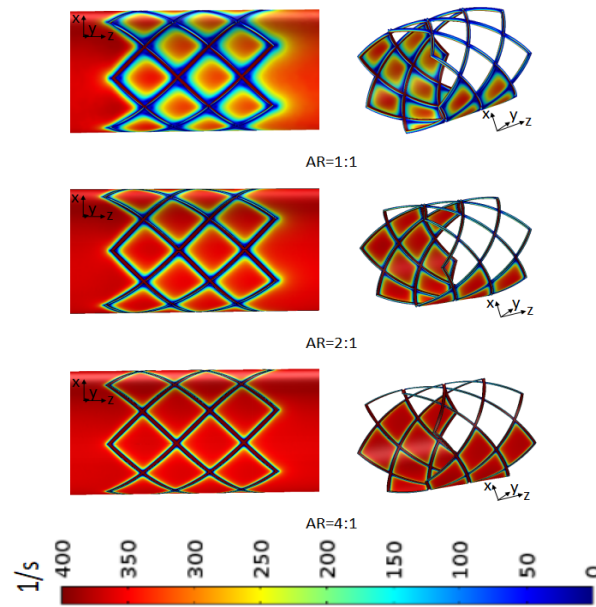
Figure 3.27: Wall shear rate distribution at different AR with $V_0 = 0.158 m/s$

80

In order to make the quantitative analysis of wall shear rate distribution affected by the strut thickness, Figure 3.28 plots the wall shear rate along lines on the vessel wall at different AR values. The lines can be divided into two parts due to the existence of strut: part one (on the left) and part two (on the right). With the increase of AR value, the wall shear rate along the lines is increased, however, the variation tends to be smaller. With larger AR value, the wall shear rate distribution along the lines tends to be more flat because of less disturbance. Comparing the wall shear rate along lines of these two parts, the difference is smaller as well with larger value of AR.
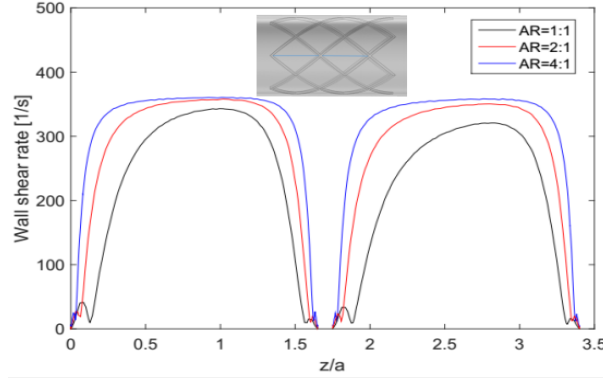
Figure 3.28: Wall shear rate along the line at different AR with $V_0 = 0.158 m/s$

Figure 3.29 shows the pressure distribution at different AR values. Along the flow direction (z axis) the pressure is gradually decreased even though the disturbance exists near struts. With the increase of AR value the pressure drop before and after the stent is getting smaller, which can be further explained by Figure 3.30. In Figure 3.30 the pressure along the lines between struts on the wall is displayed. With the increase of AR value, the pressure upstream strut tends to be unchanged, however, the pressure value downstream the strut is clearly increased. Then the pressure drop over one strut is decreased with larger AR.
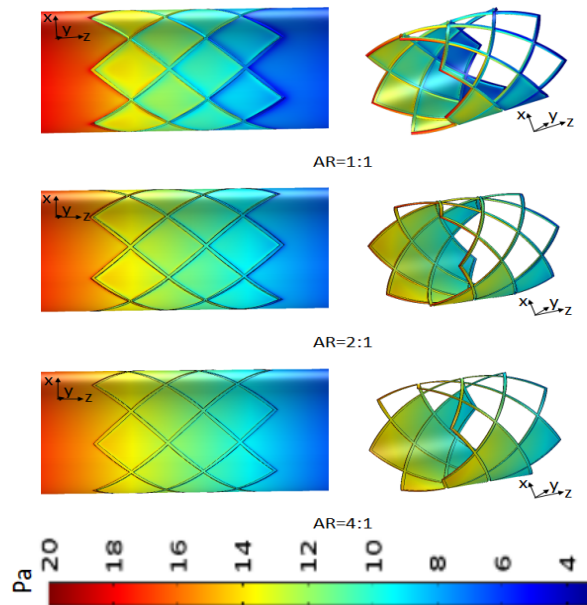
Figure 3.29: Pressure distribution at different AR with $V_0 = 0.158 m/s$
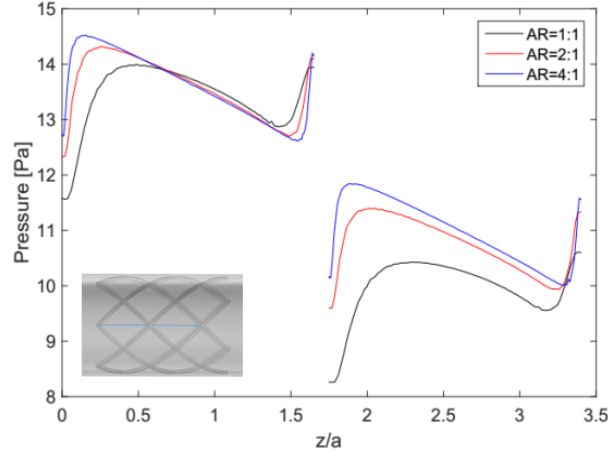
Figure 3.30: Pressure along the line at different AR with $V_0 = 0.158m/s$

As mentioned above wall shear stress gradient in space (WSSGs) is one of the WSS-based descriptors, thus the effects of different AR values on WSSGs are studied in Figure 3.31. Higher WSSGs has been observed to be located at the vicinity of struts. With the increasing of AR value, the WSSGs near the strut gets obviously increased, but the region of high WSSGs is getting decreased.
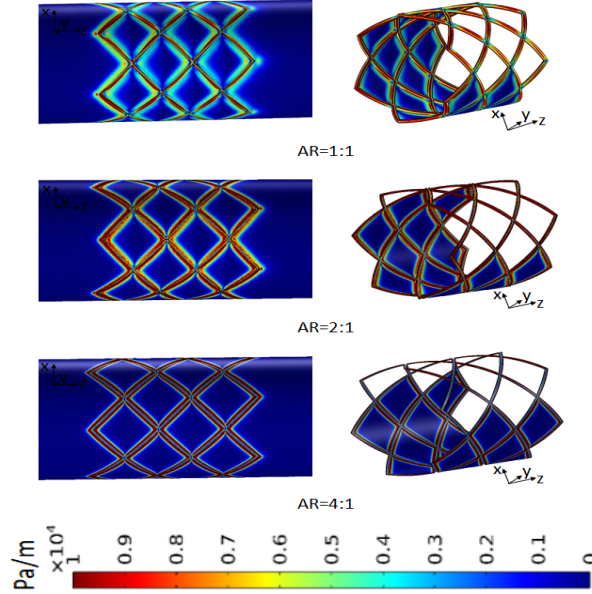
Figure 3.31: WSSGs distribution at different AR with $V_0 = 0.158m/s$

3.5.2 Pulsed flow

Blood flow is a typical pulsatile flow, thus the wall shear rate distribution on vessel wall at different time instants is investigated in Figure 3.32 with unsteady inlet flow. Similar with steady case above, the low value of wall shear rate is always located in the near region of stent. It is noted that the maximum and minimum wall shear rate distributions are obtained which is positively proportional to the flow velocity. As noticed the velocities at $t = T/4$ and $t = 3T/4$ are the same corresponding to point 2 and point 4, however, the wall shear rate distribution at these two points tend to be quite different which is

affected by the flow pulsation. Thus, in view of the influence of flow pulsation, the steady case is not sufficient.
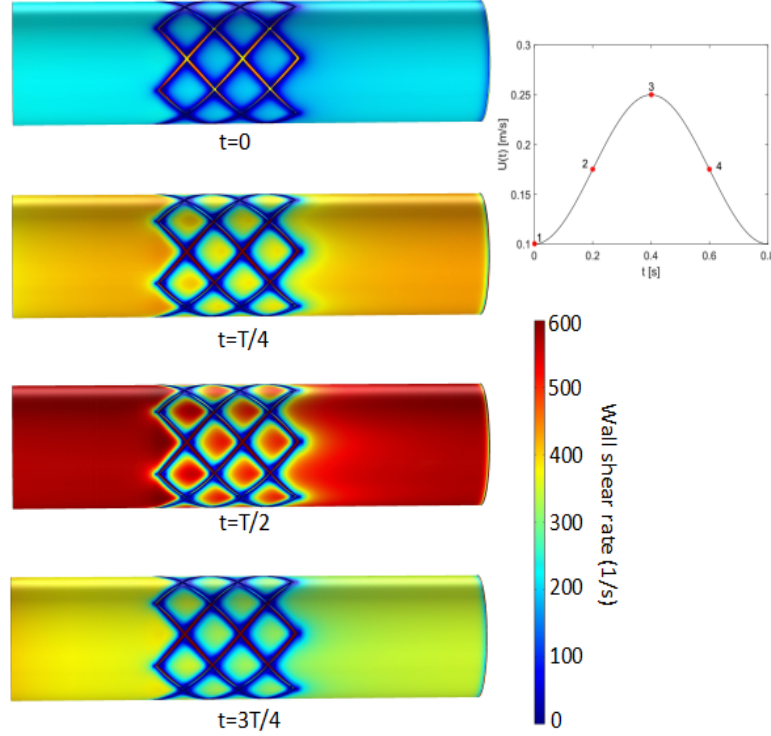
Figure 3.32: Wall shear rate distribution at different time instants in one cycle with $AR{=}1$

In order to study further the flow disturbance near stent, the streamlines based on colored wall shear rate distribution have been investigated taking the case of $t = 3T/4$ as an example shown in Figure 3.33. An extraction has been made through the black box and the streamlines within distance of 0.01 mm from wall upstream the stent have been traced. It's found that a good consistence between the disturbed streamlines and the low value region of wall shear rate has been observed.
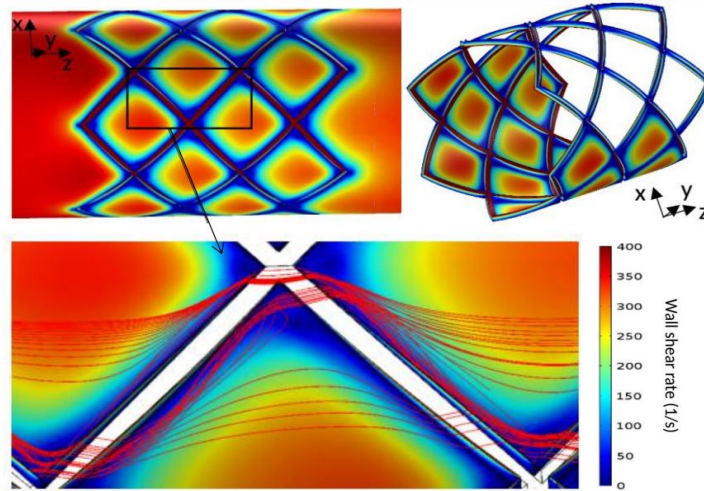
Figure 3.33: Streamlines around stent with wall shear rate background at $t = 3T/4$

WSS-based descriptors are studied afterwards focusing on the effects of different aspect ratio (AR) of stent. Figure 3.34 shows the time-averaged wall shear rate distribution in one cycle with strut of different AR of 1, 2 and 4. Similarly, the low value of wall shear rate in the near region of strut below 140 1/s is observed corresponding to the wall shear stress below 0.5 Pa. With the increase of aspect ratio, the wall shear rate will be increased, and the low value region of wall shear rate is decreased as well which is consistent with steady case. Lower height of strut intruded to lumen significantly reduces the low value region of wall shear rate which is consistent with that in 2D cases which concluded that the flow disturbance is greatly restricted by the height of stent. Thus the height of strut should be an important consideration for the geometrical optimization of stent.
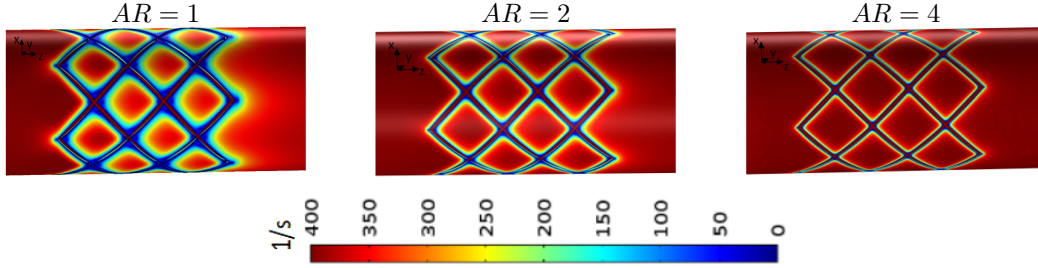
Figure 3.34: Time averaged wall shear stress distribution in one cycle at different aspect ratio of strut

In Figure 3.35, the distribution of oscillatory shear index (OSI) is displayed at different AR of strut. The definition of OSI has been explained in equation (3.2) above representing the deflection of WSS vector from the predominant direction of blood flow during cardiac cycle. When OSI > 0.1, it is more prone to deposit the fatty particles on the wall because of the frequent oscillation of the WSS direction. As seen in the Figure 3.35, the larger value of OSI is discovered at the vicinity of strut and the high value region is decreased with larger AR. It should be notable that in our case the OSI is always below the high limit of 0.1.
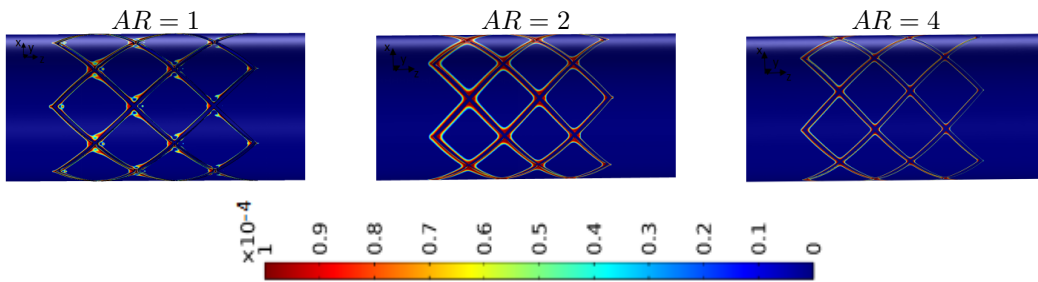
Figure 3.35: Oscillatory shear index distribution in one cycle at different aspect ratio of strut

Figure 3.36 shows the relative residence time (RRT) distribution at different aspect ratio of strut. Through the definition of RRT discussed in equation (3.3), the value of RRT relies on the effects of OSI and TAWSS. High value of RRT means more possibilities to deposit on the vessel wall. As seen in the Figure 3.36, the variation of RRT over stent tends to decrease with higher aspect ratio as RRT value is increased upstream and decreased downstream. A slight leap of RRT can be observed especially downstream the stent and the phenomena is weakened with increased AR.

84
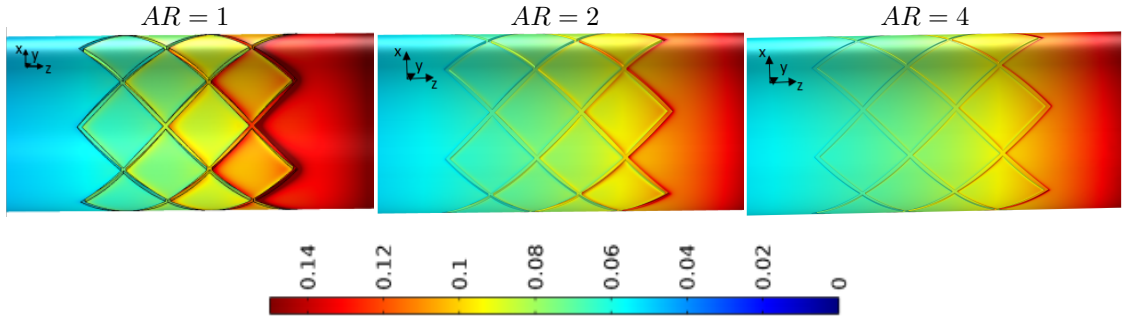
Figure 3.36: Relative residence time distribution in one cycle at different aspect ratios of strut

Figure 3.37 shows the wall shear stress gradient in space (WSSGs) distribution at different aspect ratio of strut. Similar with steady case, the high value of WSSGs is observed around the stent far beyond 200 Pa/m which indicates that deposition is more prone to be formed in the near region of strut. This phenomena is more obvious with lower aspect ratio.
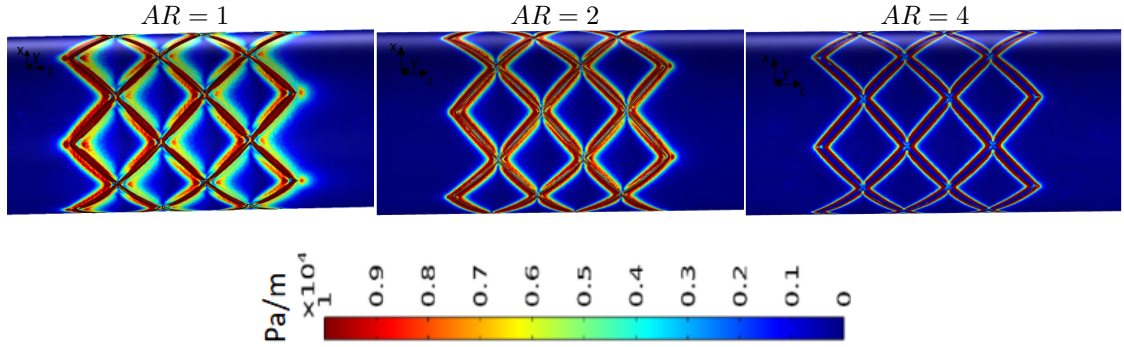
Figure 3.37: Wall shear stress gradient in space (WSSGs) distribution in one cycle at different aspect ratio of strut

3.6 Conclusion

In this chapter, an insight of interaction between stent performance with different design factors and hemodynamic variations has been presented both in 2D and 3D cases of blood flow in coronary artery. Different design factors have been investigated and identified to directly affect the flow behavior and variations of hemodynamic parameters play a crucial role to evaluate the stent performance. Flow topology and hemodynamic variations have been both focused based on the evaluations of WSS-dased descriptors. The results reveal that the formation of recirculations beside the struts can be observed and greatly affected by the pulse rate and stent geometry. Focusing on the size of vortices formed upstream and downstream the strut, the horizontal length of recirculation downstream remains higher sensitivity to the pulse rate due to the less confined inertial force. In contrast, the vertical length of recirculation downstream is less sensitive to the pulse rate which is limited by the strut height. Despite the effects of one single strut on recirculations, the interspace between two struts is introduced as one of the most important design factors and it's agreed that larger strut spacing is beneficial to improve the stent performance with increased wall shear rate. Based on the analysis in 2D study, the investigation has been further extended to the 3D study with practical stent geometry. Aspect ratio concerning the

height of the strut has been introduced and the effects on hemodynamic variations have been studied. Larger AR of stent means less strut height intruded into lumen leading to less flow disturbance as the low value of wall shear rate tends to be located at the recirculation region. Thus with the increase of AR, the low value region of wall shear rate and high value region of WSSGs located near struts are both decreased which are consistent between steady and unsteady cases. Moreover, strut of high AR is beneficial to reduce the region of high RRT and OSI which can easily result in deposition, as well as the pressure drop before and after the stent. However, even though it is consistent that the inlet velocity is positively related to the wall shear rate distribution both in steady and unsteady cases, the influences of flow pulsation considered in unsteady case make differences of the results.

Drug transport from DES and experimental validation

Contents

4.1 Introduction

As chapter 3 established the coupling between blood flow and stent performance with different design factors, a better understanding of hemodynamics affected by the stent geometry has been achieved. In this chapter, a further step has been taken by considering the drug-eluting stent (DES) with the additional mass transfer physics as the DES has attracted high attention from researchers with effective performance progress. Thus the coupling between flow mechanics and mass transfer from stent has been carried out in this chapter.

The development of DES is a significant breakthrough for the treatments of cardiovascular disease with the reduction of restenosis occurrence approximately from 20% to 5% compared to BMS. The drug loaded polymer on the stent surface helps to inhibit the cell proliferation and inflammation along with the drug release after stent implantation. However, the further widespread use of DES has been limited by the late follow-up thrombosis. Thus the stent optimization has been the hot issue among the researchers who are interested in focusing mainly on investigations of drug release mechanisms and influential factors on performance improvement of DES. Among the published articles about DES, numerical investigations have been more commonly conducted, however, a shortage of experimental validation works exists in the current research state. Therefore, in order to move forward and contribute

to the current research data both numerical and experimental investigations have been considered here. Numerical studies in 2D model have been extensively carried out compared to the simplified 1D and more complicated 3D in literature. Moreover, an adequate understanding of concerned mechanisms regarding drug transport in artery is the key point to establish the proper models. Thus before the implementation of modeling establishment, the physics relevant to mass transfer from DES should be considered and discussed carefully in the first place. A number of different influential factors on mass transfer have been taken into account among the existing literature such as the polymer properties, the drug properties, the flow characteristics and the geometrical designs of stent. However, in view of DES optimization more works are still highly required in order to better understand the internal mechanisms and settle the confusions along with the fact that some opposite results exist in literature.

In this chapter, physics of drug transport in coronary artery have been introduced in order to have a good foundation for the following establishment of numerical and mathematical models. 2D model of DES in coronary artery has been built in this research based on the validation that the drug concentration in tissue tends to be symmetrical radially in 3D model and a good fitting of drug concentration in polymer has been achieved between 2D and 3D cases. Mass transfer process from DES into lumen and tissue has been investigated with considerations of different controlling parameters. The effects of disturbed flow on drug concentration have been discussed as well. In addition to the numerical works, experimental works have been carried out in order to contribute to the lack of experimental validation in literature. The drug release process from polymer into lumen has been mainly focused with different initial drug concentrations. A prediction of drug diffusion coefficient in polymer has been achieved based on the experimental data contributing to the validation between numerical and experimental results.

4.2 Modeling characteristics regarding drug transport from DES

Investigations regarding drug transport from DES in arteries have been paid wide attention from researchers since the last two decades. Numerical study as a research tool has been commonly used to better understand the physics and give appropriate predictions to the practical trials. However, a good understanding of concerned physics is the key step to establish the proper mathematical models. Thus in this section, the physics and mechanisms of drug release from polymer into lumen and tissue have been introduced. The corresponding models for different physics has been discussed and established.

4.2.1 Physics of drug transport in coronary artery

Through the existing investigations [94, 166], it is known that the mass transfer from DES in artery involves three domains: lumen domain, polymer domain and tissue domain. Accordingly, in order to have a thorough view of the related physical activities of drug transport, Figure 4.1 [167] has displayed the main drug transport mechanisms in lumen domain, non-degradable polymer and the biological tissue separately. With the blood flow from lumen domain permeating into the polymer, the initial state of solid drugs in polymer will be broken along with the drug dissolution process in flow. Then the free (dissolved) drugs are generated out of solid drugs and can be diffused into lumen and tissue. However, the solid drugs don't diffuse. Thus the main physics in polymer domain are drug dissolution and diffusion. Degradation need to be considered as well if in the case of degradable polymer. With the polymer degradation, erosion process starts to happen generating some smaller products diffusing out of the polymer. Pores will be formed inside the coating. Consequently, the drug diffusion is accelerated as a result of the liquid-filled pores. As for the biological tissue, it concerns more complicated chemical activities despite the physical

activities. When the dissolved drugs released from polymer are diffused into the tissue, part of the drugs will be binded due to the existence of chemical sites. Binding happens when the drug molecules and binding sites hit each other due to diffusion forces in tissue. The binding drugs no longer diffuse and can not be transported by the plasma. In contrast, the unbinding drugs are controlled by the diffusion and convection. A good understanding of drug transport mechanisms play the key role on modeling establishment. Based on the theoretical analysis, the considerations of mass transfer modeling in each domain have been discussed as follows.
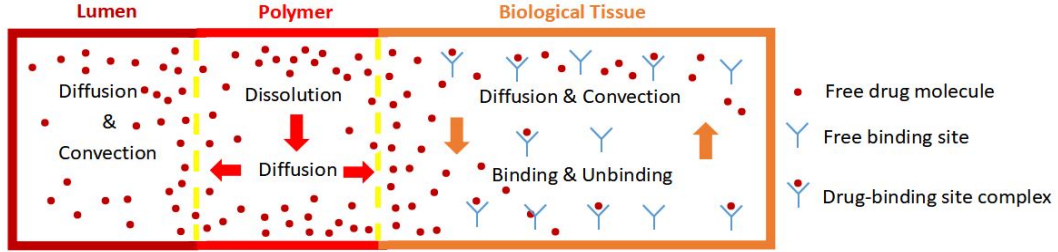
Figure 4.1: Schematic diagram of drug transport mechanism from DES into tissue and lumen [165]

- Drug transport in blood domain

As discussed above, drug diffusion and convection are both concerned due to the presence of blood flow in lumen domain. Referring to the literature [168, 169], Fick's law has been commonly adopted to describe the mass transport process. In equation (4.1), the governing equation is displayed covering both mass diffusion and convection mechanisms.

$$\frac{\partial c_f}{\partial t} + u_f \cdot \nabla c_f = D_f \nabla^2 c_f \tag{4.1}$$

Where c_f is drug concentration in flow domain, mol/m^3; u is blood velocity, m/s; D_f is diffusion coefficient in flow, m^2/s.

Among the investigations of drug transport from DES, the blood flow is widely considered as steady flow instead of pulsed unsteady flow. As mentioned in Chapter 1, P.R.S. Vijayaratnam et al. [89] approved that the flow-mediate drug transport can be neglected. Figure 4.2 shows the distribbution of drug concentration in the cases of steady blood flow (a) and unsteady blood flow (b). Similar drug distribution field can be observed in these two conditions. Thus, the adoption of steady flow is sufficient in the following research.
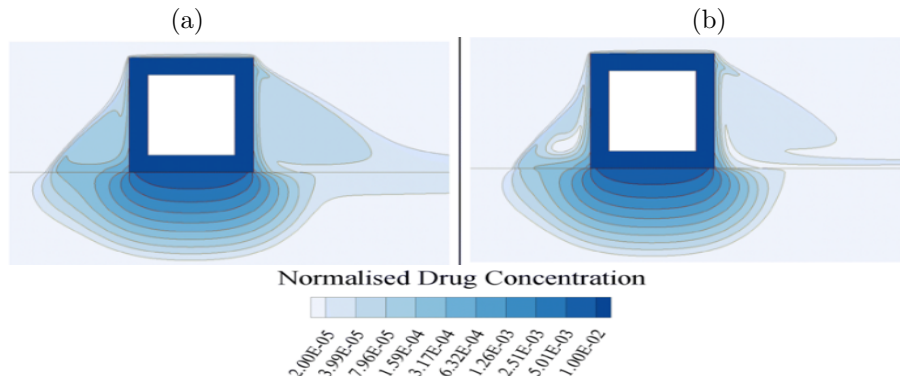
Figure 4.2: Distribution of drug concentration in steady (a) and unsteady (b) case of blood flow [89]

- Drug transport in tissue domain

In biological tissue domain, both physical and chemical activities are concerned including drug diffusion and convection as well as drug binding process with chemical sites. Among the established mass transfer models in tissue, diffusion-convection-reaction model has been put forward to better describe the drug transport physics and the chemical reactions as shown in equation (4.2) [94].

$$\frac{\partial c_t}{\partial t} + u_t \cdot \bigtriangledown c_t = D_t \bigtriangledown^2 c_t + R_i \qquad (4.2)$$

Where u_t is the flow velocity in tissue, m/s. c_t is drug concentration in tissue, mol/m^3. D_t is the diffusion coefficient in tissue, m^2/s. The reaction term R_i accounts for the binding and unbinding process of drug transport in tissue. Several different models of R_i can be found. A general expression used is shown below:

$$R_i = -\frac{1}{f_{cb}} \frac{\partial c_{BD}}{\partial t} \qquad (4.3)$$

In this expression, it considers the negative creation rate of binded drug concentration termed as c_{BD}, mol/m^3. f_{cb} is defined as the ratio of the initial drug concentration in polymer to the maximum binding site density in tissue. In recent literature another two models describing the binding reaction in tissue have been put forward. One is the equilibrium models [169, 170]:

$$R_i = (k-1)\frac{\partial c_{UB}}{\partial t} \qquad (4.4)$$

Where k stands for the total binding coefficient. c_{UD} is the unbinded drug concentration, mol/m^3 and in this case $c_t = c_{UB}$. Another one is called dynamic model describing a reversible binding process [171]:

$$\text{c}_{\text{UD}} \underset{\text{k}_u}{\overset{\text{k}_b}{\rightleftharpoons}} \text{c}_{\text{BD}}$$
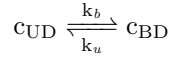
Where k_b and k_u stand for the association rate (binding) and dissociation rate (unbinding) respectively. Besides the drug binding to the specific chemical sites, non-specific binding process also exists due to the drug association with membrane constituents or trapped drug in the extracellular medium and has been not considered in the current research.

A second-order model is used to describe the dynamic model for reversible binding process:

$$R_i = -\frac{\partial c_{BD}}{\partial t} = \phi^{-1}k_b c_{UD}(B_{max} - c_{BD}) - k_u c_{BD} \qquad (4.5)$$

B_p is the binding potential, D_{a0} is called Damköhler number related to the porosity and binding site. ϕ is the tissue porosity. B_{max} is the density of binding site.

As shown in Figure 4.3 [167], the unbinding (a) and binding (b) drug concentration profile in tissue have been studied separately at three different time instants. It is found that the unbinding drug concentration (4.3-(a)) is two orders smaller compared to the binding drug concentration (4.3-(b)) with similar profile. Thus based on the significant difference between the magnitude of binding and unbinding drugs, the partition between binding and unbinding drugs has been neglected as we mainly focus on the total drug concentration in the tissue.
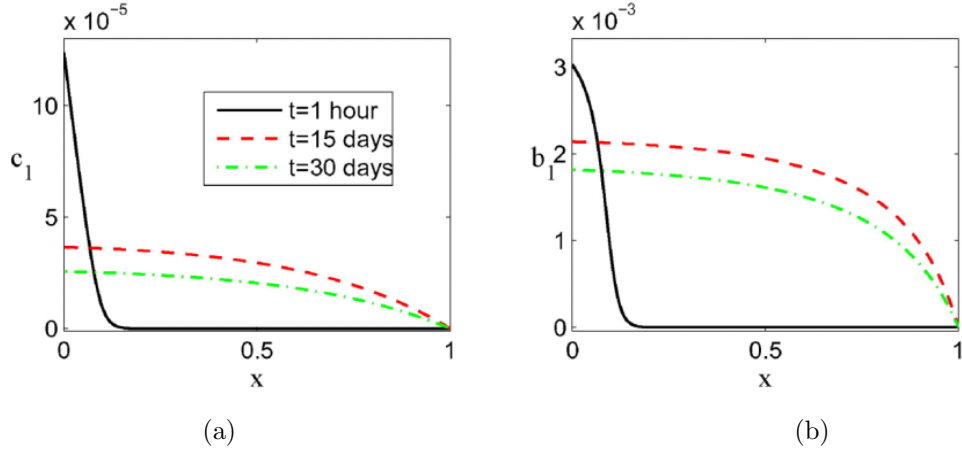
Figure 4.3: Nondimensional concentration profiles at three times for unbinding (a) and binding drug (b) [165]

In addition, as the flow filtration speed in tissue is in the order of 10^{-10} m/s [80] and the diffusion coefficient of paclitaxel used in the present study is $D_t = 10^{-13}$ m^2/s in tissue with thickness of $e = 0.5$ mm [97,172], the flow convection is neglected based on the Peclet number shown in equation (4.6). Peclet number is a type of dimensionless number describing the transportation phenomenon and represents the ratio between convection transport and diffusion transport. As the value of Pe is approximately in the order of 10^{-1} in our case, the diffusion keeps the dominant role in tissue. Thus the influence of convection is not considered here and the governing equation for mass transfer in tissue is defined in equation (4.7).

$$Pe = \frac{eu_t}{D_t} \approx 10^{-1} \tag{4.6}$$

$$\frac{\partial c_t}{\partial t} = D_t \nabla^2 c_t \tag{4.7}$$

Subsequently, the characteristic time of drug transfer can be estimated separately in tissue and lumen domains along with the parameters of $D_t = 10^{-13}$ m^2/s, tissue thickness of $e = 0.5$ mm, strut length of DES $a = 0.1$ mm and average flow velocity of $u_f = 0.16$ m/s. As calculated in the following equations, the drug transport time in blood domain (t_f) is far less than that in tissue (t_t). Thus, the drug transfer in tissue is dominant compared to that in blood.

$$t_t \approx \frac{e^2}{D_t} = 29 \ days \tag{4.8}$$

$$t_f \approx \frac{a}{u_f} = 6.25 \cdot 10^{-4} \ s \tag{4.9}$$

• Drug transport in polymer domain

Drug dissolution and diffusion are the main mechanisms in polymer as we consider the non-degradable case. The dissolution process is schematically represented by:

$$b \xrightarrow{\beta} c$$

91

Where b is the solid drug concentration and c is the dissolved drug concentration. β is the dissolution rate.

Polymer as the drug carrier plays a key role on the drug release rate. In general, Fick's law of diffusion was used to give the fundamental description of mass transport from polymer as the drug solubility in flow is over the maximum drug concentration in polymer. Thus all the drugs are capable to be at dissolved state since the flow intrudes the polymer instantly. In this case the diffusion controlled equation is adopted in polymer similar with the tissue as shown below:

$$\frac{\partial c_p}{\partial t} = D_p \bigtriangledown^2 c_p \qquad (4.10)$$

Where c_p is drug concentration in polymer, mol/m^3. D_p is drug diffusion coefficient in polymer, m^2/s.

4.2.2 Validation of 2D model establishment

Among the investigations regarding drug transport from DES, 2D models have been more widely established compared to 3D models. In this part we aim to verify if the 2D model established in our case will be reasonably sufficient. The commercial software Comsol of version 5.1 has been utilised in this study. As can be seen in Figure 4.4, the axisymmetric 3D geometrical model of artery has been established with a single circular DES corresponding to the 2D model shown in Figure 4.4-(b). The cross section of the stent is square with height of 0.1 mm. The radius of artery is 1.75 mm, the thicknesses of polymer and tissue are 0.05 mm and 0.5 mm separately. The artery lengths before and after stent are 4 mm and 6 mm respectively in order to make sure the geometrical independence.

- 3D geometrical model
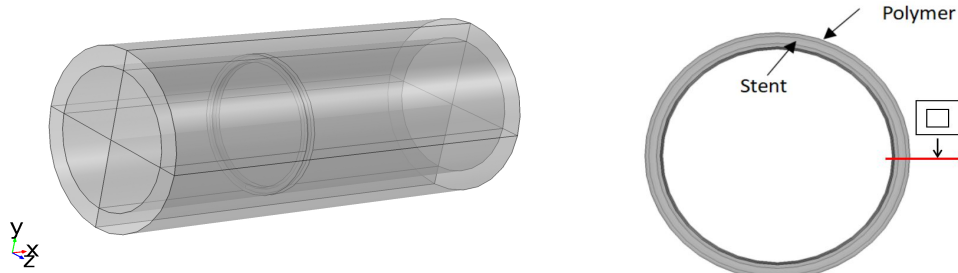
(a) 3D geometrical model of artery with DES
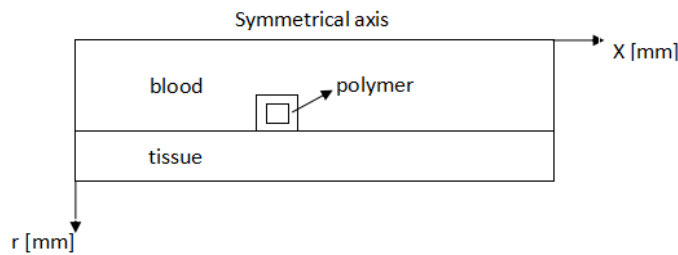
(b) 2D geometrical model of artery with DES

Figure 4.4: Establishment of geometrical model of artery with DES

- Mesh distribution

The mesh has been generated with tetrahedral mesh elements in Comsol. In order to make sure the mesh independence, four mesh sizes of 1556931, 3829422, 5181389, 8766130 have been established through the drug concentration in polymer. As shown in Figure 4.5, after the third point the accuracy of drug concentration in polymer can be controlled under 3%. Thus the mesh size of 5181389 has been finally selected as shown in Figure 4.6.
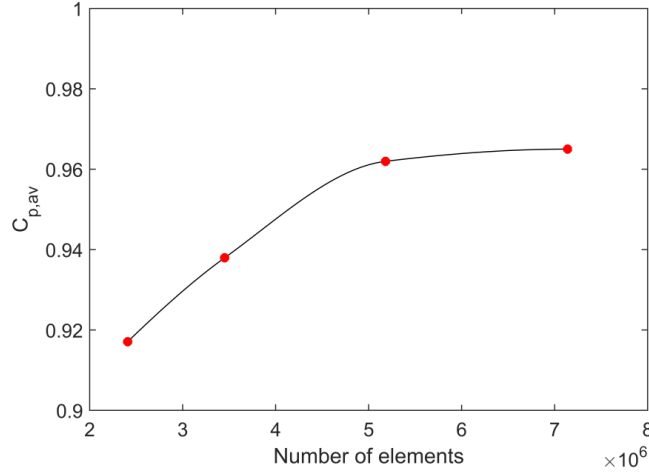
Figure 4.5: Study of mesh independence regarding volume averaged drug concentration in polymer after 1 day
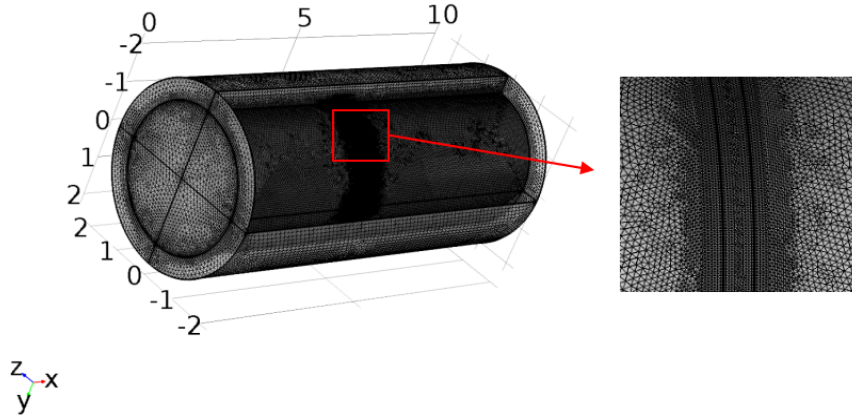
Figure 4.6: 3D mesh distribution of artery with DES

- Mathematical model and boundary conditions

The blood flow is considered as incompressible and Newtonian fluid through the coronary artery with rigid wall. Thus the density and the dynamic viscosity are constant: $\rho = 1060 \; kg/m^3$, $\mu = 0.0035 \; Pa \cdot s$. Accordingly, the governing equations for the blood domain follow the mass conservation equation (4.11) and momentum equation (4.12) in steady case. The inlet boundary condition is given a sectional mean velocity: $V_0 = 0.2 \; m/s$ following parabolic velocity profile. At outlet the pressure is imposed to be $0 \; Pa$.

$$\bigtriangledown \cdot V = 0 \tag{4.11}$$

$$\rho \frac{\partial V}{\partial t} + \rho V \cdot \nabla V = -\nabla p + \mu \bigtriangledown^2 V \tag{4.12}$$

Concerning the drug transport, as discussed above the governing equation in lumen including drug diffusion and convection has been employed shown in equation (4.13). In the tissue and polymer domains, only drug diffusion is considered following equation (4.14).

$$\frac{\partial c}{\partial t} + \bigtriangledown \cdot (-D \bigtriangledown c) + u \cdot \bigtriangledown c = 0 \tag{4.13}$$

$$\frac{\partial c}{\partial t} + \bigtriangledown \cdot (-D \bigtriangledown c) = 0 \tag{4.14}$$

Where c represents the drug concentration (mol/m^3), D represents the diffusion coefficient (m^2/s). In our case with drug paclitaxel, the diffusion coefficient in polymer and tissue is $D_p=D_t=10^{-13}$ m^2/s [172–174], in lumen domain the drug diffusion coefficients is $D_f=10^{-10}$ m^2/s [82].

The boundary conditions have been described below: a zero drug concentration is given at the inlet of blood domain, the drug flux along z axis is considered to be 0 at the outlet. For the tissue domain, a zero drug concentration is imposed both at the two lateral boundaries and there is no drug flux through the outer boundary of tissue. A continuous drug flux is considered through the interfaces including the blood-tissue interface, blood-polymer interface and polymer-tissue interface. The initial drug concentration in polymer is 100 mol/m^3, however, the initial drug concentration is set to be 0 both in blood domain and tissue domain.

$$c_f|_{inlet} = 0, \frac{\partial c_f}{\partial z}|_{outlet} = 0$$

$$D_f \bigtriangledown c_f = D_t \bigtriangledown c_t \text{ (Blood-tissue interface)}$$

$$D_p \bigtriangledown c_p = D_t \bigtriangledown c_t \text{ (Polymer-tissue interface)}$$

$$D_f \nabla c_f = D_p \nabla c_p \text{ (Blood-polymer interface)}$$

$$\frac{\partial c_t}{\partial r}|_{perivascularwall} = 0$$

$$c|_{z=0} = c|_{z=L} = 0 \text{ (Lateral boundaries of tissue)}$$

$$c = 100 \ mol/m^3 \text{ (Initial drug concentration in polymer)}$$

- Comparisons of mass transfer between 2D and 3D cases

In order to investigate if 2D model is sufficient to study the mass transfer process compared to 3D model, the drug concentration in tissue along the azimuthal direction has been studied as shown in Figure 4.7. A dimensionless parameter is introduced and defined as relative difference$=\frac{|c_{average}-c|}{c_{average}} \cdot 100$. The circular line in tissue is located at the middle location of stent with a constant radius of 1.85 mm. c represents the drug concentration along the line, $c_{average}$ is the averaged drug concentration along the circular line. Through Figure 4.7, it is observed that the drug concentration can be considered to be constant along the circular line in tissue with the relative difference around 1%. Thus the results obtained here are in favor of establishment of 2D model.
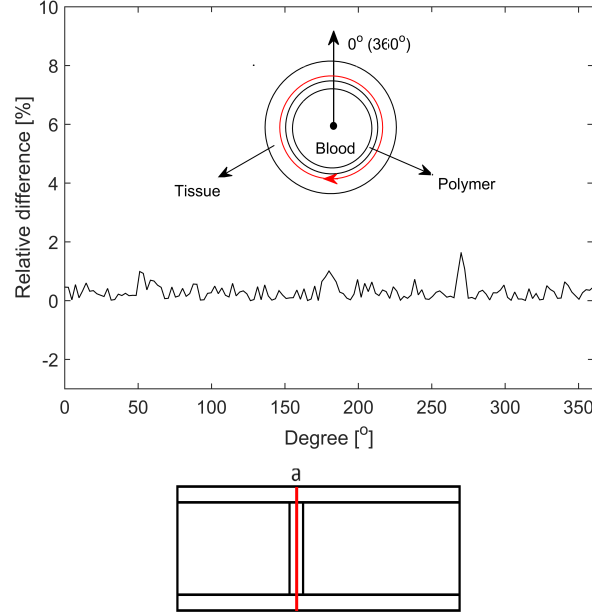
Figure 4.7: Drug concentration along line in tissue after 1 day

In addition to the drug concentration in tissue, the drug concentration in polymer has been focused as well. Figure 4.8 shows the relative difference of drug concentration in polymer versus time between 2D and 3D cases defined as relative difference=$\frac{|c_p^{2D}-c_p^{3D}|}{c_p^{3D}} \cdot 100$. c_p^{2D} and c_p^{3D} represent the drug concentration in polymer for 2D and 3D cases separately. Meanwhile, an inset has displayed the drug release profile along with the time both in 2D and 3D cases. It can be observed that the relative difference regarding drug concentration in polymer is around 2% even though a peak value of around 6% exist when t=0.1 d. Through the inset figure, the normalized drug concentration in polymer within 0.8 day has been presented. Similar drug release profile is observed complying the same drug release duration for 2D and 3D cases. Therefore, based on the results in Figure 4.7 and 4.8, it is sufficient to consider the drug transport in 2D model for the present study.
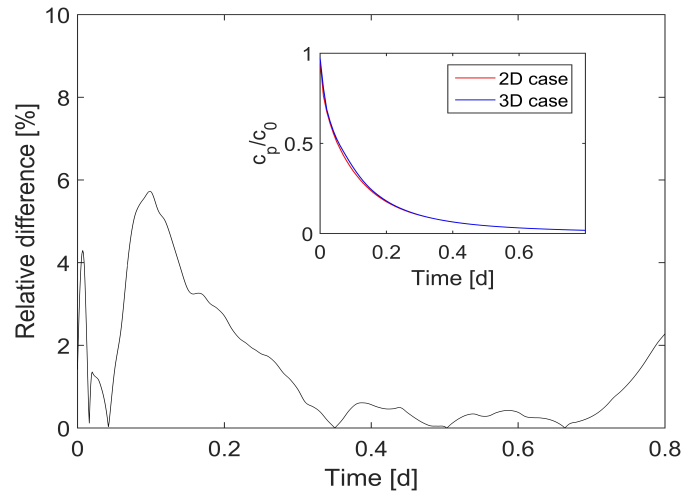
Figure 4.8: Comparison of drug release from polymer versus time between 2D and 3D cases

4.3 Mass transfer from DES in 2D case: Control parameters study

With the validation of 2D artery model with DES, the following investigations have been carried out based on the 2D model establishment. Drug release and transport from polymer into lumen and tissue domains have been studied aiming to have a better understanding of mass transfer mechanisms in artery. Moreover, in view of DES performance improvement, a controlling parameter study has been considered with different polymer thickness, different strut location and different diffusion coefficient in polymer.

4.3.1 2D Modeling establishment and methodology

Figure 4.9 shows the 2D geometrical model of artery treated by DES. Three domains are included: blood domain (Ω_b), tissue domain (Ω_t) and polymer domain (Ω_p). Three struts of square shape with length of 0.1 mm are considered with a polymer thickness of 0.05 mm. The distance between central position of struts is 0.7 mm. The radius of artery is 1.75 mm which is consistent with coronary artery. The thickness of artery wall is 0.5 mm. The artery lengths before and after the stent adopt 4 mm and 6 mm separately in order to make sure the geometrical independence.
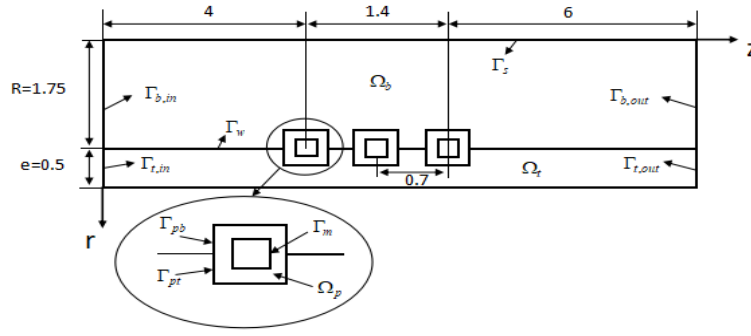
Figure 4.9: 2D geometrical model of artery with drug eluting stent (mm)

The mathematical model and boundary conditions regarding blood flow and drug transfer remain the same as discussed above. Thus, following the geometrical and mathematical models, the mesh independence has been studied in Figure 4.10 based on the normalized drug concentration at one point in tissue versus different mesh elements. Four different mesh sizes have been studied: 46630, 63470, 93125, 161513. As can be seen that the accuracy can be controlled under 1% after the third point. Thus, the final mesh distribution is finally determined based on the third mesh size as shown in Figure 4.11.
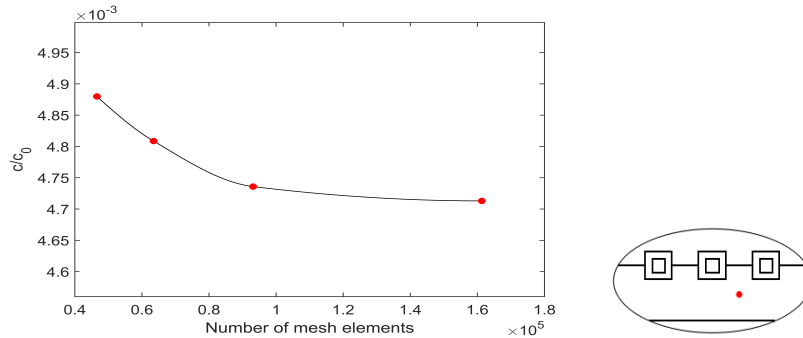
Figure 4.10: The study of mesh independence
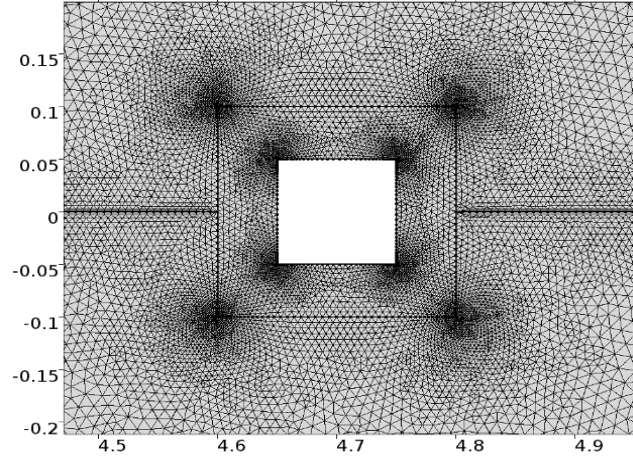
Figure 4.11: 2D grid distribution around the stent

4.3.2 Results analysis of drug release from DES

- Reference state

In order to acknowledge the drug transport process, the drug concentration in tissue domain from DES has been investigated at different time instants shown in Figure 4.12. At the beginning of drug transport, the drug distribution tends to be symmetrical around each stent independently. Within one day, the blood flow in lumen has no longer affected drug release from polymer as there is no drugs in the polymer exposed in the flow. Along with time going, in 3 days the peak values of drug concentration are observed under each location of struts, and the drug distribution tends to be more interacting between struts. Until 8 days the peak values of drug concentration have disappeared, and the drugs are distributed more evenly along the horizontal direction. In 40 days, all the drugs are totally gone in tissue.
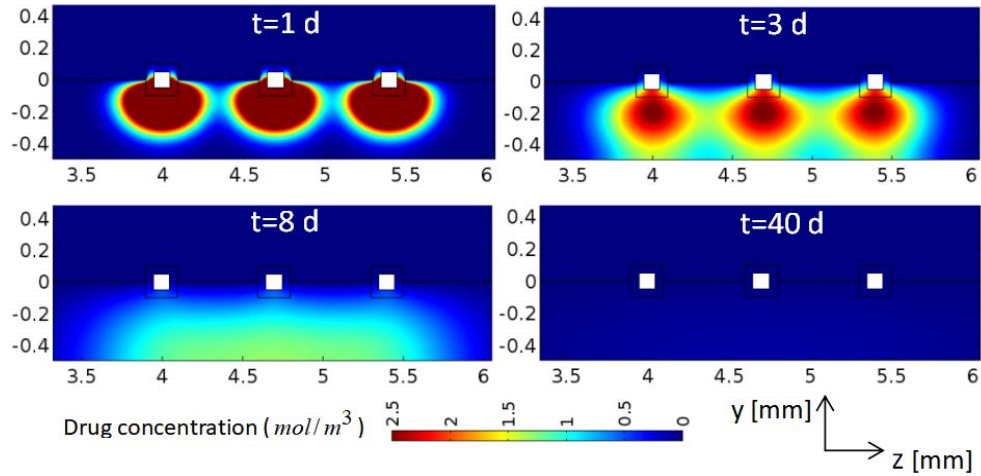
Figure 4.12: Drug concentration at different time instants

Figure 4.13 plots the drug concentration along lines in tissue horizontally and vertically at different time instants. As can be seen in Figure 4.13-(a), three peak values corresponding to the location of struts are observed especially when t=1 d and the drug concentration around each strut tends to be

97

symmetrical. Along with time going, the peak values are weakened because of diffusion process in tissue and the drug exhaust in polymer. The drug distribution tends to be more homogeneous horizontally. When focusing on Figure 4.13-(b), the drug concentration along vertical line in tissue is plotted at different time instants. It is shown that in one day's diffusion, the drug has not been fully spread into tissue. A big difference between top and bottom of tissue exists. With the proceeding of drug diffusion, the difference of drug concentration along the line is significantly decreased in 3 days. When t=8 days, larger drug concentration at the bottom can be observed compared to the top of the vertical line. The results show us that the polymer plays a dominating role during the beginning period of diffusion, and the influence is totally eliminated after around 8 days.

(a)   (b)
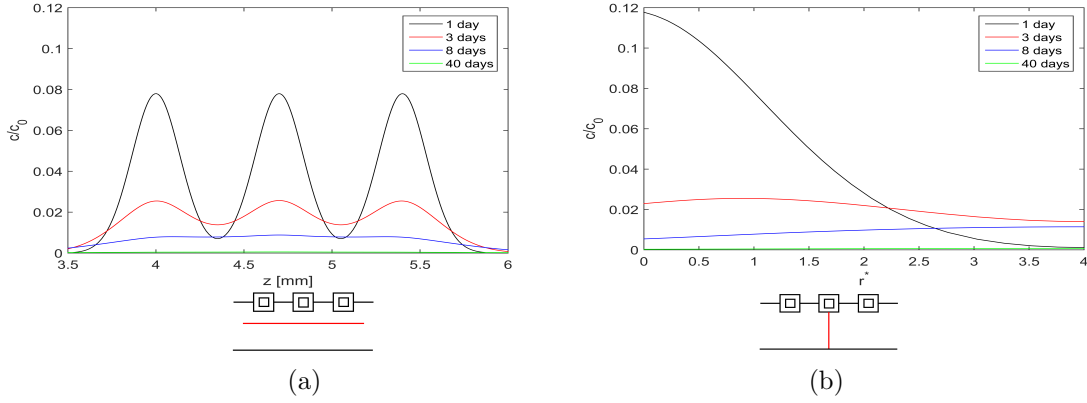
Figure 4.13: Normalized drug concentration in tissue along lines horizontally (a) and vertically (b) at different time instants

Specific to the drug concentration in the blood domain, Figure 4.14 displays the drug concentration and velocity vectors around strut at different time instants. The formation of recirculation is observed both upstream and downstream where the drugs are mainly located in blood domain. It is noticed that the drug concentration in recirculation region is in the order of 10^{-2} which is far less than the initial drug concentration in polymer. In two days all the drugs in recirculation region have been gone. Thus it can be concluded that the effect of recirculation on drug transport can be neglected.
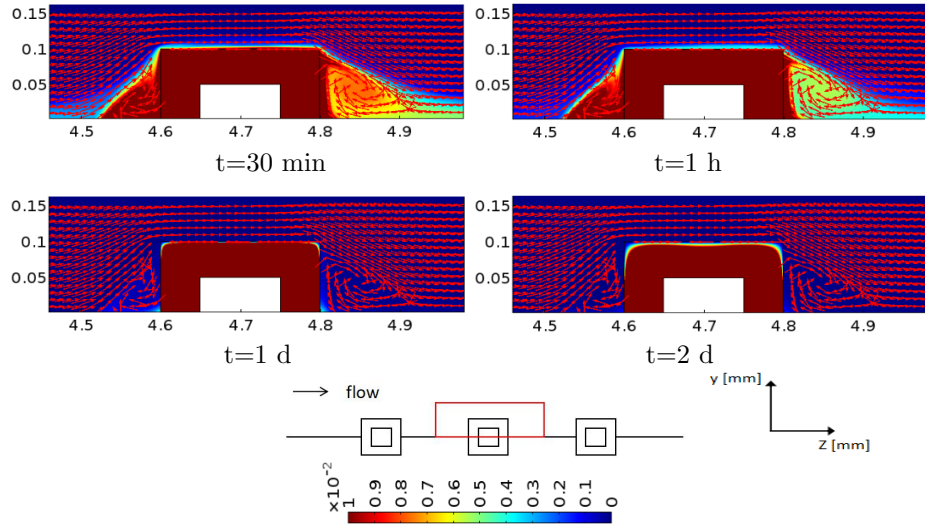
Figure 4.14: Drug concentration at different time instants (mol/m^3)

• Effects of different polymer thickness

Following the analysis of drug transport process in polymer, tissue and blood domain, the sensitivity of drug transfer to different controlling parameters has been carried out. Figure 4.15 plots the normalized drug concentration in tissue (a) and in polymer (b) versus time at different polymer thickness. As observed in figure 4.15-(a), the drug concentration in tissue is significantly affected by the polymer thickness. With the increasing of polymer thickness, larger drug concentration is obtained along time and the occurrence of peak value is delayed as well but still within 1 day in our case. The peak value is resulted from the initial drug accumulation from polymer. Afterwards, the drug concentration in tissue is decreased as the drugs diffuses in tissue. Regarding figure 4.15-(b), similarly the drug concentration in polymer is increased with the increasing of polymer thickness and the drug release time from polymer is prolonged as well. The conclusion can be obtained that higher polymer thickness contributes to higher drug concentration and the drugs can be maintained for a longer time in tissue. The reason for the current results is greatly related to the contacting surface between polymer and tissue. Larger contacting surface is beneficial to improve the stent performance.

(a) In tissue   (b) In polymer
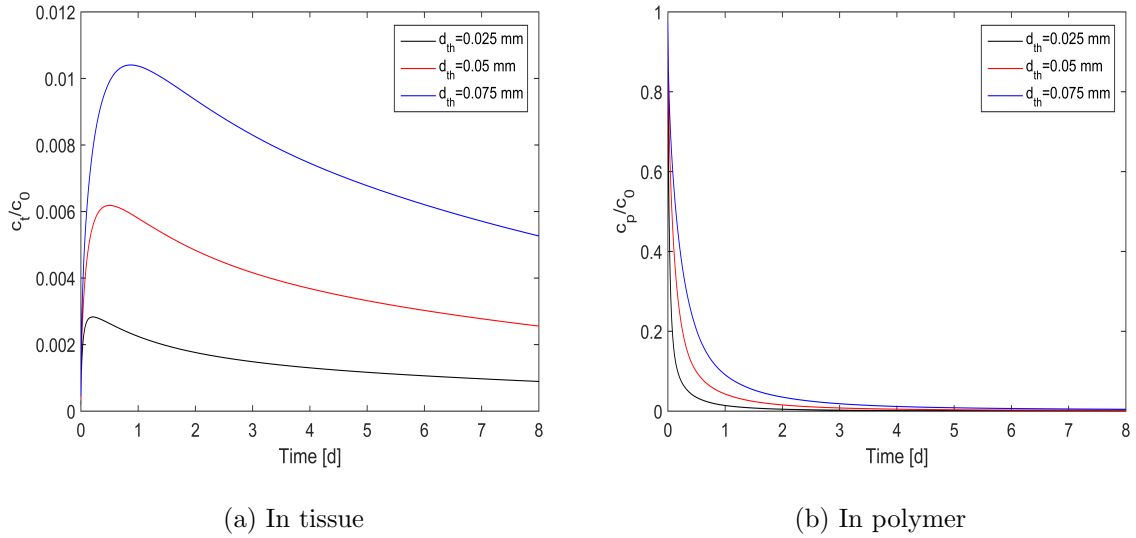
Figure 4.15: Normalized drug concentration versus time in tissue (a) and polymer (b) at different polymer thickness

• Effects of different strut locations

Figure 4.16 shows the normalized drug concentration in polymer and tissue versus time at different strut locations. As can be seen in Figure 4.16-(a), when the strut is half embedded into the tissue, the drug release rate from polymer is decreased and the drug release time is prolonged compared to the non-embedded case. Half embedded strut reduces the exposed polymer surface in the blood domain where the effect of convection and diffusion is stronger. Focusing on the tissue domain as shown in Figure 4.16-(b), the normalized drug concentration keeps higher when the strut is half embedded into the tissue and the drug retains for a longer time in tissue as well. Thus a good contacting between polymer and tissue contributes to a better performance of the stent.

(a) In polymer

(b) In tissue
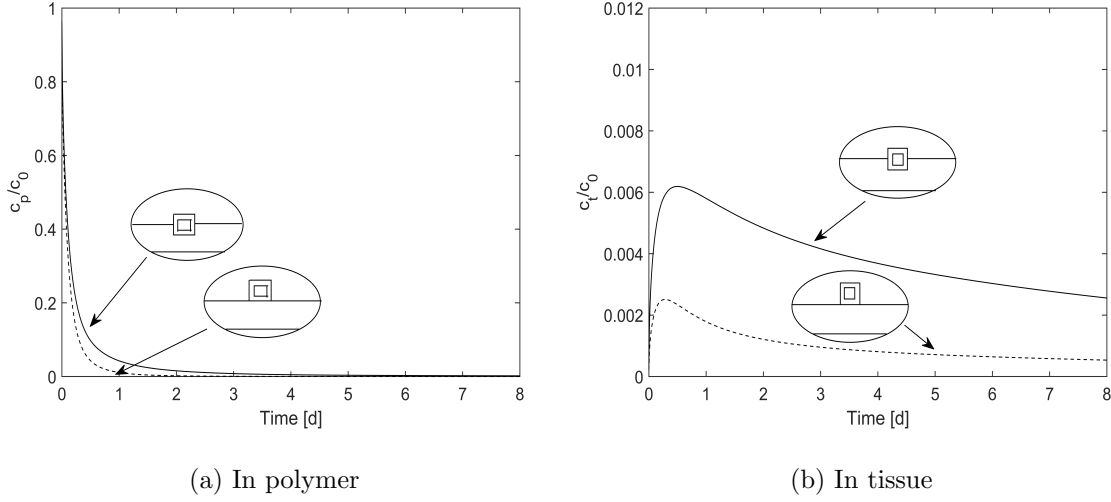
Figure 4.16: Normalized drug concentration in polymer (a) and tissue (b) versus time at different strut locations

Along with the investigation of drug concentration affected by strut locations, Figure 4.17 plots the wall shear stress within the strut region at different strut location in order to better evaluate the influencing mechanisms of strut location in multiple view. When the struts are half embedded into the tissue, the point where WSS equals to 0 can be clearly observed. However, when the struts are totally exposed in the blood domain, there is no points formed where WSS equals to 0 and values of WSS below 0.5 pa are always obtained. These phenomena confirm the key role of strut height on stent performance and also consistent with above observation.
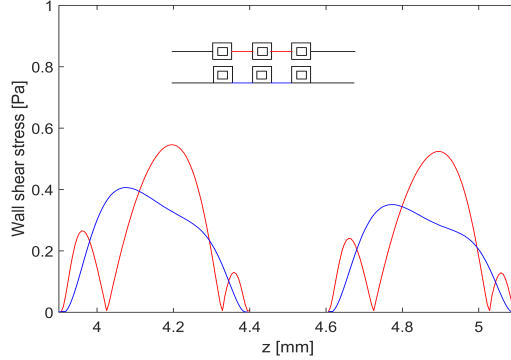
Figure 4.17: Wall shear stress between struts at different strut location

- Effects of different diffusion coefficients in polymer

Diffusion coefficient acts the key role in mass transport. Drug loaded polymer as the source of mass transfer can affect the DES performance with specific drug release rate. Diffusion coefficient in polymer (D_p) depends on the choice of drug and also the polymer material properties and dominates the drug release process. Thus the effects of different D_p on mass transfer have been studied. Figure 4.18 plots the normalized drug concentration versus time in polymer (a) and tissue (b) at different D_p. Decreased diffusion coefficient in polymer leads to the decreased drug release rate and prolonged release time as observed in Figure 4.18-(a). Focusing on the mass transfer in tissue (Figure 4.18-(b)), it is seen that

when D_p decreases from 1e-12 m^2/s to 1e-13 m^2/s, a higher drug concentration in tissue is obtained and the occurrence of peak value is prolonged. However, when D_p decreases from 1e-13 m^2/s to 1e-14 m^2/s, the drug concentration in tissue is decreased compared to the case of D_p=1e-13 m^2/s in 6 days. The peak value is weakened and the variation after the peak value tends to be more flat. After 6 days, a higher drug concentration in tissue can be found compared to the other cases. Therefore, with the results here we can found that a smaller D_p is beneficial to prolong the drug retain time with a relatively more even drug dosage versus time in tissue.

(a) In polymer (b) In tissue
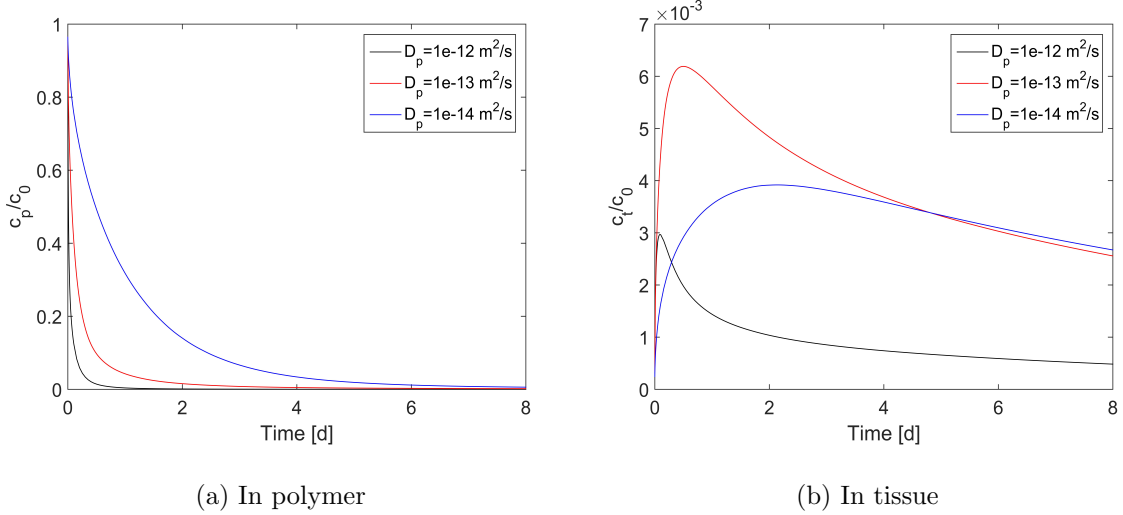
Figure 4.18: Normalized drug concentration in polymer (a) and tissue (b) versus time at different diffusion coefficients in polymer

4.4 Experimental validation about mass transfer from polymer

Along with the numerical investigations, experimental works are more interesting to be carried out and to achieve the validation with numerical results. Among the existing investigations, validation works between simulation and experiment regarding DES in artery are really limited which is greatly restricted by the incomplete mathematical model considering the quite complicated biological physics. A few recent articles regarding the validation works of DES can be found. P.R.S. Vijayaratnam et al. [89] validated the symmetrical distribution of drug in tissue between numerical and in-vitro experimental results instead of the quantitative comparison. C. M. McKittrick et al. determined the diffusion coefficient of drug in polymer through fitting the drug release profile from polymer of in-vitro experiments. With the fitting value of diffusion coefficients in polymer, a good validation has achieved for the drug concentration in tissue between numerical and in-vivo experimental results. As can be seen through the limited validation works, a big space is available here and needs to be filled up with more works and efforts.

In this section, experimental works are conducted focusing on the drug release from polymer film into lumen, the tissue domain is not considered here. The experimental data is from the LIFSE team with the closed research subject. The experimental material and methods have been introduced along with the corresponding numerical and mathematical models establishment. Based on the experimental data, a prediction of diffusion coefficient of drug in polymer has been worked out within initial drug dosage of 10% to 30% and validation has been achieved through the comparisons between numerical and in-vitro experimental results.

4.4.1 Test facility and experimental material

The components of experimental setup has been displayed in Figure 4.19 [175]. As observed, the experimental system is consist of reservoir, inverter, feeding pipe, pump, valves and test tubes as well as the flow and pressure sensors. The temperature controlled enclosure helps to make sure the stable working temperature. The fluid prepared for the test is put in the reservoir. Along with the system on, the power of pump will deliver the flow to the targeted test tubes through the feeding pipe. The pump and inverter are used to perform the flow as static, continuous or pulsed. Valves are used to adjust the flow rate. Flow and pressure sensors can help to monitor the working flow rate and pressure. As several test tubes have been fabricated in this experimental system, the parallel tests can be made at one time.
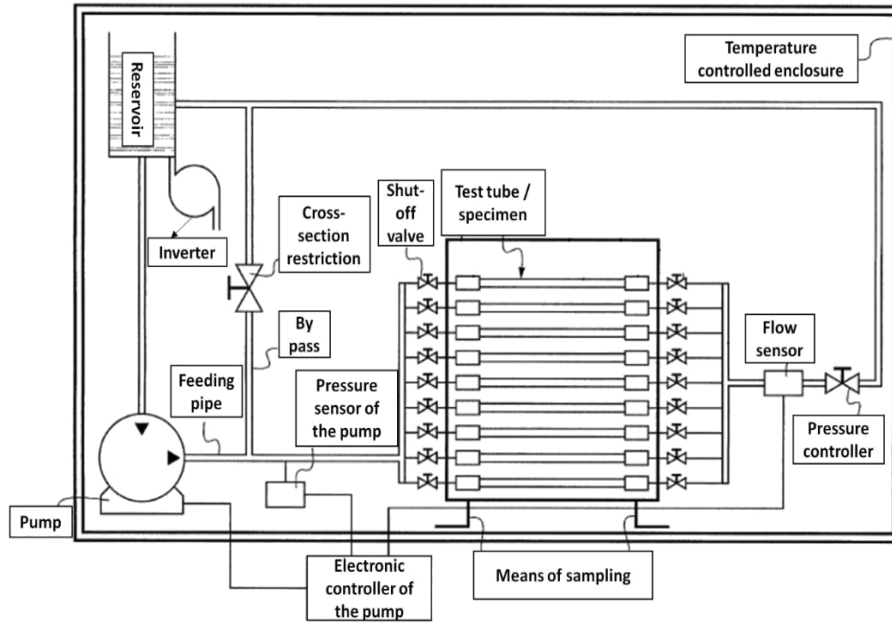
Figure 4.19: Scheme of the test facility components [170]

The test vein is shown in Figure 4.20 with parallel test tubes. The test tube is fabricated as rectangular. The length of flow channel is 130 mm and the cross section of channel is square shape with length of 30 mm.

Figure 4.20: Test bench

- Fluid property

In the current tests, water was used as the flow taking away the drugs from polymer. The density and dynamic viscosity are respectively 1000 kg/m^3 and 6.9e-4 $Pa \cdot s$. The flow rate is controlled to be 7.5 ml/s which corresponds to the flow rate of the internal carotid artery when one is at rest condition [175].

- Polymer material

Non-degradable polyurethane (PU) has been used as the carrier of drugs. Polymer samples with the dimensions of $30 \times 5 \times 2\ mm^3$ were prepared with a certain dosage of drugs (mass ratio of drug/(drug+polymer)): 10%, 20% and 30% separately. The drugs are homogeneously distributed in polymer and the polymer film was fixed at the middle of flow channel contacting the bottom surface as shown in figure below:
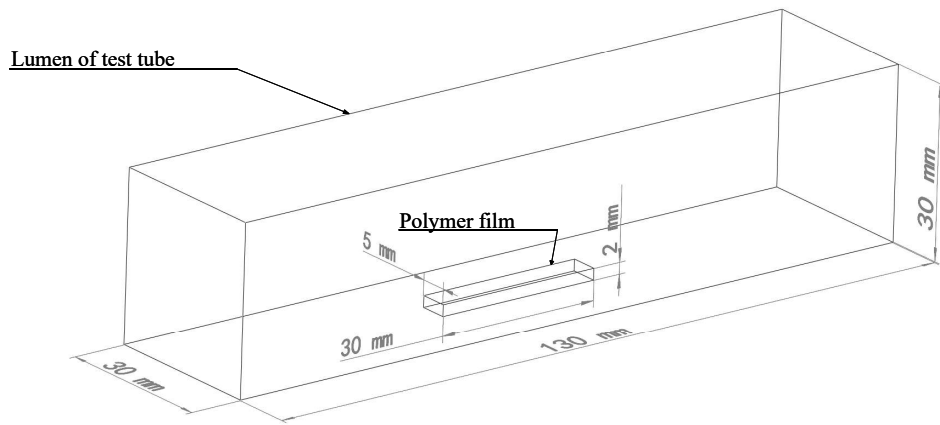
Figure 4.21: Scheme of flow channel with polymer film

- Choice of drug

The drug loaded in polymer has been selected to be diclofenac for drug release tests [176] and purchased from Genevrier Laboratory. The drug particle is in granular shape with density of approximately 450.7 mg/ml. The solubility of the drug at a temperature of 37 °C in water is about 5.554 g/L.

Measurement of drug release profile from polymer versus time mainly followed the two steps: firstly, the samples were put in the oven at 50°C for one hour to remove moisture and then were weighed immediately after cooling in the desiccator (M_1). Secondly, the dried samples were put in the test tube and measurements were made after a specified period for each test. In order to remove all the water absorbed in the polymer, the samples were put to an oven at 50 °C. The drug remained in polymer was measured after the sample weight was stabilized (M_2). Thus the drug mass loss in polymer can be calculated as $M_t = M_1 - M_2$.

4.4.2 Numerical modeling establishment and methodology

- Geometrical model

To comply with the size of test facility, the 2D geometrical model of flow channel with drug-loaded polymer inside has been established as shown in Figure 4.22. Two domains are included: flow domain

and polymer domain. The length of flow channel is 130 mm and the height is 30 mm. The polymer is 2 mm of height and 30 mm of horizontal length located at the middle of artery. The boundaries include inlet, outlet, channel wall and interfaces between lumen and polymer. The mesh independence has been investigated with the drug concentration in polymer at different mesh sizes of 40976, 66592, 93125 and 131514. The results accuracy can be controlled below 1% after the third mesh size. Thus the final mesh size of 93125 has been determined.
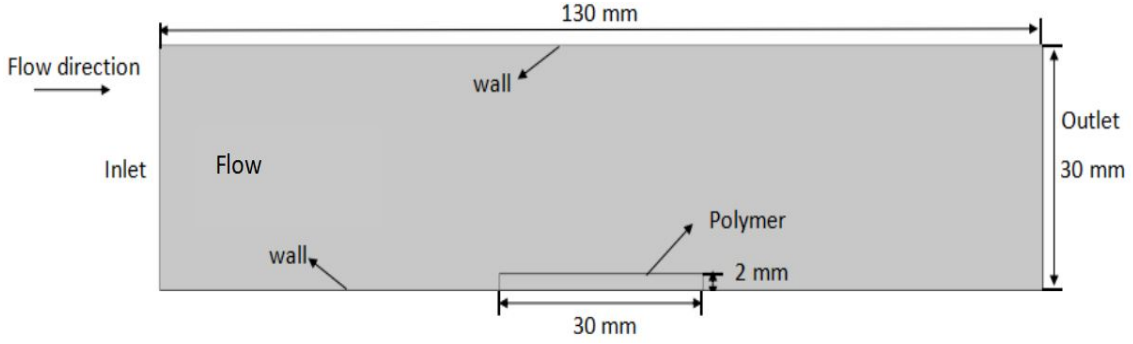
Figure 4.22: 2D geometrical model of flow channel with drug-loaded polymer

- Mathematical model of drug release in polymer

In terms of the mathematical models in polymer, both diffusion and dissolution physics have been considered in order to better describe the practical drug release process in experiments. The drugs in the polymer are in the solid phase initially and then dissolves and diffuses gradually along with the flow intrusion. When the polymer contacts with the fluid, the flow will enter through the boundaries and occupy the pores which constitute the diffusion path of the dissolved drugs. The dissolution process follows the relation below [177]:

$$b \xrightarrow{\beta} c$$

Where b is the drugs in the solid phase and c is the drugs in the dissolved phase. β represents the dissolution rate. The solid drugs as the source of dissolved drugs are not able to be diffused and the diffusion happens only with the dissolved drugs. Thus the governing equations are established as follows [167]:

$$\frac{\partial b}{\partial t} = -\beta b(S - c) \tag{4.15}$$

$$\frac{\partial c}{\partial t} = \bigtriangledown \cdot (D \bigtriangledown c) + \beta b(S - c) \tag{4.16}$$

Where S is the solubility of drugs in flow, 13.5 $mol/m3$. D is the diffusion coefficient. As the drug solubility is less than the initial drug concentrations in our study, the values of β is determined based on the criteria of nondimensional Damköhler number $>> 1$ which is defined as $Da_0{}^* = \beta B L_c^2 / D$ [167]. B is the initial drug concentration in polymer. Thus the value of β is set to be 10 $mol/(m^3 \cdot s)$. For the initial drug concentration in polymer, $c = 0$, $b = B$.

Referring to the literature [175, 178], two phases of drug release from polymer have been commonly demonstrated affected by the initial burst release. Accordingly, the drug release models describing these

two phases have been developed shown in equation (4.17) [179] and (4.18) [180]. Equation (4.17) models the early stage where less than 40% drugs are released from the polymer and Equation (4.18) describes the late stage of more than 40% drugs released from the polymer.

Early stage:

$$M_t/M_0 = 4\sqrt{\frac{D_1 t}{\pi L_c^2}} \qquad 0 < M_t/M_0 < 0.4 \tag{4.17}$$

Late stage:

$$M_t/M_0 = 1 - \frac{\pi^2}{8} exp(-\frac{\pi^2 D_2 t}{L_c^2}) \qquad 0.4 < M_t/M_0 < 1 \tag{4.18}$$

Where M_t stands for the amount of drug released from polymer instantaneously. M_0 is the initial drug amount loaded in polymer. L_c is the hydraulic diameter of the polymer, 3.75 mm. D_1 and D_2 are diffusion coefficients in these two stages separately.

The experimental works have been carried out with three different initial drug dosage of 10%, 20% and 30% respectively by LIFSE team, corresponding to 202 $mol/m3$, 356 $mol/m3$ and 591$mol/m3$ and the value of M_t versus time has been measured experimentally in these three conditions. Based on the experimental measurement of drug release (M_t versus time) in each condition provided by LIFSE team, the diffusion coefficients D_1 and D_2 have been calculated through equations (4.17) and (4.18) as shown in Table 4.1. As observed, with the increase of initial drug dosage in polymer, the diffusion coefficients in polymer are increased both for D_1 and D_2. The reason is that the increased initial drug dosage can increase the polymer pores as demonstrated in literature [181].

Initial drug dosage	D_1 $[m^2/s]$	D_2 $[m^2/s]$
10%	2.8e-11	1e-11
20%	4.1e-11	1.465 e-11
30%	5.3e-11	1.99e-11

Table 4.1: Predictions of diffusion coefficients in polymer at different drug dosage

Then Figure 4.23 shows the comparisons between numerical and experimental results of drug release from polymer with these calculated diffusion coefficients at different initial drug dosages (10%, 20% and 30%). A good fitting has been achieved with R^2 of 0.9823, 0.9793 and 0.9717 respectively. The results also demonstrate that increased initial drug concentration contributes to the decreased drug release time from polymer. Release time of 100 h, 90 h and 65 h have been obtained corresponding to initial drug concentration of 202 mol/m^3 (10%), 356 mol/m^3 (20%) and 591 mol/m^3 (30%).
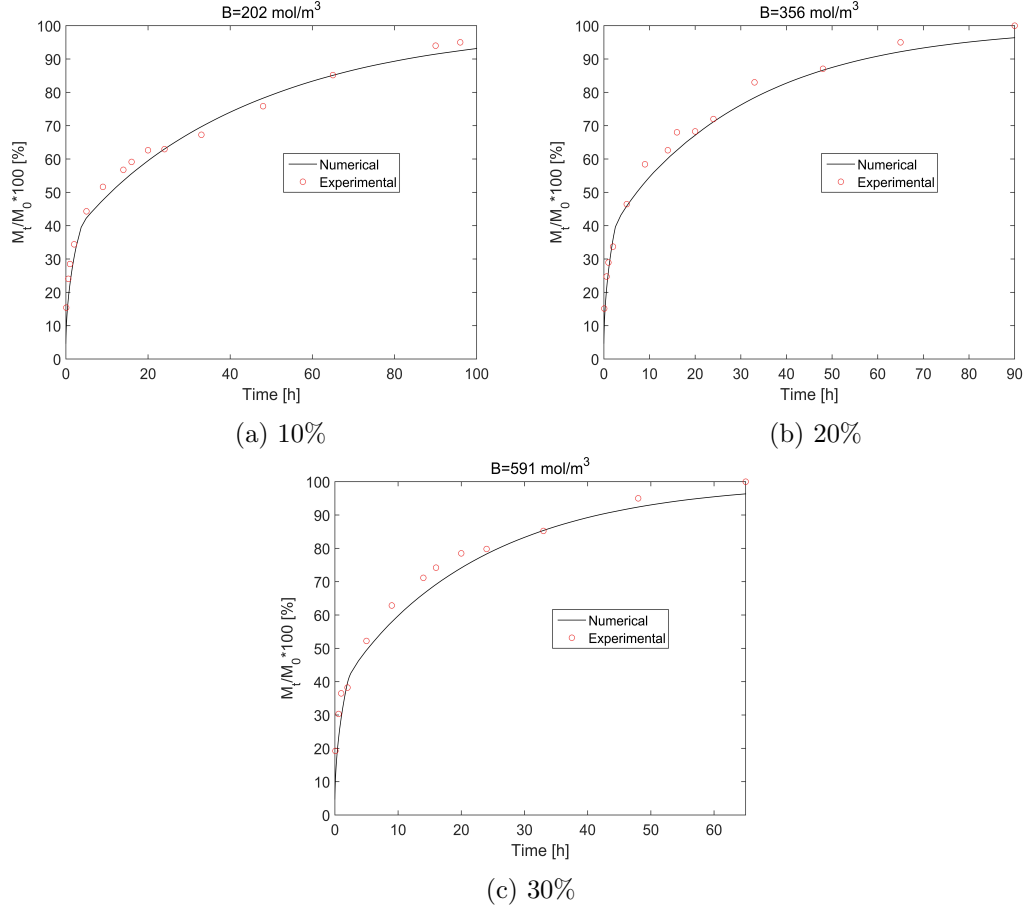
Figure 4.23: Comparison of drug release from polymer between experiment and simulation at different initial drug dosage: (a) 10%, (b) 20% and (c) 30%

- Mathematical model of drug transport in flow domain

The properties of fluid used in experiment is incompressible and Newtonian and the densidy and dynamic viscosity are 1000 kg/m^3 and $6.9e-4$ $Pa \cdot s$. Thus the flow is controlled by the Navier-stokes equations in steady case. As the flow rate of 7.5 ml/s is used in experiment, the sectional mean velocity at inlet is determined to be 0.0083 m/s corresponding to the Re number of 402. A parabolic velocity profile is set as the flow is in the laminar regime. At the outlet, the pressure is set to be 0 and the artery wall is considered to be rigid. As discussed above, both drug diffusion and convection are considered in lumen due to the existence of flow. Based on the literature [89], diffusion coefficient in flow D_f can be calculated based on the equation below:

$$D_f = \frac{KT}{6\pi\mu R} \tag{4.19}$$

Where K is Boltzmann's constant of 1.3807e-23 J/K, T is the fluid temperature, 310.15 K, the diameter of drug molecule is 1.7e-9 m referring to the Rhodamine B [89] as they have the similar structure. Thus a theoretical diffusion coefficient D_f of 3.875e-10 m^2/s is determined.

All the other boundary conditions keep the same with that discussed above.

4.4.3 Validation of drug release between simulation and experiment

Based on the determination of diffusion coefficient at 10%, 20% and 30%, the linear relationship between initial drug concentration and diffusion coefficients (D_1 and D_2) in polymer has been presented in Figure 4.24 (a) and (b). Thus a prediction of diffusion coefficient can be made through the linear relationship with initial drug dosage of 15%: D_1=3.4e-11 m^2/s and D_2=1.223e-11 m^2/s. In order to verify if the linear relationship between initial drug concentration and diffusion coefficient is practical between 10% and 30% in our case, comparison of drug release from polymer has been made between simulation and experiment with 15% (279 mol/m^3) drug in polymer as shown in Figure 4.25. As observed that a good fitting has been achieved with R^2 of 0.98.

(a)   (b)
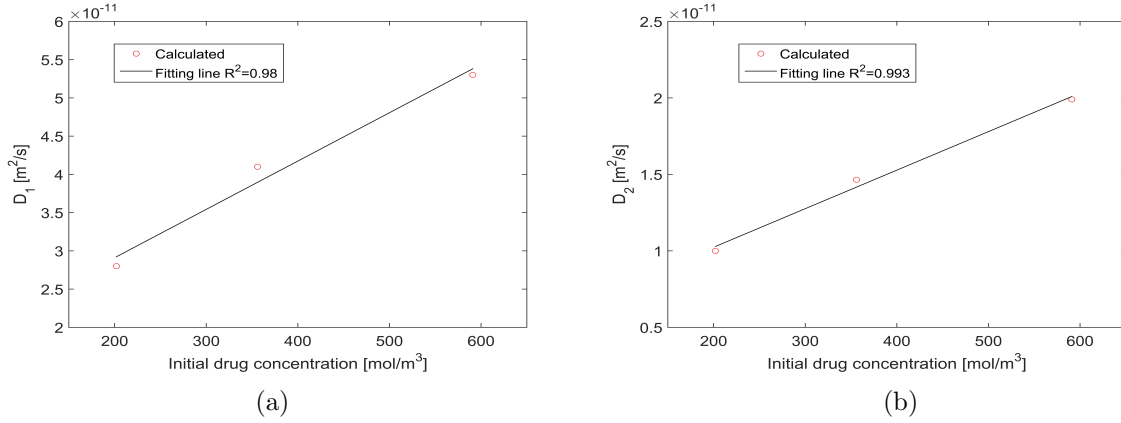
Figure 4.24: Linear fitting of initial drug concentration in polymer versus D_1 (a), and initial drug concentration versus D_2 (b)
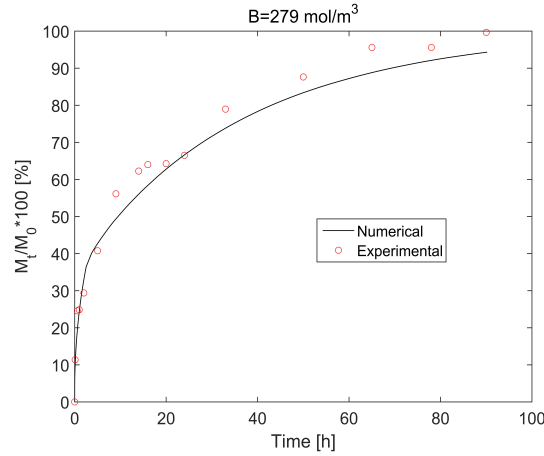
Figure 4.25: Comparison of drug release from polymer between experiment and simulation at initial drug dosage of 15%

4.5 Conclusion

Investigations regarding drug transport from DES have been focused both numerically and experimentally in this chapter. Along with the discussion of concerned physics for drug transport in artery,

the numerical and mathematical models have been determined and presented in the first place. Through comparisons of drug transport results in 3D and 2D models, a good agreement has been obtained for drug concentration in polymer and tissue. Thus the 2D model has been established sufficiently for the current research. The drug release and transport from polymer into tissue and lumen domains have been investigated in order to have a better understanding of mass transfer mechanisms in artery. The results show a relatively symmetrical drug distribution in tissue surrounding the struts. The effects of recirculation on drug transport have demonstrated to be neglected. In view of DES performance improvement, a controlling parameter study has been carried out with different polymer thickness, different strut location and different diffusion coefficient in polymer. The results show that increased polymer thickness is beneficial to prolong the drug release time from polymer and increase the drug retaining time in tissue which is consistent with the results of more embedded stent in tissue and smaller diffusion coefficient in polymer. The contacting surface between stent and tissue is a key factor on the stent performance. Besides the numerical investigations, experimental works have been conducted as well in order to contribute to the validation with numerical results. The prediction of diffusion coefficients in polymer has been achieved with initial drug dosage from 10% to 30% with a linear relationship. A good comparison of drug release from polymer has been accomplished with initial drug dosage of 15% between simulation and experiment. Moreover, through the experimental results with initial drug dosage of 10%, 20% and 30%, the increased initial drug concentration has been proved to decrease the drug release time with increased diffusion coefficient.

Conclusions and perspectives

Contents

5.1 Conclusions

This thesis aims to study the effects of arterial geometrical singularity on flow topology and hemodynamics in order to optimize the stent performance through better acknowledging the related physics as well as the mass transfer process from DES. As introduced in chapter 1, some focuses of interest have been put forward and investigated by the following chapters.

Based on the state of the art in this subject as discussed in chapter 1, it's known that the incidence of restenosis or thrombosis is greatly related to the recirculation region caused by the disturbed flow. The low value of shear rate located at the recirculation region plays a key role to contributions of deposition on vessel wall. The main conclusions among the existing literature demonstrate that the vortices' size is affected by the dynamic parameters of flow such as Reynolds number and the geometrical design of stent such as the shape and size of strut. The recirculation size formed both upstream and downstream the strut tends to be inversely affected by the Re number. Moreover, the height of the stent is demonstrated to be one of the most influential factors for recirculation size. Regarding investigations of mass transfer from DES, the study of controlling parameters on drug transport process have been commonly carried out. The controlling parameters of Re number of flow, polymer properties and polymer size on drug transport into lumen and tissue have been taken into account widely. However, the mechanisms related have not been fully explored yet and the optimization of stent requires more efforts including more considerations of flow pulse rate, multiple stent design factors, drug release characteristics and the necessary validation research works between simulations and experiments regarding DES.

Due to the complex mechanical and biological physics of blood flow in artery, the established numerical models have been taken the thorough considerations and elucidations in chapter 2 regarding blood flow in coronary artery. The main artery geometrical characteristics of bifurcation and tortuosity have been trending to be studied recently. Thus the preliminary investigation following the determination of numerical models have been carried out with the stenotic artery coupling the geometrical singularities: bifurcation and tortuosity as the modeling validations. The results reveal that either bifurcation or tortuosity can have a direct influence in flow disturbance and the potential onset sites of plaque. In the presence of bifurcation structure, when the stenosis is located in the main branch proximal, the recirculation development follows the flow orientation. However, when the stenosis is located on the side

branch, the vortices have been formed both upstream and downstream the stenosis. Compared to the stenosis length, the stenosis severity plays a more important role in hemodynamic variations. In the case of tortuous artery, both curved and spiral tortuosity have been studied. The spiral flow has been observed along spiral tortuosity and the advantages to inhibit the deposition have been shown compared to the curved tortuosity. A small part of diagnostic analysis has been introduced as well which gives a guidance to the practical treatment to some extent.

Chapter 3 conducted the coupling between coronary artery and stent performance with different design considerations. Both 2D and 3D cases have been carried out in view of different considerations of stent design. The flow topology and hemodynamic evaluations have been focused based on the WSS-based descriptors. The results show that the recirculations formed beside the struts are greatly affected by the pulse rate and stent geometry. The horizontal length of recirculation downstream stent remains the most sensitive to the pulse rate due to the less confined inertial force which is in contrast to the vertical length of recirculation downstream limited by the strut height. The larger interspace between struts is found to be beneficial to improve the stent performance with increased wall shear rate. Instead of 2D model, investigations with 3D model have been carried out with the establishment of practical stent geometry and both steady and unsteady cases have been studied. With the increase of AR, the low value region of wall shear rate and high value region of WSSGs located near struts both decrease which are consistent between steady and unsteady cases. Moreover, strut of high AR is beneficial to reduce the pressure drop through the stent and the region of high RRT and OSI which tend to result in deposition. Moreover, even though it is consistent that the inlet velocity is positively related to the wall shear rate distribution both in steady and unsteady cases, the influences of flow pulsation considered in unsteady case make differences of the results.

Following the interactions between flow and stent, chapter 4 steps into the physics coupling between flow and mass transfer by considering DES. In this chapter both numerical and experimental works are involved in order to better control the drug release process. The results demonstrated that the effects of recirculation on drug transport can be neglected. The increased polymer thickness is beneficial to prolong the drug release time from polymer and increase the drug retaining time in tissue which is consistent with the results of more embedded stent in tissue and smaller diffusion coefficient in polymer. Through experimental investigations with different initial drug dosages (10%, 20%, 30%) in polymer, the linear relationship between initial drug dosage and diffusion coefficient in polymer has been predicted. In order to verify this linear relationship, the diffusion coefficients with 15% drugs in polymer are calculated based on the linear relationship between initial drug dosage and diffusion coefficient in polymer and a good fitting has been obtained for drug release from polymer between numerical and experimental results.

5.2 Further works

On the basis of the present numerical study, many improvements of the numerical model are needed to be implemented. Moreover, the further works of experimental investigations still remain interesting. The main points have been elucidated as follows:

- Modeling improvement of blood flow in artery

In view of the practical case of blood flow in coronary artery, the artery geometry is complicated with irregular radius instead of consideration of cylinder geometry with constant radius. Thus the geometrical model establishment of coronary artery based on the practical human case is necessary in order to be

close to the reality. A few of the current investigations has put forward the multiphase property of blood flow instead of one single phase which should be implemented in the future works as well. In addition, heart curvature and movement have been neglected in the present study and should be further taken into account.

- Considerations of chemical physics in polymer and tissue

Regarding drug transport from DES, mainly drug diffusion has been considered in polymer and tissue. However, no matter polymer or the tissue both belong to the type of porous material, thus the flow intrusion into the polymer and tissue should be both considered. Moreover, the tissue as a type of biological material, the chemical reactions inside should be supplemented in the mathematical model. Instead of the non-degraded polymer, degradation of polymer should be covered in the future research.

- Improvements in experimental works and development of mathematical model regarding mass transfer

In spite of the numerical works, perspectives regarding the experiments need to be stressed as well. In the present study experimental works occupied a small part of the thesis which validated the fundamental physics of drug transport process. Thus more experimental works are needed and more mathematical models need to be developed such as the relationship between initial drug concentration in polymer and diffusion coefficient with other different materials. Moreover, the adoption of pulsed flow should be employed instead of steady flow.

Bibliography

[1] D. Lloyd-Jones, R. Adams, T. Brown, M. Carnethon, S. Dai, G. D. Simone, T. Ferguson, E. Ford, K. Furie, and C. Gillespie, "Executive summary: heart disease and stroke statistics—2010 update: a report from the american heart association," *Circulation*, vol. 121, no. 7, pp. 948–954, 2010.

[2] M. Nichols, N. Townsend, P. Scarborough, and M. Rayner, "Cardiovascular disease in europe 2014: epidemiological update," *Eur. heart j.*, vol. 35, no. 42, pp. 2950–2959, 2014.

[3] D. Wootton and D. Ku, "Fluid mechanics of vascular systems, diseases, and thrombosis," *Annu. rev. Biomed. Eng*, vol. 1, pp. 299–329, 1999.

[4] S. Morlacchi and F. Migliavacca, "Modeling stented coronary arteties: where we are, where to go," *Ann. Biomed. Eng.*, vol. 41, pp. 1428–1444, 2013.

[5] K. Kolandaivelu, R. Swaminathan, W. Gibson, V. Kolachalama, K. Nguyen-Ehrenreich, V. Giddings, L. Coleman, G. Wong, and E. Edelman, "Stent thrombogenicity early in high-risk interventional settings is driven by stent design and deployment and protected by polymer-drug coatings," *Circulation*, vol. 123, pp. 1400–1409, 2011.

[6] T. Ramanathan and H. Skinner, "Coronary blood flow," *BJA Education*, vol. 5, pp. 61–64, 2005.

[7] M. Kloc and R. Ghobrial, "Chronic allograft rejection: A significant hurdle to transplant success," *Burns Trauma*, vol. 2, pp. 3–10, 2014.

[8] X. He and D. Ku., "Pulsatile flow in the human left coronary artery bifurcation: average conditions," *J. Biomech. Eng.*, vol. 118, pp. 74–82, 1996.

[9] J. J. L. Disa, L. Oison, R. Molthen, D. Hettrick, P. Pratt, M. Hardel, J. Kersten, D. Warltier, and P. Pagel, "Alterations in wall shear stress predict sites of neointimal hyperplasia after stent implantation in rabbit iliac arteries," *Am. J. Physiol.*, vol. 288, pp. 74–82, 2005.

[10] C. Z. D. N. Ku, D.P. Giddens and S. Glagov, "Pulsatile flow and atherosclerosis in the human carotid bifurcation. positive correlation between plaque location and low oscillating shear stress," *Arterioscler.*, vol. 5, pp. 293–302, 1985.

[11] M. Joseph, E. Edelman, J. Squire, P. Seifert, M. Williams, and C. Rogers, "Stent and artery geometry determine intimal thickening independent of arterial injury," *Arterioscler.*, vol. 101, pp. 812–818, 2000.

[12] B. Timite and H. P. C. castelain, "Pulsatile viscous flow in a curved pipe: Effects of pulsation on the development of secondary flow," *Int. J. Heat Fluid Fl.*, vol. 31, pp. 879–896, 2010.

[13] M. Carpinlioglu and M. Gundogdu, "A critical review on pulsatile pipe flow studies directing towards future research topics," *Flow Measurement and Instrumentation*, vol. 12, pp. 163–174, 2001.

[14] M. Carpinlioglu, "An overview on pulsatile flow dynamics," *J. Therm. Eng.*, vol. 1, pp. 496–504, 2015.

[15] M. Carpinlioglu and E. Ozahi, "An updated portrait on transition to turbulence in laminar pipe flows with periodic time-dependence (a correlation study)," *J. Flow Turbul. Combust.*, vol. 89, pp. 691–711, 2012.

[16] O. San and A. E. Staples, "An improved model for reduced-order physiological fluid flows," *J. Mech. Med. Biol.*, vol. 6, pp. 1–37, 2012.

[17] N. Benard, D. Coisne, E. Donal, and R. Perrault, "Experimental study of laminar blood flow through an artery treated by a stent implantation: characterisation of intra-stent wall shear stress," *J. Biomech.*, vol. 36, pp. 991–998, 2003.

[18] A. Buradi and A. Mahalingam, "Impact of coronary tortuosity on the artery hemodynamics," *Biocybern. Biomed. Eng.*, vol. 40, pp. 126–147, 2020.

[19] H. Han, "Twisted blood vessels: symptoms, etiology and biomechanical mechanisms," *J. Vasc. Res.*, vol. 49, pp. 185–197, 2012.

[20] K. Dou, D. Zhang, B. Xu, Y. Yang, D. Yin, S. Qiao, Y. Wu, H. Yan, S. You, Y. Wang, Z. Wu, R. Gao, and A. J. Kirtane, "An angiographic tool for risk prediction of side branch occlusion in coronary bifurcation intervention," *J. Cadiovasc. Interv.*, vol. 8, pp. 39–46, 2015.

[21] O. Arjmandi-Tash, S. Razavi, and R. Zanbouri, "Possibility of atherosclerosis in an arterial bifurcation model," *Bioimpacts*, vol. 4, pp. 225–228, 2011.

[22] O. T. Arjmandi and E. Razavi, "Numerical investigation of pulsatile blood flow in a bifurcation model with a non-planar branch: the effect of different bifurcation angles and non-planar branch," *Bioimpacts*, vol. 4, pp. 195–205, 2012.

[23] E. Razavi, A. Omidi, and M. Z. Saghafi, "Numerical investigation of blood flow in a deformable coronary bifurcation and non-planar branch," *Bioimpacts*, vol. 4, pp. 199–204, 2014.

[24] J.Yang, Y. Eugene, and T. Lee, "Predicting bifurcation angle effect on blood flow in the microvasculature," *Microvasc. Res.*, vol. 108, pp. 22–28, 2016.

[25] D. Srinivasacharya and G. R. Madhava, "Mathematical model for blood flow through a bifurcated artery using couple stress fluid," *Math. Biosci.*, vol. 278, pp. 37–47, 2016.

[26] I. Shahzadi and N. Kousar, "Hybrid mediated blood flow investigation for atherosclerotic bifurcated lesions with slip, convective and compliant wall impacts," *Comput. Method Biomec.*, vol. 179, pp. 1–20, 2019.

[27] S. Pinto and J. Campos, "Numerical study of wall shear stress-based descriptors in the human left coronary artery," *Comput. Method Biomec.*, vol. 19, pp. 1443–1455, 2016.

[28] H. Barrett, K. der Heiden, E. Farrell, F. Gijsen, and A. Akyildiz, "Calcifications in atherosclerotic plaques and impact on plaque biomechanics," *J. Biomech Eng.*, vol. 87, pp. 1–12, 2019.

[29] V. Kumar, R. Cotran, and S. Robbins, *Basic pathology.* Elsevier Health Sciences, 1995.

[30] M. E. Joel and M. Anburajan, "3d modeling of stenotic internal carotid artery treated with stent: A cfd analysis of blood," in *International Conference on Computer, Networks and Communication Engineering (ICCNCE 2013)*. Atlantis Press, 2013/07, pp. 148–151. [Online]. Available: https://doi.org/10.2991/iccnce.2013.36

[31] F. Zhang, L. Dong, and J. Ge, "Simple versus complex stenting strategy for coronary artery bifurcation lesions in the drug-eluting stent era: a meta-analysis of randomised trials," *Heart*, vol. 95, no. 20, pp. 1676–1681, 2009.

[32] A. Medina, J. Lezo, and M. Pan, "A new classification of coronary bifurcation lesions," *Rev. Esp. Cardiol.*, vol. 59, p. 183, 2006.

[33] A. Malek and S. Alper, "Hemodynamic shear stress and its role in atherosclerosis," *J. Am. Med. Assoc.*, vol. 282, pp. 2035–2042, 1999.

[34] P. Davies, A. Remuzzi, E. Gordon, C. Dewey, and M. Gimbrone, "Turbulent fluid shear stress induces vascular endothelial cell turnover in vitro," *Proc. Natl. Acad. Sci. USA*, vol. 83, pp. 2114–2117, 1986.

[35] C. Dewey, S. BUssolari, M. G. M. A., and P. Davies, "The dynamic response of vascular endothelial cells to fluid shear stress," *J. Biomech. Eng.*, vol. 103, pp. 177–185, 1981.

[36] M. Levesque and R. Nerem, "The elongation and orientation of cultured endothelial cells in response to shear stress," *J. Biomech. Eng.*, vol. 107, pp. 341–347, 1985.

[37] S. Dhawan, R. A. Nanjundappa, J. Branch, W. Taylor, A. Quyyumi, H. Jo, M. McDaniel, J. Suo, D. Giddens, and H. Samady, "Shear stress and plaque development," *Expert Rev. Cardiovasc. Ther.*, vol. 8, pp. 545–56, 2010.

[38] C. Tan and R. Schatz, "The history of coronary stenting," *Interv. Cardiol. Clin.*, vol. 5, pp. 271–280, 2016.

[39] C. Rogers and E. Edelman, "Endovascular stent design dictates experimental restenosis and thrombosis," *Circulation*, vol. 91, pp. 2995–3001, 1995.

[40] R. Yin, D. Yang, and J. Wu, "Nanoparticle drug- and gene-eluting stents for the prevention and treatment of coronary restenosis," *Theranostics*, vol. 4, pp. 175–200, 2014.

[41] B. O'Connell, T. Mcgloughlin, and M. Walsh, "Factors that affect mass transport from drug eluting stents into the artery wall," *Biomed. Eng. Online*, vol. 9, pp. 9–15, 2010.

[42] J. Weiler, E. Sparrow, and R. Ramazani, "Mass transfer by advection and diffusion from a drug-eluting stent," *Int. J. Heat Mass Transf.*, vol. 55, pp. 1–7, 2012.

[43] D. Holmes, J. Hirshfeld, and D. Faxon, "Coronary artery stents," *J. Am. Coll. Cardiol.*, vol. 32, pp. 1471–1482, 1998.

[44] E. B. MD, "Chapter 3 - care of the patient with coronary stents undergoing noncardiac surgery," in *Essentials of Cardiac Anesthesia for Noncardiac Surgery*. New York: Content Repository Only!, 2019, pp. 33 – 69.

[45] V. Dehlaghi, M. Shadpoor, and S. Najarian, "Analysis of wall shear stress in stented coronary artery using 3d computational fluid dynamics modeling," *J. Mater. Process. Technol.*, vol. 197, pp. 174–181, 2008.

[46] A. Kastrati, J. Mehilli, J. Dirsschinger, K. Pachejulm, H. Schuhlen, and M. Seyforth, "Restenosis after coronary placement of various stent types," *Am. J. Cardiol.*, vol. 877, pp. 34–39, 2001.

[47] S. Beier, J. Ormiston, M. Webster, J. Cater, S. Norris, P. Medrano-Gracia, A. Young, and B. Cowan, "Hemodynamics in idealized stented coronary arteries: important stent design considerations," *Ann. Biomech. Eng.*, vol. 44, pp. 315–329, 2016.

[48] H. Hsiao, K. Lee, Y. Liao, and Y. Cheng, "Cardiovascular stent design and wall shear distribution in coronary stented arteries," *Micro. Nano. Letters*, vol. 5, pp. 430–433, 2012.

[49] H. Hsiao, K. Lee, Y. Liao, and Y. Cheng, "Hemodynamic simulation of intra-stent blood flow," *Procedia Eng.*, vol. 36, pp. 128–136, 2012.

[50] F. Chabi, S. Champmartin, C. Sarraf, and R. Noguera, "Critical evaluation of three hemodynamic models for the numerical simulation of intra-stent flows," *J. Biomech.*, vol. 48, pp. 1769–1776, 2015.

[51] A. Rouhi, U. Piomelli, and P.Vlachos, "Numerical investigation of pulsatile flow in endovascular stents," *Phys. Fluids*, vol. 25, p. 091905, 2013.

[52] Y. He, N. Duraiswamy, A. Frank, and J. Moore, "Blood flow in stented arteries: a parametric comparison of strut design patterns in three dimensions," *J. Biomech. Eng.*, vol. 127, pp. 637–647, 2005.

[53] R. Piccolo and T. Pilgrim, "The impact of thin-strut, biodegradable polymer stent designs," *Cardiac Interv. Today*, vol. 11, pp. 43–46, 2017.

[54] F. LaDisa, L. Olson, I. Guler, D. Hettrick, S. Audi, J. Kersten, D. Warltier, and P. Pagel, "Stent design properties and deployment ratio influence indexes of wall shear stress: a three-dimensional computational fluid dynamics investigation within a normal artery," *J. Appl. Physiol.*, vol. 97, pp. 424–430, 2004.

[55] H. Hsiao, Y. Chiu, K. Lee, and C. Lin, "Computational modeling of effects of intravascular stent design on key mechanical and hemodynamic behavior," *Comput. Aided Des.*, vol. 44, pp. 757–765, 2012.

[56] I. Hudrea, A. Totorean, and D. Gaita, "Computational fluid dynamics analysis of coronary stent malapposition," *World Congress on Medical Physics and Biomedical Engineering*, vol. 68, pp. 761–765, 2018.

[57] D. Lee and J. Chiu, "Intimal thickening under shear stress in a carotid bifurcation, a numerical study," *J. Biomech.*, vol. 29, pp. 1–11, 1996.

[58] R. Mongrain and J. Rodes-Cabau, "Role of shear stress in atherosclerosis and restenosis after coronary stent implantation," *Rev. Esp. Cardiol.*, vol. 59, pp. 350–356, 2006.

[59] R. Balossina, F. Gervaso, F. Migliavacca, and G. Dubini, "Effect of different stent designs on local hemodynamics in stented arteries," *J. Biomech.*, vol. 41, pp. 1053–1061, 2008.

[60] N. Duraiswamy, R. Schoephoerster, and J. Moore, "Comparison of near-wall hemodynamic parameters in stented artery models," *J. Biomech. Eng.*, vol. 131, p. 061006, 2009.

[61] J. Daemen and W. Patrick, "Drug-eluting stent update 2007: part i. a survey of current and future generation drug-eluting stents: meaningful advances or more of the same?" *Circulation*, vol. 116, pp. 316–328, 2007.

[62] M. Santin, P. Colombo, and G. Bruschi, "Interfacial biology of in-stent restenosis," *Expert Rev. Med. Devices.*, vol. 2, pp. 429–443, 2005.

[63] J. Sousa, P. Serruys, and M. Costa, "New frontiers in cardiology: drug-eluting stents: Part i," *Circulation*, vol. 107, pp. 2274–2279, 2003.

[64] R. Mueller and T. Sanborn, "The history of interventional cardiology: cardiac catheterization, angioplasty, and related interventions," *Am. Heart J.*, vol. 129, pp. 146–172, 1995.

[65] Y. Huang, H. Anthony, X. Wen, and V. Subbu, "Drug-eluting biostable and erodible stents," *J. Control Release*, vol. 193, pp. 188–201, 2014.

[66] Y. Wang, X. Lou, X. Xu, J. Zhu, and Y. Shang, "Drug-eluting balloons versus drug-eluting stents for the management of in-stent restenosis: A meta-analysis of randomized and observational studies," *J. Cardiol.*, vol. 70, pp. 446–453, 2017.

[67] G. Acharya and K. Park, "Mechanisms of controlled drug release from drug-eluting stents," *Adv. Drug Deliv. Rev.*, vol. 58, pp. 387–401, 2006.

[68] R. Byrne, P. serruys, A. Baumbach, J. Escaned, J. fajadet, S. James, M. Joner, S. Oktay, P. Juni, A. Kastrati, G. Stefanini, W. Wijins, and S. Windecker, "Report of a european society of cardiology-european association of percutaneous cardiovascular interventions task force on the evaluation of coronary stents in europe: executive summary," *Eur. Heart J.*, vol. 36, pp. 2608–2620, 2015.

[69] M. Farkouh, M. Domanski, L. Sleeper, F. Siami, G. Dangas *et al.*, "Strategies for multivessel revascularization in patients with diabetes," *N. Engl. J. Med.*, vol. 367, pp. 2375–2384, 2012.

[70] P. Serruys, M. Morice, A. Kappetein, A. Colombo, D. Holmes, M. Mack, E. Stahle, T. Feldman, M. V. Brand, E.J.Bass, N. V. Dyck, K. Leadley, K. Dawking, and F. Mohr, "Percutaneous coronary intervention versus coronary-artery bypass grafting for serve coronary artery disease," *N. Engl. J. Med.*, vol. 360, pp. 961–972, 2009.

[71] A. Abizaid and J. Coasta, "New drug-eluting stents an overview on biodegradable and polymer-free next generation stent systems," *Circ. Cardiovasc. Interv.*, vol. 3, pp. 384–393, 2010.

[72] J. Mikkonen, I. Uurto, T. Isotalo, A. Kotsar, T. Tammel, and M. Talja, "Drug-eluting bioabsorbable stents-an in vitro study," *Acta. Biomater.*, vol. 5, pp. 2894–2900, 2009.

[73] S. McGinty, T. Vo, M. Meere, S. McKee, and C. McCormick, "Some design considerations for polymer-free drug-eluting stents: a mathematical approach," *Acta. Biomater.*, vol. 18, pp. 213–225, 2015.

[74] S. Fredenberg, M. Wahlgren, M. Reslow, and A. Axelsson, "The mechanisms of drug release in poly (lactic-co-glycolic acid)-based drug delivery systems—a review," *Int. J.*, vol. 415, pp. 34–52, 2011.

[75] J. Wu, J. Way, L. Kritharides, and D. Brieger, "Polymer-free versus durable polymer drug-eluting stents in patients with coronary artery disease: A meta-analysis," *Ann. Med. Surg.*, vol. 38, pp. 13–21, 2018.

[76] X. Zhu, D. Pack, and R. Braatz, "Modelling intravascular delivery from drug-eluting stents with biodurable coating: investigation of anisotropic vascular drug diffusivity and arterial drug distribution," *Comput. Methods Biomech. Biomed. Engin.*, vol. 17, pp. 187–198, 2014.

[77] S. hossainy and S. Prabhu, "A mathematical model for predicting drug release from a bio-durable drug eluting stent coating," *J. Biomed. Mater. Res. A.*, vol. 87A, pp. 487–493, 2008.

[78] P. Vijayaratnam, T. Barber, and J. Reizes, "The localized hemodynamics of drug-eluting stents are not improved by the presence of magnetic struts," *ASME. J. Biomech. Eng.*, vol. 139, p. 014502, 2016.

[79] B. Balakrishnan, J. Dooley, G. Kopia, and E. Edelman, "Intravascular drug release kinetics dictate arterial drug deposition, retention, and distribution," *J. Control. Release*, vol. 123, pp. 100–108, 2007.

[80] C. McKittrick, S. McKee, S. Kennedy, K. Oldroyd, M. Wheel, G. Pontrelli, S. Dixon, S. McGinty, and C. McCormick, "Combining mathematical modelling with in vitro experiments to predict in vivo drug-eluting stent performance," *J. Control. Release*, vol. 303, pp. 151–161, 2019.

[81] S. Morlacchi, C. Chiastra, E. Cutri, P. Zunino, F. Burzotta, L. Formaggia, G. Dubini, and F. Migliavacca, "Stent deformation, physical stress, and drug elution obtained with provisional stenting, conventional culotte and tryton-based culotte to treat bifurcations: a virtual simulation study," *EuroIntervention: journal of EuroPCR in collaboration with the Working Group on Interventional Cardiology of the European Society of Cardiology*, vol. 9, pp. 1441–1453, 2014.

[82] R. Mongrain, I. Faik, R. Leask, J. Rodés-Cabau, E. Larose, and O. Bertrand, "Effects of diffusion coefficients and struts apposition using numerical simulations for drug eluting coronary stent," *J. Biomech. Eng.*, vol. 129, pp. 733–742, 2007.

[83] F. Chabi, "Etude numérique et expérimentale du transfèrt de masse, par advection et diffusion en écoulement pulsé, sur des stents actifs," *Thèse de doctorant*, 2016.

[84] A. Mandal and P. Mandal, "Computational modelling of three-phase stent-based delivery," *Journal of Exploratory Research in Pharmacology*, vol. 2, pp. 31–40, 2017.

[85] Y. Chen, Y. Xiong, W. Jiang, F. Yan, M. Guo, Q. Wang, and Y. Fan, "Numerical simulation on the effects of drug eluting stents at different reynolds numbers on hemodynamic and drug concentration distribution," *Biomed. Eng. Online*, vol. 14, pp. 1–16, 2015.

[86] Y. Chen, Y. Xiong, W. Jiang, M. Wong, F. Yan, Q. Wang, and Y. Fan, "Numerical simulation on the effects of drug-eluting stents with different bending angles on hemodynamics and drug distribution," *Med. Biol. Eng. Comput.*, vol. 54, pp. 1859–1870, 2016.

[87] V. Kolachalama, A. Tzafriri, D. Arifin, and E. Edelman, "Luminal flow patterns dictate arterial drug deposition in stent-based delivery," *J. Control. Release*, vol. 133, pp. 24–30, 2009.

[88] A. Mandal, Sarifuddin, and P. Mandal, "An unsteady analysis of arterial drug transport from half-embedded drug-eluting stent," *Applied Mathematics and Computation*, vol. 266, pp. 968–981, 2015.

[89] P. Vijayaratnam, J. Reizes, and T. Barber, "Flow-mediated drug transport from drug-eluting stents is negligible: numerical and in-vivo investigations," *Ann. Biomed. Eng.*, vol. 1, pp. 1–13, 2018.

[90] Balakrishnan, A. Tzafriri, P. Seifert, A. Groothuis, C. Rogers, and E. Edelman, "Strut position, blood flow, and drug deposition implications for single and overlapping drug-eluting stents," *Circulation*, vol. 111, pp. 2958–2965, 2005.

[91] Seo, L. Schachter, and A. Barakat, "Computational study of fluid mechanical disturbance induced by endovascular stents," *Ann. Biomed. Eng.*, vol. 33, pp. 444–456, 2005.

[92] Hara, M. Nakamura, J. Palmaz, and R. Schwartz, "Role of stent design and coating on restenosis and thrombosis," *Adv. Drug Deliv. Rev.*, vol. 58, pp. 377–386, 2006.

[93] Y. Chen, F. Yan, W. Jiang, Q. Wang, and Y. Fan, "Numerical study on effects of drug-coating position of drug-eluting stents on drug concentration," *Journal of Medical and Biological Engineering*, vol. 34, pp. 487–494, 2014.

[94] F. Bozsak, J. Chomaz, and A. Barakat, "Modeling the transport of drugs eluted from stents: physical phenomena driving drug distribution in the arterial wall," *Biomech. Model Mechanobiol.*, vol. 13, pp. 327–347, 2014.

[95] B. Franz, G. David, S. Zachary, B. Paul, B. Thomas, J. Chomaz, and A. Baraka, "Optimization of drug delivery by drug-eluting stents," *PLoS One*, vol. 6, p. e0130182, 2015.

[96] J. Ferreira, L. Gonçalves, J. Naghipoor, P. de Oliveira, and T. Rabczuk, "the effect of plaque eccentricity on blood hemodynamics and drug release in a stented artery," *Med. Eng. Phys.*, vol. 60, pp. 47–60, 2018.

[97] G. Vairo, M. Cioffi, R. Cottone, G. Dubini, and F. Migliavacca, "Drug release from coronary eluting stents: A multidomain approach," *J. Biomech.*, vol. 43, pp. 1580–1589, 2010.

[98] M. Zarandi, R. Mongrain, and O. Bertrand, "Modeling drug eluting stents for coronary artery bifurcation considering non-newtonian effects," *3rd Joint US-European Fluids Engineering Summer Meeting*, vol. 1, pp. 1895–1899, 2010.

[99] A. Mandal and P. Mandal, "Distribution and retention of drug through an idealized atherosclerotic plaque eluted from a half-embedded stent," *Int. J. Dynam. Control*, vol. 6, pp. 1183–1193, 2018.

[100] T. Seo, A. Lafont, S. Choi, and A. Barakat, "Drug-eluting stent design is a determinant of drug concentration at the endothelial cell surface," *Annals of Biomedical Engineerin*, vol. 44, pp. 302–314, 2016.

[101] P. Vijayaratnam, C. O'Brien, J. Reizes, T. Barber, and E. Edelman, "The impact of blood rheology on drug transport in stented arteries: Steady simulations," *PLoS One*, vol. 10, p. e0128178, 2015.

[102] P. Douglas, J. Fiolkoski, B. Berko, and N. Reinchek, "Echocardiographic visualization of coronary artery anatomy in the adult," *J. Am. Coll. Cardiol.*, vol. 11, pp. 565–571, 1988.

[103] J. Dodge, B. Brown, E. Bolson, and H. Dodge, "Lumen diameter of normal human coronary arteries. influence of age, sex, anatomic variation, and left ventricular hypertrophy or dilation," *Circulation*, vol. 86, pp. 232–246, 1992.

[104] S. Kelle, A. Hays, G. Hirsch, G. Gerstenblith, J. Miller, A. Steinberg, M. Schär, J. Texter, E. Wellnhofer, R. Weiss, and M. Stuber, "Coronary artery distensibility assessed by 3.0 tesla coronary magnetic resonance imaging in subjects with and without coronary artery disease," *Am J Cardiol*, vol. 108, pp. 491–497, 2011.

[105] I. Ozolanta, G. Tetere, B. Purinya, and V. Kasyanov, "Changes in the mechanical properties, biochemical contents and wall structure of the human coronary arteries with age and sex," *Med Eng Phys*, vol. 20, no. 7, pp. 523 – 533, 1998.

[106] P. Siogkas, A. Sakellarios, T. Exaechos, and O. Parodi, "Blood flow in arterial segments: rigid vs. deformable walls simulationsn," *J. Serb. Soc. Comput. Mech.*, vol. 5, pp. 69–77, 2011.

[107] H. Oh, *Advanced fluid dynamics*. InTech, 2012.

[108] S. Pope, *Turbulent Flows*. Cambridge University Press, 1990.

[109] J. Soulis, O. Lampri, D. Fytanidis, and G. D. Giannoglou, "Relative residence time and oscillatory shear index of non-newtonian flow models in aorta," *10th International Workshop on Biomedical Engineering*, pp. 1–4, 2011.

[110] N. S. Akbar, "Heat and mass transfer effects on carreau fluid model for blood flow through a tapered artery with a stenosis," *Int. J. Biomath.*, vol. 7, p. 1450004, 2014.

[111] N. Casson, "Rheology of disperse systems," *Pergamon Press, London*, p. 84, 1959.

[112] S. Shibeshi and W. Collins, "The rheology of blood flow in a branched arterial system," *Appl. Rheol.*, vol. 6, pp. 398–405, 2005.

[113] R. Vinoth, D. Kumar, A. Raviraj, and S. Vijay, "Non-newtonian and newtonian blood flow in human aorta: A transient analysis," *Biomed. Res. J.*, vol. 7, pp. 3194–3203, 2017.

[114] E. Merrill, E. Gilliland, G. Cokelet, H. Shin, A. Britten, and R. Wells Jr, "Rheology of blood and flow in the microcirculation," *J. appl. physiol.*, vol. 18, no. 2, pp. 255–260, 1963.

[115] D. McDonald, "The relation of pulsatile pressure to flow in arteries," *J. Physiol.*, vol. 127, no. 3, pp. 533–552, 1955.

[116] S. Sutera and R. Skalak, "The history of poiseuille's law," *Annu. Rev. fluid mech.*, vol. 25, pp. 1–19, 1998.

[117] J. Pfitzner, "Poiseuille and his law," *Anaesthesia*, vol. 31, no. 2, pp. 273–275, 1976.

[118] A. Semple and A. Lenardic, "Plug flow in the earth's asthenosphere," *Earth Planet. Sci. Lett.*, vol. 496, pp. 29–36, 2018.

[119] C. O'Brien, V. Kolachalama, T. Barber, A. Simmons, and E. Edelman, "Impact of flow pulsatility on arterial drug distribution in stent-based therapy," *J. Control. Release*, vol. 168, pp. 115–124, 2013.

[120] J. Womersley, "Method for the calculation of velocity, rate of flow and viscous drag in arteries when the pressure gradient is known," *J. Physiol.*, vol. 127, pp. 553–563, 1955.

[121] G. Heusch, "Heart rate in the pathophysiology of coronary blood flow and myocardial ischaemia: benefit from selective bradycardic agents," *Br. J. Pharmacol.*, vol. 153, pp. 1589–1601, 2008.

[122] H. Kim, I. Vignon-Clementel, C. Figueroa, K. Jansen, and C. Taylor, "Developing computational methods for three-dimensional finite element simulations of coronary blood flow," *Finite Elem. Anal. Des.*, vol. 46, pp. 514–525, 2010.

[123] S. Kyriacou, J. Humphrey, and C. Schwab, "Finite element analysis of non-linear orthotropic hyperelastic membranes," *Comput. Mech.*, vol. 18, pp. 269–278, 1996.

[124] P. Khamdaengyodtai, K. Vafai, P. Sakulchangsatjatai, and P. Terdtoon, "Effects of pressure on arterial failure," *J. Biomech.*, vol. 45, pp. 2577–2588, 2012.

[125] K. Mekheimer and M. Kot, "Suspension model for blood flow through catheterized curved artery with time-variant overlapping stenosis," *Eng. Sci. Technol. Int. J.*, vol. 18, pp. 452–462, 2015.

[126] R. Jahromi, H. Pakravan, M. Saidi, and B. Firoozabadi, "Primary stenosis progression versus secondary stenosis formation in the left coronary bifurcation: A mechanical point of view," *Biocybern. Biomed. Eng.*, vol. 39, pp. 188–198, 2019.

[127] M. Nagargoje and R. Gupta, "Effect of asymmetry on the flow behavior in an idealized arterial bifurcation," *Comput. Methods in Biomec.*, vol. 23, pp. 232–247, 2020.

[128] J. Frattolin, M. Zarandi, C. Pagiatakis, O. Bertrand, and R. Mongrain, "Numerical study of stenotic side branch hemodynamics in true bifurcation lesions," *Comput. Biol. Med.*, vol. 57, pp. 130–138, 2015.

[129] M. Sadeghi, E. Shirani, M. Tafazzoli-Shadpour, and M. Samaee, "The effects of stenosis severity on the hemodynamic parameters—assessment of the correlation between stress phase angle and wall shear stress," *J. Biomech.*, vol. 44, pp. 2614–2626, 2011.

[130] L. DiCarlo, W. Holdsworth, and L. Poepping, "Study of the effect of stenosis severity and non-newtonian viscosity on multidirectional wall shear stress and flow disturbances in the carotid artery using particle image velocimetry," *Med. Eng. Phys.*, vol. 65, pp. 8–23, 2019.

[131] A. Martínez, S. Choi, O. Tammisola, and D. McNally, "On the axial distribution of plaque stress: Influence of stenosis severity, lipid core stiffness, lipid core length and fibrous cap stiffness," *Med. Eng. Phys.*, vol. 68, pp. 76–84, 2019.

[132] T. Sood, S. Roy, and M. Pathak, "Effect of pulse rate variation on blood flow through axisymmetric and asymmetric stenotic artery models," *Math. Biosci.*, vol. 298, pp. 1–18, 2018.

[133] M. Zarandi and R. Mongrain, "Modeling drug eluting stent for coronary artery bifurcaitons considering non-newtonian effects," *ASME 2010 3rd Joint US-European Fluids Engineering Summer Meeting*, vol. 1, pp. 1895–1899, 2010.

[134] F. Zhou, Y. Liu, P. Ge, Z. Chen, X. Ding, J. Liu, Q. Jia, F. An, L. Li, L. Wang, W. Ma, Z. Yang, and E. Jia, "Coronary artery diameter is inversely associated with the severity of coronary lesions in patients undergoing coronary angiography," *Cell Physiol. Biochem.*, vol. 43, pp. 1247–1257, 2017.

[135] L. Gundelwein, J. Miro, F. G. Barlatay, C. Lapierre, K. Rohr, and L. Duoong, "Personalized stent design for congenital heart defects using pulsatile blood flow simulations," *J. Biomech.*, vol. 81, pp. 68–75, 2018.

[136] M. Bukac, S. Canic, J. Tambaca, and Y. Wang, "Fluid-structure interaction between pulsatile blood flow and a curved stented coronary artery on a beating heart: A four stent computational study," *Comput. Method Appl. M.*, vol. 350, pp. 679–700, 2019.

[137] K. Foong, M. Zarringhalam, D. Toghraie, N. Izadpanahi, S. Yan, and S. Rostami, "Numerical study for blood rheology inside an artery: The effects of stenosis and adius on the flow behavior," *Comput. Meth. Prog. Bio.*, vol. 193, pp. 1054–1057, 2020.

[138] S. Yan, M. Zarringhalam, D. Toghraie, K. Foong, and P. Talebizadehsardari, "Numerical investigation of non-newtonian blood flow within an artery with cone shape of stenosis in various stenosis angles," *Comput. Meth. Prog. Bio.*, vol. 193, pp. 1034–1054, 2020.

[139] H. Gharahi, B. Zambrano, D. Zhu, J. DeMarco, and P. S. Baek, "Computational fluid dynamic simulation of human carotid artery bifurcation based on anatomy and blood flow velocity measured with magnetic resonance imaging-manuscript draft," *Int. J. Adv. Eng. Sci. Appl. Math. Comput.*, vol. 8, pp. 1–9, 2016.

[140] K. Kolli, I. Arif, S. Peelukhana, P. Succop, L. Back, T. Helmy, M. Leesar, M. Effat, and R. Banerjee, "Diagnostic performance of pressure drop coefficient in relation to fractional flow reserve and coronary flow reserve," *J. Invasive. Cardiol.*, vol. 26, pp. 2–9, 2014.

[141] S. Peelukhana, R. Banerjee, T. van de Hoef, K. Kolli, M. Effat, T. Helmy, M. Leesar, H. Kerr, J. Piek, and P. S. P, "Evaluation of lesion flow coefficient for the detection of coronary artery disease in patient groups from two academic medical canters," *Cardiovasc. Revasc. Med.*, vol. 19, pp. 348–354, 2018.

[142] M. Khosravani-Rudpishi, A. Joharimoghadam, and E. Rayzan, "The significant coronary tortuosity and atherosclerotic coronary artery disease; what is the relation?" *J. Cardiovasc. Thorac. Res.*, vol. 10, pp. 209–221, 2018.

[143] C. Zhang, S. Xie, S. Li, F. Pu, X. Deng, Y. Fan, and D. Li, "Flow patterns and wall shear stress distribution in human internal carotid arteries: the geometric effect on the risk for stenoses," *J. Biomech.*, vol. 45, pp. 83–9, 2012.

[144] A. Qiao, X. Guo, S. Wu, Y. Zeng, and X. Xu, "Numerical study of nonlinear pulsatile flow in s-shaped curved arteries," *Med. Eng. Phys.*, vol. 26, pp. 545–52, 2004.

[145] X. Xie, Y. Wang, H. Zhu, and J. Zhou, "Computation of hemodynamics in tortuous left coronary artery: a morphological parametric study," *J. Biomech. Eng.*, vol. 136, p. 101006, 2014.

[146] M. Jarrahi, C. Castelain, and H. Peerhossaini, "Laminar sinusoidal and pulsatile flows in a curved pipe," *J. Appl. Fluid Mech.*, vol. 4, pp. 21–26, 2011.

[147] M. Najjari and M. Plesniak, "Evolution of vortical structures in a curved artery model with non-newtonian blood-analog fluid under pulsatile inflow conditions," *Exp. Fluids*, vol. 57, pp. 1–28, 2016.

[148] J. Siggers and S. Waters, "Steady flows in pipes with finite curvature," *Phys. Fluids*, vol. 17, pp. 1–18, 2005.

[149] N. Shahcheraghi, H. Dwyer, A. Cheer, A. Barakat, and T. Rutaganira, "Unsteady and three-dimensional simulation of blood flow in the human aortic arch," *J. Biomech. Eng.*, vol. 124, p. 378, 2002.

[150] R. Dash, G. Jayaraman, and K. Mehta, "Flow in a catheterized curved artery with stenosis," *J. Biomech.*, vol. 32, pp. 49–61, 1999.

[151] L. Wang, F. Zhao, D. Wang, S. Hu, J. Liu, Z. Zhou, J. Lu, P. Qi, and S. Song, "Pressure drop in tortuosity/kinking of the internal carotid artery: Simulation and clinical investigation," *BioMed. Research International*, vol. 32, pp. 1–8, 2016.

[152] A. Santamarina, E. Weydahl, J. Siegel, and J. Moore, "Computational analysis of flow in a curved tube model of the coronary arteries: effects of time-varying curvature," *Ann. Biomed. Eng.*, vol. 26, pp. 944–954, 1998.

[153] X. Xie, Y. Wang, and H. Zhou, "Impact of coronary tortuosity on the coronary blood flow: a 3d computational study," *J. Biomech.*, vol. 46, pp. 1833–1841, 2013.

[154] Y. Li, Z. Shi, Y. Cai, Y. Feng, and G. Ma, "Impact of coronary tortuosity on coronary pressure: Numerical simulation study," *PLoS ONE*, vol. 7, p. e42558, 2012.

[155] G. Liu, J. Wu, W. Huang, W. Wu, H. Zhang, K. Wong, and D. Ghista, "Numerical simulation of flow in curved coronary arter-ies with progressive amounts of stenosis using fluid-structure interaction modelling," *J. Med. Imaging Health Inform.*, vol. 4, pp. 605–11, 2014.

[156] B. Liu, "The influences of stenosis on the downstream flow pattern in curved arteries," *Med. Eng. Phys.*, vol. 29, pp. 868–876, 2007.

[157] M. Biglarian, M. Larimi, H. Afrouzi, A. Moshfegh, D. Toghraie, A. Javadzadegan, and S. Rostami, "Computational investigation of stenosis in curvature of coronary artery within both dynamic and static models," *Comput. Methods Programs Biomed.*, vol. 185, p. 105170, 2020.

[158] Y. Li, Y. Feng, G. Ma, C. Shen, and N. Liu, "Coronary tortuosity is negatively correlated with coronary atherosclerosis," *J. Int. Med. Res.*, vol. 46, pp. 5205–5209, 2018.

[159] R. Mazzitelli, F. Boyle, E. Murphy, A. Renzulli, and G. Fragomeni, "Numerical prediction of the effect of aortic left ventricular assist device outflow-graft anastomosis location," *Biocybern. Biomed. Eng.*, vol. 36, pp. 327–343, 2016.

[160] F. Zhan, Y.Fan, and X. Deng, "Effect of swirling flow on platelet concentration distribution in small-caliber artificial grafts and end-to-end anastomoses," *Acta. Mech. Sin.*, vol. 27, pp. 833–839, 2011.

[161] A. Sun, Y. Fan, and X. Deng, "Intentionally induced swirling flow may improve the hemodynamic performance of coronary bifurcation stenting," *Catheter. Cardiovasc. Interv.*, vol. 79, pp. 371–377, 2012.

[162] D. Wootton and D. Ku, "Fluid mechanics of vascular systems, diseases, and thrombosis," *Annu. Rev. Biomed. Eng.*, vol. 01, pp. 299–329, 1999.

[163] A. Amirjani, M. Yousefi, and M. Cheshmaroo, "Parametrical optimization of stent design: a numerical-based approach," *Comput. Meter. Sci.*, vol. 90, pp. 210–220, 2014.

[164] M. Simao, J. Ferreira, J. Mora-Rodriguez, J. Fragata, and H. Ramos, "Behaviour of two typical stents towards a new stent evolution," *Med. Biol. Eng. Comput.*, vol. 55, pp. 1019–1037, 2017.

[165] E. Finol and C. Amon, "Blood flow in abdominal aortic aneurysms: pulsatile flow hemodynamics," *J. Biomech. Eng.*, vol. 123, pp. 474–484, 2001.

[166] X. Zhu and R. Braatz, "A mechanistic model for drug release in plga biodegradable stent coatings coupled with polymer degradation and erosion," *J. Biomed. Mater. Res.*, vol. 7, pp. 2269–2279, 2015.

[167] S. McGinty and G. Pontrelli, "A general model of coupled drug release and tissue absorption for drug delivery devices," *J. Control. Release*, vol. 217, pp. 327–336, 2015.

[168] S. McGinty, S. McKee, R. Wadsworth, and C. McCormick, "Modeling arterial wall drug concentrations following the insertion of a drug-eluting stent," *SIAM J. Appl. Math.*, vol. 73, no. 6, pp. 2004–2028, 2013.

[169] J. Abraham, J. Gorman, E. Sparrow, J. Stark, and R. Kohler, "A mass transfer model of temporal drug deposition in artery walls," *Int. J. Heat Mass Trans.*, vol. 58, no. 2, pp. 632–638, 2013.

[170] S. McGinty, S. Mckee, R. Wadsworth, and C. McCormick, "Modelling drug-eluting stents," *Math. Med. Biol.*, vol. 28, pp. 1–29, 2011.

[171] A. Tzafriri, A. Levin, and E. Edelman, "Diffusion-limited binding explains binary dose response for local arterial and tumour drug delivery," *Cell Prolif.*, vol. 3, pp. 348–363, 2009.

[172] A. Levin, N. Vukmirovic, C. Hwang, and E. Edelman, "Specific binding to intracellular proteins determines arterial transport properties for rapamycin and paclitaxel," *Proceedings of the National Academy of Sciences of the United States of America*, vol. 101, pp. 9463–9467, 2004.

[173] J. Naghipoor, J. Ferreira, P. de Oliveira, and T. Rabczuk, "Tuning polymeric and drug properties in a drug eluting stent: A numerical study," *Applied Mathematical Modelling*, vol. 40, pp. 8067–8086, 2016.

[174] J. Abraham, J. Gorman, E. Sparrow, J. Stark, and R. Kohler., "A mass transfer model of temporal drug deposition in artery walls," *Int. J. Heat Mass Transf.*, vol. 58, pp. 632–638, 2013.

[175] N. Abbasnezhad, N. Zirak, M. Shirinbayan, S. Kouidri, E. Salahinejad, A. Tcharkhtchi, and F. Bakir, "Controlled release from polyurethane films: Drug release mechanisms," *J. Appl. Polym. Sci*, 2020.

[176] S. Fouad, E. Basalious, M. El-Nabarawi, and S. Tayel, "Microemulsion and poloxamer microemulsion-based gel for sustained transdermal delivery of diclofenac epolamine using in-skin drug depot: in vitro/in vivo evaluation," *Int. J. Pharm.*, vol. 453, pp. 569–578, 2013.

[177] A. Borghi, E. Foa, R. Balossino, F. Migliavacca, and G. Dubini, "Modelling drug elution from stents: effects of reversible binding in the vascular wall and degradable polymeric matrix," *Comput. Methods Biomech. Biomed. Eng.*, vol. 11, pp. 367–377, 2008.

[178] X. Huang and C. Brazel, "On the importance and mechanisms of burst release in matrix-controlled drug delivery systems," *J. Control. Release*, vol. 73, pp. 121–136, 2001.

[179] C. Ferrero, D. Massuelle, and E. Doelker, "Towards elucidation of the drug release mechanism from compressed hydrophilic matrices made of cellulose ethers. ii. evaluation of a possible swelling controlled drug release mechanism using dimensionless analysis," *J. Control. Release*, vol. 141, pp. 223–233, 2020.

[180] K. Park, W. Shalaby, and H. Park, "Biodegradable hydrogels for drug delivery," *PA: Technomic publishing company*, vol. 141, p. 191, 1993.

[181] N. Abbasnezhad, M. Shirinbayan, A. Tcharkhtchi, and F. Bakir, "In vitro study of drug release from various loaded polyurethane samples and subjected to different non-pulsed flow rates," *Journal of Drug Delivery Science and Technology*, vol. 55, p. 101500, 2020.

Publications

Jianfei SONG, Smaine KOUIDRI, Farid BAKIR. Numerical study of hemodynamic and diagnostic parameters affected by stenosis in bifurcated artery, Computer Methods in Biomechanics and Biomedical Engineering, doi: 10.1080/10255842.2020.1771557. 23: 894-905, 2020.

Jianfei SONG, Smaine KOUIDRI, Farid BAKIR. Numerical study on flow topology and hemodynamics in tortuous coronary artery with symmetrical and asymmetrical stenosis, Biocybernetics and Biomedical Engineering, 41: 142-155, 2021.

Resumé de la thèse en français

Introduction

Les maladies cardiovasculaires ont occupé 1/3 des décès dans les pays en développement et développés. L'athérosclérose est l'une des formes les plus graves et les plus courantes de maladies cardiovasculaires causées par l'accumulation de dépôts graisseux, de cholestérol et de matières calcifiées dans la paroi artérielle, en particulier dans l'artère coronaire. Sur la base des statistiques cliniques, l'artère coronaire est plus susceptible de former une sténose que la plupart des autres artères. Tout trouble ou maladie de l'artère coronaire peut en provoquer un dans un état dangereux avec une crise cardiaque ou un accident vasculaire cérébral. En raison de l'athérosclérose, l'artère rétrécie se développe, ce qui entraîne une réduction de l'apport sanguin au cœur (ischémie myocardique), un manque d'oxygène (hypoxie) ou des lésions cellulaires (nécrose). Face à cette énorme menace pour nos vies, plusieurs traitements efficaces ont été développés et utilisés dans la pratique grâce à d'énormes efforts de chercheurs tels que l'angioplastie par ballonnet, le stent en métal nu (BMS) et le stent à élution médicamenteuse (DES). Cependant, les complications de suivi nécessitent encore les optimisations des traitements actuels. L'angioplastie par ballonnet a été développée comme la première procédure non chirurgicale pour agrandir les artères obstruées généralement suivie de la resténose en réponse à la lésion de la paroi vasculaire causée par l'expansion du ballon. BMS a amélioré les résultats cliniques en réduisant le taux de resténose, mais toujours de plus de 20% en plaçant un treillis métallique gonflé sur le site de blocage. Pour tenter de réduire davantage ce taux, le DES a été proposé avec le BMS recouvert de médicaments anti-prolifératifs. L'incidence de la resténose intra-stent a été réduite à moins de 5% grâce à l'inhibition de la prolifération intima. Cependant, la thrombose tardive suivie peut provoquer une occlusion soudaine d'une artère. Ainsi, face aux deux causes majeures (resténose et thrombose) de l'échec du stent, une compréhension approfondie de la pathologie et des mécanismes de survenue de la maladie est hautement nécessaire actuellement.

Le sang en tant que type de biofluide possède des propriétés physiques et hémodynamiques assez complexes, en particulier dans l'artère avec des diamètres, des courbures et même des bifurcations irréguliers. La sténose et le stent sont tous deux considérés comme les singularités géométriques de l'artère entraînant la perturbation du flux. On constate qu'un faible taux de cisaillement favorise la prolifération des cellules musculaires dans la paroi artérielle, en particulier dans les régions de recirculation en amont et en aval de la jambe de force. Les variations des paramètres hémodynamiques ont été couramment ciblées et utilisées pour prédire les sites potentiels de la maladie dans les études existantes. De plus, les altérations de l'hémodynamique sont fortement liées aux singularités géométriques artérielles telles que la présence de stent. Outre les facteurs humains, la performance du stent est fortement liée aux voies d'implantation prises par le cardiologue, aux conceptions géométriques du stent et même au principe pharmaceutique dans le cas du DES.

Sur la base de l'état actuel des connaissances liées à ce sujet, de grands efforts sont encore nécessaires pour maîtriser les mécanismes internes et améliorer les performances du stent car un certain nombre de questions restent ouvertes et doivent être résolues. Ainsi, la présente étude est proposée dans le but de reconnaître l'hémodynamique du corps humain et d'éviter les altérations causées par l'envoi. Le stent actif a également été concerné. Un intérêt particulier a été accordé au transfert de masse du polymère dans la lumière et le tissu. Les travaux de recherche réalisés au cours de cette thèse ont été présentés comme suit:

- Mise en place de la modélisation numérique et mathématique suivie de l'étude préliminaire des effets sur la topologie des écoulements et les viriations hémodynamiques induites par les singularités géométriques artérielles. La bifurcation artérielle et la tortuosité sont toutes deux prises en compte. Les sites potentiels et l'orientation du développement de la sténose affectés par la singularité géométrique artérielle spécifique ont été évalués sur la base de la topologie du flux et de l'analyse hémodynamique. De plus, afin d'avoir une orientation directe vers le traitement clinique à partir de travaux numériques, l'analyse diagnostique a été adoptée pour donner des évaluations auxquelles on n'a pas encore accordé suffisamment d'attention.

- Plusieurs facteurs de conception du stent ont été considérés dans le but d'optimiser la géométrie du stent sur la base de la perturbation de l'écoulement et des évaluations hémodynamiques.

- Les mécanismes de libération des médicaments ont été étudiés numériquement et expérimentalement.

Étude bibliographique

Recherche sur le développement d'un stent en métal nu

BMS est la première génération de stent et aussi le début d'un traitement efficace pour l'athérosclérose. Cependant, environ 20% à 30% des patients nécessitent une intervention supplémentaire après l'implantation d'un stent [44]. La performance du stent dépend de plusieurs facteurs: la conception du stent, l'hémodynamique du sang, les procédures d'implantation, les lésions vasculaires et l'inflammation chronique [45]. Parmi la littérature, l'optimisation des conceptions de stents a fait l'objet d'une grande attention de la part des chercheurs afin d'améliorer les performances d'implantation [46].

La dynamique des fluides computationnelle (CFD) en tant qu'outil de recherche peut aider à mieux comprendre le flux sanguin et à améliorer l'optimisation du stent. La conception du stent s'est tout d'abord avérée être liée à des résultats cliniques défavorables dans les artères iliaques de lapin endoprothésées en 2000, et la variation de contrainte de cisaillement du mur (WSS) est fortement associée à l'hyperplasie néointimale. Les principales considérations relatives aux caractéristiques géométriques du stent sont résumées à la figure B.1 [47]. Ces deux types de stents conçus sont comparés à travers différentes caractéristiques géométriques: cellule de stent, espacement moyen des cellules, creux et pic de la jambe de force, angle de la jambe de force et s'il s'agit d'un décalage de cellule ou d'un alignement de cellule. Il est démontré que les variations hémodynamiques défavorables de caractéristiques de conception spécifiques (telles qu'un espace de jambe de force étroit et une grande taille de jambe de force) peuvent être atténuées tout en combinant les autres caractéristiques de conception avantageuses. De plus, une protrusion plus lumineuse du stent peut aggraver considérablement les conditions hémodynamiques.
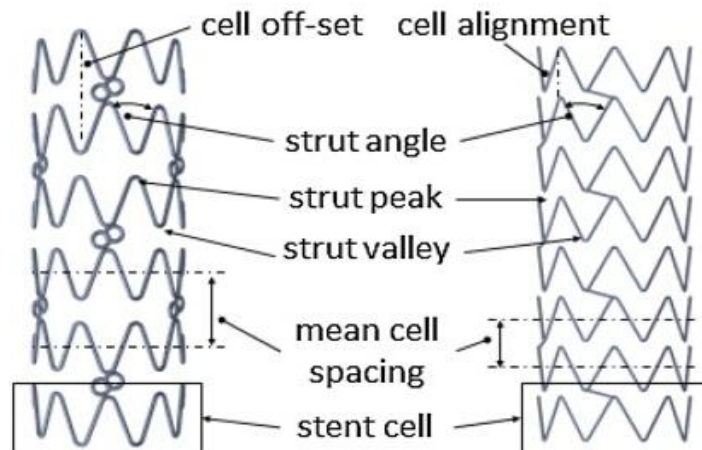
Figure B.1: Géométries avec étiquettes de conception de stent [47]

Les propriétés rhéologiques et les distributions hémodynamiques sont les principaux axes de résultats parmi les enquêtes. Les oeuvres de N. Benard [17], H.M. Hsiao [48, 49], F. Chabi [50] and A. Rouhi [51] ont prouvé l'écoulement perturbé causé par la présence de stents. Un espacement plus grand entre les entretoises s'est avéré bénéfique pour restaurer l'écoulement perturbé. À travers les œuvres de V. Dehlaghi et al. [45], au lieu de l'espacement des entretoises, il s'est concentré sur l'effet du rapport entre l'espacement des entretoises et la hauteur des entretoises sur l'hémodynamique. Les rapports de 2, 3, 4,

6 ont été étudiés et ont découvert que lorsque le rapport est inférieur à 3, le flux secondaire est plein de tout l'espace des entretoises. Lorsque le rapport est supérieur à 6, le point de rattachement peut être obtenu avec deux tourbillons séparés. Selon les travaux de [52], Lorsque les entretoises suivent davantage la direction du flux sanguin, la zone de recirculation du flux a tendance à être réduite. Un angle de jambe plus petit signifie que l'orientation de la jambe de force est plus cohérente avec la direction d'écoulement. Une déformation réduite entre l'orientation de la jambe de force et la direction de l'écoulement peut induire moins de turbulence d'écoulement, ce qui inhibe le développement de la recirculation. De plus, l'épaisseur des entretoises a fait l'objet de nombreuses études numériques et cliniques. La conclusion commune a démontré qu'une jambe de force plus épaisse est plus susceptible de générer des résultats indésirables [53–55]. Une jambe de force plus mince causera moins d'effet d'obstacle et limitera la taille de recirculation. I.C. Hudrea et al. [56] a étudié la formation de recirculations avec des entretoises de malapposition comme le montre la figure B.2. Les lignes de courant sont plus perturbées avec une augmentation limitée de la saillie du stent dans la lumière. Ensuite, lorsque le stent est plus proche du flux central, la perturbation du flux est plus soulagée.
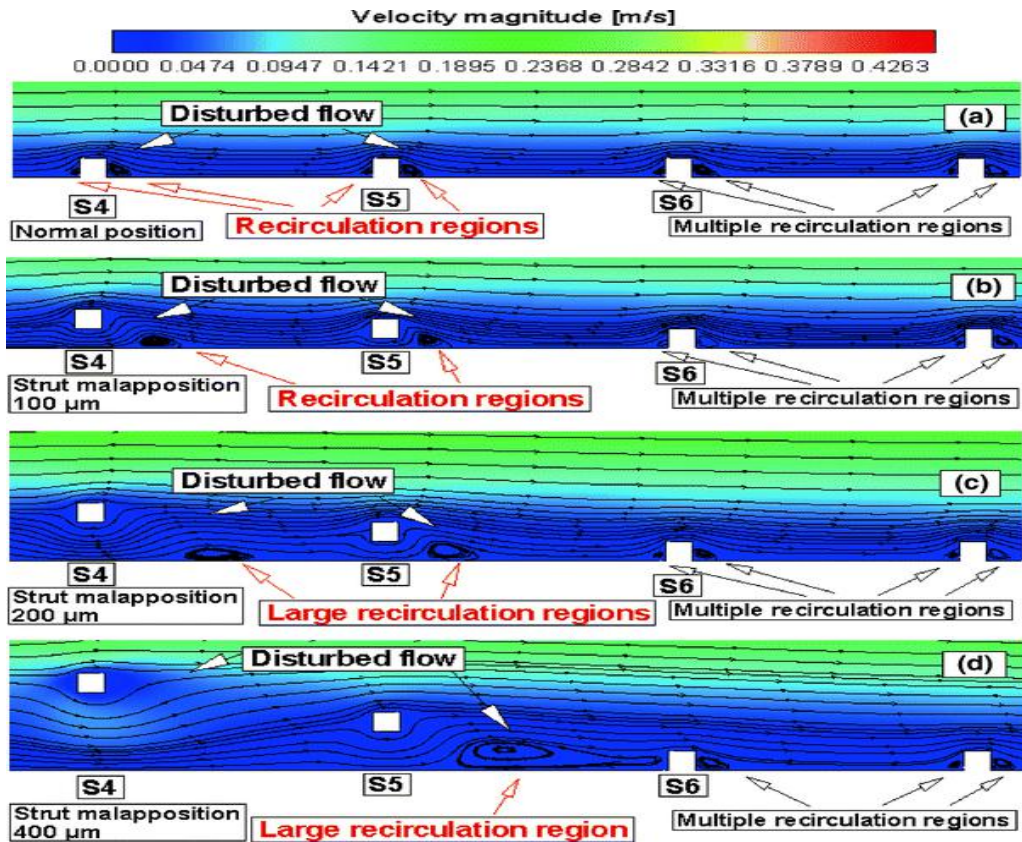
Figure B.2: Rationalise avec les stents de malapposition [56]

Une faible contrainte de cisaillement, un temps de séjour des particules élevé et un écoulement non laminaire sont des attributs hémodynamiques courants aux endroits où l'hyperplasie néointimale est susceptible de se produire [57, 58]. Par conséquent, de nombreuses recherches ont été menées dans le but d'optimiser la conception du stent sur la base de l'évaluation des variations des paramètres hémo- dynamiques. Même si une partie des recherches a vérifié la distribution hémodynamique symétrique en modèle 3D avec un stent circulaire simplifié, une modélisation 3D plus complète est encore nécessaire pour avoir une vue globale de la distribution hémodynamique, notamment en tenant compte de la com-

plexité géométrique pratique de l'artère et du stent. R. Balossino et al. [59] ont utilisé des modèles 3D pour analyser la distribution spatiale et temporelle du WSS artériel sous des formes de stent différemment conçues et différentes épaisseurs de jambe de force. On a observé que la région de faible valeur de WSS en dessous de 0,5 Pa était augmentée avec une jambe de force plus épaisse. Une conclusion similaire a été obtenue dans les travaux de N. Duraiswamy et al. [60]. Quatre stents de conceptions différentes ont été étudiés et la distribution WSS près de la paroi a été étudiée comme le montre la figure B.3. On trouve toujours que la faible valeur de WSS suit la région proche du stent.
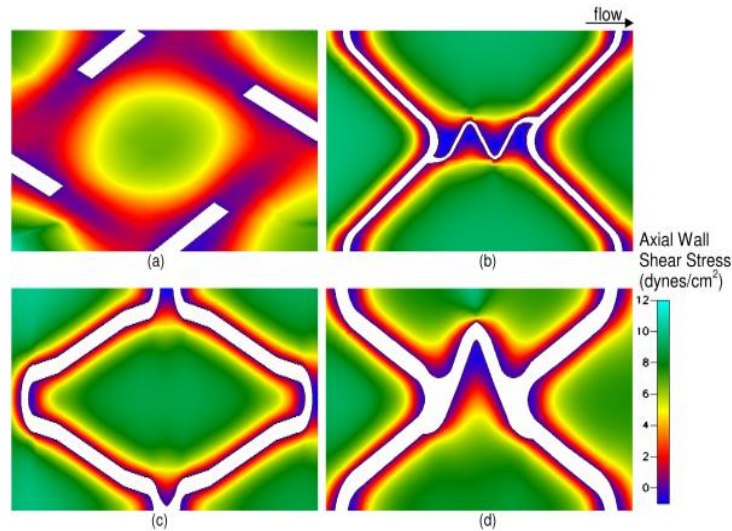
Figure B.3: Distribution WSS pour (a) Wallstent, (b) Bx Velocity stent, (c) Aurora stent et (d) NIR stent [60]

Recherche sur le développement d'un stent à élution médicamenteuse

Le DES a apporté des avantages significatifs en empêchant le développement de la resténose artérielle après l'implantation d'un stent par rapport au BMS [61–63]. Le premier BMS appelé Palmaz-Schatz a été approuvé avec autorité en 1994 face à la menace de maladies cardiovasculaires [64]. Cependant, la resténose en tant que complication ultérieure limite fortement l'utilisation large du BMS qui est nécessaire pour faire évoluer et améliorer davantage [65–67]. Jusqu'en 2003, le premier DES était approuvé par la Food and Drug Administration aux États-Unis. En tant que stent nouvellement développé, l'effet thérapeutique a été grandement amélioré avec les revêtements médicamenteux anti-prolifératifs conçus. Cependant, en raison de l'existence durable du stent après la libération du médicament, de nouveaux risques apparaissent avec la thrombose très tardive après l'implantation du DES d'un an [68–70]. Ainsi, le développement du DES est toujours nécessaire malgré les progrès significatifs réalisés. En tant que tendance du développement des stents, les stents solubles et sans polymère ont été proposés ces dernières années [71–73], mais ils sont encore limités dans les recherches à ce jour. Le stent soluble est conçu pour être dissous ou absorbé dans le corps progressivement après l'implantation du stent, ce qui peut réduire les risques de thrombose ultérieure par rapport au BMS [74]. Pour le stent sans polymère, les médicaments seront directement filmés sur les surfaces du stent au lieu d'utiliser le support polymère qui agit comme un stimulus inflammatoire chronique potentiel [75].

Des recherches approfondies ont été menées afin de mieux comprendre le mécanisme de libération du médicament et d'améliorer le stent. La méthode numérique a été largement adoptée pour modéliser le

DES physiquement et mathématiquement, ce qui est plus rentable par rapport aux expériences / essais cliniques [76]. Du point de vue de la modélisation physique, trois domaines sont liés à la libération du médicament: le domaine polymère, le domaine du flux sanguin et le domaine tissulaire. Un certain nombre d'études ont été menées pour étudier la libération de médicament du DES de la manière uni-dimensionnelle [77], bidimensionnel [78, 79] et modèles tridimensionnels [80, 81] séparément. Le premier article sur le transport simultané de médicaments à la fois dans le domaine tissulaire et sanguin a été publié en 2007 [82]. Les publications antérieures se concentrent sur le transport du médicament soit dans le domaine tissulaire soit dans le domaine sanguin [83,84]. De plus, dans de nombreuses études, le domaine des polymères est simplifié en tant que limite où une concentration initiale de médicament sera imposée et maintenue inchangée, ce qui ne correspond évidemment pas au cas pratique. [85–88]. Des simplifications et des hypothèses sont communément trouvées à travers les travaux numériques. Le flux de médicament est généralement supposé être continu à travers les limites de l'interface, ce qui est raisonnable lorsque la solubilité du médicament est similaire entre les deux domaines voisins. Dans le cas des médicaments hydrophobes, ils sont plus enclins à se répartir dans le tissu, ce qui entraînera des discontinuités. De plus, en raison de la différence d'échelle de temps distinguée entre le flux sanguin pulsé et le transport de médicament dans les tissus, le flux constant est pris en compte lors du couplage avec le transport de médicament. Récemment, les travaux de R.S. Pujith [89] ont vérifié que le transport de médicaments à médiation par le flux à partir du DES est négligeable, même si d'autres travaux doivent être achevés. De plus, il est intéressant de constater que des résultats opposés existent parmi les études existantes qui indiquent l'importance des modèles établis plus conformes à la réalité. Dans le but d'optimiser le stent, plusieurs paramètres de contrôle ont été considérés pour étudier l'influence de la concentration du médicament, en particulier le rôle des caractéristiques géométriques détaillées [54,90,91] et les propriétés du polymère [92]. Y. Chen et al. a étudié l'effet des positions de revêtement du médicament, des angles de flexion des artères et du nombre de Reynolds sur la concentration du médicament [85,86,93] en modélisation 3D. A.I. Barakat et al. ont modélisé le processus de transport des médicaments de deux types de médicaments [94] et étudié l'effet de la cinétique de libération sur la concentration de médicament dans les tissus [95]. J.A. Ferreira et al. a étudié l'influence de différentes excentricités de plaque sur le transport du médicament dans le vaisseau sténosé [96]. Plus de paramètres de contrôle tels que le coefficient de diffusion, l'espacement des entretoises, l'apposition des entretoises et la forme des entretoises ont également reçu une attention particulière de la part des chercheurs [97–99]. Il a été démontré qu'un plus grand espacement des entretoises diminue la valeur maximale de la concentration de médicament mais augmente la concentration moyenne de médicament dans les tissus [90]. Il est intéressant pour les travaux numériques réalisés par T. Seo et al. [100] en 2016, qui a introduit un nouvel indice sans dimension: l'indice de pénalité des stents (SPI) pour quantifier la perturbation de l'écoulement et la concentration de médicament à la surface endothéliale. Un certain nombre de recherches effectuées dans les cas d'écoulement constant et de libération régulière de médicament ont conclu que les recirculations formées autour du stent avaient un effet significatif sur le transport du médicament et la distribution asymétrique du médicament dans les tissus a été observée. [87]. Cependant, de nombreux travaux récents sur la libération instable de médicaments ont nié les résultats auparavant en cas stable. Au lieu de l'asymétrie de la distribution du médicament affectée par le flux en cas stationnaire, une distribution symétrique du médicament autour de la jambe dans le tissu sera trouvée dans le cas instable et l'influence de la rhéologie du flux dans le transport du médicament peut être négligée. Comme le montre la figure B.4 fait par P.R.S. Vijayaratnam et al. [89, 101], la concentration du médicament a été comparée entre les cas stables et instables. La figure montre la concentration de médicament autour du stent dans un cas stable 2D d'écoulement et de libération de médicament. Le polymère est considéré comme une frontière avec une concentration initiale constante de médicament. On peut constater que les dépôts de médica-

ment à côté du stent occupaient le même ordre de concentration de médicament par rapport à celui dans les tissus, ce qui indique que la concentration de médicament est grandement affectée par l'écoulement. Cependant, avec la poursuite de l'enquête en 2018, le domaine polymère a été établi plus complètement comme le montre la figure B.4-(b) and (c). La concentration de médicament dans les domaines sanguins et tissulaires n'a pas de grande différence entre les cas à flux constant et à flux pulsatile. L'amplitude de la concentration de médicament autour du stent est suffisamment faible par rapport à celle du tissu, ce qui indique que l'influence de la pulsatilité du flux dans le transport du médicament peut être négligée. Avec ces résultats, il a confirmé qu'il est raisonnable d'envisager le transport du médicament en cas de flux sanguin constant.

(a)

(b)   (c)
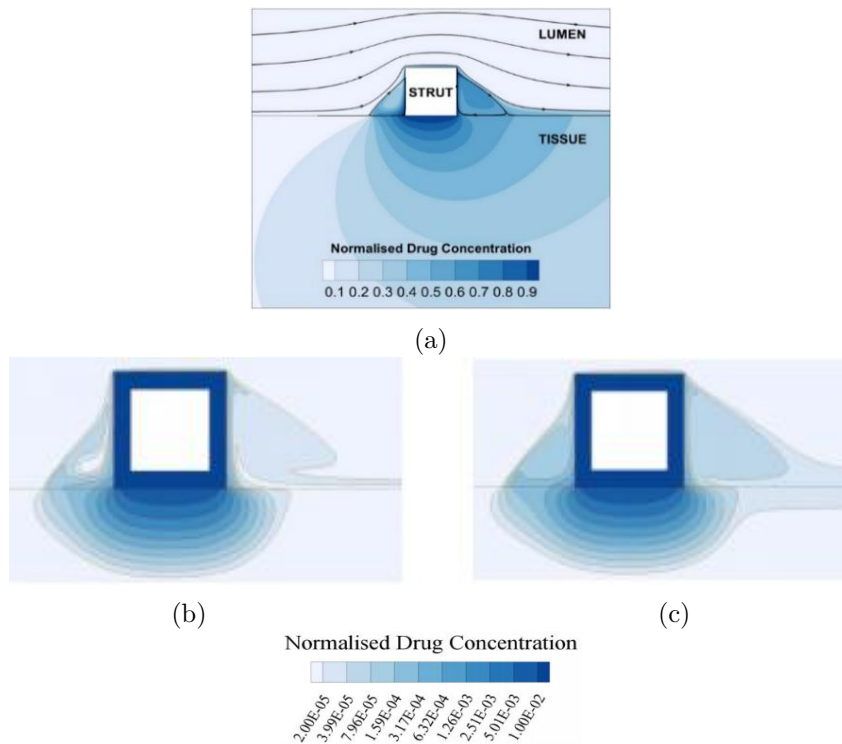
Figure B.4: La concentration de médicament normalisée en cas stationnaire (débit et transport de médicament) en (a), et accumulation de médicament instable à 60 s avec (b) débit constant et (c) débit pulsatile [89].

Modélisation des caractéristiques et validation du flux sanguin dans l'artère coronaire

Généralement, le flux sanguin est laminaire dans le corps, en particulier dans les petites artères. Pour l'artère coronaire gauche, les valeurs moyennes et maximales de Re_{moyen} et $Re_{maximal}$ sont évaluées respectivement à 166 et 431 [83] quand on est au repos. Par conséquent, l'équation qui régit le flux est les équations instables de Navier-stokes et la forme générale des équations de Navier-Stokes est décrite ci-dessous:

$$\frac{\partial \rho}{\partial t} + \bigtriangledown \cdot (\rho V) = 0 \tag{B.1}$$

$$\rho \frac{\partial V}{\partial t} + \rho V \cdot \bigtriangledown V = -\bigtriangledown p + \bigtriangledown \cdot \tau + f \tag{B.2}$$

À travers les travaux de P.S.R. Vijayaratnam et al. [89], il est conclu que le transport de drogue par flux à partir du DES peut être négligeable. De plus, se référant aux travaux de E.W. Merrill et al. [114] et D.A. Mcdonald [115], les caractéristiques non newtoniennes se produisent généralement dans les petits vaisseaux pour de faibles valeurs de taux de cisaillement $\dot{\gamma} < 100\ s^{-1}$ et le nombre de Womersley $Wo < 1$. Dans notre cas, le nombre de Womersley est 2,7 et le taux de cisaillement est estimé à 114 s^{-1}. Par conséquent, pour nos investigations, il est raisonnable de définir le flux sanguin avec le modèle newtonien. Ainsi l'expression finale des équations de Momentum peut être décrite comme suit en ignorant les effets de la force corporelle:

$$\rho \frac{\partial V}{\partial t} + \rho V \cdot \bigtriangledown V = -\bigtriangledown p + \mu \bigtriangledown^2 V \tag{B.3}$$

Dérivé du modèle de profil de flux sanguin stable de Poiseuille, le modèle pulsatile simplifié est développé afin de capturer les caractéristiques instationnaires du flux sanguin [119]:

$$u(r,t) = 2V(t)(1 - \frac{r^2}{R^2}) \tag{B.4}$$

Le flux sanguin pulsé dans l'artère coronaire à une fréquence de 1,25 Hz peut être obtenu grâce à des travaux de N. Bénard comme le montre la figure B.5. Afin de reconstruire numériquement le profil d'écoulement, une équation de Fourier à huit coefficients est établie avec Matlab comme indiqué dans l'équation (B.5). Les coefficients calculés sont présentés dans le tableau 2.1 faisant référence aux travaux de F. Chabi [83].

$$V(t) = V_o + \sum_{n=1}^{8}(V_n cos(nwt) + W_n sin(nwt)) \tag{B.5}$$

Où $V_0 = \frac{1}{T}\int_0^T V(t)dt$ pour $n = 0$, $V_n = \frac{2}{T}\int_0^T V(t)cos(nwt)dt$ pour $n \geq 1$, $W_n = \frac{2}{T}\int_0^T V(t)sin(nwt)dt$ pour $n \geq 1$.
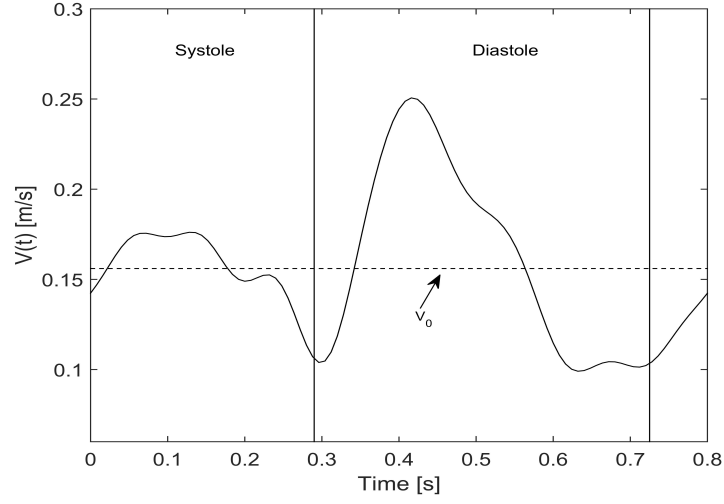
Figure B.5: Inlet blood flow profile at $f = 1.25$ [83]

Table B.1: Valeurs numériques du coefficient W_n et V_n [83]

ordre harmonique	V_n (m/s)	W_n (m/s)
0	0.15634	0
1	-0.02995	0.00808
2	0.02458	0.03887
3	-0.01182	-0.00838
4	0.00985	0.0028
5	-0.01009	0.00313
6	0.00618	-0.00113
7	0.00133	$8.74149 * 10^{-4}$
8	-0.0036	$-2.35276 * 10^{-4}$

La paroi du vaisseau est considérée comme rigide en référence à la littérature [50, 137, 138]. À l'entrée et aux sorties, le débit et la pression pulsés à différentes fréquences d'impulsions seront imposés séparément comme indiqué sur la figure B.6. Les débits d'entrée à des fréquences d'impulsion de 75 bpm, 100 bpm et 120 bpm ont été utilisés. Pour la condition aux limites de sortie, une forme d'onde de pression avec différentes fréquences est prescrite correspondant à différents taux d'impulsions. Un modèle à deux éléments est utilisé comme indiqué dans l'équation (B.6) [139]:

$$Q(t) = \frac{P(t)}{R} + C\frac{dP(t)}{dt} \tag{B.6}$$

Où $Q(t)$ est le débit volumétrique pulsatile d'entrée du sang, m^3/s. $P(t)$ est la forme d'onde de pression pulsatile de sortie, Pa. R est la résistance périphérique, $1e10\ Pa \cdot s/m^3$. C est la compliance artérielle, $1e - 11\ m^3/Pa$. Il a été prouvé que le modèle à deux éléments reconstruit bien la fluctuation de pression aux sorties du domaine artériel avec une fréquence plus basse ($< 5\ Hz$) [34]. Compte tenu de la plage de nombres de Reynolds de 90 à 570, le flux sanguin laminaire est considéré comme étant pleinement développé avec un profil de vitesse parabolique.
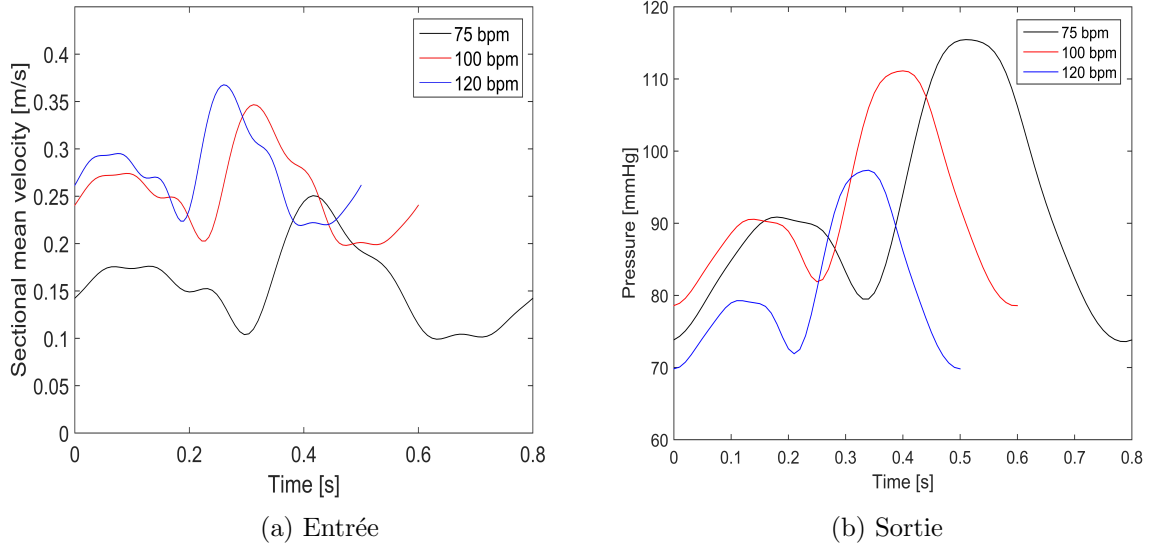
(a) Entrée

(b) Sortie

Figure B.6: Débit pulsé d'entrée et pression de sortie en fonction du temps dans un cycle à différentes fréquences d'impulsions

Les travaux de modélisation, de maillage et de calcul ont tous été réalisés avec Comsol 5.1. Les éléments de maillage tétraédrique non structurés ont été générés et la méthode multigrille a été utilisée pour accélérer la vitesse de convergence d'une méthode itérative de base. Les méthodes itératives ont choisi GMRES avec le nombre d'itération maximum de 500. Le pas de temps initial est fixé à 0,001 s afin d'assurer $CFL < 1$ qui sera déterminé de manière adaptative par Comsol en fonction de la physique. Pour s'assurer de la stabilité périodique des résultats, les simulations ont été réalisées sur quatre cycles pulsatiles.

- Paramètres hémodynamiques

- WSS

$$WSS = n \cdot \mu(\frac{\partial u_i}{\partial x_j} + \frac{\partial u_j}{\partial x_i})|_{wall} \quad i, j\epsilon(x, y, z) \ \ and \ \ i \neq j \tag{B.7}$$

μ est la viscosité dynamique, n est un vecteur tangentiel le long de la paroi du vaisseau. La valeur critique de WSS est de 0,5 Pa.

- Moyenne temporelle WSS (TAWSS)

$$TAWSS = \frac{1}{T} \int_0^T |WSS| dt \tag{B.8}$$

Où T est la durée totale d'un cycle pour le flux sanguin. TAWSS représente la charge de cisaillement dans le temps à laquelle la paroi artérielle est soumise et la valeur seuil est de 0,4 Pa [33].

- Chute de pression relative (RPD)

$$RPD = \frac{(p_{proximal} - p_{distal})}{p_{distal}} \cdot 100 \tag{B.9}$$

Où $p_{proximal}$ est la pression proximale avant la sténose, p_{distal} est la pression distale après la sténose.

- Surface artérielle de TAWSS inférieure à 0,4 Pa (S_{TA})

$$S_{TA} = \int_{S_T} si(TAWSS < 0.4, 1, 0) ds \tag{B.10}$$

Où S_T est la surface totale de la paroi artérielle. La fonction «si» a été utilisée pour intégrer la surface où TAWSS $< 0,4$ Pa ($= 1$ si oui, $= 0$ sinon). Ainsi S_{TA} représente la surface des sites potentiels de maladies.

- Pourcentage de surface de WSS inférieur à 0,5 Pa (S_p)

$$S_p = \frac{S_b}{S_T} \cdot 100 \tag{B.11}$$

Où S_b est la surface artérielle pour WSS en dessous de 0,5 Pa.

- Paramètres de diagnostic

- Coefficient de chute de pression (CDP)

$$CDP = \frac{\Delta \overline{p}}{0.5 \rho V_0^2} \tag{B.12}$$

Où $\Delta \overline{p} = \overline{p}_{proximal} - \overline{p}_{distal}$, $\Delta \overline{p}$ indique la différence entre la pression proximale moyenne temporelle et la pression distale moyenne dans le temps.

- Coefficient de flux de lésion (LFC)

$$LFC = \frac{AS}{\sqrt{\frac{\Delta \overline{p}}{0.5 \rho V_0^2}}} \tag{B.13}$$

Où $AS = \frac{S_{original} - S_{resté}}{S_{original}}$, $S_{original}$ représente la surface d'origine de la section transversale du navire, $S_{resté}$ est la surface restante de la section transversale du vaisseau en raison de la formation de sténose.

Validations avec singularités géométriques

Avec la détermination de l'établissement de la modélisation de l'artère coronaire, une étude préliminaire est réalisée avec une artère sténosée couplant les singularités géométriques artérielles. Deux cas sont menés: la bifurcation et la tortuosité.

Les résultats révèlent que dans le cas d'artère bifurquée, lorsque la sténose est située dans la branche principale proximale, la recirculation suit l'orientation du flux. Cependant, lorsque la sténose est située dans la branche latérale, la recirculation se fera à la fois en amont et en aval de la sténose. La sévérité de la sténose joue un rôle clé pour la taille de recirculation et la perte de charge relative par rapport à la longueur de la sténose dans le cas d'une sténose à la branche proximale principale. Cependant, dans le cas d'une sténose au niveau de la branche latérale, les influences de la sévérité de la sténose et de la longueur de la sténose dans la chute de pression relative peuvent être négligées. Pour le WSS le long de la sténose, soit à la branche principale proximale, soit à la branche latérale, la distribution à l'emplacement haut et bas est asymétrique affectée par la structure de bifurcation. L'augmentation de la sévérité de la sténose contribue au WSS plus grand, ce qui contraste avec la longueur de la sténose. Pour l'évaluation diagnostique, lorsque la sténose est à la branche proximale principale, la variation de la longueur de la sténose et de la fréquence du pouls dans notre cas n'affecte pas les résultats finaux de l'évaluation.

Le second cas est lié à une tortuosité courbe et spirale avec l'existence d'une sténose symétrique et asymétrique en amont. Les résultats ont conclu que la faible valeur du TAWSS situé en aval de la sténose peut être observée. Le long de la tortuosité courbe, la région de faible valeur de TAWSS est située sur la paroi externe en amont et la paroi interne en aval pour chaque courbure. Cependant, la faible valeur de TAWSS a tendance à être toujours située au niveau de la paroi interne le long de la tortuosité en spirale. Un plus grand pourcentage de surface de WSS inférieur à 0,5 Pa et une surface de TAWSS inférieure à 0,4 Pa vont avec une plus grande sévérité de sténose, une fréquence du pouls plus petite et une plus grande distance entre la sténose et la tortuosité à la fois pour l'artère courbe et spirale, sauf dans les cas de sténose symétrique dans l'artère courbe avec une distance 6 mm et sévérité de la sténose de 50% dans l'artère spirale. L'artère spirale est plus sensible à la morphologie de la sténose de l'état symétrique à asymétrique par rapport à l'artère courbe. La valeur de S_p a tendance à être plus élevée pour la sténose asymétrique par rapport à la sténose symétrique sous l'effet de la sévérité de la sténose et de la fréquence du pouls qui peut être inversée en augmentant la distance entre la sténose et la tortuosité pour l'artère courbe. Cependant, pour l'artère spirale, la valeur plus élevée de S_p va toujours avec une sténose symétrique par rapport à une sténose asymétrique. Pendant ce temps, la perturbation de l'écoulement a tendance à être plus forte avec une sévérité de sténose et une fréquence du pouls plus importantes, et une distance plus petite entre la sténose et la tortuosité, en particulier pour la sténose asymétrique dans l'artère courbe. La perturbation du flux en aval et les lignes de courant se déplaçant en spirale le long de la tortuosité peuvent être facilement observées dans l'artère en spirale.

Circulation sanguine à travers l'artère coronaire traitée par stent

Il a été démontré pour la première fois que la conception du stent était liée à des résultats cliniques indésirables dans les artères iliaques endoprothétiques de lapin en 2000, et la variation du WSS s'est avérée fortement associée à l'hyperplasie néointimale. Un écoulement perturbé a été couramment trouvé avec un vortex en amont et en aval du stent et la faible valeur de WSS dans la région de recirculation a également été démontrée [48–50].De nombreuses considérations relatives aux caractéristiques de conception de stent ont été prises en compte dans la littérature existante dans le but de minimiser l'altération de l'écoulement telle que l'emplacement du stent, le type de stent et le paramètre de conception spécifique de l'entretoise. Le modèle 2D a été plus couramment établi en tenant compte de la forme de la section transversale de la jambe de force, de l'espace inter-jambe et de l'épaisseur du stent dans la littérature. Cependant, dans la pratique de la fabrication du stent, certains conflits doivent également être équilibrés entre la résistance requise du stent et les facteurs de conception optimaux du stent.

En vue d'explorer plus de méthodes possibles d'optimisation du stent et de contribuer aux données de recherche actuelles, l'interaction entre les facteurs de conception du stent et les variations hémodynamiques a été analysée ici et les effets des activités physiques sur l'hémodynamique ont également été couverts dans cette recherche. La topologie du flux et les variations hémodynamiques ont été évaluées sur la base de différents descripteurs basés sur le WSS.

- Modèle géométrique 3D

Se référant à la géométrie commerciale du stent de Palmaz-Schatz [163, 164], la géométrie du stent 3D est établie comme le montre la figure B.7. Le long de la direction de l'axe z (sens du flux), la section transversale de la jambe simple est affichée avec différents rapports d'aspect (AR): 1, 2 et 4 séparément où a=0,1 mm. La longueur totale du stent est de 4,475 mm. Le rayon externe est égal à 1,75 mm conformément au rayon interne de l'artère coronaire. Suite à cela, le modèle d'artère stentée 3D complet a été obtenu illustré sur la figure B.8. De même, la longueur de l'artère avant et après le stent est de 4 mm et de 6 mm séparément. Les limites peuvent être divisées en limite d'entrée, limite de sortie et paroi de cuve.
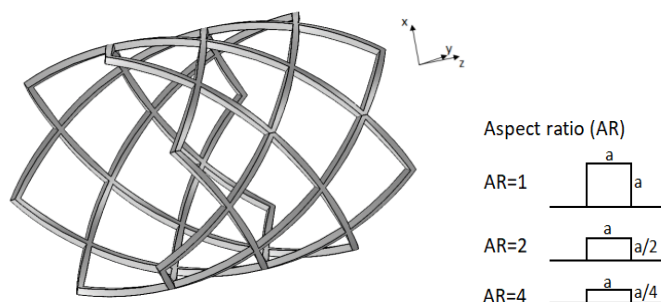
Figure B.7: Schéma du modèle de stent 3D
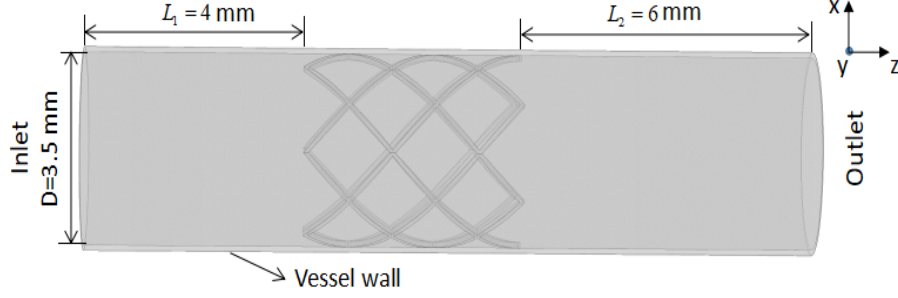
Figure B.8: Schéma du modèle d'artère 3D avec stent

- Modèle mathématique et conditions aux limites

Les modèles mathématiques et les conditions aux limites restent les mêmes avec les discussions ci-dessus, à l'exception de la condition aux limites d'entrée. Une vitesse moyenne de section constante de V_0=0,1 m/s, 0,158 m/s et 0,2 m/s respectivement a été imposée à l'entrée pour le cas stationnaire. Cependant, pour le cas instable, une forme d'onde pulsatile simplifiée de la vitesse est imposée afin de réduire le coût comme le montre la figure B.9. Le profil de vitesse simplifié fait référence à la plage de vitesse couverte dans le cas de 75 bpm présenté à la figure 3.2 avec une vitesse moyenne de $V_0 = 0,175 \ m/s$. Ainsi le nombre de Reynolds lié est 90-265 appartenant au régime laminaire.
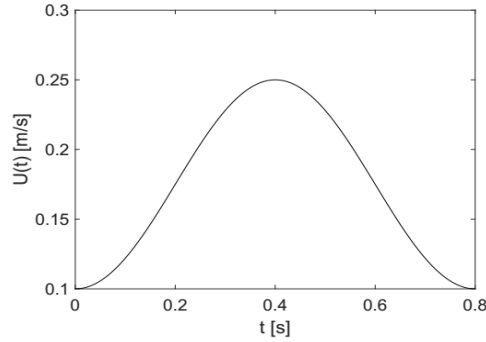
Figure B.9: Vitesse moyenne de section instantanée pendant un cycle

- Paramètres hémodynamiques liés

Gradient WSS moyenné dans le temps dans l'espace (TAWSSGs)

$$TAWSSGs = \frac{1}{T} \int_0^T \sqrt{(\frac{\partial WSS_x}{\partial x})^2 + (\frac{\partial WSS_y}{\partial y})^2 + (\frac{\partial WSS_z}{\partial z})^2} dt \tag{B.14}$$

Selon la littérature, une valeur élevée des TAWSSG indique une forte possibilité de dépôt et la valeur critique des TAWSSG est de 200 Pa/m [47, 165].

Indice de cisaillement oscillatoire (OSI)

OSI en tant qu'autre paramètre basé sur WSS est défini sous la forme d'une équation (B.15). Il représente la déviation entre le vecteur WSS et la direction du flux sanguin. Lorsque la direction du WSS est cohérente avec le flux sanguin, il est avantageux d'éloigner les dépôts de la paroi du vaisseau.

140

Cependant, si la direction WSS oscille fréquemment, il est plus facile de former des dépôts sur un emplacement de la paroi du vaisseau. D'après la littérature [47], la valeur critique de OSI est de 0,1. Lorsqu'il est supérieur à 0,1, la possibilité de dépôt sera fortement augmentée.

$$OSI = 0.5 \times (1.0 - \frac{|\int_0^T WSSdt|}{\int_0^T |WSS|dt}) \tag{B.15}$$

Temps de séjour relatif (RRT)

La définition de RRT est introduite dans l'équation (B.16). La valeur RRT repose sur les effets de l'OSI et du TAWSS. Une valeur RRT élevée indique plus de possibilités de dépôt sur la paroi du navire.

$$RRT = [(1 - 2.0 \times OSI) \times TAWSS]^{-1} \tag{B.16}$$

Le rapport d'aspect concernant la hauteur de la jambe de force a été introduit et les effets sur les variations hémodynamiques ont été étudiés. Un AR plus grand du stent signifie moins de hauteur d'entretoise pénétrée dans la lumière conduisant à moins de perturbation de l'écoulement car la faible valeur du taux de cisaillement de la paroi a tendance à être située dans la région de recirculation. Ainsi, avec l'augmentation de AR, la région de faible valeur du taux de cisaillement du mur et la région de valeur élevée des WSSG situés près des entretoises sont toutes deux diminuées, ce qui est cohérent entre les cas stables et instables. De plus, un montant de AR élevé est avantageux pour réduire la région de RRT et OSI élevés qui peuvent facilement entraîner un dépôt, ainsi que la chute de pression avant et après le stent. Cependant, même s'il est cohérent que la vitesse d'entrée est positivement liée à la distribution du taux de cisaillement de la paroi à la fois dans les cas stationnaires et instables, les influences de la pulsation d'écoulement considérées dans le cas instable font des différences dans les résultats.

Transport de médicaments à partir du DES et validation expérimentale

Le développement du DES est une avancée significative pour les traitements des maladies cardio-vasculaires avec la réduction de la survenue de resténose d'environ 20% à 5% par rapport au BMS. Cependant, l'utilisation encore plus répandue du DES a été limitée par la thrombose de suivi tardif. Ainsi, l'optimisation du stent a été la question brûlante parmi les chercheurs qui souhaitent se concentrer principalement sur les enquêtes sur les mécanismes de libération de médicaments et les facteurs influents sur l'amélioration des performances du DES. Parmi les articles publiés sur le DES, des enquêtes numériques ont été plus couramment menées, cependant, il existe une pénurie de travaux de validation expérimentale dans l'état actuel de la recherche. Par conséquent, afin d'aller de l'avant et de contribuer aux données de recherche actuelles, des investigations numériques et expérimentales ont été considérées ici. Un certain nombre de différents facteurs influents sur le transfert de masse ont été pris en compte dans la littérature existante tels que les propriétés du polymère, les propriétés du médicament, les caractéristiques d'écoulement et les conceptions géométriques du stent. Cependant, en vue de l'optimisation du DES, des travaux supplémentaires sont encore très nécessaires afin de mieux comprendre les mécanismes internes et régler les confusions ainsi que le fait que certains résultats opposés existent dans la littérature.

Mise en place du modèle géométrique

La figure B.10 montre le modèle géométrique 2D de l'artère traitée par DES. Trois domaines sont inclus: le domaine sanguin (Ω_b), le domaine tissulaire (Ω_t) et le domaine polymère (Ω_p). Trois entretoises de forme carrée d'une longueur de 0.1 mm sont considérées avec une épaisseur de polymère de 0,05 mm. La distance entre la position centrale des entretoises est de 0.7 mm. Le rayon de l'artère est de 1.75 mm, ce qui correspond à l'artère coronaire. L'épaisseur de la paroi artérielle est de 0.5 mm. Les longueurs d'artère avant et après le stent adoptent 4 mm et 6 mm séparément afin de garantir l'indépendance géométrique.
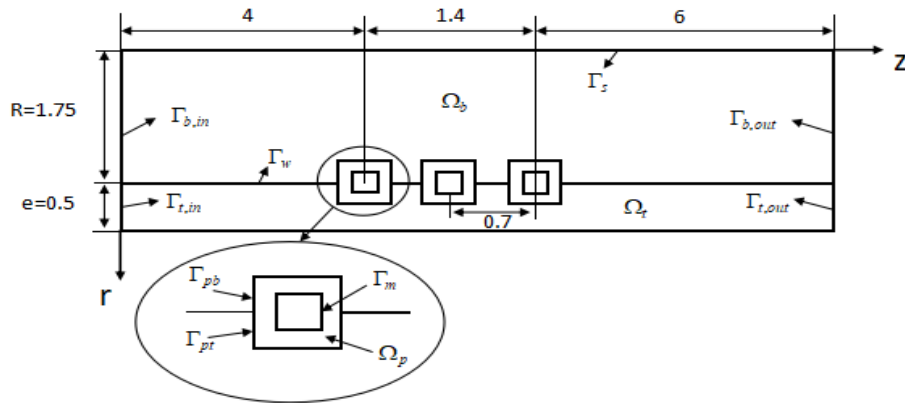

Figure B.10: Modèle géométrique 2D d'artère avec stent à élution de médicament (mm)

Transport de médicaments dans le domaine sanguin

La diffusion du médicament et la convection sont toutes deux concernées en raison de la présence d'un flux sanguin dans le domaine de la lumière. Se référer à la littérature [168, 169], la loi de Fick a été couramment adoptée pour décrire le processus de transport de masse. Dans l'équation (B.17), l'équation gouvernante est affichée couvrant à la fois les mécanismes de diffusion de masse et de convection.

$$\frac{\partial c_f}{\partial t} + u_f \cdot \bigtriangledown c_f = D_f \bigtriangledown^2 c_f \tag{B.17}$$

Où c_f est la concentration de médicament dans le domaine d'écoulement, mol/m^3; u est la vitesse du sang, m/s; D_f est le coefficient de diffusion en flux, m^2/s.

Transport de médicaments dans le domaine tissulaire

Car la vitesse de filtration du débit dans les tissus est de l'ordre de 10^{-10} m/s [80] et le coefficient de diffusion du paclitaxel utilisé dans la présente étude est $D_t = 10^{-13}$ m^2/s dans un tissu d'épaisseur $e = 0.5$ mm [97, 172], la convection d'écoulement est négligée en fonction du nombre de Peclet indiqué dans l'équation (B.18). Le nombre de Peclet est un type de nombre sans dimension décrivant le phénomène de transport et représente le rapport entre le transport par convection et le transport par diffusion. Comme la valeur de Pe est approximativement de l'ordre de 10^{-1} dans notre cas, la diffusion garde le rôle dominant dans les tissus. Ainsi, l'influence de la convection n'est pas prise en compte ici et l'équation gouvernant le transfert de masse dans les tissus est définie dans l'équation (B.19).

$$Pe = \frac{eu_t}{D_t} \approx 10^{-1} \tag{B.18}$$

$$\frac{\partial c_t}{\partial t} = D_t \bigtriangledown^2 c_t \tag{B.19}$$

Transport de médicaments dans le domaine des polymères

Le polymère en tant que vecteur de médicament joue un rôle clé sur la vitesse de libération du médicament. En général, la loi de diffusion de Fick a été utilisée pour donner la description fondamentale du transport de masse à partir du polymère car la solubilité du médicament dans l'écoulement est supérieure à la concentration maximale du médicament dans le polymère. Ainsi, tous les médicaments sont capables d'être à l'état dissous puisque le flux pénètre instantanément dans le polymère. Dans ce cas, l'équation à diffusion contrôlée est adoptée dans un polymère similaire au tissu comme indiqué ci-dessous:

$$\frac{\partial c_p}{\partial t} = D_p \bigtriangledown^2 c_p \tag{B.20}$$

Où c_p est la concentration de médicament dans le polymère, mol/m^3. D_p est le coefficient de diffusion du médicament dans le polymère, m^2/s.

Les conditions aux limites ont été décrites ci-dessous: une concentration de médicament nulle est donnée à l'entrée du domaine sanguin, le flux de médicament le long de l'axe z est considéré comme égal à 0 à la sortie. Pour le domaine tissulaire, une concentration de médicament nulle est imposée aux

deux limites latérales et il n'y a pas de flux de médicament à travers la limite externe du tissu. Un flux de médicament continu est considéré à travers les interfaces, y compris l'interface sang-tissu, l'interface sang-polymère et l'interface polymère-tissu. La concentration initiale du médicament dans le polymère est de 100 mol/m^3, cependant, la concentration initiale du médicament est fixée à 0 à la fois dans le domaine sanguin et dans le domaine tissulaire.

$$c_f|_{entrée} = 0, \frac{\partial c_f}{\partial z}|_{sortie} = 0$$

$$D_f \bigtriangledown c_f = D_t \bigtriangledown c_t \text{ (Interface sang-tissu)}$$

$$D_p \bigtriangledown c_p = D_t \bigtriangledown c_t \text{ (Interface polymère-tissu)}$$

$$D_f \nabla c_f = D_p \nabla c_p \text{ (Interface sang-polymère)}$$

$$\frac{\partial c_t}{\partial r}|_{perivascularwall} = 0$$

$$c|_{z=0} = c|_{z=L} = 0 \text{ (Limites latérales des tissus)}$$

$$c = 100 \ mol/m^3 \text{ (Concentration initiale du médicament dans le polymère)}$$

Transfert de masse depuis DES: étude des paramètres de contrôle

La libération et le transport du médicament du polymère dans les domaines des tissus et des lumières ont été étudiés afin d'avoir une meilleure compréhension des mécanismes de transfert de masse dans l'artère. Les résultats montrent une distribution de médicament relativement symétrique dans les tissus entourant les entretoises. Les effets de la recirculation sur le transport des médicaments se sont avérés négligés. En vue de l'amélioration des performances du DES, une étude des paramètres de contrôle a été réalisée avec différentes épaisseurs de polymère, différents emplacements des entretoises et différents coefficients de diffusion dans le polymère. Les résultats montrent qu'une épaisseur de polymère accrue est bénéfique pour prolonger le temps de libération du médicament à partir du polymère et augmenter le temps de rétention du médicament dans le tissu, ce qui est cohérent avec les résultats d'un stent plus intégré dans le tissu et d'un coefficient de diffusion plus petit dans le polymère. La surface de contact entre le stent et le tissu est un facteur clé sur les performances du stent.

Validation expérimentale du transfert de masse du polymère

Outre les investigations numériques, des travaux expérimentaux ont également été menés afin de contribuer à la validation avec des résultats numériques.La veine de test est représentée sur la figure B.11 avec tubes à essai parallèles. Le tube à essai est fabriqué de manière rectangulaire. La longueur du canal d'écoulement est de 130 mm et la section transversale du canal est de forme carrée avec une longueur de 30 mm.
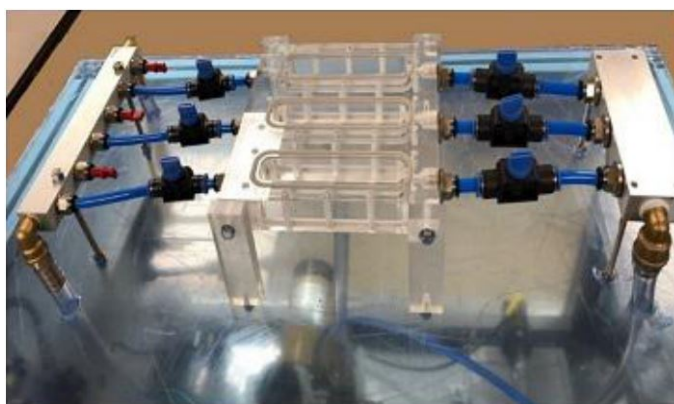
Figure B.11: Banc d'essai

- Propriété fluide

Dans les tests actuels, l'eau a été utilisée comme écoulement éliminant les médicaments du polymère. La densité et la viscosité dynamique sont respectivement de 1000 kg/m^3 et 6.9e-4 $Pa \cdot s$. Le débit est contrôlé à 7.5 ml/s ce qui correspond au débit de l'artère carotide interne lorsque l'on est au repos [175].

- Matériau polymère

Le polyuréthane non dégradable (PU) a été utilisé comme vecteur de médicaments. Des échantillons de polymère de dimensions $30 \times 5 \times 2$ mm^3 ont été préparés avec un certain dosage de médicaments (rapport massique médicament/(médicament+polymère)): 10%, 20% et 30% séparément. Les médicaments sont répartis de manière homogène dans le polymère et le film polymère a été fixé au milieu du canal d'écoulement en contact avec la surface inférieure comme indiqué sur la figure ci-dessous:
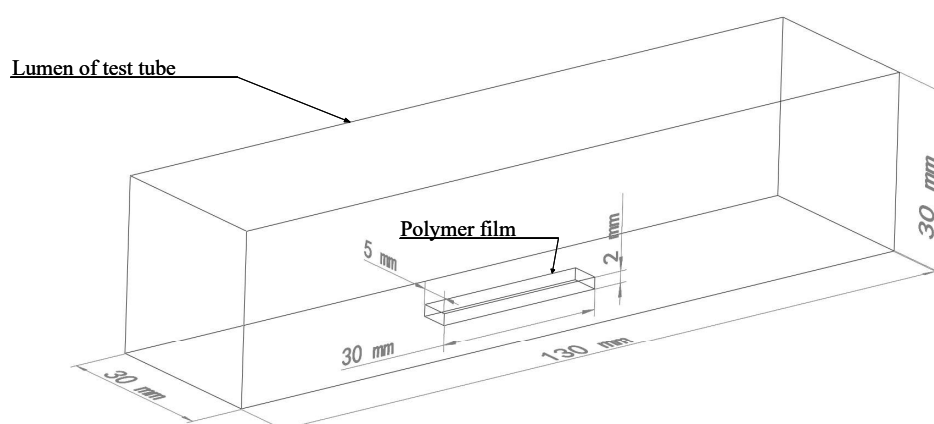
Figure B.12: Schéma du canal d'écoulement avec film polymère

- Choix du médicament

Le médicament chargé dans le polymère a été sélectionné pour être le diclofénac pour les tests de libération de médicament [176] et acheté au laboratoire de Genevrier. La particule de médicament

est de forme granulaire avec une densité d'environ 450,7 mg/ml. La solubilité du médicament à une température de 37°C dans l'eau est d'environ 5,554 g/L.

Pour se conformer à la taille de l'installation d'essai, le modèle géométrique 2D du canal d'écoulement avec un polymère chargé de médicament à l'intérieur a été établi comme le montre la figure B.13. Deux domaines sont inclus: le domaine d'écoulement et le domaine polymère. La longueur du canal d'écoulement est de 130 mm et la hauteur de 30 mm. Le polymère mesure 2 mm de hauteur et 30 mm de longueur horizontale situé au milieu de l'artère. Les limites comprennent l'entrée, la sortie, la paroi du canal et les interfaces entre la lumière et le polymère. L'indépendance du maillage a été étudiée avec la concentration de médicament dans le polymère à différentes tailles de mailles de 40976, 66592, 93125 et 131514. La précision des résultats peut être contrôlée en dessous de 1 % après le troisième maillage. Ainsi, le maillage final de 93125 a été déterminé.
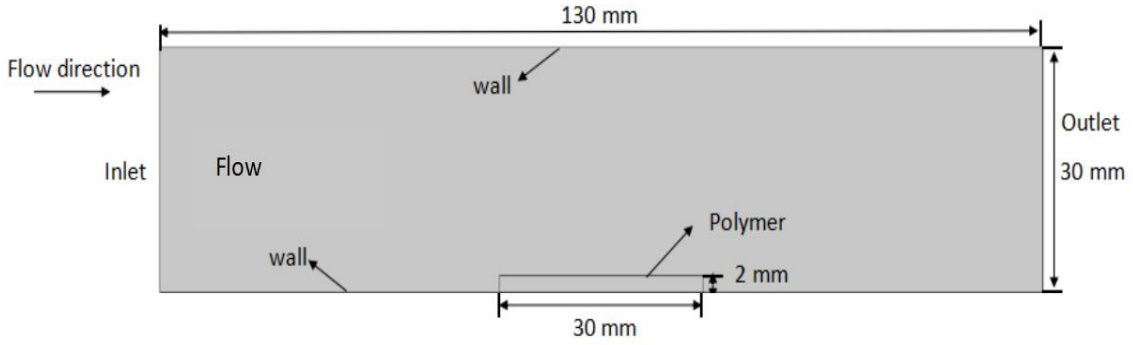

Figure B.13: Modèle géométrique 2D du canal d'écoulement avec polymère chargé de médicament

En termes de modèles mathématiques dans les polymères, la physique de diffusion et de dissolution a été considérée afin de mieux décrire le processus pratique de libération de médicaments dans les expériences. Les médicaments dans le polymère sont initialement en phase solide, puis se dissolvent et se diffusent progressivement avec l'intrusion d'écoulement. Lorsque le polymère entre en contact avec le fluide, le flux entrera par les limites et occupera les pores qui constituent le chemin de diffusion des médicaments dissous. Le processus de dissolution suit la relation ci-dessous [177]:

$$b \xrightarrow{\beta} c$$

Où b représente les médicaments en phase solide et c les médicaments en phase dissoute. β représente le taux de dissolution. Les médicaments solides comme source de médicaments dissous ne peuvent pas être diffusés et la diffusion se produit uniquement avec les médicaments dissous. Ainsi, les équations gouvernantes sont établies comme suit [167]:

$$\frac{\partial b}{\partial t} = -\beta b(S - c) \tag{B.21}$$

$$\frac{\partial c}{\partial t} = \nabla \cdot (D \nabla c) + \beta b(S - c) \tag{B.22}$$

Où S est la solubilité des médicaments dans le flux, 13,5 $mol/m3$. D est le coefficient de diffusion. Comme la solubilité du médicament est inférieure aux concentrations initiales du médicament dans notre étude, les valeurs de β sont déterminées en fonction des critères du nombre de Damköhler non dimensionnel $>> 1$ qui est défini comme $Da_0{}^* = \beta B L_c^2/D$ [167]. B est la concentration initiale du

médicament dans le polymère. Ainsi, la valeur de β est fixée à 10 $mol/(m^3 \cdot s)$. Pour la concentration initiale du médicament dans le polymère, $c = 0$, $b = B$.

Les coefficients de diffusion dans le polymère avec différents dosages de médicament initial (10%, 20% et 30%) ont été calculés sur la base des données expérimentales de libération de médicament. Une relation linéaire a été obtenue entre le dosage initial du médicament et le coefficient de diffusion. Ainsi, le coefficient de diffusion dans le cas d'une dose de médicament à 15% peut être prédit sur la base de la relation linéaire et une bonne validation a été obtenue entre les résultats numériques et expérimentaux avec une dose de médicament de 15% dans le polymère.

Conclusions et perspectives

Conclusions

Cette thèse vise à étudier les effets de la singularité géométrique artérielle sur la topologie des flux et l'hémodynamique afin d'optimiser les performances du stent en reconnaissant mieux la physique associée ainsi que le processus de transfert de masse du DES. Comme présenté dans le chapitre 1, certains centres d'intérêt ont été mis en avant et étudiés dans les chapitres suivants.

Sur la base de l'état de l'art dans ce sujet tel que discuté au chapitre 1, il est connu que l'incidence de la resténose ou de la thrombose est fortement liée à la région de recirculation provoquée par l'écoulement perturbé. La faible valeur du taux de cisaillement située dans la région de recirculation joue un rôle clé dans les contributions du dépôt sur la paroi du vaisseau. Les principales conclusions parmi la littérature existante démontrent que la taille des tourbillons est affectée par les paramètres dynamiques de l'écoulement tels que le nombre de Reynolds et la conception géométrique du stent telle que la forme et la taille de la jambe de force. La taille de recirculation formée à la fois en amont et en aval de la jambe de force a tendance à être inversement affectée par le nombre Re. De plus, la hauteur du stent s'avère être l'un des facteurs les plus influents pour la taille de la recirculation. En ce qui concerne les enquêtes sur le transfert de masse à partir du DES, l'étude des paramètres de contrôle du processus de transport des médicaments a été couramment réalisée. Les paramètres de contrôle du nombre de flux, des propriétés du polymère et de la taille du polymère sur le transport du médicament dans la lumière et le tissu ont été largement pris en compte. Cependant, les mécanismes liés n'ont pas encore été pleinement explorés et l'optimisation du stent nécessite plus d'efforts, y compris plus de considérations sur le débit d'impulsion, les facteurs de conception de plusieurs stents, les caractéristiques de libération du médicament et les travaux de recherche de validation nécessaires entre les simulations et les expériences concernant le DES.

En raison de la physique mécanique et biologique complexe du flux sanguin dans l'artère, les modèles numériques établis ont été pris en compte dans les considérations et éclaircissements approfondis du chapitre 2 concernant le flux sanguin dans l'artère coronaire. Les principales caractéristiques géométriques artérielles de la bifurcation et de la tortuosité ont été étudiées récemment. Ainsi les investigations préliminaires suite à la détermination des modèles numériques ont été réalisées avec l'artère sténotique couplant les singularités géométriques: bifurcation et tortuosité comme les validations de modélisation. Les résultats révèlent que la bifurcation ou la tortuosité peuvent avoir une influence directe sur la perturbation de l'écoulement et les sites potentiels d'apparition de la plaque. En présence de structure de bifurcation, lorsque la sténose est située dans la branche principale proximale, le développement de la recirculation suit l'orientation du flux. Cependant, lorsque la sténose est située sur la branche latérale, les vortex se sont formés à la fois en amont et en aval de la sténose. Par rapport à la longueur de la sténose, la sévérité de la sténose joue un rôle plus important dans les variations hémodynamiques. Dans le cas de l'artère tortueuse, la tortuosité courbe et spirale a été étudiée. L'écoulement en spirale a été observé le long de la tortuosité en spirale et les avantages d'inhiber le dépôt ont été montrés par rapport à la tortuosité courbe. Une petite partie de l'analyse diagnostique a également été introduite, ce qui donne dans une certaine mesure des indications sur le traitement pratique.

Le chapitre 3 a mené le couplage entre l'artère coronaire et la performance du stent avec différentes considérations de conception. Des cas 2D et 3D ont été réalisés en vue de différentes considérations de conception de stent. La topologie du flux et les évaluations hémodynamiques ont été axées sur les descripteurs basés sur WSS. Les résultats montrent que les recirculations formées à côté des entretoises

sont fortement affectées par la fréquence du pouls et la géométrie du stent. La longueur horizontale de recirculation en aval du stent reste la plus sensible à la fréquence du pouls en raison de la force d'inertie moins confinée qui contraste avec la longueur verticale de recirculation en aval limitée par la hauteur de l'entretoise. L'espace plus grand entre les entretoises s'avère bénéfique pour améliorer les performances du stent avec un taux de cisaillement de paroi accru. Au lieu du modèle 2D, des investigations avec un modèle 3D ont été effectuées avec l'établissement d'une géométrie pratique du stent et des cas stables et instables ont été étudiés. Avec l'augmentation de AR, la région de faible valeur du taux de cisaillement du mur et la région de valeur élevée des WSSG situés près des entretoises diminuent toutes deux, ce qui est cohérent entre les cas stables et instables. De plus, un montant de AR élevé est avantageux pour réduire la chute de pression à travers le stent et la région de RRT et d'OSI élevés qui ont tendance à entraîner un dépôt. De plus, même s'il est cohérent que la vitesse d'entrée est positivement liée à la distribution du taux de cisaillement de la paroi à la fois dans les cas stables et instables, les influences de la pulsation d'écoulement considérées dans le cas instable font des différences dans les résultats.

Suite aux interactions entre le flux et le stent, le chapitre 4 aborde le couplage physique entre le flux et le transfert de masse en considérant le DES. Dans ce chapitre, des travaux à la fois numériques et expérimentaux sont impliqués afin de mieux contrôler le processus de libération du médicament. Les résultats ont démontré que les effets de la recirculation sur le transport des médicaments peuvent être négligés. L'épaisseur accrue du polymère est bénéfique pour prolonger le temps de libération du médicament à partir du polymère et augmenter le temps de rétention du médicament dans le tissu, ce qui est cohérent avec les résultats d'un stent plus intégré dans le tissu et d'un coefficient de diffusion plus petit dans le polymère. Grâce à des études expérimentales avec différentes doses de médicament initiales (10%, 20%, 30%) dans le polymère, la relation linéaire entre le dosage initial du médicament et le coefficient de diffusion dans le polymère a été prédite. Afin de vérifier cette relation linéaire, les coefficients de diffusion avec 15% de médicaments dans le polymère sont calculés sur la base de la relation linéaire entre le dosage initial du médicament et le coefficient de diffusion dans le polymère et un bon ajustement a été obtenu pour la libération de médicament à partir du polymère entre les résultats numériques et expérimentaux.

Perspectives

Sur la base de la présente étude numérique, de nombreuses améliorations du modèle numérique doivent être mises en œuvre. De plus, les travaux ultérieurs d'investigations expérimentales restent encore intéressants. Les principaux points ont été élucidés comme suit:

- Modélisation de l'amélioration du flux sanguin dans l'artère

Compte tenu du cas pratique du flux sanguin dans l'artère coronaire, la géométrie de l'artère est compliquée avec un rayon irrégulier au lieu de prendre en compte la géométrie du cylindre à rayon constant. Ainsi l'établissement du modèle géométrique de l'artère coronaire basé sur le cas humain pratique est nécessaire pour être proche de la réalité. Quelques-unes des recherches en cours ont mis en avant la propriété multiphase du flux sanguin au lieu d'une seule phase qui devrait également être mise en œuvre dans les travaux futurs. De plus, la courbure et le mouvement du cœur ont été négligés dans la présente étude et devraient être davantage pris en compte.

- Considérations de physique chimique dans les polymères et les tissus

En ce qui concerne le transport de médicaments à partir du DES, la diffusion de médicaments a été principalement envisagée dans le polymère et les tissus. Cependant, quel que soit le polymère ou le tissu appartiennent tous deux au type de matériau poreux, ainsi l'intrusion d'écoulement dans le polymère et le tissu doit être considérée à la fois. De plus, le tissu en tant que type de matériel biologique, les réactions chimiques à l'intérieur devraient être complétées dans le modèle mathématique. Au lieu du polymère non dégradé, la dégradation du polymère devrait être couverte dans les recherches futures.

- Améliorations des travaux expérimentaux et développement d'un modèle mathématique concernant le transfert de masse

Malgré les travaux numériques, les perspectives concernant les expériences doivent également être soulignées. Dans la présente étude, les travaux expérimentaux occupaient une petite partie de la thèse qui validait la physique fondamentale du processus de transport des médicaments. Ainsi, des travaux plus expérimentaux sont nécessaires et des modèles plus mathématiques doivent être développés, tels que la relation entre la concentration initiale du médicament dans le polymère et le coefficient de diffusion avec d'autres matériaux différents. De plus, l'adoption d'un débit pulsé doit être employée au lieu d'un débit constant.

Jianfei SONG

Etude numérique des paramètres de contrôle du couplage entre l'hémodynamique artérielle et le stent à élution médicamenteuse

Arts Sciences et Technologies **et Métiers**

HESAM UNIVERSITÉ

Résumé : Les maladies cardiovasculaires ont fortement menacé la vie des gens surtout dans les pays occidentaux. Face à la génération de sténoses bloquant la circulation sanguine, l'implantation de stent a été un progrès significatif actuellement pour les traitements. Cependant, les complications consécutives à l'implantation du stent nécessitent nécessairement l'optimisation du stent. Par conséquent, dans la présente étude, la dynamique des fluides computationnelle est effectuée dans le but de mieux reconnaître les caractéristiques physiques et mécaniques du flux sanguin ainsi que le transfert de masse à partir du stent à élution médicamenteuse afin d'améliorer les performances du stent. Compte tenu de la physique complexe liée à l'artère, les caractéristiques de modélisation du flux sanguin dans l'artère coronaire ont été discutées et déterminées dans des vues numériques et mathématiques. La validation de la modélisation a été réalisée en parallèle avec les études préliminaires concernant le flux sanguin dans l'artère sténotique couplant les principales caractéristiques géométriques artérielles: bifurcation et tortuosité séparément. Des analyses diagnostiques et hémodynamiques ont été menées pour évaluer la progression de la sténose. Dans le but d'optimiser le stent, les travaux suivants ont été réalisés en se concentrant sur le flux sanguin dans l'artère coronaire stentée visant à étudier l'interaction entre le flux sanguin et les performances du stent avec différents facteurs de conception géométrique. De plus, compte tenu du transfert de médicament à partir du stent à élution médicamenteuse, le couplage physique entre flux et transfert de masse a été établi numériquement et expérimentalement. Les résultats révèlent qu'une moindre intrusion de stent dans le domaine d'écoulement est bénéfique pour réduire les perturbations d'écoulement et prolonger le temps de rétention du médicament dans les tissus. Une bonne comparaison de la libération de médicament à partir du polymère a été réalisée entre les résultats numériques et expérimentaux.

Mots clés : hémodynamique, topologie d'écoulement, contrainte de cisaillement de la paroi, transfert de masse, stent à élution médicamenteuse, dynamique des fluides computationnelle.

Abstract : Cardiovascular disease has been strongly threatening people's life leading to heart attacks, stokes and even deaths especially in western countries. Confronting the generation of stenosis blocking the blood flow, stent implantation has been a significant progress currently for the treatments. However, the complications following stent implantation require the optimization of stent necessarily. Therefore, in the present study, the computational fluid dynamics is carried out aiming to better acknowledge the physical and mechanical characteristics of blood flow as well as mass transfer from drug-eluting stent (DES) in order to improve the stent performance. Considering the complex physics related in artery, the modeling characteristics of blood flow in coronary artery have been discussed and determined in numerical and mathematical views. Modeling validation has been carried out with the preliminary studies regarding blood flow in stenotic artery coupling the main arterial geometrical characteristics: bifurcation and tortuosity separately. Both hemodynamic and practical diagnostic analysis have been conducted to evaluate the stenosis development, potential stenosis sites and give guidance to practice treatment. With the purpose of stent optimization, the following research were carried out focusing on the blood flow in stented coronary artery aiming to investigate the interaction between the blood flow and stent performance with different geometrical design factors. Furthermore, considering the drug transfer from DES, the physical coupling between flow and mass transfer has been established in order to better acknowledge the drug transport process numerically and experimentally. The results reveal that less intrusion of stent in flow domain is beneficial to reduce flow disturbance and prolong drug retain time in tissue. A good comparison of drug release from polymer has been achieved between simulation and experiment.

Keywords : hemodynamics, flow topology, wall shear stress, mass transfer, drug-eluting stent, computational fluid dynamics.